Characterisation and integration of an optomechanical system for an all-optical CQNC experiment

Von der QUEST-Leibniz-Forschungsschule
der Gottfried Wilhelm Leibniz Universität Hannover

zur Erlangung des akademischen Grades

Doktor der Naturwissenschaften
– Dr. rer. nat. –

genehmigte Dissertation von

M. Sc. Bernd Wolfgang Schulte

2023

Referentin: Prof. Dr. Michèle Heurs
Korreferent: Prof. Dr. Klemens Hammerer
Korreferent: Assoc. Prof. Dr. Stefan Danilishin
Tag der Promotion: 19. September 2023

Abstract

This thesis presents the development and characterisation of an optomechanical system (OMS) with the aim to be part of an all-optical coherent quantum noise cancellation scheme (CQNC), as proposed by Tsang & Caves in 2010. The goal of such a CQNC experiment is to enhance the sensitivity of conventional optomechanical displacement and force detectors. Their sensitivity limit is described by a trade-off between shot noise and quantum backaction noise, forming the standard quantum limit of interferometry. This thesis explores the fundamental principles of CQNC and investigates the potential benefits of modifying the mechanical oscillator's dynamics in the OMS through dynamical backaction using a second beam. The findings suggest that such modifications may be advantageous in the resolved sideband regime. Further investigations are needed due to the vast parameter space involved. However, as shown in previous studies and recapitulated within this thesis, even without a cooling beam quantum backaction noise suppression within an all-optical CQNC experiment is feasible.

The experimental setup for an all-optical CQNC involves a shot noise limited probe beam. To achieve this condition, a filter cavity is used to suppress laser amplitude noise. The results indicate that the amplitude noise in transmission is shot noise limited above frequencies of 1 MHz at a power of 1 mW, making this stabilisation scheme suitable for a CQNC experiment.

The main focus of this thesis is the development and characterisation of the optomechanical system, one subsystem of the CQNC experiment. The work focused on achieving and measuring a high optomechanical coupling strength (g) between light and a silicon nitride membrane representing the mechanical oscillator. Thus, experimental investigations are conducted to determine the optimal position within the optomechanical system where the coupling strength is highest. However, measurements at cryogenic temperatures, necessary for quantum backaction noise limitation, could not be performed due to technical challenges. The operation of the optomechanical oscillator in a cryogenic environment remains a pending task.

Nevertheless, two experiments of the optomechanical system are successfully performed at room temperature and low pressure (10^{-7} mbar). Both experiments, an optomechanically induced transparency (OMIT) experiment and a dynamical backaction (DBA) experiment provide relevant values. The measurements reveal that the membrane used in the experiments is unsuitable for all-optical CQNC due to its quality factors and coupling strength, which do not meet the quantum backaction cooperativity requirement. To improve precision in extracting quality factors and achieve higher sensitivity, a ring-down measurement is recommended for future investigations. Also, once measurements at cryogenic temperature are feasible, techniques like displacement calibration and quantum noise thermometry for accurate temperature measurements have to be established.

In conclusion, the developed optomechanical system holds promise for realising all-optical CQNC once optomechanical oscillators with higher quality factors are used, and cryogenic temperature operation becomes feasible. The thesis also touches upon strategies to surpass the standard quantum limit (SQL) and cancel quantum

backaction noise using an all-optical CQNC scheme with an *effective* negative mass oscillator. Further characterisation and investigation of the positive mass oscillator are conducted to advance the implementation of all-optical CQNC.

Keywords: coherent quantum-noise cancellation, standard quantum limit, optomechanical induced transparency, dynamical backaction, quantum backaction cooperativity

Kurzfassung

Diese Arbeit präsentiert die Charakterisierung und Entwicklung eines optomechanischen Systems (OMS) mit dem Ziel, Teil eines kohärenten Quantenrauschunterdrückungs (CQNC) -Experimentes zu werden. Die grundlegende Idee hierfür wurde bereits 2010 von Tsang & Caves vorgeschlagen. Das Ziel eines solchen CQNC-Experiments ist es, die Empfindlichkeit konventioneller optomechanischer Kraft- und Längendetektoren zu erhöhen. Ihre Empfindlichkeit wird durch einen Kompromiss zwischen quantenmechanischem Rückwirkungsrauschen und Schrotrauschen beschrieben. Das Zusammenspiel beider Rauscharten bildet das Standard-Quantenlimit der Interferometrie.

Diese Arbeit untersucht die grundlegenden Prinzipien von CQNC sowie die möglichen Vorteile einer Modifikation der Dynamik des optomechanischen Systems durch Verwendung eines zusätzlichen Strahles. Die theoretische Betrachtung legt nahe, dass Modifikationen, hervorgerufen durch den zusätzlichen Strahl, nur im Bereich des aufgelösten Seitenbandes (resolved sideband regime) vorteilhaft sein können. Weitere Untersuchungen sind aufgrund des umfangreichen Parameterbereichs erforderlich. Früheren CQNC Studien zeigten, dass selbst ohne einen zusätzlichen Stahl, eine Unterdrückung des quantenmechanischen Rückwirkungsrauschens innerhalb eines CQNC-Experiments möglich ist.

Der experimentelle Aufbau des CQNC Experiments beinhaltet einen Schrottrausch-begrenzten Laserstrahl. Um einen solchen Strahl zu erzeugen, wird eine Filterkavität verwendet, um das Amplitudenrauschen des Lasers zu unterdrücken. Die Messergebnisse zeigen, dass das Amplitudenrauschen des Laserstrahles, aufgrund der Filterkavität, oberhalb einer Frequenz von 1 MHz bei einer Leistung von 1 mW schrottrauschbegrenzt ist. Daher ist diese Filterkavität zur Unterdrückung von Amplitudenrauschen hinsichtlich der Anforderung für ein CQNC Experiment geeignet.

Das Hauptaugenmerk dieser Arbeit liegt auf der Charakterisierung und Entwicklung des optomechanischen Systems, da dieser ein Teilsystem des CQNC-Experiments ist. Die Arbeit konzentriert sich darauf, eine hohe optomechanische Kopplungsstärke zwischen Licht und einer Siliziumnitridmembran als mechanischem Oszillator zu erreichen. Aus diesem Grund wurden experimentelle Untersuchungen durchgeführt, um die Position der Membran im optomechanischen System zu bestimmen, an der die Kopplungsstärke am höchsten ist. Messungen bei kryogenen Temperaturen, die für die Begrenzung des quantenmechanischen Rückwirkungsrauschens erforderlich sind, konnten aufgrund technischer Herausforderungen nicht umgesetzt werden. Der Betrieb des optomechanischen Oszillators in einer kryogenen Umgebung bleibt daher eine offene Aufgabe.

Dennoch wurden zwei Experimente mit dem optomechanischen System erfolgreich bei niedrigem Druck (10^{-7} mbar) und Raumtemperatur durchgeführt. Beide Experimente, das eine Experiment zur optomechanisch induzierten Transparenz (OMIT) und das andere Experiment zur dynamischen Rückwirkung (DBA), lieferten relevante Werte. Die Messungen zeigen jedoch, dass die für die Experimente verwendete Membran aufgrund ihrer Gütefaktoren und Kopplungsstärke nicht für ein

CQNC-Experiment geeignet ist. Um die Genauigkeit der Messung von Gütefaktoren zu verbessern und eine höhere Empfindlichkeit zu erreichen, wird für zukünftige Untersuchungen der Membranen eine Ring-Down-Messung empfohlen. Außerdem müssen, sobald Messungen bei kryogenen Temperaturen möglich sind, Techniken zur genauen Temperaturmessung etabliert werden.

Zusammenfassend hat das entwickelte optomechanische System das Potenzial, ein Teilsystem für ein CQNC-Experiment zu werden, sofern optomechanische Oszillatoren mit höheren Gütefaktoren verwendet werden und der Betrieb bei kryogenen Temperaturen möglich wird. Weiterführende Charakterisierungen und Untersuchungen des Oszillators mit positiver Masse werden durchgeführt, um die Umsetzung von all-optischem CQNC voranzutreiben.

Schlagwörter: kohärente Quantenrauschunterdrückung (CQNC), Standard-Quantenlimit (SQL), optomechanisch induzierte Transparenz (OMIT), dynamische Rückwirkung (DBA), Quantenrückwirkungkooperativität

Contents

List of Figures

List of Tables

Chapter 1

Introduction

Our everyday lives are governed by measurements of distances and lengths. These fundamental physical quantities play a crucial role in our daily activities, e.g. in navigation. Taking GPS as an example, these measurements have to take into account relativistic corrections for useful accuracy. Additionally, the groundbreaking interferometric distance measurement between satellites, capable of sensing earth's gravitational field, has enabled precise gravimetric surveys [Tap+19].

In the microscopic world of quantum physics, lengths and their measurements also play a fundamental role. Here, quantum mechanical fluctuations impose a limit on the achievable accuracy. This is impressively exemplified in ground based interferometric gravitational wave detectors such as Advanced LIGO (aLIGO) [Bui+20]. Here, gravitational waves were directly detected for the first time in 2015 [Abb+16], which ushered in a new era of astrophysics. Achieving this unprecedented level of precision in length measurements is not without challenges. Even if all classical noise sources are diminished, one major obstacle is the presence of quantum backaction noise, where the act of measurement itself introduces disturbances into the system being observed.

Fundamentally, aLIGO interferometrically measures the distance between a Michelson interferometer's free-falling end mirrors (test masses) [Sau17]. When the limiting technical noise sources are sufficiently reduced, the system is inherently susceptible to quantum noise, which manifests as quantum shot noise and quantum backaction noise. Together, these two noise sources form the standard quantum limit (SQL) of interferometry, which limits the sensitivity of current second-generation gravitational wave detectors in most of their detection band [Bui+20]. Quantum shot noise is described by the Poissonian photon statistic of the coherent state of the employed interferometric laser light source. This coherent state, with inherent uncorrelated fluctuations, leads, due to the random arrival of photons at the detector, to the detection of quantum shot noise. To minimise relative shot noise, one can increase the laser power. However, this results in more uncorrelated photons being reflected by the mirrors, causing random momentum transfer and mirror movement due to quantum radiation pressure (shot) noise. Hence, both shot noise and quantum radiation pressure noise stem from the quantum nature of light[1]. While increasing optical power reduces relative shot noise, it amplifies quantum radiation pressure noise as photons randomly interact with mirrors. This causes a quantum backaction, on the light field due to the restoring force on the mirrors.

In conclusion, higher power reduces relative shot noise but increases radiation pressure noise. The trade-off between shot and quantum backaction noise leads to the standard quantum limit (SQL) for optimal displacement sensitivity, assuming these noise sources are uncorrelated. It is worth noting that both quantum backaction and quantum shot noise are clear manifestations of the Heisenberg uncertainty principle.

[1] Weiss already pointed out the quantum backaction noise contribution in 1972 [Wei72]

While quantum shot noise can be readily observed, detecting quantum radiation pressure noise has proven challenging [PPR13].

In treating the SQL, correlations between quantum shot noise and quantum backaction noise are not accessed. However, the correlation between quantum shot noise and quantum backaction noise can be addressed and used to reach sub-SQL performance [DKM19]. For example, one way to surpass the SQL is by utilising ponderomotive squeezing [Nie+17][2], which arises from the correlation between shot noise and quantum backaction noise (induced by optomechanical interaction). Also, a different technique, frequency-dependent squeezing, allows to effectively mitigate both shot noise at high frequencies and quantum radiation pressure noise at low frequencies simultaneously [McC+20; Jun+22].

In general, there are also other strategies to surpass the sensitivity of the SQL. For example, achieving a system within a negative mass frame [TC12; PH15] counteracts the quantum backaction noise and leads to backaction evasion. One such approach involves creating a system within a negative mass frame [TC12; PH15], which can effectively reduce or cancel quantum backaction noise. This negative mass frame was realised by preparing a spin ensemble within a magnetic field. Through coupling light to both the *effective* negative and positive mass frames in an optomechanical setup, quantum backaction cancellation was observed [Moe+17].

This thesis explores an approach to cancel quantum backaction noise, utilising an all-optical coherent quantum noise cancellation (CQNC) scheme. Unlike previous work by Moeller et al. [Moe+17], this scheme incorporates an optical cavity with a beam splitter process and a two-mode conversion process, suggested by Tsang and Caves [TC10], creating an *effective* negative mass oscillator. A sketch of a possible all-optical CQNC realisation is depicted in Figure 1.1.

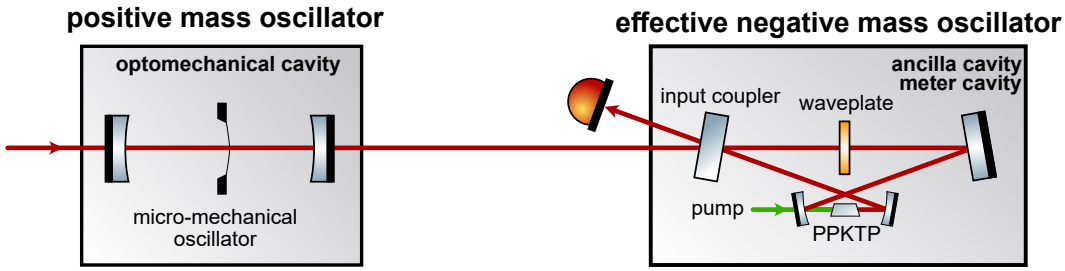

FIGURE 1.1: Proposed cascaded scheme for an all-optical CQNC experiment. The left cavity has an optomechanical device and forms the positive mass oscillator. The right cavity acts as an *effective* negative mass oscillator. It contains a wave-plate coupling two optical modes of orthogonal polarisations (beamsplitter process) and a non-linear (PPKTP-crystal) exemplifying the two-mode process.

The all-optical coherent quantum noise cancellation (CQNC) experiment shown in Figure 1.1 comprises a positive mass oscillator within a cavity, subject to quantum radiation pressure noise. The output field from this optomechanical cavity is directed to an *effective* negative mass oscillator, formed by another cavity with a waveplate and a two-mode conversion process. The waveplate acts as a beam splitter, combining fields of different polarisations. The aim of the negative mass oscillator is to mimic the behaviour of the positive oscillator but with an opposite direction, leading to the effective cancellation of quantum backaction noise.

For successful coherent quantum noise cancellation, two conditions must be satisfied. Firstly, ensuring that both oscillators are equally coupled to the light field

[2]Originally described by [BM67].

is essential, allowing their random motion to be imprinted with equal efficiency to the light field. Secondly, their susceptibility should have equal magnitudes but opposite signs to achieve noise cancellation. As former group members have already explored the feasibility and parameter range for the all-optical CQNC experiment [Wim+14; Ste19; Sch+22; Sch23], this thesis focuses on the positive mass system, which needs to fulfil the specific requirements detailed in [Sch+22]. The thesis will also provide a brief introduction and will discuss the potential for improvement by additional cooling of the positive mass oscillator. Subsequently, the focus is directed towards conducting the initial characterisation and investigation of the positive mass oscillator. This investigation involves measurements of key parameters for CQNC, such as the coupling strength g and mechanical properties of the mechanical oscillator in use. To be more precise, these parameters are derived from two experiments: an optomechanically induced transparency experiment and another experiment utilising dynamical backaction.

Structure of the thesis

Chapter 2 introduces relevant basic building blocks and paves the way for a description of optomechanical interaction and its consequences. Therefore it starts with the classical description of light, including modulation techniques and optical resonators. After this, the quantisation of the electromagnetic light field and the mechanical harmonic oscillator will be explained, revealing that also the electromagnetic field is described by a harmonic oscillator. After this, optomechanical coupling of these two oscillators is introduced, which leads to the classical optomechanical consequences, such as dynamical backaction, and to quantum mechanical consequences resulting in the standard quantum limit (SQL). With this background, the effect of ponderomotive squeezing will be explored, followed by a brief outline of the CQNC experiment and its requirements. At the end of the chapter, a technique using sideband cooling induced by an additional beam to improve the CQNC experiment is shown.

Chapter 3 is devoted to generating shot noise limited light, a basic premise for a successful CQNC experiment. Also, the generation of a second beam, different in frequency, will be explored. This thesis uses this beam for calibration purposes or to apply sideband cooling to the optomechanical oscillator.

Chapter 4 first introduces the mechanical oscillator, a silicon-nitride (SiN) membrane, utilised in this work. Followed by the description of the SiN membrane, the optomechanical setup, and a Fabry-Pérot cavity in which the membrane is embedded will be discussed. As the membrane is close to one end mirror of the cavity, the investigated setup is named membrane-at-the-edge (MatE)-setup [Dum+19]. The investigation contains inferring the membrane position at which the coupling between the membrane and the intracavity field is highest. This is followed by an optomechanically induced transparency (OMIT) experiment used to measure relevant parameters of the MatE setup, especially the coupling strength between the light and the membrane. Also, an experiment utilising the effect of dynamical backaction is used to measure the coupling strength.

Part I

Theory

Chapter 2

Measuring with light

This chapter introduces the thesis's relevant building blocks and paves the way for a description of optomechanical interaction and its consequences.

First, the classical properties of light and modulation techniques are explored in Section 2.1.1. Based on this, a Mach-Zehnder-Interferometer (Section 2.1.3) is introduced to measure the phase-modulation depth.

This description is followed by a discussion of Fabry-Pérot cavities , a specific type of cavity configuration used primarily throughout this study (Section 2.1.4). Within this description the properties and filter characteristics Fabry-Pérot cavities are discussed.

The classical description of the light is finished with an explanation of the Fabry-Pérot cavity. Section 2.2 introduces the quantum mechanical description of light. Thus, Section 2.2 explains the quantisation of the electromagnetic field and reveals that an electromagnetic field is described as a harmonic oscillator. Two utilised detection schemes within this thesis are presented in Section 2.3 to measure the quantum nature of light. After discussing these detection schemes, the basic theory of mechanical oscillators is briefly discussed in the classical and quantum regimes (Section 2.4).

By introducing these two oscillators, namely the electromagnetic field and the mechanical oscillator, Section 2.5 discusses their interaction. Therefore, the equations of motion for a canonical[1] optomechanical system are derived; this canonical system is described by a Fabry-Pérot cavity, with an end mirror treated as the mechanical oscillator. Once the equations of motion for the optomechanical system are derived, classical phenomenons like static bistability (Section 2.5.1), dynamical backaction (Section 2.5.2) and the optomechanically-induced transparency (OMIT) (Section 2.5.5) effect are theoretically described.

After discussing these classical effects, the output spectrum of the optomechanical system is treated quantum mechanically (Section 2.5.7). Within this quantum mechanical treatment, it is shown that by the measurement itself, noise is introduced to the measurement. As this introduced noise acts back on the measurement, it is called quantum backaction noise. Section 2.5.7 discusses the requirement to be sensitive to this noise source. This discussion is followed by introducing the standard quantum limit (SQL). It is shown (Section 2.5.7) that the SQL describes the displacement sensitivity of a conventional phase readout of an optomechanical cavity bounded by quantum backaction and imprecision noise. Fortunately, SQL is not a fundamental limit, as there is no obligation to perform a phase measurement for displacement detection. Hence, an effect which can be used to surpass the SQL is ponderomotive squeezing, explained in Section 2.5.8. Due to ponderomotive squeezing, the signal-to-noise ratio of the measurement can be increased if the noise reduction outweighs the accompanied signal loss.

[1] Canonical - "simplest representative of a class".

However, ponderomotive squeezing only causes an improvement of the displacement sensitivity below the SQL in a small frequency band. To surpass the SQL in a broad frequency range, Section 2.6 briefly discusses an all-optical coherent quantum noise cancellation experiment, which was theoretically investigated by former colleagues in detail [Sch+22; Ste19; Wim+14]. This experiment is the primary motivation to investigate suitable optomechanical systems in Chapter 4. It will be shown that with an ideal all-optical CQNC experiment, the SQL is surpassed by means of backaction noise cancellation at all frequencies except the resonance frequency of the mechanical oscillator. Nevertheless, due to mismatches and losses affecting the ideal CQNC experiment, Section 2.6.4 presents a primary idea to improve the non-ideal CQNC experiment.

The chapter concludes with an overview of the CQNC experiment. In the subsequent chapters (Chapter 3 and Chapter 4), the focus shifts to discussing the experimental setup, where the investigation and enhancement of noise properties in both light and optomechanical systems take place.

2.1 Classical description of light

Before describing the quantum mechanical aspects of light, this section introduces its classical behaviour and consequences, e.g., interference and phase modulation (Section 2.1). After the theoretical description, it will be explained how modulations and interferences are achieved and measured within this thesis by mainly two types of interferometers (Section 2.1.2) .

The starting point for describing light and its propagation is a set of coupled partial differential equations, the so-called Maxwell equations. For an isotropic and insulating medium, the solution of the Maxwell equations is an electric field vector consisting of discrete modes j given by [Ors16; WM08]

$$\mathbf{E}(\mathbf{r},t) = i\sum_j \left(\frac{\hbar\omega_\mathrm{j}}{2\epsilon_0}\right)^{1/2}\left[a_\mathrm{j}\mathbf{u}_\mathrm{j}(\mathbf{r})e^{-i\omega_\mathrm{j}t} - a_\mathrm{j}^*\mathbf{u}_\mathrm{k}^*(\mathbf{r})e^{i\omega_\mathrm{j}t}\right], \tag{2.1}$$

with ϵ_0 being the electric permittivity, ω_j the mode frequency in angular unit and a_j the dimensionless complex amplitude. The factor $u(\mathbf{r})$ (in units of $\mathrm{m}^{3/2}$) contains the information about the polarisation $\hat{\mathbf{e}}^\lambda$ and the spatial mode profile of an electromagnetic plane wave is given by

$$u(\mathbf{r}) = L^{-3/2}\hat{\mathbf{e}}^\lambda e^{i\mathbf{kr}} \tag{2.2}$$

with L being the side length of a cubic volume V, k being the wave vector, and $\hat{\mathbf{e}}^\lambda$ a unit polarisation vector. Equation (2.1) will later also be the starting point for the quantum mechanical description of light in Section 2.2[2]. For now, without loss of generality, a single mode plane wave with angular frequency ω_0 propagating in z-direction and $a = |\alpha|e^{-i\phi_0}$ is assumed, where ϕ_0 describes an arbitrary phase offset of the electromagnetic field. Under these assumptions, the electric field can be written as

$$E(z,t) = E_0\cos(kz - \omega_0 t + \phi_0') = E_0\Re(e^{-i(kz-\omega_0 t+\phi_0)}) \tag{2.3}$$

with $E_0 = \sqrt{\frac{2\hbar\omega_0}{\epsilon_0 V}}|\alpha|$ being the amplitude of the classical electromagnetic wave.

[2]Quantization is done by interpreting a and a^* as operators, $a \to \hat{a}$ and $a^* \to \hat{a}^\dagger$.

Important notational remark

Henceforth within this thesis, a slightly different representation is used for the classical description of the field, namely,

$$E'(z,t) = E_0 e^{-i(kz-\omega_0 t+\phi_0)}\,. \tag{2.4}$$

Comparing this notation with Equation (2.3) reveals that only the real part of $E'(z,t)$ is a meaningful physical quantity. However, transformations of an electric field are more convenient to calculate with the help of the complex representation E'. The usage of the "amplitude-phase" description $E = E_0\cos(\phi)$ is impractical because any transformations are non-linear in phase ϕ due to the cos function[DK12]. The following chapters use the unprimed version of Equation 2.4 for simplicity. Again, the reader should keep in mind that only the real part of this is a meaningful physical quantity.

Optical power

The intensity of the light field is given by the magnitude of the Poynting vector S [Bon+16]

$$|S| = \frac{\epsilon_0 c}{2} E_0^2\,(1+\cos(\omega_0 t)) \tag{2.5}$$

which reduces, to due the bandwidth BW_{PD} of standard photodetectors[3], to

$$|S| = \frac{\epsilon_0 c}{2} E_0^2 \tag{2.6}$$

with the unit $\frac{\mathrm{W}}{\mathrm{m}^2}$. Usually, what is measured is defined as the integral of the intensity $|S|$ over a certain area A, defined as

$$P = \int |S| dA = \frac{\epsilon_0 c}{2} \int E_0 E_0^* dA\,. \tag{2.7}$$

Often and also in this thesis, the calculation of the light power P is without loss of generality done slightly differently, via

$$P = E_0 E_0^*\,. \tag{2.8}$$

The reasoning is that the integration over the area A in Equation (2.7) is done by a measurement with a photodiode so that Equation (2.8) is sufficient to calculate the light power[4].

Modulation techniques

Two modulation techniques are widely used in this thesis and will be explained in this subsection. Experimentally, this thesis uses phase modulation to generate sidebands for two purposes. First, it is used to generate sidebands to create an error signal. Second, it generates a frequency-shifted beam (Section 3.2) as a filter cavity filters one generated sideband from its phase-modulated carrier. The other modulation technique is amplitude modulation which is herein used to explain and

[3] Used laser light frequency $\omega_0 = 2\pi \cdot 282\,\mathrm{THz}$ is much higher as the bandwidth $BW_{\mathrm{PD}} \ll 100\,\mathrm{MHz}$.
[4] For ease of notation the factor $\frac{\epsilon_0 c}{2}$ is neglected in Equation (2.8).

measure amplitude noise properties. Both modulation techniques are explained in the following based on [Bon+16].

2.1.1 Phase modulation

A phase-modulated electromagnetic wave is given by

$$E(z,t) = E_0 e^{i(\omega_0 t + \beta\cos(\omega_{\mathrm{mod}} t))} e^{-ikz} \tag{2.9}$$

where β is the modulation index and ω_{mod} is the modulation frequency. Because the phase modulation does not affect the position z we set without loss of generality $z = 0$ in the following derivations .
Equation (2.9) can be expanded by using the Jacobi–Anger identity [FAS66; DK12]

$$e^{im\cos(\phi)} = \sum_l i^l J_0(m) e^{ij\phi}\,, \tag{2.10}$$

with J_0 being the so-called Bessel functions of the first kind [Kol+95] defined as

$$J_{\mathrm{m}} = (\frac{m}{2})^l \sum_{n=0}^{\infty} \frac{\left(-\frac{m^2}{4}\right)^n}{n!(k+n)!} \tag{2.11}$$

and plotted in Figure 2.1. With these Bessel functions, Equation (2.9) can be written as

$$E(t) = E_0 e^{i(\omega_0 t)} \sum_{l=-\infty}^{\infty} i^l J_0(\beta) e^{il\omega_{\mathrm{mod}} t}\,. \tag{2.12}$$

The solution for a small modulation index ($\beta < 1$) will be investigated to see how the modulation changes the electric field. This solution is given by [Bon+16]

$$E(t) = E_0 e^{i\omega_0 t}\left(J_0(\beta) - iJ_{\text{-}1}(\beta)e^{-i\omega_{\mathrm{mod}} t} + iJ_1(\beta)e^{i\omega_{\mathrm{mod}} t}\right) \tag{2.13}$$

with

$$J_{\text{-}1}(\beta) = (-1)^l J_0(\beta)\,. \tag{2.14}$$

As one can see in Equation (2.13) two additional sidebands with frequency $\pm\omega_{\mathrm{mod}}$ away from the carrier frequency ω_0 are generated.
Small modulation sidebands in this thesis are generated to create a Pound-Drever-Hall error signal [Dre+83; Bla01]. In contrast, higher modulation indices (used in 3.2) are used in conjunction with a filter cavity to create a sideband solely oscillating at frequency $-\omega_{\mathrm{mod}}$ or $+\omega_{\mathrm{mod}}$. In the latter case, a modulation index of roughly $\beta \approx 1.8$ is applied to enhance the first order sideband maximally[5] and suppress the carrier. In contrast, any other orders are additionally decreased in amplitude (Figure 2.1).

[5] From which the filter cavity filters out one sideband.

FIGURE 2.1: Bessel functions of the first kind for k ∈[0,4].

2.1.2 Amplitude modulation

As explained in the introduction of this subsection, amplitude modulation is used within this thesis to explain noise sources. For example, the current noise of a laser diode could lead to amplitude noise and mask the quantum noise in detection, named shot noise[6] (Section 2.2). Slightly different from phase modulation, an amplitude-modulated electromagnetic wave can be written as

$$\begin{aligned} E(z,t) &= E_0(1 + m\cos(\Omega_{\text{mod}}))e^{-i(kz-\omega_0 t+\phi_0)} \\ &= E_0 e^{-i(kz-\omega_0 t+\phi_0)}(1 + \frac{m}{2}e^{i\Omega_{\text{mod}}t} + \frac{m}{2}e^{-i\Omega_{\text{mod}}t}) \end{aligned} \tag{2.15}$$

where m and Ω_{mod} are the modulation index and frequency. Comparing amplitude modulation with phase modulation (Equation (2.12)) shows that amplitude modulation always creates only two sidebands. Also, Equation (2.15) shows that for active elements like lasers, sidebands at $\pm\Omega_{\text{mod}}$ are generated without reducing the amplitude of the carrier.
This differs from amplitude modulation caused by a passive element (like acousto-optic modulators). For the sake of completeness, amplitude modulation induced by passive elements is described by

$$\begin{aligned} E(z,t) &= E_0(1 - \frac{m}{2}(1 - \cos(\Omega_{\text{mod}}))e^{-i(kz-\omega_0 t+\phi_0)} \\ &= E_0 e^{-i(kz-\omega_0 t+\phi_0)}(1 - \frac{m}{2} + \frac{m}{4}e^{i\Omega_{\text{mod}}t} + \frac{m}{4}e^{-i\Omega_{\text{mod}}t}) . \end{aligned} \tag{2.16}$$

In this case, energy is transferred from the carrier to the sidebands, which reduces the amplitude of the carrier while sidebands are created. Hence, due to energy conservation, m is between 0 and 1.

[6]Shot noise will be explained later in Section 2.2.

Theory of used interferometers

In this section, the Mach-Zehnder interferometer, which measures tiny phase fluctuations, will be explained. The theory of a Fabry-Pèrot interferometer follows this description. The Fabry-Pèrot interferometer is a key element in this thesis. It will be used for an optomechanical force sensor and a filter cavity to suppress noise or filter out one phase modulated sideband.

2.1.3 Mach-Zehnder-interferometer

As stated in the previous section, phase modulation is mainly used in this thesis to create a Pound-Drever-Hall [Bla01] error signal or to create a single sideband oscillating at $\omega_0 + \Omega_{\mathrm{mod}}$. Additionally, in Section 4.3.1, phase modulation sidebands are used for an optomechanically induced transparency (OMIT) experiment. A signal proportional to the modulation strength β is needed in this OMIT experiment and measured with a Mach-Zehnder-interferometer (MZI). Therefore, this section explains the specific principle of the MZI used in Section 4.3.1. More specifically, it will be shown that an MZI locked on mid-fringe converts a phase modulation, induced in one arm, into an amplitude modulation at the output of the MZI.

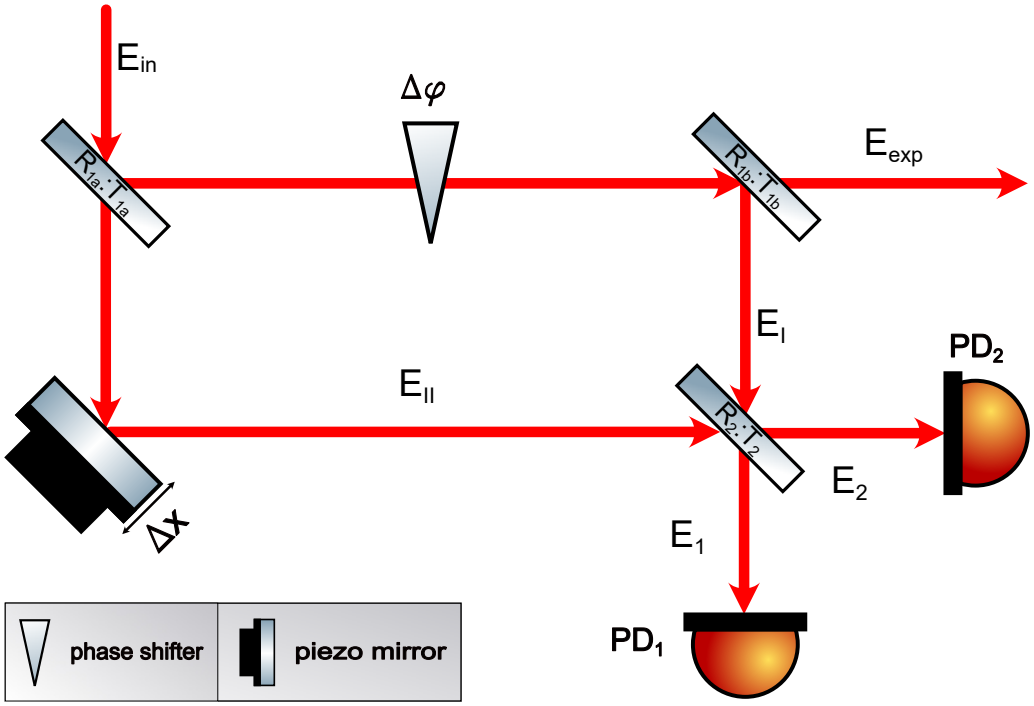

FIGURE 2.2: Principle layout of the Mach-Zehnder-interferometer used in the experiments consisting of three beamsplitters, two photodetectors, a phase shifter, and a piezoelectric actuated mirror.

The MZI used for the OMIT measurement is depicted in Figure 2.2. It consists of three beam splitters BS_{j} with splitting ratios $R_{\mathrm{j}} : T_{\mathrm{j}}$ ($j \in (1\mathrm{a}, 1\mathrm{b}, 2)$), one phase shifter introducing a phase shift $\Delta\phi$, one mirror, whose displacement Δx can be actively controlled via a piezoelectric actuator, and two photodetectors PD_{i} at its output. This MZI scheme slightly differs from usual textbook versions (like in [BR19]) in which

usually two mirrors and two beam splitters are used[7].
This difference is because the MZI described in this section monitors the phase modulation strength β of a light field E_{exp} sent to another experiment. For this purpose, the MZI depicted in Figure 2.2 needs a pick-off for light, which is ensured by the additional beam splitter BS_{1b}.
Including the additional beam splitter, the electromagnetic fields of the MZI shown in Figure 2.2 are given by

$$E_{\text{in}}(z,t) = E_0 e^{-i(kz-\omega_0 t)}\,, \tag{2.17a}$$
$$E_{\text{I}}(z,t) = E_0\sqrt{R_{1a}R_{1b}}e^{-i(kz-\omega_0 t+\Delta\phi)}\,, \tag{2.17b}$$
$$E_{\text{II}}(z,t) = E_0 i\sqrt{T_{1a}}e^{-i(k(z+\Delta x)-\omega_0 t)}\,, \tag{2.17c}$$
$$E_{\text{exp}}(z,t) = E_0\sqrt{R_{1a}T_{1b}}e^{-i(kz-\omega_0 t+\Delta\phi)}\,. \tag{2.17d}$$
$$\begin{aligned} E_1(z,t) &= \sqrt{R_2}E_{\text{II}}(z,t) + i\sqrt{T_2}E_{\text{I}}(z,t)\,, \\ &= i\sqrt{T_{1a}R_2}E_0 e^{-i(k(z+\Delta x)-\omega_0 t)} + i\sqrt{R_{1a}R_{1b}T_2}E_0 e^{-i(kz-\omega_0 t+\Delta\phi)}\,. \end{aligned} \tag{2.17e}$$
$$\begin{aligned} E_2(z,t) &= i\sqrt{T_2}E_{\text{II}}(z,t) + \sqrt{R_2}E_{\text{I}}(z,t)\,, \\ &= -\sqrt{T_{1a}T_2}E_0 e^{-i(k(z+\Delta x)-\omega_0 t)} + \sqrt{R_{1a}R_{1b}R_2}E_0 e^{-ik(z-\omega_0 t+\Delta\phi)}\,. \end{aligned} \tag{2.17f}$$

Due to energy conservation, the splitting ratio of any beam splitter has to fulfil

$$R_{\text{j}} + T_{\text{j}} + \delta_{\text{BS}_{\text{j}}} = 1 \tag{2.18}$$

with ($j \in (1a, 1b, 2)$) and $\delta_{\text{BS}_{\text{j}}}$ describing losses[8]. For the lossless case ($\delta_{\text{BS}_{\text{j}}} = 0$) the output power P_{i} ($i = 1, 2$) is calculated as

$$\begin{aligned} P_1 &= E_1(z,t)(E_1(z,t))^* = |E_1(z,t)|^2 \\ &= P_0^2\left(R_2T_{1a} + R_{1a}R_{1b}T_2 + 2\sqrt{R_{1a}R_{1b}R_2T_{1a}T_2}\cos(k\Delta x - \Delta_\phi)\right) \\ P_2 &= E_2(z,t)(E_2(z,t))^* = |E_2(z,t)|^2 \\ &= P_0^2\left(R_2R_{1a}R_{1b} + T_{1a}T_2 - 2\sqrt{R_{1a}R_{1b}R_2T_{1a}T_2}\cos(k\Delta x - \Delta_\phi)\right)\,, \end{aligned} \tag{2.19}$$

with $P_0 = |E_0|^2$. In the experiment we set $R_1 = R_{1a} \cdot R_{1b} = T_{1a}$ to ensure that the power of field E_{I} and E_{II} interfering at the beam splitter BS_2 are the same. Hence in the actual experiment (Section 4.3.1), power beam splitters are replaced by $\frac{\lambda}{2}$-wave plates in conjunction with a polarising beam splitter, to employ tunable beamsplitters. Additionally, the splitting ratio of beamsplitter BS_2 is set to $R_2 = T_2$. With these assumptions, the output power $P_{1,2}$ becomes

$$\begin{aligned} P_1 &= 2R_1R_2P_0\left(1 + \cos\left(k\Delta x - \Delta\phi\right)\right) \\ P_2 &= 2R_1R_2P_0\left(1 - \cos\left(k\Delta x - \Delta\phi\right)\right)\,. \end{aligned} \tag{2.20}$$

Figure 2.3 shows the output power $P_{1,2}$ of the MZI with $\Delta\phi = 0$, lossless beam splitters ($T_{\text{j}} = 1 - R_{\text{i}}$), $R_{1a} = \frac{5}{120}$, $R_{1b} = \frac{5}{115}$ and $R_2 = \frac{1}{2}$[9].

[7] The transfer between this scheme and the one in [BR19] can be done via $R_{1b} = 1$ and $R_{1b} + T_{1b} = 1$.
[8] For sake of clarity in Figure 2.2 $\delta_{\text{BS}_{\text{j}}}$ is omitted for beamsplitter description.
[9] Values approximately like in OMIT experiment (Section 4.3.1) where $P_{\text{in}} \approx 2mW$, $P_{\text{exp}} \approx 1mW$ and $P_{\text{I}} = P_{\text{II}} \approx 500\mu W$.

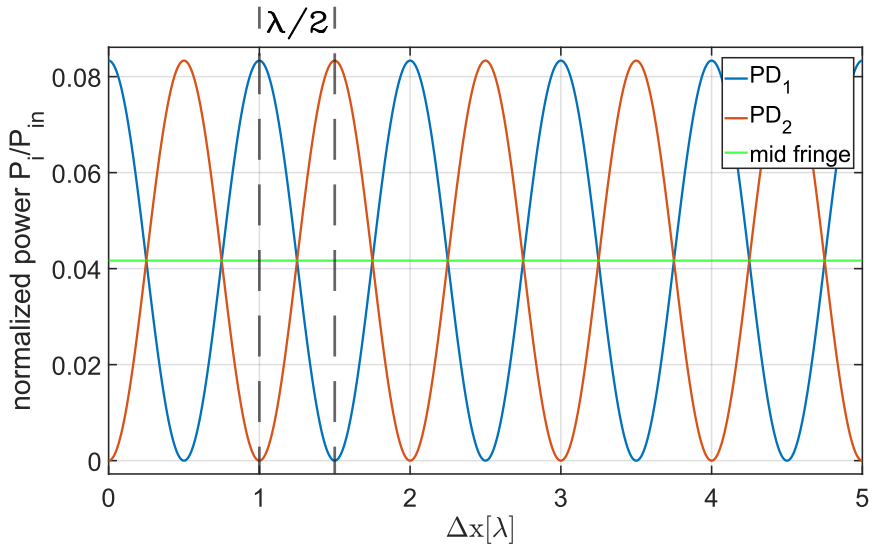

FIGURE 2.3: Power P_1 and P_2 at the output of the MZI (depicted in fig.2.2) over displacement Δx with $\Delta\phi = 0$, $R_{1a} = \frac{5}{120}$, $R_{1b} = \frac{5}{115}$, $R_2 = \frac{1}{2}$ and $T_i - R_i = 1$. The vertical dashed lines indicate the distance between two consecutive minima and maxima measured by one photodiode PD_i, whereas the green line indicates the mid fringe.

As it can be seen in Figure 2.3, the output power P_i is linear in small variations of Δx ($\Delta x = \lambda/4 + n\lambda/2$ with $n \in \mathbb{N}$) at mid-fringe. For an MZI at locked on mid-fringe [10] introduced phase modulations $\Delta\phi = \beta\cos(\Omega_{mod}t)$ with small modulation depths ($\beta \ll 1$) are transduced to amplitude modulations at the output. The phase modulation in Figure 2.2 is introduced through a phase shifter. With this the measured power P_i at the output reads[11,12]

$$\begin{aligned} P_1 &\approx 2R_1R_2\Big(1 + \beta\cos(\omega_{mod}t)\Big)\,, \\ P_2 &\approx 2R_1R_2\left(1 - \beta\cos(\omega_{mod}t)\right)\,. \end{aligned} \tag{2.21}$$

Similarly, the phase-modulated electric field E_{exp} sent to the experiment remains unaffected by the MZI measurement and is still given by Equation 2.17d. Hence the modulation depth β of the light sent to the experiment can be deduced by the MZI.

$$E_{exp}(z,t) = E_0\sqrt{R_{1a}T_{1b}}e^{-i(kz-\omega_0 t+\beta\cos(\omega_{mod}t))}\,. \tag{2.22}$$

A plot of the output powers $P_{1,2}$ calculated in Equation 2.21 for an MZI locked on mid-fringe, with an induced phase modulation of $\Delta\phi = \beta\cos(\omega_{mod}t)$ can be seen in Figure 2.4. In this figure, the reflectivities R_j are the same as in Figure 2.3.

[10] Accomplished by piezoelectric actuated mirror.
[11] $\cos(\frac{\pi}{2} - x) = \sin(x)$.
[12] Small angle approximation: $\sin(x) \approx x$, for $x \ll 1$.

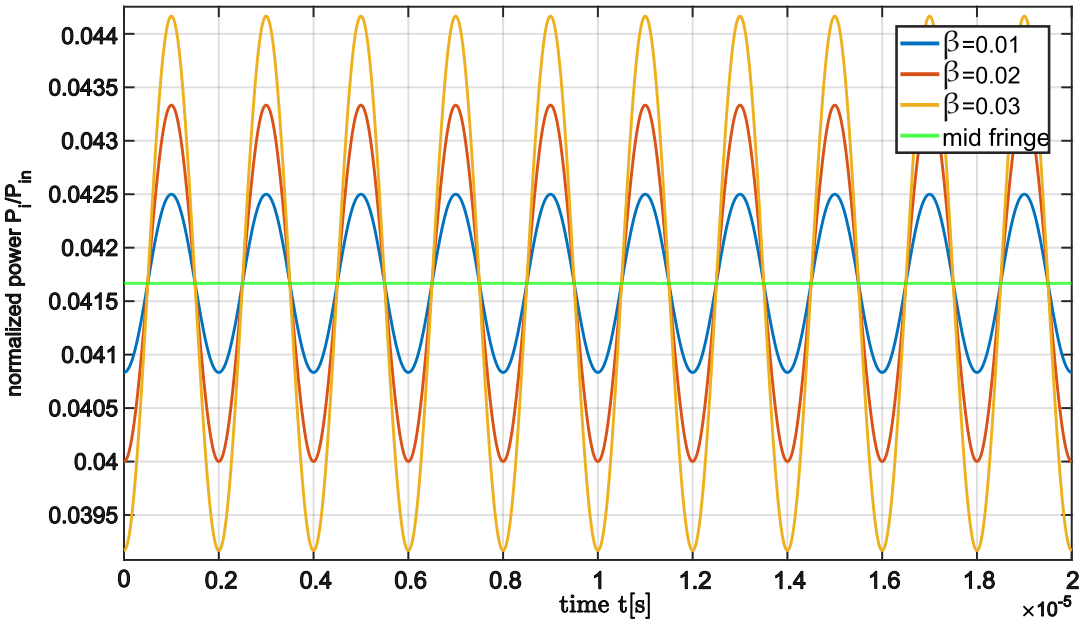

FIGURE 2.4: Power P_1 at the output of the mid fringe locked MZI ($k\Delta x = \lambda/4$) over time t measured by PD_1 for different phase modulation strengths β with $\omega_{\mathrm{mod}}/(2\pi) = 500\,\mathrm{kHz}$. As in Figure 2.3 the reflectivity and transmissivity are given by $R_{1a} = \frac{5}{120}$, $R_{1b} = \frac{5}{115}$, $R_2 = \frac{1}{2}$ and $R_i + T_i = 1$. The green line indicates the mid-fringe.

Figure 2.4, together with Equation (2.21) reveals that the described MZI locked on mid-fringe converts a phase modulation $\Delta\phi = \beta\cos(\omega_{\mathrm{mod}}t)$, induced in one arm, into an amplitude modulation at the output of the MZI. Moreover, the amplitude of the output power $P_{1,2}$ at the output is proportional to the induced phase modulation. Even more important (for the OMIT experiment (4.3.1)), it has been shown that the measured amplitude of the $P_{1,2}$ is also proportional to the phase modulation depth β of the field E_{exp} sent to the experiment.

2.1.4 Fabry-Pérot cavity

Optical resonators are a crucial element for optomechanical experiments, like the coherent quantum noise cancellation experiment in Section 2.6.2. On the one hand, Fabry-Pérot cavities can be used as filters to generate shot noise-limited light (Section 3.1), and on the other hand, they serve as a component for optomechanical systems to amplify the coupling between light and mechanical devices (Section 2.5). For these reasons, optical resonators, especially the Fabry-Pérot cavity resonators, are an essential part of this work, and therefore, their characteristics are introduced within this Section.

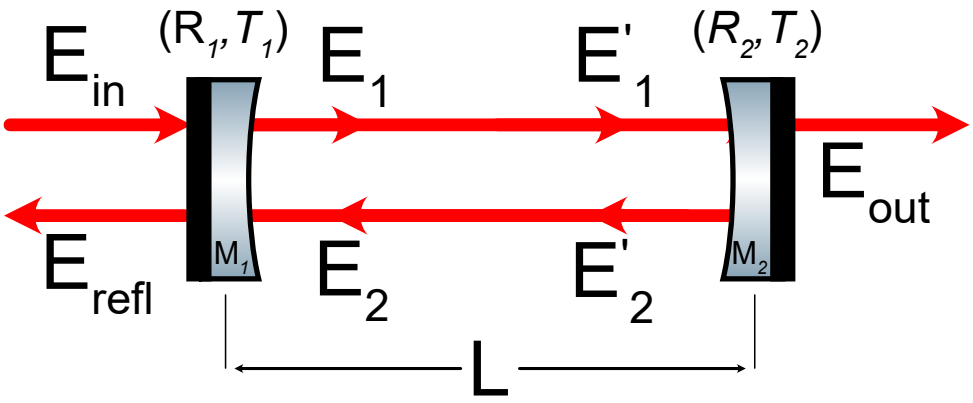

FIGURE 2.5: principle layout of a Fabry-Pérot cavity consisting of two mirrors M_i with power reflectivity R_i and transmittivity T_i. The distance between the mirrors is given by the length L.

A sketch of a Fabry-Pérot cavity and the electromagnetic fields can be seen in Figure 2.5. The electromagnetic fields depicted in Figure 2.5 can be written as [BR19; Bon+16]

$$E_1 = i\sqrt{T_1}E_{\text{in}} + \sqrt{R_1}E_2\,, \tag{2.23a}$$
$$E_1' = e^{-ikL}E_1\,, \tag{2.23b}$$
$$E_{\text{out}} = i\sqrt{T_2}E_1'\,, \tag{2.23c}$$
$$E_2 = \sqrt{R_2}E_1'\,, \tag{2.23d}$$
$$E_2' = e^{-ikL}E_2\,, \tag{2.23e}$$
$$E_{\text{refl}} = \sqrt{R_1}E_{\text{in}} + i\sqrt{T_1}E_2'\,, \tag{2.23f}$$

with $R_{1,2}$ and $T_{1,2}$ describing the power reflectivity and transmissivity of the mirror $M_{1,2}$ and L being the cavity length. As in Equation (2.18), the reflectivity and transmissivity have to fulfill $R_i + T_i + \delta_i = 1$, where δ_i accounts for losses induced by mirror i (e.g., by absorption). From the field Equations (2.23) the intracavity power $P_1 = |E_1|^2$ is deduced as

$$\begin{aligned}\frac{|E_1|^2}{|E_{\text{in}}|^2} &= \frac{T_1}{1-\sqrt{R_1R_2}e^{2ikL}} \\ &= \frac{T_1}{1+R_1R_2-2\sqrt{R_1R_2}\cos(2kL)}\,.\end{aligned} \tag{2.24}$$

Two examples of the intracavity power $|E_1(2kL)|^2$ together with the reflected phase $\arg(E_{\text{refl}})$ are shown in Figure 2.6.

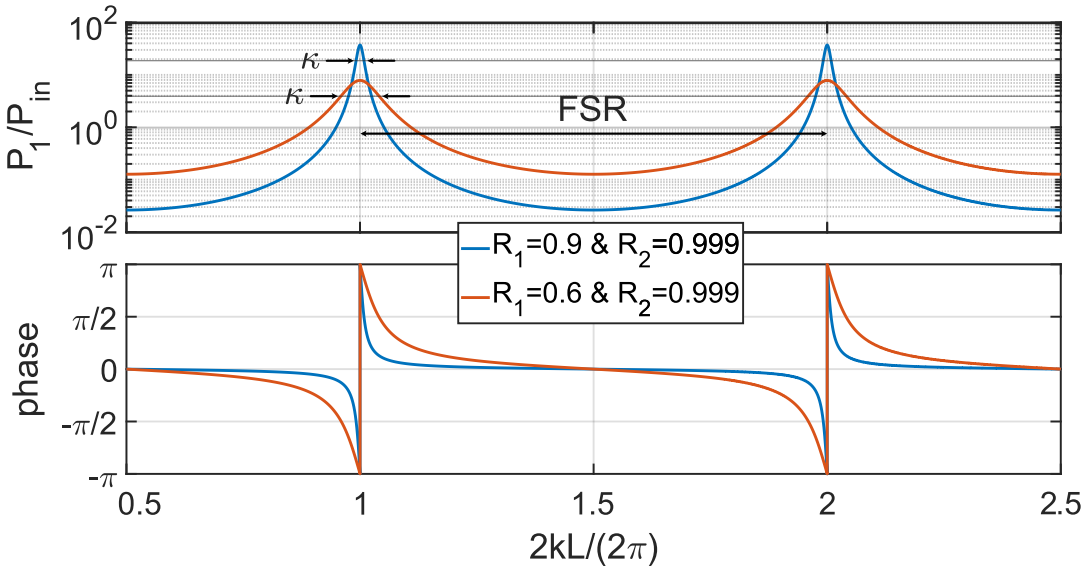

FIGURE 2.6: Intracavity Power P_1/P_{in} over $2kL$, for different mirror reflectivity R_i. The free spectral range FSR and the linewidth κ are also visualized.

The behaviour of the reflected phase will be used in Section 4.2.1 to explain the resonant behaviour of a Fabry-Pérot cavity with a thin low reflective membrane inside. Figure 2.6 also showcases two important cavity parameters, namely the free spectral range (FSR) and the cavity linewidth (defined as FWHM). These parameters will be introduced in the following. As depicted in Figure 2.6 the distance between consecutive resonances defines the FSR. From Equation (2.24) and evidenced by Figure 2.6 the maximum circulating power $|E_1^{\max}|^2$ is reached when the cosine in the denominator satisfies the resonant condition

$$\cos(2kL) = 1\,. \tag{2.25}$$

This condition can be achieved either by altering the length L or by changing $k = \frac{2\pi}{\lambda_{\text{laser}}} = \frac{2\pi f_{\text{laser}}}{c}$ via the laser frequency f_{laser}. For a fixed length L, the resonant condition is fulfilled when the frequency f_{laser} satisfies the relation

$$f_{\text{res}} = nc/2L = n \cdot FSR_{\delta\nu}\,, \tag{2.26}$$

with $n \in \mathbb{N}$ and $FSR_{\delta\nu} = c/2L$ describing the free spectral range in the frequency domain[13].

On the other hand, for a fixed laser frequency f_{laser}, on can show that the resonant condition is fulfilled if the length L is equal to

$$L_{\text{res}} = n\frac{\lambda_{\text{laser}}}{2} = n \cdot FSR_{\lambda}\,, \tag{2.27}$$

with $FSR_{\lambda} = \frac{\lambda_{\text{laser}}}{2}$ and again with $n \in \mathbb{N}$. Correspondingly to Equation (2.26) $FSR_{\delta\nu}$ describes the spacing between consecutive resonances, but in the spatial domain. Besides the FSR, the other important parameter is the linewidth κ, which describes the leakage rate of the intracavity field. In this thesis, κ is defined as the full-width half maximum (FWHM) and describes the frequency at which the circulating power

[13] $FSR_{\delta\nu}$ is defined within this thesis in **non**-linear units.

$|E_1|^2$ becomes half its maximum:

$$|E_1(f_{\text{res}} \pm \frac{\kappa}{2})|^2 \stackrel{!}{=} \frac{1}{2}|E_1(f_{\text{res}})|\,. \tag{2.28}$$

Together with the round-trip time $\tau_{\text{RT}} = \frac{2L}{c}$ and the coupling rates associated with mirror 1 and 2

$$\frac{\kappa_{1,2}}{2\pi} = \frac{T_{1,2}}{\tau_{\text{RT}}} \tag{2.29}$$

the leakage rate κ can be written as

$$\begin{aligned} \kappa &= \frac{T_1 + T_2 + \delta_1 + \delta_2 + \delta_{\text{loss}}}{\tau_{\text{RT}}} \\ &= \kappa_1 + \kappa_2 + \kappa_{\text{loss}} \end{aligned} \tag{2.30}$$

where δ_{loss} and κ_{loss} describes additional losses not associated with mirrors, such as absorption.

Filter characteristic of a Fabry-Pérot cavity

To describe the filter characteristics used in Section 3.1 and Section 3.2 of the Fabry-Pérot cavity or a ring cavity, the time evolution $E_1(t)$ will be calculated. For this, the intracavity field $E_1(\tau_{\text{RT}})$ on the time scale of a round-trip τ_{RT} is used, which is given by [Wil12]

$$E_1(t + \tau_{\text{RT}}) = i\sqrt{T_1}E_{\text{in}}(t) + \sqrt{R_1 R_2}e^{2ikL}E_1(t)\,. \tag{2.31}$$

Assuming a laser frequency $\omega_0 = 2\pi f_{\text{laser}}$ close to the cavity resonance ω_{cav} and introducing the detuning Δ

$$\Delta = \omega_{\text{cav}} - \omega_0 \tag{2.32}$$

the time evolution $E_1(t)$ is calculated as [14]

$$\dot{E}_1(t) \approx \frac{E_1(t + \tau_{\text{RT}}) - E_1(t)}{\tau_{\text{RT}}} \tag{2.33a}$$

$$\approx \left(i\Delta - \frac{\kappa}{2}\right) E_1 + \frac{i\sqrt{T_1}}{\tau_{\text{RT}}}E_{\text{in}} \tag{2.33b}$$

$$= \left(i\Delta - \frac{\kappa}{2}\right) E_1 + \frac{i\sqrt{\kappa_1}}{\sqrt{\tau_{\text{RT}}}}E_{\text{in}}\,. \tag{2.33c}$$

The Fourier transformation of the equation yields

$$|E_1(\omega)|^2 = \frac{\kappa_1}{(\kappa/2)^2 + (\Delta + \Omega)^2}|E_{\text{in}}(\Omega)|^2/\tau_{\text{RT}}\,. \tag{2.34}$$

To calculate the transmitted output field E_{out}, Equation (2.34) has to be multiplied by T_2, which results in

$$\begin{aligned} |E_{\text{out}}(\omega)|^2 &= \frac{\kappa_1\kappa_2}{(\kappa/2)^2}\frac{1}{1 + \left(\frac{\Delta+\omega}{\kappa/2}\right)^2}|E_{\text{in}}(\omega)|^2 \\ &= \frac{\kappa_1\kappa_2}{(\kappa/2)^2}|\chi_{\text{LP}}(\omega')|^2|E_{\text{in}}(\omega)|^2 \end{aligned} \tag{2.35}$$

[14] Also high mirror reflectivities are assumed $R_{1,2} \approx 1 \rightarrow \sqrt{1 - T_{1,2}} \approx 1 - \frac{T_{1,2}}{2}$.

Here $\chi_{\mathrm{LP}}(\omega') = 1/(1 - i\frac{\Delta+\omega}{\kappa/2})$ describes a low pass filter with respect to the frequency $\omega' = \Delta + \omega$ with the corner frequency given by $\kappa/2$. These filter characteristic of the cavity is used within this thesis to suppress laser amplitude noise (Section 3.1 or to filter out one sideband of a phase modulated beam to generate a light field solely oscillating at a $\omega_0 + \omega_{\mathrm{mod}}$ (Section 3.2). In both cases, a critically coupled cavity is desirable ($\kappa/2 = \kappa_1 = \kappa_2$,) which results in

$$|E_{\mathrm{out}}|^2 = \frac{1}{1 + \left(\frac{\Delta+\omega}{\kappa/2}\right)^2} |E_{\mathrm{in}}(\omega)|^2 \tag{2.36a}$$

$$= |\chi_{\mathrm{LP}}(\omega')|^2 |E_{\mathrm{in}}(\omega)|^2 . \tag{2.36b}$$

The advantage of a critically coupled cavity is that the carrier at resonance $\Delta = \omega_{\mathrm{cav}} - \omega_0 = 0$ is completely transmitted at $\omega = 0$. At the same time, unwanted sidebands at frequency $\omega > 0$ are suppressed because of the low pass filter characteristic. For now, the introduced characteristics and features of optical resonators are sufficient, and more details for interested readers should refer to [BR19; Bon+16].

2.2 Quantum mechanical description of light

In this section, the quantum mechanical properties of light will be introduced. The starting point is the electric field given in Section 2.1. For the sake of simplicity, the electric field is given by a plane wave propagating in z-direction and results in [15]

$$E(z,t) = i \sum_j \left(\frac{\hbar\omega_j}{2\epsilon_0 V}\right)^{1/2} \left[a_j e^{i(kz-\omega_j t)} - a_j^* e^{-i(kz-\omega_j t)}\right] \tag{2.37}$$

with $V = L^3$. The following overview of the quantisation of the electromagnetic field Equation (2.37) and its properties is based on [GK04; WM08]. The quantisation of the electromagnetic field is accomplished by converting the dimensionless amplitude a into mutually adjoint operators

$$a_j \to \hat{a}_j, \quad a_j^* \to \hat{a}_j^\dagger \tag{2.38}$$

for which are commutation relations

$$[\hat{a}_j, \hat{a}_{j'}] = [\hat{a}_j^\dagger, \hat{a}_{j'}^\dagger] = 0, \quad [\hat{a}_j, \hat{a}_{j'}^\dagger] = \delta_{jj'} . \tag{2.39}$$

In the following, the summation over j will be omitted because, in the experiments in this thesis, a monochromatic laser source is used and can be approximated by a single-mode source. With this and Equation (2.38) in mind the electric field Equation (2.37) changes to

$$\hat{E}(z,t) = i \left(\frac{\hbar\omega_0}{2\epsilon_0 V}\right)^{1/2} \left[\hat{a} e^{i(kz-\omega_0 t)} - \hat{a}_j^\dagger e^{-i(kz-\omega_0 t)}\right] \tag{2.40}$$

with ω_0 being the laser frequency in angular units. Also the Hamiltonian of an electromagnetic field is given as[Ors16]

$$H = \frac{1}{2} \int \left(\epsilon_0 \mathbf{E}^2 + \mu_0 \mathbf{H}^2\right) d\mathbf{r} , \tag{2.41}$$

[15] $u(\mathbf{r}) \to u(x) = L^{-3/2} e^{ikx}$.

with $\mu_0\mathbf{H}$ describing the magnetic field[16]. The Hamiltonian is rewritten with the commutation relation (Equation (2.38)) as

$$\hat{H} = \hbar\omega_0 \left(\hat{a}^\dagger \hat{a} + \frac{1}{2}\right) \tag{2.42}$$

where now $\hat{H}$ describes an energy operator associated with the total energy of the system.

2.2.1 Eigenstates and energy of quantised field

To make sense of the Hamiltonian operator $\hat{H}$ given in Equation (2.42), one can look at the energy eigenvalue Equation [GK04]

$$\begin{aligned} \hat{H}\,|n\rangle &= \hbar\omega_0 \left(\hat{a}^\dagger \hat{a} + \frac{1}{2}\right) |n\rangle = E_\mathrm{n}\,|n\rangle \\ &= \hbar\omega_0 \left(\hat{n} + \frac{1}{2}\right) |n\rangle = E_\mathrm{n}\,|n\rangle\ . \end{aligned} \tag{2.43}$$

The eigenvalue Equation (2.43) relates the so-called number- or Fock state $|n\rangle$ to an eigenvalue E_n consisting of n photons, where $\hat{n}$ is the number operator defined as $\hat{n} = \hat{a}^\dagger\hat{a}$. Together with the commutation relation (Equation (2.38)) one can show that [GK04]

$$\hat{H}(\hat{a}^\dagger\,|n\rangle) = (E_\mathrm{n} + \hbar\omega_0)\,(\hat{a}^\dagger\,|n\rangle) \tag{2.44}$$

and

$$\hat{H}(\hat{a}\,|n\rangle) = (E_\mathrm{n} - \hbar\omega_0)\,(\hat{a}\,|n\rangle)\,. \tag{2.45}$$

These equations reveal that the creation operator $\hat{a}^\dagger$ creates a new eigenstate $\hat{a}^\dagger\,|n\rangle$ with raised energy $E_\mathrm{n} + \hbar\omega_0$ while the annihilation operator $\hat{a}$ creates an eigenstate $\hat{a}\,|n\rangle$ with lower energy $E_\mathrm{n} - \hbar\omega_0$. Lower energy levels can be reached by using the annihilation operator $\hat{a}$ multiple times. Because the lowest energy cannot be negative, there must be a ground state $|0\rangle$ that satisfies the following condition [GK04]

$$\hat{H}(\hat{a}^\dagger\,|0\rangle) = (E_\mathrm{n} + \hbar\omega_0)\,|n\rangle\,(\hat{a}^\dagger\,|n\rangle) \tag{2.46}$$

from which $\hat{a}\,|0\rangle = 0$ follows. So the eigenvalue problem of the groundstate $|0\rangle$ is given by

$$\hat{H}\,|0\rangle) = \hbar\omega_0 \left(\hat{a}^\dagger \hat{a} + \frac{1}{2}\right) |0\rangle = \frac{1}{2}\hbar\omega_0\,|0\rangle \tag{2.47}$$

and defines the lowest energy eigenvalue $E_0 = \frac{1}{2}\hbar\omega$ of the *vacuum state*. In general the energy E_n is given by

$$E_\mathrm{n} = \hbar\omega_0 \left(n + \frac{1}{2}\right), \qquad n \in \mathbb{N}\,. \tag{2.48}$$

For completeness, the eigenstates $|n\rangle$ are the Fock number with a defined photon number n and are calculated as[17]

$$|n\rangle = \frac{(\hat{a}^\dagger)^n}{\sqrt{n!}}\,|0\rangle\ . \tag{2.49}$$

[16] For Completness: $\mu_0\vec{\mathbf{H}} = \frac{-i}{c\mu_0}\left(\frac{\hbar\omega_0}{2\epsilon_0 V}\right)^{1/2} \vec{\mathbf{e}} \times \vec{\mathbf{k}} \left(\hat{a}e^{i(kz-\omega_0 t)} - \hat{a}_\mathrm{j}^\dagger e^{-i(kz-\omega_0 t)}\right)$[Ors16].

[17] Follows from the normalisation $\langle n|n\rangle = 1$.

2.2.2 Coherent state

For an operator $\hat{o}$ acting on a state $|x\rangle$ the expectation value is defined as $\langle x\rangle_o = \langle x|\hat{o}|x\rangle$. As the expectation value $\langle n|\hat{E}(x,t)|n\rangle = 0$ of the number state $|n\rangle$ equals 0, the number state is not representative to resemble the classical field. A state which solves this issue is the coherent state $|\alpha\rangle$ which is constructed as [GK04]

$$|\alpha\rangle = e^{-\frac{1}{2}|\alpha|^2} \sum_{n=0}^{\infty} \frac{\alpha^n}{\sqrt{n!}} |n\rangle \tag{2.50}$$

where α is the eigenvalue satisfying

$$\hat{a}\,|\alpha\rangle = \alpha\,|\alpha\rangle\ . \tag{2.51}$$

With $\alpha = |\alpha|e^{i\theta}$, the state $|\alpha\rangle$ has a non-vanishing expectation value for the electric field operator $\hat{E}(x,t)$

$$\langle\alpha|\hat{E}(x,t)|\alpha\rangle = |\alpha|\sqrt{\frac{2\hbar\omega_0}{\epsilon_0 V}}\sin\left(\omega_0 t - kr - \theta\right) \tag{2.52}$$

which by comparing with Equation (2.3) looks like the classical electromagnetic field [18]. It is also apparent that α is related to the classical amplitude of an electromagnetic field. Because of

$$\bar{n} = \langle\alpha|\hat{n}|\alpha\rangle = |\alpha|^2\,, \tag{2.53}$$

$|\alpha|$ also describes the square root of the average photon number $\bar{n}$ of the field. Note also that the fluctuations of the electric field ΔE is given by

$$\Delta E = \sqrt{\langle\hat{E}^2(x,t)\rangle - \langle\hat{E}(x,t)\rangle^2} = \left(\frac{\hbar\omega_0}{2\epsilon_0 V}\right)^{\frac{1}{2}} \tag{2.54}$$

and hence is independent of the amplitude strength α. Importantly, the fluctuations of a coherent state $|\alpha\rangle$ are the same as of the number state $|n=0\rangle$[19]. So, the fluctuations of the coherent state are the same as the fluctuations of the so-called *vacuum state* $|n=0\rangle$ with energy $\frac{\hbar\omega_0}{2}$ (according to Equation 2.48). This result also manifests in the fact that a coherent state $|\alpha\rangle$ can be constructed by displacing the vacuum state $|0\rangle$ via a displacement operator $\hat{D}(\alpha)$ [GK04; WM08]

$$|\alpha\rangle = \hat{D}(\alpha)\,|0\rangle = e^{-\frac{1}{2}|\alpha|^2} \sum_{n=0}^{\infty} \frac{\alpha^n}{\sqrt{n!}} |n\rangle\ , \tag{2.55}$$

with

$$\hat{D}(\alpha) = e^{\alpha\hat{a}^\dagger - \alpha^*\hat{a}}\,. \tag{2.56}$$

The phase space representation is most suitable to visualise the construction of a coherent state $|\alpha\rangle$ via the displacement of the vacuum $|0\rangle$. For this purpose, the next chapter introduces quadrature operators, which are used for moving into phase space representations.

[18] For $\theta \to \phi' - \frac{\pi}{2}$.
[19] Equation (2.50) reveals that $|\hat{\alpha}=0\rangle = |\hat{n}=0\rangle$.

2.2.3 Quadrature operators and squeezed states

The amplitude quadrature X_1 and the phase quadrature X_2 are defined as[20]

$$\hat{X}_1 = \frac{1}{\sqrt{2}}\left(\hat{a} + \hat{a}^\dagger\right), \quad \hat{X}_2 = \frac{1}{i\sqrt{2}}\left(\hat{a} - \hat{a}^\dagger\right) \tag{2.57}$$

fulfilling the commutation relation

$$[\hat{X}_1, \hat{X}_2] = i. \tag{2.58}$$

Rewriting the Hamiltonian (Equation(2.42)) with the optical quadratures $\hat{X}_1$ and $\hat{X}_2$ as

$$\hat{H} = \frac{\hbar\omega_0}{2}\left(\hat{X}_1^2 + \hat{X}_2^2\right). \tag{2.59}$$

and comparing it with the Hamiltonian of a quantum mechanical oscillator (Equation 2.82) suggests that the amplitude and phase quadrature $\hat{X}_1$ and $\hat{X}_2$ are associated with a position and momentum operator.
Evaluating the fluctuations of the quadrature operators acting on the vacuum state $|0\rangle$ or on the coherent state $|\alpha\rangle$ reveals that these fluctuations are equal and given by [GK04]

$$\Delta X_1 = \Delta X_2 = \frac{1}{\sqrt{2}}. \tag{2.60}$$

Together with the commutator relation of Equation (2.58) the Heisenberg relation

$$\Delta X_1 \Delta X_2 \geq \frac{1}{2} \tag{2.61}$$

can be derived. As can be seen by inserting Equation (2.60) into equation (2.61), both the vacuum state $|0\rangle$ and the coherent state $|\alpha\rangle$ describe a minimum-uncertainty state with $\Delta X_1 \Delta X_2 = \frac{1}{2}$.
Minimum-uncertainty states with $\Delta X_1 \neq \Delta X_2$ are called squeezed states. A possible representation of vacuum and squeezed states is in Figure 2.7a and 2.7b depicted phase space representation [BR19]. Analogously to Equation (2.57), one can also measure the variance of a state in an arbitrary quadrature $\hat{X}^\theta$ that is rotated by an angle θ

$$\hat{X}^\theta = \frac{1}{\sqrt{2}}\left(\hat{a}e^{-i\theta} + \hat{a}^\dagger e^{i\theta}\right). \tag{2.62}$$

In the phase space representation, an arbitrary quadrature is visualised by a rotated new coordinate system in Figure 2.7c. In this coordinate system, rotated by θ, one can measure the associated phase and amplitude quadrature fluctuations ΔX_1^θ and ΔX_2^θ. The concept of showing the quadrature states in phase space representations will be used in Section 2.5 to visualise effects induced by optomechanical interaction. It is especially used in Section 2.6.2 to explain the effect of coherent quantum noise cancellation more intuitively. The next section aims to explain the detection scheme, that are used to measure the quadratures and it fluctuations.

[20] For this reason X_1 and X_2 are also called sin- and cos-quadrature as in [DK12].

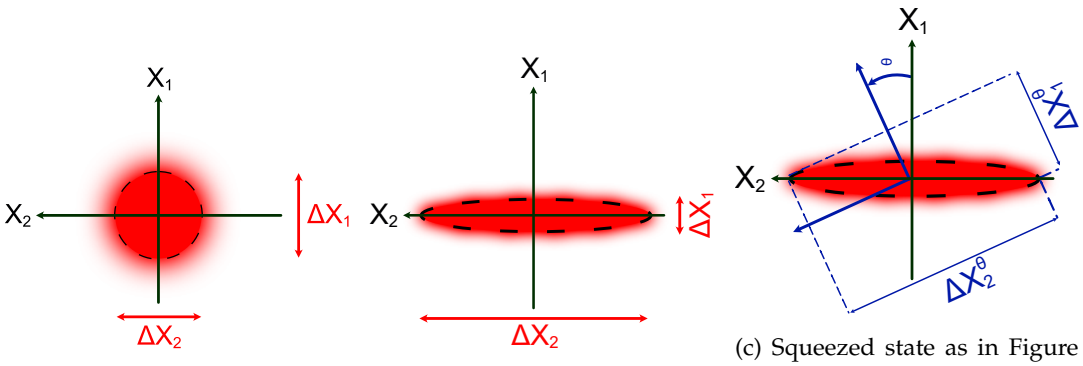

(a) Vacuum state satisfying Heisenberg relation (Equation (2.61)) with $\Delta X_1 = \Delta X_2$.

(b) Squeezed vacuum satisfying Heisenberg relation (Eqaution (2.61)) with $\Delta X_2 > \Delta X_1$

(c) Squeezed state as in Figure 2.7b together with by θ rotated coordinate system to visualise arbitrary quadratures.

FIGURE 2.7: Phase-space representation of (a) a vacuum state, (b) squeezed vacuum state and (c) a squeezed state in an arbitrary quadrature.

2.3 Detection schemes

The work this thesis covers mainly makes us of two detection schemes, the direct detection, and the homodyne detection scheme. In order to describe these schemes the light field is linearised as

$$\begin{aligned} \hat{a} &\rightarrow \alpha + \delta\hat{a}\,, \\ \hat{a}^\dagger &\rightarrow \alpha^* + \delta\hat{a}^\dagger\,, \end{aligned} \tag{2.63}$$

with α being the mean complex amplitude corresponding to the classical amplitude of the electromagnetic field. With this linearisation, the variance of the quadratures can be expressed as

$$\begin{aligned} \langle \left(\delta\hat{X}_1\right)^2 \rangle := \Delta^2 X_1 &= \langle \left(\frac{\delta\hat{a} + \delta\hat{a}^\dagger}{\sqrt{2}} \right)^2 \rangle\,, \\ \langle \left(\delta\hat{X}_2\right)^2 \rangle := \Delta^2 X_2 &= \langle \left(\frac{\delta\hat{a} - \delta\hat{a}^\dagger}{i\sqrt{2}} \right)^2 \rangle\,. \end{aligned} \tag{2.64}$$

2.3.1 Direct detection

In the case of direct detection with a single photodetector, the photocurrent $I(t)$ is proportional to the number n of detected photons[21]

$$\begin{aligned} I(t) \propto \hat{n}(t) &= (\alpha \ + \delta\hat{a}(t)) \left(\alpha^* + \delta\hat{a}^\dagger(t)\right) \\ &\approx \alpha^2 + \sqrt{2}\alpha\delta\hat{X}_1(t) \end{aligned} \tag{2.65}$$

with $\delta\hat{X}_1 = \frac{1}{\sqrt{2}}$ and α being real. Equation (2.65) reveals that only the amplitude quadrature fluctuations $\delta\hat{X}_1$ and no phase quadrature information is accessible by using a direct detection scheme. Typically, the measured photocurrent $I(t)$ is transformed into a voltage and fed to a spectrum analyser to obtain a power spectrum. This spectrum is the equivalent of the measured variance $\Delta^2 X_1$, but in the frequency

[21] For a strong field $\alpha \ggg \hat{a}$ fluctuations as $\delta\hat{a}^\dagger\delta\hat{a}$ are negligible.

domain. Using the Fourier Transformation[22] the measured variance $V(\omega)$ of the coherent state (Equation (2.50)) is expressed as

$$V(\omega) \propto 2\alpha^2 \left\langle \left(\delta \hat{X}_1\right)^2 \right\rangle . \tag{2.66}$$

Dividing the quadrature fluctuation $\delta\hat{X}_1$ into quantum and classical amplitude fluctuations leads to [23]

$$\begin{aligned} I(t) &\approx \left(\alpha\left(1+\frac{m(t)}{2}\right)+\hat{a}\right)\left(\alpha^*\left(1+\frac{m(t)^*}{2}\right)+\hat{a}^\dagger\right) \\ &\approx |\alpha|^2 + \frac{\alpha^2}{\sqrt{2}} \underbrace{\left(\frac{m(t)+m(t)^*}{\sqrt{2}}\right)}_{\delta X_{1,\text{classical}}} + \underbrace{\sqrt{2}\alpha\delta\hat{X}_1(t)}_{\text{'shot noise'}} . \end{aligned} \tag{2.67}$$

So, in direct detection, the detected power $P = |I(t)|^2$ has three contributions. The first one is the mean power $P = |\alpha|^2$; the second one contains classical amplitude quadrature fluctuations $\delta X_{1,\text{classical}}$[24] and the third contribution describes quantum mechanical amplitude quadrature noise. The quantum quadrature fluctuations $\delta\hat{X}_1$ are named shot noise.

In Section 3.1 the direct detection scheme is used to measure the amplitude quadrature noise to investigate at which frequency ω the noise is limited by shot noise. In the later discussed experiment, quantum mechanical effects should be investigated. Hence the classical amplitude noise contribution $\delta\hat{X}_{1,\text{ classical}}$ should be much lower than the quantum mechanical shot noise. According to Equation (2.65) this can be achieved by increasing the light power. However, lower power is needed for the presented experiments and most optomechanical experiments. To achieve a shot noise limited beam, a cavity can be used as it can be treated as low pass behaviour (Section 2.1.2), which suppresses classical amplitude noise above a particular frequency ω, which is defined by the cavity linewidth κ.

2.3.2 Balanced homodyne detection

As seen in Section 2.3.1, the direct measurement of light with one photodiode is only susceptible to the amplitude quadrature X_1. The restriction to amplitude quadrature measurements can be overcome with the homodyne detection method that allows for phase or amplitude quadrature measurements. The derivation of homodyne detection is referred to [WM08]; for further detailed derivations, the theses by Mehmet [Meh12] and Vahlbruch [Vah08] is recommended. As depicted in Figure 2.8 a signal field $\hat{E}_\text{S}$ and local oscillator (LO) field $\hat{E}_\text{LO}$ (the LO is not measuring the signal) of the same frequency ω_0

$$\begin{aligned} \hat{E}_\text{S} &= i\left(\frac{\hbar\omega_0}{2\epsilon_0 V}\right)^{1/2}\left[\hat{a}_\text{S}e^{i(kx-\omega_0 t)} - \hat{a}_\text{S}^\dagger e^{-i(kx-\omega_0 t)}\right] \\ \hat{E}_\text{LO} &= i\left(\frac{\hbar\omega_0}{2\epsilon_0 V}\right)^{1/2}\left[\hat{a}_\text{LO}e^{i(kx-\omega_0 t)} - \hat{a}_\text{LO}^\dagger e^{-i(kx-\omega_0 t)}\right] \end{aligned} \tag{2.68}$$

[22] Definiton of used Fourier transformation and spectral density is given in Appendix A and B.

[23] Classical amplitude fluctuations can be written as $\alpha \to \alpha(1+\frac{m(t)}{2})$ with $m(t) \ll \alpha$ describing classical noise processes with amplitude m(t) (compare Equation 2.15).

[24] For example, induced by current noise of the laser.

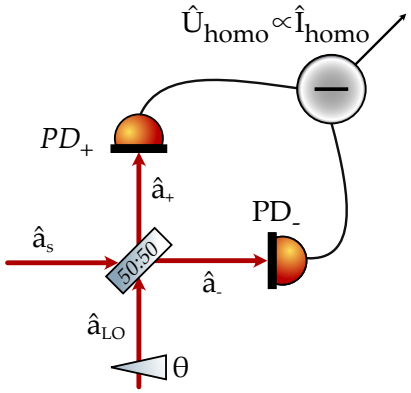

FIGURE 2.8: Balanced homodyne detection scheme. The signal field $\hat{a}_s$ is combined by a 50%:50% beamsplitter with an intense local oscillator field $\hat{a}_{LO}$. After combining each field $\hat{a}_-$ and $\hat{a}_+$ is measured with a photodetector PD_- and PD_+, respectively. Finally, the difference between both currents is taken in an analogue way. The depicted phase shifter changes the phase θ between the local oscillator and signal and thereby defines the quadrature measurement (see text).

are combined on a 50:50 beamsplitter. The fields propagating towards the photodiodes are given as

$$\begin{aligned}\hat{E}_- &= i\left(\frac{\hbar\omega_0}{2\epsilon_0 V}\right)^{1/2}\left[\hat{a}_- e^{i(kx-\omega_0 t)} - \hat{a}_-^\dagger e^{-i(kx-\omega_0 t)}\right], \\ \hat{E}_+ &= i\left(\frac{\hbar\omega_0}{2\epsilon_0 V}\right)^{1/2}\left[\hat{a}_+ e^{i(kx-\omega_0 t)} - \hat{a}_+^\dagger e^{-i(kx-\omega_0 t)}\right]\end{aligned} \tag{2.69}$$

with

$$\hat{a}_\pm = \frac{1}{\sqrt{2}}\left(\hat{a}_S \pm \hat{a}_{LO}\right). \tag{2.70}$$

In the following the linearised fields

$$\begin{aligned}\hat{a}_S &\to \alpha_S + \delta\hat{a}_S, \\ \hat{a}_{LO} &\to \left(\alpha_{LO} + \delta\hat{a}_{LO}\right) e^{i\theta},\end{aligned} \tag{2.71}$$

are used, with α_i being the mean amplitude, $\delta\hat{a}_i$ the corresponding fluctuations, and θ the phase difference between the signal and local oscillator field. With this one finds for the difference photocurrent $\hat{I}_{homo}(t)$ detected by PD_- and PD_+

$$\begin{aligned}\hat{I}_{homo} \propto \hat{I}_+ - \hat{I}_- &= \hat{a}_+^\dagger\hat{a}_+ - \hat{a}_-^\dagger\hat{a}_- \\ &= \sqrt{2}\alpha_S\hat{X}_{LO}^\theta + \sqrt{2}\alpha_{LO}\hat{X}_S^{-\theta} + 2\alpha_S\alpha_{LO}\cos\theta\end{aligned} \tag{2.72}$$

where the definition of an arbitrary quadrature rotated by an angle θ (Equation 2.133) has been used. The angle θ is also called homodyne angle. The two following conditions

$$\alpha_{LO} \gg \alpha_S, \tag{2.73a}$$

$$\alpha_{LO}\hat{X}_S^{-\theta} \gg \alpha_S\hat{\mathcal{X}}_{LO}^\theta, \tag{2.73b}$$

have to be fulfilled to ensure that the measured photocurrent is dominated by the signal quadrature $\hat{X}_S^{-\theta}$ one seeks to measure. The Variance $V_{\text{homo}}(\omega)$ is derived as in Section 2.3.1 via the Fourier transformation as

$$V_{\text{homo}}(\omega) = \alpha_{\text{LO}}^2 \left\langle (\delta \hat{X}_S^{\theta})^2 \right\rangle . \tag{2.74}$$

2.4 Mechanical oscillators

This section explores the theory of mechanical oscillators coupled to a light field in optomechanical experiments. It begins by introducing the classical description of harmonic oscillators and their modelling in relation to the thermal environment. The subsequent part establishes the quantum mechanical description of these oscillators.

Classical description

One example of a mechanical oscillator is a pendulum oscillating in one direction x, described by its equation of motion[Dem08]

$$\ddot{X} + \gamma_{\text{m}} \dot{X} + \omega_{\text{m}}^2 X = \frac{F_{\text{ext}}(t)}{m} . \tag{2.75}$$

Here F_{ext} is any external force, γ_{m} the damping and ω_{m} the resonance frequency of the system. γ_{m} is also identified as the mechanical linewidth of the resonator. In Fourier space, the equation of motion [25] reads

$$X(\omega) = \chi_{\text{m}}^{\text{cl}}(\omega) \frac{F_{\text{ext}}(\omega)}{m} \tag{2.76}$$

with

$$\chi_{\text{m}}^{\text{cl}}(\omega) = \frac{1}{(\omega_{\text{m}}^2 - \omega^2 + i\omega\gamma_{\text{m}})} \tag{2.77}$$

being the classical mechanical susceptibility to an external force F_{ext} of the mechanical oscillator.

Quantum mechanical description

The classical Hamiltonian of an undamped harmonic oscillator with is given by

$$H = \frac{m\omega_{\text{m}} X^2}{2} + \frac{P^2}{2m} \tag{2.78}$$

with X being the position and P being the momentum. The quantisation is done by converting the position and momentum into operators by requiring $[\hat{Q}, \hat{P}] = i\hbar$. As for the quantization of the light field, dimensionless operators can be defined as

$$\hat{x}_{\text{m}} = \frac{\hat{X}}{x_{\text{zpf}}} , \tag{2.79}$$

$$\hat{p}_{\text{m}} = x_{\text{zpf}} \frac{\hat{p}}{\hbar} \tag{2.80}$$

[25] Definition of Fourier transform in Appendix A.

with the mechanical zero point fluctuation

$$x_{\mathrm{zpf}} = \sqrt{\frac{\hbar}{m\omega_{\mathrm{m}}}}. \tag{2.81}$$

Their commutation relation is $[\hat{x}_{\mathrm{m}}, \hat{p}_{\mathrm{m}}] = i$. With these transformations the quantum mechanical Hamiltonian can be written as

$$\hat{H} = \frac{1}{2}\hbar\omega_{\mathrm{m}}\left(\hat{x}_{\mathrm{m}}^2 + \hat{p}_{\mathrm{m}}^2\right) = \hbar\omega_{\mathrm{m}}\left(\hat{b}^\dagger\hat{b} + \frac{1}{2}\right) \tag{2.82}$$

with the phonon annihilation and creation operators $\hat{b} = \left(\hat{x}_{\mathrm{m}} + i\hat{p}_{\mathrm{m}}\right)/\sqrt{2}$ and $\hat{b}^\dagger = \left(\hat{x}_{\mathrm{m}} - i\hat{p}_{\mathrm{m}}\right)/\sqrt{2}$. Equation (2.82) reveals by comparison with Equation (2.59) why amplitude and phase quadratures $\hat{X}_1$ and $\hat{X}_2$ of light are associated with the position and momentum of a mechanical oscillator. Furthermore, using the same procedure for the phonon operators as for the photon operators in Section 2.2 entails that the ground state energy of the mechanical oscillator is given by $\frac{\hbar\omega_{\mathrm{m}}}{2}$.

To include damping to the mechanical oscillator, the Quantum-Langevin equations are used to obtain the following equations of motion

$$\dot{\hat{x}}_{\mathrm{m}} = \omega_{\mathrm{m}}\hat{p}_{\mathrm{m}} \tag{2.83}$$

$$\dot{\hat{p}}_{\mathrm{m}} = -\omega_{\mathrm{m}}\hat{x}_{\mathrm{m}} - \gamma_{\mathrm{m}}\hat{p}_{\mathrm{m}} + \sqrt{\gamma_{\mathrm{m}}}\hat{\mathcal{F}}_{\mathrm{ext}} \tag{2.84}$$

where the scaled force operator is defined following [Sch+22], as $\hat{\mathcal{F}}_{\mathrm{ext}} = F_{\mathrm{ext}}/\sqrt{\hbar m\gamma_{\mathrm{m}}\omega_{\mathrm{m}}}$ in units of $\mathrm{Hz}^{1/2}$. In general $\hat{\mathcal{F}}_{\mathrm{ext}} = \hat{\mathcal{F}}_{\mathrm{th}} + \hat{\mathcal{F}}_{\mathrm{other}} + \hat{\mathcal{F}}_{\mathrm{signal}}$ consists of a thermal noise contribution F_{th}, other noise sources F_{other} and the signal force $\hat{F}_{\mathrm{signal}}$. Assuming $\hat{F}_{\mathrm{other}} = 0$ entails that a signal force F_{signal} can be inferred by measuring the momentum $\hat{p}_{\mathrm{m}}$, if it is not masked by thermal noise $\hat{\mathcal{F}}_{\mathrm{th}}$. Solving the equation of motion in the Fourier domain[26] yields

$$\hat{x}_{\mathrm{m}}(\omega) = \sqrt{\gamma_{\mathrm{m}}}\chi_{\mathrm{m}}(\omega)\hat{\mathcal{F}}_{\mathrm{ext}} \tag{2.85}$$

with

$$\chi_{\mathrm{m}}(\omega) = \frac{\omega_{\mathrm{m}}}{\omega_{\mathrm{m}}^2 - \omega^2 + i\omega\gamma_{\mathrm{m}}} \tag{2.86}$$

representing the (scaled) mechanical susceptibility to an external force $\hat{\mathcal{F}}_{\mathrm{ext}}$ of the mechanical oscillator. One important figure of merit of the mechanical oscillator is the quality factor

$$Q = \frac{\omega_{\mathrm{m}}}{\gamma_{\mathrm{m}}}, \tag{2.87}$$

which essentially describes the ratio of initially stored energy and energy dissipated per cycle. With the definition of the power spectral density given in Appendix B, the symmetrised[27] position power spectral density $\bar{S}_{\hat{x}_{\mathrm{m}},\hat{x}_{\mathrm{m}}}(\omega)$ of a is written as

$$\bar{S}_{\hat{x}_{\mathrm{m}},\hat{x}_{\mathrm{m}}}(\omega) = \gamma_{\mathrm{m}}|\chi_{\mathrm{m}}(\omega)|^2\bar{S}_{\hat{\mathcal{F}}_{\mathrm{ext}},\hat{\mathcal{F}}_{\mathrm{ext}}}(\omega) \tag{2.88}$$

with $\bar{S}_{\hat{\mathcal{F}}_{\mathrm{ext}},\hat{\mathcal{F}}_{\mathrm{ext}}}(\omega)$ being the (symmetrised) force power spectral density.

[26] $\frac{d}{dt} \to i\omega$

[27] Symmetrised spectra are denoted by a bar, e.g. $\bar{S}(\omega)$ (Appendix B).

Based on [BM15; Cle14; Che19] a small outline of the coupling of thermal noise to a mechanical oscillator, described by the Quantum fluctuation-dissipation theorem, will be given.

Quantum Fluctuation-Dissipation Theorem

In the Markovian limit[28], the (symmetrised) power spectral density[29] of a thermal Brownian noise with[30][BM15; Cle14; Che19]

$$S_{\hat{\mathcal{F}}_{\mathrm{th}},\hat{\mathcal{F}}_{\mathrm{th}}}(\omega) = 2\,(\bar{n}_{\mathrm{th}}+1) \tag{2.89a}$$

$$S_{\hat{\mathcal{F}}_{\mathrm{th}},\hat{\mathcal{F}}_{\mathrm{th}}}(-\omega) = 2\bar{n}_{\mathrm{th}} \tag{2.89b}$$

is given by[31]

$$\bar{S}_{\hat{\mathcal{F}}_{\mathrm{th}},\hat{\mathcal{F}}_{\mathrm{th}}}(\omega) = \frac{S_{\hat{\mathcal{F}}_{\mathrm{th}},\hat{\mathcal{F}}_{\mathrm{th}}}(\omega)+S_{\hat{\mathcal{F}}_{\mathrm{th}},\hat{\mathcal{F}}_{\mathrm{th}}}(-\omega)}{2} = 2(\bar{n}_{\mathrm{th}}+\frac{1}{2})\,, \tag{2.90}$$

where $\bar{n}_{\mathrm{th}} = \frac{k_{\mathrm{B}}T}{\hbar\omega_{\mathrm{m}}}$. It is worth noting that the asymmetry of the positive and negative frequency components in Equation (2.89) can be used to calibrate the thermal occupancy $\bar{n}_{\mathrm{th}}$ of the mechanical oscillator[Qiu+20] as[32]

$$\bar{n}_{\mathrm{th}}(\omega) = \frac{S_{\hat{x}_{\mathrm{m}},\hat{x}_{\mathrm{m}}}(\omega)}{S_{\hat{x}_{\mathrm{m}},\hat{x}_{\mathrm{m}}}(\omega)-S_{\hat{x}_{\mathrm{m}},\hat{x}_{\mathrm{m}}}(\omega)} = \frac{S_{\hat{\mathcal{F}}_{\mathrm{th}},\hat{\mathcal{F}}_{\mathrm{th}}}(-\omega)}{S_{\hat{\mathcal{F}}_{\mathrm{th}},\hat{\mathcal{F}}_{\mathrm{th}}}(\omega)-S_{\hat{\mathcal{F}}_{\mathrm{th}},\hat{\mathcal{F}}_{\mathrm{th}}}(-\omega)}\,. \tag{2.91}$$

In this thesis experiments are carried out in the high-temperature limit $\frac{k_{\mathrm{B}}T}{\hbar\omega_{\mathrm{m}}} \gg 1$ [33], for which

$$\bar{S}_{\hat{\mathcal{F}}_{\mathrm{th}},\hat{\mathcal{F}}_{\mathrm{th}}}(\omega) = 2\frac{k_{\mathrm{B}}T}{\hbar\omega_{\mathrm{m}}}+1 \approx 2\frac{k_{\mathrm{B}}T}{\hbar\omega_{\mathrm{m}}}\,. \tag{2.92}$$

By Parseval's theorem the variance $\langle\hat{x}_{\mathrm{m}}^2\rangle$ of the displacement is connected to the position spectral density $\bar{S}_{\hat{x}_{\mathrm{m}},\hat{x}_{\mathrm{m}}}(\omega)$ and results using Equation (2.88) in[34]

$$\langle\hat{x}_{\mathrm{m}}^2\rangle = \int_{-\infty}^{\infty}\bar{S}_{\hat{x}_{\mathrm{m}},\hat{x}_{\mathrm{m}}}(\omega)\frac{d\omega}{2\pi} = \gamma_{\mathrm{m}}\int_{-\infty}^{\infty}|\chi_{\mathrm{m}}(\omega)|^2\bar{S}_{\hat{\mathcal{F}}_{\mathrm{th}},\hat{\mathcal{F}}_{\mathrm{th}}}(\omega)\frac{d\omega}{2\pi} \tag{2.93}$$

$$= \bar{n}_{\mathrm{th}}+1/2 \approx \frac{k_{\mathrm{B}}T}{\hbar\omega_{\mathrm{m}}}\,, \tag{2.94}$$

or in the dimensionful case

$$\langle\hat{X}^2\rangle = x_{\mathrm{ZPF}}^2\int_{-\infty}^{\infty}\bar{S}_{\hat{x}_{\mathrm{m}},\hat{x}_{\mathrm{m}}}(\omega)\frac{d\omega}{2\pi} \approx \frac{k_{\mathrm{B}}T}{m\omega_{\mathrm{m}}^2} \tag{2.95}$$

Equation (2.95) is remarkable, because it reveals that from a position spectral density $\bar{S}_{\hat{x}_{\mathrm{m}},\hat{x}_{\mathrm{m}}}(\omega)$ the temperature T of the oscillator can be inferred.

[28] Vanishing correlation time, absence of memory effects [AKM14].

[29] See Footnote 27.

[30] $\langle\hat{\mathcal{F}}_{\mathrm{th}}(t),\hat{\mathcal{F}}_{\mathrm{th}}(t')\rangle = \mathbf{2}\bar{n}_{\mathrm{th}}$, due to the definition of the scaled force operator $\hat{\mathcal{F}} = F_{\mathrm{ext}}/\sqrt{\hbar m\gamma_{\mathrm{m}}\omega_{\mathrm{m}}}$.

[31] Here, the semi-classical regime in that bath fluctuations are dominated by thermal noise $\frac{\hbar\omega_{\mathrm{m}}}{k_{\mathrm{B}}T} \ll 1$ is treated [BM15].

[32] $|\chi_{\mathrm{m}}(\omega)|^2 = |\chi_{\mathrm{m}}(-\omega)|^2$.

[33] $\omega_{\mathrm{m}}/(2\pi) \approx 1\,\mathrm{MHz}$ and $T = 4\,\mathrm{K}$ or $300\,\mathrm{K}$.

[34] Detailed calculation of the integral can be found in appendix B.1 of [Sch09].

The following section explains how the (symmetrised) position spectral density $\bar{S}_{\hat{x}_m,\hat{x}_m}(\omega)$ is measured by utilising light and what kind of consequences arise from this measurement.

2.5 Optomechanical interaction of light and mechanics

In this chapter, the focus is on the introduction of various classical effects, as well as the quantum mechanical consequences resulting from optomechanical interaction. After introducing a canonical optomechanical system and its equations of motion, they will be used to explore several consequences that arise due to optomechanical coupling.

Firstly, the phenomenon of static bistability is presented in Section 2.5.1. Static bistability refers to the classical effect where the optical field exhibits two stable states in response to the mechanical oscillator's displacement. The optical intensity can remain in either of these states until a certain threshold is reached, leading to a bistable behaviour.

Dynamic backaction is another classical effect discussed in Section 2.5.3. Dynamical backaction occurs when the motion of the mechanical oscillator induces changes in the optical field. This interaction between the mechanical and optical degrees of freedom leads to a mutual influence, resulting in a modification of their dynamics, such as sideband cooling.

The chapter then proceeds to introduce optomechanically induced transparency (OMIT - Section 2.5.5). This effect enables the manipulation of the transmission properties of the optical field through the control of the mechanical motion, leading to enhanced transparency or opacity. This thesis uses the OMIT feature to investigate the optomechanical system parameters (4.3.1).

In addition to these classical effects, the quantum mechanical consequences of optomechanical interaction are explored (Section 2.5.7). One such consequence is the standard quantum limit (SQL), which represents a sensitivity bound for conventional measurements of the position of the mechanical oscillator [Mas+19]. The SQL arises from quantum noise associated with the measurement process and imposes limitations on the achievable measurement precision. In this section the quantum backaction cooperativity C_{qba}, an important figure of merit for optomechanical systems, will be introduced. Essentially it describes the ratio of the quantum backaction and thermal decoherence rate.

Lastly, the Section 2.5.8 discusses the concept of ponderomotive squeezing. Ponderomotive squeezing allows for the suppression of quantum noise in a specific frequency range, surpassing the limitations imposed by the SQL. This technique utilises the coupling between the optical and mechanical degrees of freedom to manipulate the quantum fluctuations of the mechanical oscillator's position.

As the SQL is only surpassed in a specific frequency band, a coherent quantum noise cancellation scheme 2.6 based on [Sch+22; Wim+14; Ste19; Sch23][35] will be discussed in Section 2.6, as such an experiment leads to a broadband sensitivity enhancement. The CQNC scheme is also the main motivation to develop the optomechanical system, which will be experimentally characteriszed in chapter 3.2. Additionally, an enhanced CQNC scheme, incorporating an additional beam to induce optomechanical sideband cooling, will be theoretically explored in Section 2.6.4. The additional beam could improve sensitivity, as it can be used to accomplish the requirements given by the ideal CQNC discussion given in Section 2.6.2.

[35] [Sch23; Ste19] are Ph.D. theses associated to the papers [Sch+22; Wim+14].

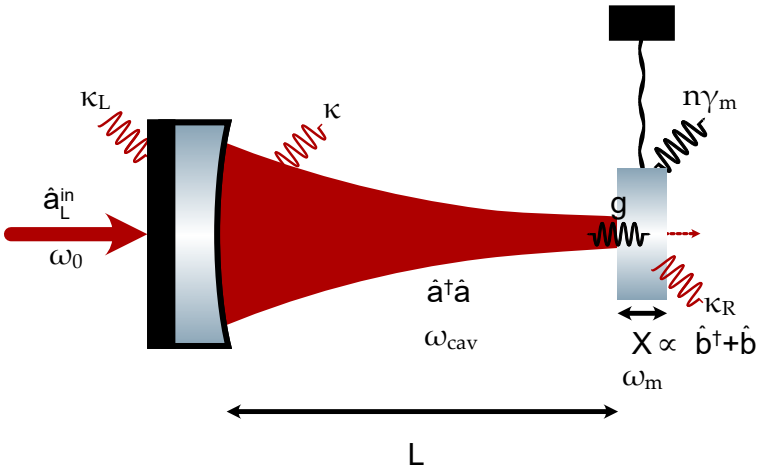

FIGURE 2.9: Optomechanical cavity with resonance frequency ω_{cav} and intracavity photon number $\hat{a}^\dagger\hat{a}$ driven from the left by the laser field $\hat{a}_{\mathrm{L}}^{\mathrm{in}}$ with frequency ω_0. On the right, an optomechanical oscillator with resonance frequency ω_{m} and linewidth γ_{m}, which changes its position X due to the radiation pressure force is depicted as a suspended mirror. The coupling of the intracavity field and the mechanical oscillator is described by the coupling strength g. Also depicted are the linewidths of the corresponding mirrors κ_{i} and the overall decay rate κ of the intracavity field.

Figure 2.9 shows a Fabry-Pérot cavity with a suspended end mirror. This end mirror serves as the mechanical oscillator (therefore, it is drawn with an attached spring), while the input mirror is fixed. As described in Section 2.1.4 κ_{i} describes the linewidth of associated mirrors i (Equation(2.30)). The Hamiltonian $\hat{H}_{\mathrm{cav}}$ of the intracavity light field is given

$$\hat{H}_{\mathrm{cav}} = \hbar\omega_{\mathrm{cav}}(X)\hat{a}^\dagger\hat{a} \tag{2.96}$$

and depends implicitly on the position X through the resonance frequency ω_{cav} (as in the classical case (Section 2.1.4)). By linearising ω_{cav} by $\omega_{\mathrm{cav}}(X) = \omega_{\mathrm{cav}}(0) + \frac{\partial\omega_{\mathrm{cav}}(X)}{\partial X}X$ the intracavity Hamiltonian H_{cav} becomes

$$\hat{H}_{\mathrm{cav}} = \hbar\omega_{\mathrm{cav}}(X)\hat{a}^\dagger\hat{a} = \hbar\omega_{\mathrm{cav}}(X)\hat{a}^\dagger\hat{a} + \hbar GX\hat{a}^\dagger\hat{a}\,, \tag{2.97}$$

with $G = \frac{\partial\omega_{\mathrm{cav}}(X)}{\partial X}$ introducing the optomechanical coupling of the light field $\hat{a}$ and the mechanics (position X). Hence the last term in Equation (2.97) is interpreted as the interaction Hamiltonian $\hat{H}_{\mathrm{int}}$ and is rewritten in dimensionless quantities as

$$\hat{H}_{\mathrm{int}} = g_0\hat{a}^\dagger\hat{a}\hat{x}_{\mathrm{m}}\,. \tag{2.98}$$

Here

$$g_0 = Gx_{\mathrm{zpf}} \tag{2.99}$$

is the vacuum optomechanical coupling strength [AKM14]. With this, the complete Hamiltonian $\hat{H}_{\mathrm{sys}}$ of the optomechanical system depicted in Figure 2.9 is given by

$$\hat{H}_{\mathrm{sys}} = \hat{H}_{\mathrm{cav}} + \hat{H}_{\mathrm{mech}} + \hat{H}_{\mathrm{int}} + \hat{H}_{\mathrm{drive}}\,, \tag{2.100}$$

where

$$\hat{H}_{\mathrm{drive}} = i\hbar\alpha_{\mathrm{L}}^{\mathrm{in}}(\hat{a}^\dagger e^{-i\omega_0 t} + \hat{a}e^{i\omega_0 t}) \tag{2.101}$$

describes the input field, which drives the optomechanical interaction. By using

the unitary transformation $H \rightarrow UHU^\dagger + i\frac{\delta U}{\delta t}U^\dagger$ with $U(t) = \exp\left(i\omega_0 t\hat{a}^\dagger\hat{a}\right)$, the Hamiltonian can be written in a frame rotating with the laser frequency ω_0 as[36]

$$\hat{H}_{\text{sys}}^{\text{int}} = \hbar\tilde{\Delta}\hat{a}^\dagger\hat{a} + \frac{\hbar\omega_{\text{m}}}{2}(\hat{x}_{\text{m}} + \hat{p}_{\text{m}}) + g_0\hbar\hat{a}^\dagger\hat{a}\hat{x}_{\text{m}} + i\hbar\alpha_{\text{L}}^{\text{in}}(\hat{a}^\dagger + \hat{a}) \tag{2.102}$$

where $\tilde{\Delta} = \omega_{\text{cav}} - \omega_0$ is the detuning between the cavity resonance frequency Δ_{cav} and the impinging laser and $\alpha_{\text{L}}^{\text{in}} = \sqrt{P_{\text{L}}^{\text{in}}\kappa_{\text{L}}/(\hbar\omega_0)}$ with P_{L}^{in} being the power of drive field $\alpha_{\text{L}}^{\text{in}}$. The time evolution of the operators can be modelled by inserting the Hamiltonian H_{sys} into the Heisenberg-Langevin equations [GZ10; BM15][37]

$$\dot{\hat{a}} = -\left[\frac{\kappa}{2} + i\left(\tilde{\Delta} + g_0\hat{x}_{\text{m}}\right)\right]\hat{a} + \sqrt{\kappa_{\text{L}}}\hat{a}_{\text{L}}^{\text{in}} + \sqrt{\kappa_{\text{R}}}\hat{a}_{\text{R}}^{\text{in}} \tag{2.103a}$$

$$\dot{\hat{x}}_{\text{m}} = \omega_{\text{m}}\hat{p}_{\text{m}} \tag{2.103b}$$

$$\dot{\hat{p}}_{\text{m}} = -\omega_{\text{m}}\hat{x}_{\text{m}} - \gamma_{\text{m}}\hat{p}_{\text{m}} - g_0\hat{a}^\dagger\hat{a} + \sqrt{\gamma_{\text{m}}}\hat{\mathcal{F}}_{\text{ext}} \tag{2.103c}$$

where, as in Equation (2.30) the leakage rate is given by $\kappa = \kappa_{\text{L}} + \kappa_{\text{R}} + \kappa_{\text{loss}}$ with $\kappa_{(\text{L,R})}$ describing the coupling rates of the left or right mirror $M_{\text{L,R}}$ and κ_{loss} describing additional losses, while the operator $\hat{a}_{(\text{R,L})}^{\text{in}}$ describes fields (coherent or vacuum field) coupling in from the left (L) or right (R) mirror.

Based on the Heisenberg-Langevin equations, classical phenomena arising in optomechanical systems, like static bistability (Section 2.5.1) and dynamical back-action (Section 2.5.2) will be explained. Additionally, quantum mechanical consequences of the Heisenberg-Langevin equations, namely the Standard quantum limit (Section 2.5.7) and ponderomotive squeezing (Section 2.5.8) will be introduced. At the end of the theoretical description, the mentioned effects will be used to motivate and explain the coherent quantum noise cancellation scheme in Section 2.6.4.

2.5.1 Static bistability

This section, based on [Lör15; Hof15], explains the phenomena of static bistability, which limits the optomechanical sideband cooling (which will be introduced in Section 2.5.2). For this, the classical equation of motion of the optomechanical system will be written by replacing the operators in Equation (2.103) with their average values

$$\dot{\alpha} = -\left[\frac{\kappa}{2} + i\left(\tilde{\Delta} + g_0\left\langle x_{\text{m}}\right\rangle\right)\right]\alpha + \sqrt{\kappa_{\text{L}}}\alpha_{\text{L}}^{\text{in}} \tag{2.104a}$$

$$\left\langle \dot{x}_{\text{m}}\right\rangle = \omega_{\text{m}}\left\langle p_{\text{m}}\right\rangle \tag{2.104b}$$

$$\left\langle \dot{p}_{\text{m}}\right\rangle = -\omega_{\text{m}}\left\langle x_{\text{m}}\right\rangle - \gamma_{\text{m}}\left\langle p_{\text{m}}\right\rangle + \sqrt{\gamma_{\text{m}}}\left\langle \hat{\mathcal{F}}_{\text{ext}}\right\rangle - g_0|\alpha|^2 \tag{2.104c}$$

where the average field amplitudes are defined as $\langle\hat{a}_{\text{i}}\rangle = \alpha_{\text{i}}$ and $\alpha_{\text{R}}^{\text{in}} = 0$.
Using $\langle\hat{\mathcal{F}}_{\text{ext}}\rangle = \langle\dot{x}_{\text{m}}\rangle = \langle\dot{p}_{\text{m}}\rangle = 0$, the steady-state solution for the position $\langle x_{\text{m}}\rangle$ and

[36] Also called interaction picture.

[37] A more detailed description based on the same normalisations used in this thesis is given in Section 2.3.1 of [Ste19].

the classical intracavity field $\langle\alpha\rangle$ reads

$$\alpha = \frac{\sqrt{\kappa_L}}{\frac{\kappa}{2} + i\left(\tilde{\Delta} + g_0\langle x_m\rangle\right)}\alpha_L^{in} \tag{2.105a}$$

$$\langle x_m\rangle = -\frac{g_0|\alpha|^2}{\omega_m}. \tag{2.105b}$$

Substituting Equation (2.105b) into (2.105a) results in

$$\left(\frac{\kappa^2}{4} + \tilde{\Delta}^2 - 2\tilde{\Delta}\frac{g_0^2}{\omega_m}n_{cav} + \frac{g_0^4}{\omega_m^2}n_{cav}^2\right)n_{cav} = \kappa_L n_L^{in} \tag{2.106}$$

with $n_{cav} = |\alpha|^2$ the photon number of the intracavity field and n_L^{in} the photon flux of the driving/input field[38]. Equation (2.106) reveals that the intracavity photon number n_{cav} is connected to the input field n_L^{in} via a third-order polynomial. For negative detuning $\tilde{\Delta}$ (blue-detuned)[39] the cubic function is monotonically increasing. In a certain positive detuning range and for specific input powers ($\propto n_L^{in}$), static bistability occurs, which is depicted in Figure 2.10.

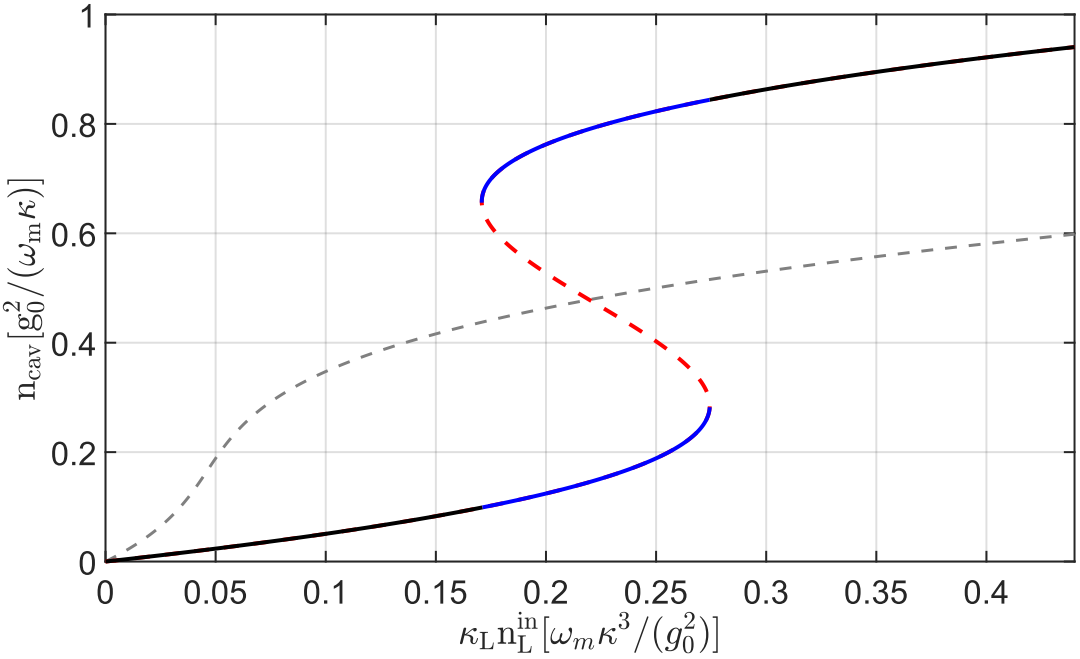

FIGURE 2.10: Intracavity photon number n_{cav} for $\tilde{\Delta} = \frac{1}{4}\kappa$ (dashed grey line - without bistability) and $\tilde{\Delta} = \frac{8}{4}\kappa$ (coloured solid line - with bistability) against the cavity drive $\kappa_L n_L^{in}$. The black solid shows where Equation (2.106) has one stable solution, whereas the blue solid line shows regions where two stable solutions exist, and hence bistability appears. The red dashed line represents a third unstable solution between two stable inflection points.

Specifically, static bistability appears for a particular detuning regime in which Equation (2.106) has three possible solutions (the solid line in Figure 2.10). To see for which detuning $\tilde{\Delta}$ the bistability behaviour sets in, one should consider the inflection

[38] n_L^{in}[Hz].
[39] $\Delta = \omega_{cav} - \omega_0$.

points[40]

$$n_{\mathrm{cav}} = \frac{4g_0^2\omega_m\tilde{\Delta} \pm \sqrt{g_0^4\omega_{\mathrm{m}}^2(4\Delta^2 - 3\kappa^2)}}{6g_0^4} \tag{2.107}$$

which reveal that real solutions exists only for $4\tilde{\Delta}^2 > 3\kappa^2$. Conversely, if

$$\Delta > \sqrt{\frac{3}{4}}\kappa\,, \tag{2.108}$$

then the bistability regime can be accessed. An even more sophisticated analysis shows that only two of the three solutions of Equation (2.106) are stable for $\Delta > \sqrt{\frac{3}{4}}\kappa$ [Hof15]. The input power at which bistability can be observed is given by[41]

$$n_{\mathrm{L}}^{\mathrm{in,onset}} \geq \frac{\kappa^3\omega_{\mathrm{m}}}{3\sqrt{3}g_0^2\kappa_{\mathrm{L}}}. \tag{2.109}$$

As mentioned in the beginning, within this thesis, the regime of static bistability is not accessed. However, it is mentioned since it limits to sideband cooling. Optomechanical sideband cooling, a consequence of dynamical backaction, is explained in the following section as it is used experimentally in Section 4.3.2 to deduce the coupling strength g.

Coherent optomechanical interactions

In this chapter, the introduction of several classical effects and the quantum mechanical consequences of optomechanical interaction are presented.

Firstly, the phenomenon of dynamical backaction is discussed. Dynamical backaction refers to the classical effect where the motion of the mechanical oscillator influences the behaviour of the optical field. This interaction results in a modification of the dynamics of both the mechanical oscillator and the optical field.

Additionally, the concept of optomechanical induced transparency is introduced. This classical effect arises from the coupling between the mechanical oscillator and the optical field. It leads to changes in the transmission properties of the optical field, allowing for the control and manipulation of light based on mechanical motion.

Furthermore, the chapter delves into the quantum mechanical consequences of optomechanical interaction, focusing on two key aspects. The first is the standard quantum limit (SQL), which sets a fundamental sensitivity bound for measuring certain physical quantities, such as the position of the mechanical oscillator. The SQL arises due to quantum noise inherent in the measurement process and imposes limitations on the precision with which such quantities can be measured.

Lastly, the chapter explores the concept of ponderomotive squeezing, which is a quantum mechanical effect resulting from optomechanical interaction. Ponderomotive squeezing enables the suppression of quantum noise in a specific frequency range, thereby enhancing the precision of measurements beyond the limitations imposed by the SQL. This technique utilises optomechanical coupling to manipulate the quantum fluctuations of the mechanical oscillator's position.

[40] $\frac{d(\kappa_{\mathrm{L}} n_{\mathrm{L}}^{\mathrm{in}})}{dn_{\mathrm{cav}}}$=0.

[41] To see this evaluate Equation (2.107) for $\tilde{\Delta} = \sqrt{\frac{3}{4}}\kappa$ and insert solution in Equation (2.106).

Throughout this chapter, these classical effects and quantum mechanical consequences are discussed in detail, shedding light on their significance and implications in the field of optomechanics.

2.5.2 Dynamical backaction and sideband cooling

To compute the dynamics of the optomechanical system, the equations of motion (Equation (2.103)) are again considered. This time the operators are linearised via $\hat{a} \to \alpha + \delta\hat{a}$ and $\hat{x}_\mathrm{m} \to \langle x_\mathrm{m}\rangle + \hat{x}_\mathrm{m}$ where small fluctuations $\delta\hat{a}$ and $\hat{x}_\mathrm{m}$ are defined and added to the steady state solutions. Substituting the linearised operators together with the steady solutions (Equation (2.105b)and (2.105a)) into the equation (2.103) results in

$$\delta\dot{\hat{a}} = -\left(\frac{\kappa}{2}\delta\hat{a} - i\Delta\right)\delta\hat{a} - ig_0\hat{x}_\mathrm{m}|\alpha|e^{i\theta} + \sqrt{\kappa_\mathrm{L}}\hat{a}_\mathrm{L}^\mathrm{in} + \sqrt{\kappa_\mathrm{R}}\hat{a}_\mathrm{R}^\mathrm{in}\,, \tag{2.110a}$$

$$\dot{\hat{x}}_\mathrm{m} = \omega_\mathrm{m}\hat{p}_\mathrm{m}\,, \tag{2.110b}$$

$$\dot{\hat{p}}_\mathrm{m} = -\omega_\mathrm{m}\hat{x}_\mathrm{m} - \gamma_\mathrm{m}\hat{p}_\mathrm{m} + \sqrt{\gamma_\mathrm{m}}\hat{\mathcal{F}}_\mathrm{ext} + g_0|\alpha|(e^{-i\theta}\hat{a} + e^{i\theta}\hat{a}^\dagger)\,, \tag{2.110c}$$

where $\Delta = \tilde{\Delta} + g_0\langle x_\mathrm{m}\rangle$. From these equations the amplitude quadrature $\hat{X}_\mathrm{om}$ and phase quadrature $\hat{Y}_\mathrm{om}$ of the intracavity field (see Equation (2.59)) are deduced as

$$\dot{\hat{X}}_\mathrm{om} = -\frac{\kappa}{2}\hat{X}_\mathrm{om} + \Delta\hat{Y}_\mathrm{om} + \sqrt{\kappa_\mathrm{L}}\hat{X}_\mathrm{om,L}^\mathrm{in} + \sqrt{\kappa_\mathrm{R}}\hat{X}_\mathrm{om,R}^\mathrm{in}\,, \tag{2.111a}$$

$$\dot{\hat{Y}}_\mathrm{om} = -\frac{\kappa}{2}\hat{Y}_\mathrm{om} - \Delta\hat{X}_\mathrm{om} - g\hat{x}_\mathrm{m} + \sqrt{\kappa_\mathrm{L}}\hat{X}_\mathrm{om,L} + \sqrt{\kappa_\mathrm{R}}\hat{X}_\mathrm{om,R}^\mathrm{in}\,, \tag{2.111b}$$

$$\dot{\hat{x}}_\mathrm{m} = \omega_\mathrm{m}\hat{p}_\mathrm{m}\,, \tag{2.111c}$$

$$\dot{\hat{p}}_\mathrm{m} = -\omega_\mathrm{m}\hat{x}_\mathrm{m} - \gamma_\mathrm{m}\hat{p}_\mathrm{m} + \sqrt{\gamma_\mathrm{m}}\hat{\mathcal{F}}_\mathrm{ext} - g\hat{X}_\mathrm{om}\,, \tag{2.111d}$$

with the light enhanced coupling strength given by

$$g = \sqrt{2}g_0\alpha = \sqrt{2}Gx_\mathrm{zpf}\alpha = \sqrt{2}\frac{d\omega_\mathrm{cav}}{dx}x_\mathrm{zpf}\alpha\,, \tag{2.112}$$

where $g_0 = Gx_\mathrm{zpf}$ is used (Equation (2.99)) and the intracavity amplitude α is given in Equation (2.105a). Thus, the coupling strength g is proportional to the intracavity steady state amplitude α. The intracavity amplitude is connected to the input power $\alpha_\mathrm{L}^\mathrm{in}$ via (Equation (2.105a))

$$\alpha = \frac{\sqrt{\kappa_\mathrm{L}}}{\frac{\kappa}{2} + i\Delta}\alpha_\mathrm{L}^\mathrm{in}\,. \tag{2.113}$$

Typically, these equations are solved in the frequency domain. The Fourier transform[42] yields

$$i\omega\hat{X}_\mathrm{om}(\omega) = -\frac{\kappa}{2}\hat{X}_\mathrm{om}(\omega) + \Delta\hat{Y}_\mathrm{om}(\omega) + \sqrt{\kappa_\mathrm{L}}\hat{X}_\mathrm{om,L}^\mathrm{in}(\omega) + \sqrt{\kappa_\mathrm{R}}\hat{X}_\mathrm{om,R}^\mathrm{in}(\omega)\,, \tag{2.114a}$$

$$i\omega\hat{Y}_\mathrm{om}(\omega) = -\frac{\kappa}{2}\hat{Y}_\mathrm{om}(\omega) - \Delta\hat{X}_\mathrm{om}(\omega) - g\hat{x}_\mathrm{m}(\omega) + \sqrt{\kappa_\mathrm{L}}\hat{Y}_\mathrm{om,L}^\mathrm{in}(\omega) + \sqrt{\kappa_\mathrm{R}}\hat{Y}_\mathrm{om,R}^\mathrm{in}(\omega)\,, \tag{2.114b}$$

$$i\omega\hat{x}_\mathrm{m}(\omega) = \omega_\mathrm{m}\hat{p}_\mathrm{m}(\omega)\,, \tag{2.114c}$$

$$i\omega\hat{p}_\mathrm{m}(\omega) = -\omega_\mathrm{m}\hat{x}_\mathrm{m}(\omega) - \gamma_\mathrm{m}\hat{p}_\mathrm{m}(\omega) + \sqrt{\gamma_\mathrm{m}}\hat{\mathcal{F}}_\mathrm{ext}(\omega) - g\hat{X}_\mathrm{om}(\omega)\,. \tag{2.114d}$$

[42] $\frac{d}{dt} \to i\omega$ of Equation (2.111).

Combining these equations, it follows that

$$\hat{x}_\mathrm{m} = \chi_\mathrm{m}(\omega)\left(\sqrt{\gamma_\mathrm{m}}\hat{\mathcal{F}}_\mathrm{ext}(\omega) - g\hat{X}_\mathrm{om}(\omega)\right), \tag{2.115a}$$

$$\hat{X}_\mathrm{om}(\omega) = \chi_\mathrm{phase}(\omega)\left(\left(\sqrt{\kappa_\mathrm{L}}\hat{Y}^\mathrm{in}_\mathrm{om,L} + \sqrt{\kappa_\mathrm{R}}\hat{Y}^\mathrm{in}_\mathrm{om,R}\right) - g\hat{x}_\mathrm{m}\right) \tag{2.115b}$$

$$+ \chi_\mathrm{ampl}(\omega)\left(\sqrt{\kappa_\mathrm{L}}\hat{X}^\mathrm{in}_\mathrm{om,L} + \sqrt{\kappa_\mathrm{R}}\hat{X}^\mathrm{in}_\mathrm{om,R}\right), \tag{2.115c}$$

$$\hat{Y}_\mathrm{om}(\omega) = -\chi_\mathrm{phase}(\omega)\left(\sqrt{\kappa_\mathrm{L}}\hat{X}^\mathrm{in}_\mathrm{om,L} + \sqrt{\kappa_\mathrm{R}}\hat{X}^\mathrm{in}_\mathrm{om,R}\right) \tag{2.115d}$$

$$+ \chi_\mathrm{ampl}(\omega)\left(\sqrt{\kappa_\mathrm{L}}\hat{Y}^\mathrm{in}_\mathrm{om,L} + \sqrt{\kappa_\mathrm{R}}\hat{Y}^\mathrm{in}_\mathrm{om,R} - g\hat{x}_\mathrm{m}\right), \tag{2.115e}$$

where $\chi_\mathrm{m}(\omega)$ is the mechanical susceptibility defined in (Equation (2.86)) and the cavity phase quadrature χ_phase[43] and amplitude quadrature susceptibility $\chi_\mathrm{phase}(\omega)$[44] are defined as

$$\chi_\mathrm{phase}(\omega) = \frac{\Delta}{\Delta^2 + \left(\frac{\kappa}{2} + i\omega\right)^2}, \tag{2.116}$$

$$\chi_\mathrm{ampl}(\omega) = \frac{\frac{\kappa}{2} + i\omega}{\Delta^2 + \left(\frac{\kappa}{2} + i\omega\right)^2}. \tag{2.117}$$

Equation (2.115a) shows that the position $\hat{x}_\mathrm{m}$ experiences an additional force, besides the external force $\hat{\mathcal{F}}_\mathrm{ext}$, namely the quantum radiation pressure force $\hat{F}_\mathrm{rad} = -g\hat{X}_\mathrm{om}$[45]. By inserting Equation (2.115c) into Equation (2.115a) the position $\hat{x}_\mathrm{m}$ is written as

$$\hat{x}_\mathrm{m}(\omega) = \chi_\mathrm{eff}(\omega)\left(\sqrt{\gamma_\mathrm{m}}\hat{\mathcal{F}}_\mathrm{ext} + \hat{f}_\mathrm{q}\right), \tag{2.118}$$

with the effective susceptibility

$$\chi_\mathrm{eff}(\omega) = \frac{\omega_\mathrm{m}}{\omega_\mathrm{m}^2 - \omega^2 + i\omega\gamma_\mathrm{m} + \Sigma(\omega)}, \tag{2.119}$$

and the quantum noise $\hat{f}_\mathrm{q}$

$$\hat{f}_\mathrm{q} = g\chi_\mathrm{phase}\left(\sqrt{\kappa_\mathrm{L}}\hat{Y}^\mathrm{in}_\mathrm{om,L} + \sqrt{\kappa_\mathrm{R}}\hat{Y}^\mathrm{in}_\mathrm{om,R}\right) + g\chi_\mathrm{ampl}\left(\sqrt{\kappa_\mathrm{L}}\hat{X}^\mathrm{in}_\mathrm{om,L} + \sqrt{\kappa_\mathrm{R}}\hat{X}^\mathrm{in}_\mathrm{om,R}\right). \tag{2.120}$$

Equation (2.119) contains also $\Sigma(\omega)$ which describes the modification due to the radiation pressure force and is given by

$$\Sigma(\omega) = -g^2\omega_\mathrm{m}\chi_\mathrm{phase}(\omega). \tag{2.121}$$

Comparing equation (2.118) to Equation (2.115a), it follows that radiation pressure in addition also alters the position $\hat{x}_\mathrm{m}$, which is expressed by the $\Sigma(\omega)$ in

[43] χ_phase rotates the phase quadrature $\hat{Y}_\mathrm{om}(\omega)$ into amplitude quadrature $\hat{X}_\mathrm{om}(\omega)$ (see Equation (2.115)).

[44] $\chi_\mathrm{ampl}(\omega)$ rotates the amplitude quadrature $\hat{X}_\mathrm{om}(\omega)$ into phase quadrature $\hat{Y}_\mathrm{om}(\omega)$ (see Equation (2.115)).

[45] $\hat{F}_\mathrm{rad} = \frac{\hat{H}_\mathrm{int}}{d\hat{x}_\mathrm{m}} = g_0\left(\alpha^* + \delta\hat{a}^\dagger\right)\left(\alpha + \delta\hat{a}\right) \to gX_\mathrm{om}$.

Equation (2.118). The resulting susceptibility $\chi_{\mathrm{eff}}(\omega)$ can be rewritten as

$$\begin{aligned}\chi_{\mathrm{eff}}(\omega) &= \frac{\omega_{\mathrm{m}}}{\omega_{\mathrm{m}}^2 + 2\omega_{\mathrm{m}}\delta\omega_{\mathrm{m}} - \omega^2 + i\omega\left(\gamma_{\mathrm{m}} + \Gamma_{\mathrm{opt}}\right)} \\ &= \frac{\omega_{\mathrm{m}}}{\omega_{\mathrm{eff}}^2 - \omega^2 + i\omega\gamma_{\mathrm{eff}}}\end{aligned} \tag{2.122}$$

with the effective resonance frequency $\omega_{\mathrm{eff}} = \omega_{\mathrm{m}} + \delta\omega_{\mathrm{m}}$[46] and the effective optomechanical damping $\gamma_{\mathrm{eff}} = \gamma_{\mathrm{m}} + \Gamma_{\mathrm{opt}}(\omega)$. Here the frequency shift $\delta\omega_{\mathrm{m}}$ and the linewdith change $\Gamma_{\mathrm{opt}}(\omega)$ are given by

$$\begin{aligned}\delta\omega_{\mathrm{m}}(\omega) &= \frac{\Re(\Sigma(\omega))}{2\omega_{\mathrm{m}}} \\ &= -\frac{g^2\omega_{\mathrm{m}}}{4\omega_{\mathrm{m}}}\left(\frac{\Delta-\omega}{(\Delta-\omega)^2+\frac{\kappa^2}{4}} + \frac{\Delta+\omega}{(\Delta+\omega)^2+\frac{\kappa^2}{4}}\right), \qquad (2.123a) \\ &\approx -\frac{g^2}{4}\left(\frac{\Delta-\omega_{\mathrm{m}}}{(\Delta-\omega_{\mathrm{m}})^2+\frac{\kappa^2}{4}} + \frac{(\Delta+\omega_{\mathrm{m}})}{(\Delta+\omega_{\mathrm{m}})^2+\frac{\kappa^2}{4}}\right) \\ \Gamma_{\mathrm{opt}}(\omega) &= \frac{\Im(\Sigma(\omega))}{\omega} \\ &= \frac{g^2\omega_{\mathrm{m}}}{4\omega}\left(\frac{\kappa}{(\Delta-\omega)^2+\frac{\kappa^2}{4}} - \frac{\kappa}{(\Delta+\omega)^2+\frac{\kappa^2}{4}}\right) \qquad (2.123b) \\ &\approx \frac{g^2}{4}\left(\frac{\kappa}{(\Delta-\omega_{\mathrm{m}})^2+\frac{\kappa^2}{4}} - \frac{\kappa}{(\Delta+\omega_{\mathrm{m}})^2+\frac{\kappa^2}{4}}\right).\end{aligned}$$

In the last line of Equation (2.123a) and (2.123b) a weak laser drive ($g \ll \kappa$) was assumed for which it is valid to calculate the optical spring effect $\delta\Omega$ and the optomechanical damping rate Γ_{opt} at the unperturbed resonance frequency $\omega = \omega_{\mathrm{m}}$ [AKM14]. A simulation of $\delta\omega_{\mathrm{m}}$ and Γ_{opt} for the sideband resolved ($\omega_{\mathrm{m}} > \kappa$) and unresolved ($\omega_{\mathrm{m}} < \kappa$) regime is given in Figure 2.11. Moreover, a real measurement of this effect, which is used to extract the coupling strength g, can be seen in Section 4.3.2.1.

[46] For $\delta\omega_{\mathrm{m}} \ll \omega_{\mathrm{m}}$ resonance condition changes: $(\omega_{\mathrm{m}} + \delta\omega_{\mathrm{m}}(\omega))^2 \approx \omega_{\mathrm{m}}^2 + 2\omega_{\mathrm{m}}\delta\omega_{\mathrm{m}}$.

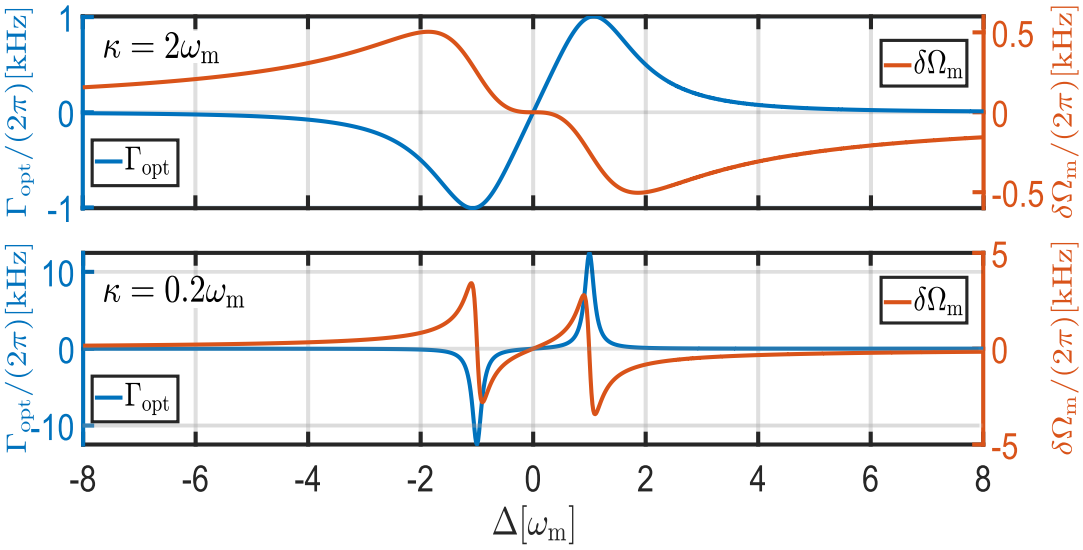

FIGURE 2.11: Dynamical backaction (Equation (2.123)) in the unresolved (upper panel) and resolved (lower panel) sideband regime. For the unresolved sideband regime $\kappa = 2\omega_m$ was used, whereas for the resolved sideband regime $\kappa = 0.2\omega_m$ was used. Apart from this both plots are simulated with $g/(2\pi) = 50\,\text{kHz}$, $\omega_m/(2\pi) = 1\,\text{MHz}$.

The modification, as depicted in Figure 2.11, of the mechanical parameters arises from the fact that a movement of the mechanical oscillator changes the intracavity field which in turn acts back via radiation pressure on the mechanical oscillator position[47]. Therefore, the process is called dynamical backaction. One effect related to dynamical backaction, specifically due to the broadening of the effective linewidth γ_{eff}, is called optomechanical sideband cooling. This effect will be discussed in more detail in the following Section 2.5.3.

2.5.3 Optomechancial sideband cooling

As seen in Equation (2.119), the position $\hat{x}_m$ is not only affected by thermal noise but also under the effect of quantum fluctuations $\hat{f}_q$ due to the optomechanical interaction. If the system is treated classically ($\hat{f}_q = 0$), the mean variance $\langle \hat{x}_m \rangle$ of the optomechanical coupled oscillator is derived in the same manner as for the uncoupled mechanical oscillator in Equation (2.95). Hence, the position variance $\langle \hat{x}_m^2 \rangle$ of an mechanical oscillator experiencing optomechanical interaction is given by

$$\langle \hat{x}_m^2 \rangle = \int_{-\infty}^{\infty} \bar{S}_{\hat{x}_m,\hat{x}_m}(\omega)\frac{d\omega}{2\pi} = \gamma_m \int_{-\infty}^{\infty} |\chi_{eff}(\omega)|^2 \bar{S}_{\hat{f}_{th},\hat{f}_{th}}(\omega)\frac{d\omega}{2\pi} \approx \frac{k_B T_{eff}}{\hbar\omega_m} \tag{2.124}$$

with

$$T_{eff} = \frac{\gamma_m}{\gamma_{eff}} T = \frac{\gamma_m}{\Gamma_{opt} + \gamma_m} T\,. \tag{2.125}$$

In the red-detuned regime, $\Delta > 0$, the (optomechanical) damping rate increases (see Figure 2.11), leading to an effective cooling of the mechanical oscillator as $T_{eff} < T$. The minimal effective temperature for a given coupling strength g that can be reached corresponds to the maximum value of Γ_{opt}. This maximum is reached at[48]

[47] Two harmonic oscillators - the light field and the mechanical oscillator are coupled.

[48] $\frac{d\Gamma_{opt}}{d\Delta}|_{\Delta=\Delta_{opt}} = 0$.

(Equation (2.123b))

$$\Delta_{\mathrm{opt}} = \sqrt{-\frac{\kappa}{12} + \frac{\omega^2}{3} + \frac{1}{6}\left(\kappa^4 + 4\kappa^2\omega_{\mathrm{m}}^2 + 16\omega_{\mathrm{m}}^2\right)^{\frac{1}{2}}}\,. \tag{2.126}$$

For the unresolved sideband (URSB: $\omega_{\mathrm{m}} \ll \kappa$) the maximum is reached at

$$\Delta_{\mathrm{opt}}^{\mathrm{URSB}} = \frac{\kappa}{2\sqrt{3}}\,, \tag{2.127}$$

and for the resolved sideband (RSB: $\omega_{\mathrm{m}} \gg \kappa$) at

$$\Delta_{\mathrm{opt}}^{\mathrm{RSB}} = \omega_{\mathrm{m}}\,. \tag{2.128}$$

Because one also often works with a resonance-tuned cavity ($\Delta = 0$), it is worth mentioning that the mechanical susceptibility χ_{m}, in this case, remains unchanged as $\Gamma_{\mathrm{opt}} = 0$ and $\delta\omega_{\mathrm{m}} = 0$. For the blue-detuned regime, $\Delta < 0$, the optomechanical damping rate Γ_{opt} is negative and leads to a decrease of the effective linewidth γ_{eff}. Ultimately, in the blue-detuned regime, the effective optomechanical damping rate γ_{eff} can become zero or negative, leading to parametric instability. Finally, it should be mentioned that more intuitively optomechanical cooling and heating can be understood as an effect that is generated due to the phase retardation of the intracavity field, causing the radiation pressure force and the mechanical oscillator motion [AKM14]. So far, optomechanical sideband cooling ($\Delta > 0$) is a consequence of classical dynamical backaction. Taking the quantum mechanical noise $\hat{f}_{\mathrm{q}}$ into account leads even for $\Delta = 0$ to displacement noise of the mechanical oscillator due to quantum radiation pressure noise. This effect can be considered as a heating process that causes an increase of the phonon occupation number given in the tuned case ($\Delta = 0$) by

$$\bar{n}_{\mathrm{eff}} = \bar{n} + \frac{1}{2} + |C_{\mathrm{eff}}|\,. \tag{2.129}$$

with $|C_{\mathrm{eff}}| = \frac{g^2\kappa}{4\gamma_{\mathrm{m}}}\frac{1}{\frac{\kappa^2}{4}+\omega^2}$, which will be derived in Section 2.5.7. For completeness, the quantum radiation pressure noise limits the minimal occupation attainable in an optomechanical system [49] to [AKM14]

$$\bar{n}_{\mathrm{f}} = \frac{\bar{n}_{\mathrm{th}}\gamma_{\mathrm{m}} + \bar{n}_{\mathrm{m}}^{\mathrm{c}}\Gamma_{\mathrm{opt}}}{\gamma_{\mathrm{m}} + \Gamma_{\mathrm{opt}}}. \tag{2.130}$$

Here $\bar{n}_{\mathrm{m}}^{\mathrm{c}}$ describes the minimum occupation number due to quantum backaction given by

$$\bar{n}_{\mathrm{m}}^{\mathrm{c}} = \frac{(\omega_{\mathrm{m}} + \Delta)^2 + \left(\frac{\kappa}{2}\right)^2}{-4\Delta\omega_{\mathrm{m}}}. \tag{2.131}$$

Equations (2.129)-(2.131) reveal that the mechanical oscillator is not only coupled to a thermal bath but also in addition to an optical bath due to the measurement process. Thereby, the optomechanical coupling sets the lower bound for the final occupation number reachable in an optomechanical system.

So far, the change of the mechanical occupation number $\bar{n}$ due to quantum radiation pressure noise and the effect of dynamical backaction on the mechanical oscillator dynamics (Equation (2.123)) has been introduced. The following section deals with the measurement of these effects. For this purpose, the next chapter is

[49] More precisely, this description is only valid in the weak drive regime ($g < \kappa$).

devoted to calculating the output spectra of the cavity, which can be measured, for example, with a homodyne detector (Section 2.3.2). After this, the Standard quantum limit (SQL) will be introduced, and a technique to surpass it, named ponderomotive squeezing will be discussed.

2.5.4 Input-output relation

The output spectrum of the optomechanical system can be calculated with the help of the input-output relations [GZ10]

$$\hat{X}^{\text{out}}_{\text{om,i}} = \sqrt{\kappa_{\text{i}}}\hat{X}_{\text{om}} - \hat{X}^{\text{in}}_{\text{om,i}}\,, \tag{2.132a}$$
$$\hat{Y}^{\text{out}}_{\text{om,i}} = \sqrt{\kappa_{\text{i}}}\hat{Y}_{\text{om}} - \hat{Y}^{\text{in}}_{\text{om,i}}\,. \tag{2.132b}$$

Here, the subscript $\text{i} \in R, L$ defines on which side the output is taken.
In experiments, the output can be measured under different quadrature angles θ[50] with a homodyne detector. For arbitrary quadrature angles θ the output is described as (derived from Equation (2.62))

$$\hat{\mathcal{X}}^{\theta,\text{out}}_{\text{om,i}} = \underbrace{\hat{X}^{\text{out}}_{\text{om,i}}\cos(\theta)}_{\hat{X}^{\theta,\text{out}}_{\text{om,i}}} + \underbrace{\hat{Y}^{\text{out}}_{\text{om,i}}\sin(\theta)}_{\hat{Y}^{\theta,\text{out}}_{\text{om,i}}}\,, \tag{2.133}$$

and entails that for $\theta = \frac{\pi}{2}$ the output phase quadrature $\hat{Y}^{\text{out}}_{\text{om,i}}$ and for $\theta = 0$ the output amplitude quadrature $\hat{X}^{\text{out}}_{\text{om,i}}$ is measured, while at other angles θ the measured output quadrature $\hat{\mathcal{X}}^{\theta,\text{out}}_{\text{om,i}}$ is a combination of the output phase and amplitude quadrature $\hat{Y}^{\text{out}}_{\text{om,i}}$ and $\hat{X}^{\text{out}}_{\text{om,i}}$. As shown in Figure 2.7c the arbitrary quadrature $\hat{\mathcal{X}}^{\theta,\text{out}}_{\text{om,i}}$ is also visualised in a coordinate system rotated by θ in that the rotated phase and amplitude quadrature is given by $\hat{X}^{\theta,\text{out}}_{\text{om,i}} = \hat{X}^{\text{out}}_{\text{om,i}}\cos(\theta) + \hat{Y}^{\text{out}}_{\text{om,i}}\sin(\theta)$ and
$\hat{Y}^{\theta,\text{out}}_{\text{om,i}} = \hat{X}^{\text{out}}_{\text{om,i}}\cos(\theta+\frac{\pi}{2}) + \hat{Y}^{\text{out}}_{\text{om,i}}\sin(\theta+\frac{\pi}{2})$.

In the upcoming section, the focus will be on explaining the classical effect of optomechanical induced transparency. This effect will be discussed before delving into the detailed calculation and description of the output spectra, as outlined in Sections 2.5.7 and 2.5.8.

2.5.5 OMIT

This section is devoted to the effect of optomechanically induced transparency (OMIT), first proposed in [Sch09] and first demonstrated in [Wei+10]. The effect that led to the name OMIT will become apparent by the end of this section. OMIT generally describes how a detuned optomechanical system converts a phase-modulated input field into its amplitude quadrature. In this thesis, the OMIT effect is used as a relatively quick and convenient way to characterise the key parameters (κ, Δ, ω_{m}, γ_{m} and g) of the optomechanical system in use.

Hence for an OMIT experiment, the drive input field $\alpha^{\text{in}}_{\text{L}}$[51] is a phase modulated beam with a small modulation depth β and tunable modulation frequency ω_{p} and is

[50] Quadrature angle θ is the phase between the local oscillator and output field (see Section 2.3.2).
[51] As depicted in 2.9 the left (L) port of the optomechanical cavity is the input for the drive.

given by (Equation (2.13))

$$\alpha_{\mathrm{L}}^{\mathrm{in}} e^{i\omega_0 t} \rightarrow \alpha_{\mathrm{L}}^{\mathrm{in}} e^{i(\omega_0 t + \beta \sin(\omega_{\mathrm{p}} t))} \tag{2.134a}$$

$$= \alpha_{\mathrm{L}}^{\mathrm{in}} e^{i\omega_0 t} \left[1 + \frac{\beta}{2}\left(e^{i\omega_{\mathrm{p}} t} - e^{-i\omega_{\mathrm{p}} t}\right)\right] + \cancelto{\approx 0}{\mathcal{O}(\beta^2)} = \bar{\alpha}_{\mathrm{L}}^{\mathrm{in}} + \delta\alpha_{\mathrm{L}}^{\mathrm{in}} \tag{2.134b}$$

$$\delta\alpha_{\mathrm{L}}^{\mathrm{in}} = \bar{\alpha}_{\mathrm{L}}^{\mathrm{in}} \frac{\beta}{2}\left(e^{i\omega_{\mathrm{p}} t} - e^{-i\omega_{\mathrm{p}} t}\right) . \tag{2.134c}$$

Within the OMIT section $\delta\alpha_{\mathrm{L}}^{\mathrm{in}}$ is called probe beam, while $\bar{\alpha}_{\mathrm{L}}^{\mathrm{in}}$ describes the pump field as it drives the optomechanical interaction. Compared to quantum effects, the probe light is considerably large, and hence any fluctuations are described classically[52]. In Equation (2.110), the intracavity field α was chosen as real. Therefore the transduction of the detuned cavity is lumped to the input field by an effective phase, from which (see Equation (2.105a))

$$\bar{\alpha}_{\mathrm{L}}^{\mathrm{in}} \rightarrow \frac{i(\Delta + \frac{\kappa}{2})}{\sqrt{\Delta^2 + (\frac{\kappa}{2})^2}}\alpha \tag{2.135a}$$

$$\delta\alpha_{\mathrm{L}}^{\mathrm{in}}(\omega) \rightarrow \frac{i(\Delta + \frac{\kappa}{2})}{\sqrt{\Delta^2 + (\frac{\kappa}{2})^2}}\delta\alpha_{\mathrm{L}}^{\mathrm{in}}(\omega) , \tag{2.135b}$$

follows. By inserting Equation (2.134) and (2.135a) into the equations of motion in Equation (2.110) the mechanical motion $x_{\mathrm{m}}(\omega)$ and the intracavity field fluctuations $\delta a(\omega)$ are calculated as

$$x_{\mathrm{m}}(\omega) = -\chi_{\mathrm{m}}(\omega) g X_{\mathrm{om}}(\omega) , \tag{2.136a}$$

$$\delta a = \frac{1}{\frac{\kappa}{2} + i\,(\Delta - \omega)}\left(\sqrt{\kappa_{\mathrm{L}}}\frac{i(\Delta + \frac{\kappa}{2})}{\sqrt{\Delta^2 + (\frac{\kappa}{2})^2}}\delta\alpha_{\mathrm{L}}^{\mathrm{in}}(\omega) - ig x_{\mathrm{m}}\right) \tag{2.136b}$$

$$= \chi_{\mathrm{cav}}(\omega)\left(\sqrt{\kappa_{\mathrm{L}}}\frac{|\chi_{\mathrm{cav}}(0)|}{\chi_{\mathrm{cav}}(0)}\delta\alpha_{\mathrm{L}}^{\mathrm{in}}(\omega) - ig x_{\mathrm{m}}(\omega)\right) , \tag{2.136c}$$

where the cavity susceptibility

$$\chi_{\mathrm{cav}}(\omega) = \frac{1}{\frac{\kappa}{2} + i(\Delta - \omega)}$$

is used. From Equation (2.136a)-(2.136c) the intracavity amplitude quadrature fluctuations $\delta X_{\mathrm{om}} = \frac{\delta a(\omega) + \delta a^{\dagger}(-\omega)}{\sqrt{2}}$[53] are deduced as

$$\delta X_{\mathrm{om}} = \sqrt{\kappa_{\mathrm{L}}}\frac{C(\omega)}{1 - M(\omega)}\delta\alpha_{\mathrm{L}}^{\mathrm{in}}(\omega) , \tag{2.137}$$

with

$$C(\omega) = \left(\chi_{\mathrm{cav}}(\omega)\frac{|\chi_{\mathrm{cav}}(0)|}{\chi_{\mathrm{cav}}(0)} - \chi_{\mathrm{cav}}^{*}(-\omega)\frac{|\chi_{\mathrm{cav}}(0)|}{\chi_{\mathrm{cav}}^{*}(0)}\right) , \tag{2.138}$$

and

$$M(\omega) = i\frac{g^2}{2}\chi_{\mathrm{m}}(\omega)\left(\chi_{\mathrm{cav}}(\omega) - \chi_{\mathrm{cav}}^{*}(-\omega)\right) . \tag{2.139}$$

[52] The $\hat{}$ is dropped as classical quantities are treated.

[53] $\delta\alpha_{\mathrm{L}}^{\mathrm{in}}(\omega) = -\left(\delta\alpha^{\mathrm{in}\dagger}\right)_{\mathrm{L}}(-\omega)$ (see Equation (2.136c)).

Equation (2.137) reveals that the OMIT response of the optomechanical system to input phase modulated input light is described by two contributions. The first contribution $C(\omega)$ in Equation (2.138) describes the transduction of the input phase modulation $\delta\alpha_{\mathrm{L}}^{\mathrm{in}}$ into intracavity amplitude fluctuations X_{om} by the cavity. The second contribution $M(\omega)$ in Equation (2.139) describes the mixing of the phase quadrature into the amplitude quadrature induced by the mechanical oscillator. Both contributions, $C(\omega)$ and $M(\omega)$, are a sum of $\chi_{\mathrm{cav}}(\pm\omega)$ as the signal consists of the two sidebands respectively. However, to get access to the intracavity amplitude fluctuations δX_{om} one typically measures the amplitude quadrature in transmission. Using the input-output relation (Section 2.5.4) the (classical) amplitude quadrature fluctuations $\delta X_{\mathrm{om,R}}^{\mathrm{out}}$ in transmission, leaking out at the right (R) port (see Figure 2.9), are derived as

$$\delta X_{\mathrm{om,R}}^{\mathrm{out}} = \sqrt{\kappa_{\mathrm{R}}}\delta X_{\mathrm{om}} = \sqrt{\kappa_{\mathrm{R}}}\sqrt{\kappa_{\mathrm{L}}}\frac{C(\omega)}{1-M(\omega)}\underbrace{\bar{\alpha}_{\mathrm{in,L}}\frac{\beta}{2}\left(\delta(\omega+\omega_{\mathrm{p}})+\delta(\omega-\omega_{\mathrm{p}})\right)}_{\text{FT of } \delta\alpha_{\mathrm{L}}^{\mathrm{in}}(\omega)\,(\text{Equation}(2.134c))}. \tag{2.140}$$

Equation (2.140) describes how phase modulation of the input field $\alpha_{\mathrm{L}}^{\mathrm{in}}$ is transduced to the output quadrature fluctuation $\delta X_{\mathrm{om,R}}^{\mathrm{out}}$ and reveals [54] that for a measurement the detected quadrature $\delta X_{\mathrm{om,R}}^{\mathrm{out}}$ has to be demodulated at $\omega = \omega_{\mathrm{p}}$.

Multi-mode OMIT

Before a theoretical picture of the OMIT response is shown, a short comment on the mechanical contribution $M(\omega)$ will be given. As the mechanical oscillator used within this thesis exhibits different independent mechanical resonances (Section 4.1), the contribution of $M(\omega)$ is rewritten as

$$M(\omega) = \frac{i}{2}\left(\chi_{\mathrm{cav}}(\omega) - \chi_{\mathrm{cav}}^{*}(-\omega)\right)\sum_{i}^{m} g_i^2\chi_{\mathrm{m},i}(\omega)\,. \tag{2.141}$$

Here g_i describes the optomechanical coupling to the i-th resonance given by $\chi_{\mathrm{m},i}(\omega)$. In the following, three mechanical resonance frequencies are considered for a visual representation of OMIT.

In Figure 2.12 the broad OMIT response in transmission is depicted[55], whereas Figure 2.13 shows the response in the vicinity of a mechanical resonance frequency $\omega_{\mathrm{m,i}} = \omega_{1,1}$. Also depicted in these figures is the phase response, which is also be measured during the OMIT experiment presented in Section 4.3.1.

[54] Revealed by the δ-function.

[55] Choice of resonance frequency $\omega_{\mathrm{m,i}} = \omega_{\mathrm{i,i}}$ is motivated by the used mechanical oscillator in the experiment (Section 4.1).

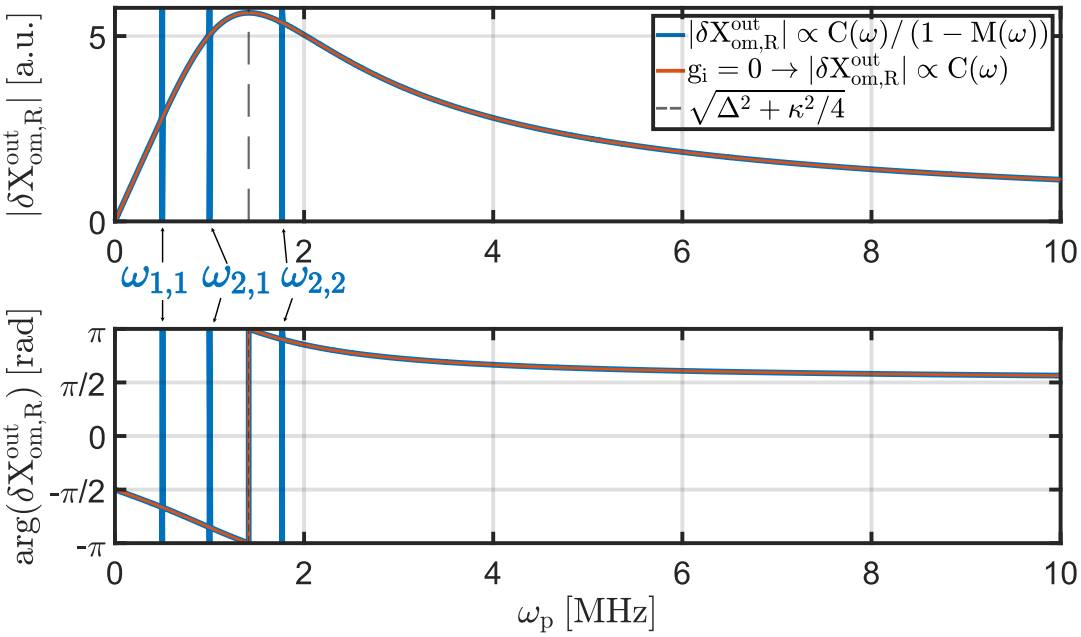

FIGURE 2.12: Broadband OMIT magnitude $|\delta X^{out}_{om,R}|$ and phase response $\arg(\delta X^{out}_{om,R})$. The red line indicates the cavity response $C(\omega)$ without a mechanical oscillator. In contrast, the blue line represents the full response with the multi-mode mechanical features visible $\omega_{1,1}/(2\pi) = 500\,\text{kHz}$, $\omega_{1,2}/(2\pi) = \frac{5}{\sqrt{2}}\omega_{1,2}$ and $\omega_{2,2}/(2\pi) = 2\omega_{1,2}$. Other parameters are: $g_i/(2\pi) = 20\,\text{kHz}$, $\kappa/(2\pi) = 2\,\text{MHz}$, $\Delta/(2\pi) = \frac{\kappa}{2}$ and $\gamma_m/(2\pi) = 3\,\text{Hz}$.

From the OMIT response in a broad frequency range ($\omega \gg \kappa$) one can identify the resonance frequencies $\omega_{i,i}$. This broad response is used to deduce the detuning Δ and the linewdith κ of the optomechanical system. Additionally, an enhanced view of the response near one mechanical resonance is depicted in Figure 2.13.

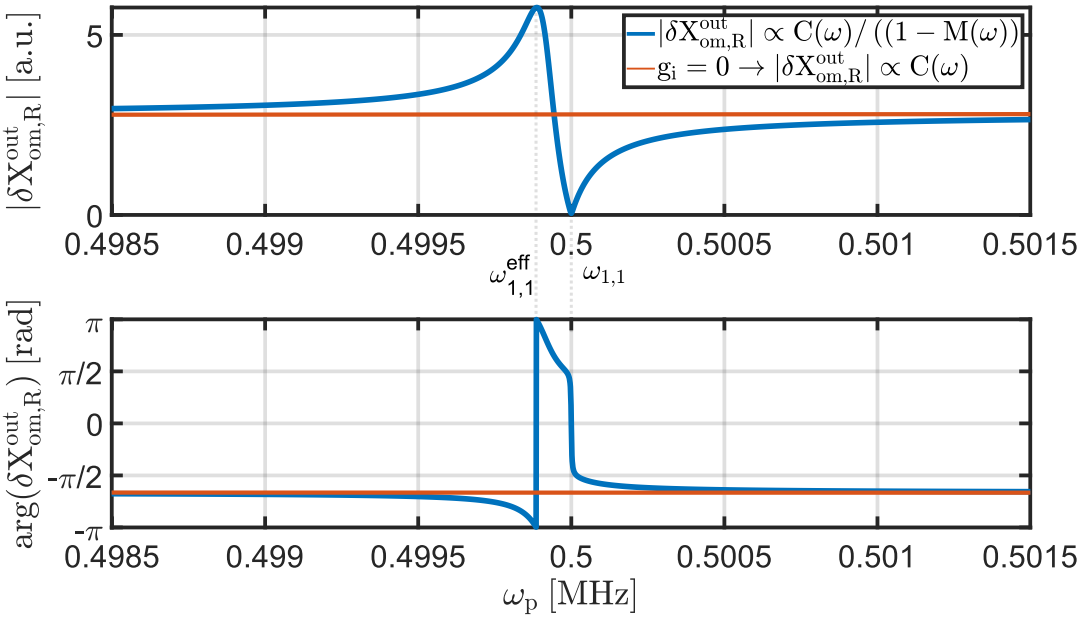

FIGURE 2.13: Enhanced view of the OMIT magnitude $\delta X^{out}_{om,R}$ and phase response $\arg(\delta X^{out}_{om,R})$ near the mechanical resonance frequency $\omega_{1,1} = 500\,\text{kHz}$. The red line indicates the cavity response $C(\omega)$ without a mechanical oscillator. In contrast, the blue line represents the full OMIT response at the mode mechanical resonance frequency $\omega_{1,1}/(2\pi) = 500\,\text{kHz}$. A dip-peak feature due to OMIT appears and is clearly visible near the resonance $\omega_{1,1}$ (more information in the text). Parameters as in Figure 2.12.

It is visible that the feature in Figure 2.13 constitutes a peak and a dip structure. A theoretical reason for the peak-dip feature lies in the fact that $\frac{1}{1-M(\omega)}$ can be written as [Che19]

$$\frac{1}{1-M(\omega)} = \frac{\chi_{\text{eff}}(\omega)}{\chi_{\text{m}}(\omega)}\,. \tag{2.142}$$

The peak corresponds to the effective mechanical resonance frequency, $\omega_{\text{eff}} = \omega^{\text{eff}}_{1,1}$, resulting from the optomechanical coupling of the detuned pump beam $\alpha^{\text{in}}_{\text{L}}$. The dip occurs at the bare mechanical resonance frequency, $\omega_{\text{m}} = \omega_{1,1}$. Having the dip at the mechanical resonance frequency indicates that the phase-modulated sidebands do not affect the amplitude quadrature ($\delta X^{out}_{om,R} = 0$) in transmission. This implies transparency of the cavity to a phase-modulated input field. This effect is known as "Optomechanical Induced Transparency" (OMIT). Examining, the peak-dip feature allows for the measurement of mechanical properties (ω_{m} and γ_{m}) and the optomechanical coupling strength g.

In summary, while the broad cavity OMIT response $C(\omega)$ (see Figure 2.12) provides information about the optical properties, a closer examination of the OMIT response near a mechanical resonance enables the determination of mechanical properties and the coupling strength g.

The remaining part of this theory section will explore quantum (opto)mechanical aspects. In doing so, it comprehensively discusses all optomechanical effects utilised within the context of this thesis. Subsequently, Section 2.5.6 is devoted to the general formalism of the optical output spectrum, which is computed using the input-output outlined in Section 2.5.4. This analysis leads to the derivation and discussion of the corresponding spectral densities for displacement and force. After the general description of the output spectra has been given, two specific cases are discussed

in Section 2.5.7 and 2.5.8. These cases pertain to the standard quantum limit (SQL) and the manifestation of ponderomotive squeezing—an outcome of optomechanical coupling that can be used to surpass the SQL. At the end of the theory part, Section 2.6 provides a brief introduction to coherent quantum noise cancellation (CQNC). This scheme facilitates a broadband enhancement in sensitivity compared to the SQL, thereby serving as the primary motivation behind the construction of the optomechanical system discussed in the experimental part of this thesis (Part II).

2.5.6 Output spectrum of the system

In the following, the symmetrised[56] output spectrum, deduced from a quadrature measurement is calculated for a lossless single-sided cavity ($\kappa_L = \kappa$[57]) at the left output (denoted by "L"). Also, within the rest of the thesis the definition of commutation relations in Fourier space and the definition of spectral densities, given in Appendix A and B, are used.

With the input-output relations and the intracavity field solutions for $\hat{X}_{om}$ and $\hat{Y}_{om}$ (Equation (2.115c) and (2.115e)) the output quadrature spectrum $\bar{S}^{\Delta}_{\hat{\mathcal{X}}^{\theta,out}_{om,L},\hat{\mathcal{X}}^{\theta,out}_{om,L}}(\omega)$[58] of Equation (2.133) is given by [Che19][59]

$$\bar{S}^{\Delta}_{\hat{\mathcal{X}}^{\theta,out}_{om,L},\hat{\mathcal{X}}^{\theta,out}_{om,L}}(\omega) = \frac{1}{2} + f^{\theta,\Delta}_{transfer}\bar{S}_{\hat{x}_m,\hat{x}_m}(\omega) + \bar{S}^{\theta,\Delta}_{corr}(\omega). \tag{2.143}$$

The following will explain the three different noise contributions of the output spectra, seen in Equation (2.143). The first contribution describes the shot noise of the measured output light field ($\frac{1}{2}$). The second describes the transduction of the mechanical oscillator displacement $\bar{S}_{\hat{x}_m,\hat{x}_m}(\omega)$ via $f^{\theta,\Delta}_{transfer}(\omega)$ to the optical output quadrature $\hat{\mathcal{X}}^{\theta,out}_{om,L}$. The displacement noise spectrum $S_{\hat{x}_m,\hat{x}_m}(\omega)$ is calculated as

$$\begin{aligned}
\bar{S}_{\hat{x}_m,\hat{x}_m}(\omega) =& |\chi_{eff}(\omega)|^2 \left(2\Gamma^{\Delta}_{QBA}(\omega)\right) && \text{(2.144a)}\\
&+ \gamma_m|\chi_{eff}(\omega)|^2\bar{S}_{\hat{\mathcal{F}}_{th},\hat{\mathcal{F}}_{th}}(\omega) && \text{(2.144b)}\\
&+ \gamma_m|\chi_{eff}(\omega)|^2\bar{S}_{\hat{\mathcal{F}}_{sig},\hat{\mathcal{F}}_{sig}}(\omega)\,. && \text{(2.144c)}
\end{aligned}$$

Here the first contribution of the displacement noise spectrum $\bar{S}_{\hat{x}_m,\hat{x}_m}(\omega)$[60] (Equation (2.144a)) shows that the displacement $\hat{x}_m$ is driven by quantum backaction noise described by the quantum backaction rate

$$\Gamma^{\Delta}_{QBA}(\omega) = \frac{g^2\kappa}{4}\left(|\chi_{phase}(\omega)|^2 + |\chi_{ampl}(\omega)|^2\right) \tag{2.145}$$

$$= \frac{g^2\kappa}{4}\frac{\Delta^2 + \frac{\kappa^2}{4} + \omega^2}{\Delta^4 + 2\Delta^2(\frac{\kappa^2}{4} - \omega^2) + (\frac{\kappa^2}{4} + \omega^2)^2}\,. \tag{2.146}$$

[56] From now only symmetrised spectra (denoted by the bar) are calculated (definition in Appendix B).

[57] Thereby $\kappa_R + \kappa_{loss} = 0$ see definition of κ (Equation 2.30).

[58] For (later) readability function parameters are sometimes written as superscripts (e.g. $\bar{S}_{\hat{\mathcal{X}}^{\theta,out}_{om,L},\hat{\mathcal{X}}^{\theta,out}_{om,L}}(\omega,\theta,\Delta) \to \bar{S}^{\Delta}_{\hat{\mathcal{X}}^{\theta,out}_{om,L},\hat{\mathcal{X}}^{\theta,out}_{om,L}}(\omega)$ or $f_{transfer}(\omega,\theta,\Delta) \to f^{\theta,\Delta}_{transfer}$).

[59] Spectras and transduction factors differ slightly from [Che19] due to different normalisations within this thesis.

[60] By rewriting Equation (2.144) one can identify the total external noise spectral density as $\bar{S}^{\Delta}_{\hat{\mathcal{F}}_{ext},\hat{\mathcal{F}}_{ext}}(\omega) = \frac{2\Gamma^{\Delta}_{QBA}(\omega)}{\gamma_m} + \bar{S}_{\hat{\mathcal{F}}_{th},\hat{\mathcal{F}}_{th}}(\omega) + \bar{S}_{\hat{\mathcal{F}}_{sig},\hat{\mathcal{F}}_{sig}}(\omega)$, which contains an additional external noise contribution ($\frac{2\Gamma^{\Delta}_{QBA}(\omega)}{\gamma_m}$) due to radiation pressure (shot) noise, indicated by the superscript Δ.

The second part (Equation (2.144b)) describes the intrinsic noise which is given by[61]

$$\bar{S}^{\Delta}_{\mathrm{intr}}(\omega) = \gamma_{\mathrm{m}} |\chi_{\mathrm{eff}}(\omega)|^2 \bar{S}_{\hat{\mathcal{F}}_{\mathrm{th}},\hat{\mathcal{F}}_{\mathrm{th}}}(\omega)\,, \tag{2.147}$$

with the thermal noise defined as (see Equation (2.90))

$$\bar{S}_{\hat{\mathcal{F}}_{\mathrm{th}},\hat{\mathcal{F}}_{\mathrm{th}}} = 2\left(n_{\mathrm{th}} + \frac{1}{2}\right) = 2\left(\frac{k_{\mathrm{B}}T}{\hbar\omega_{\mathrm{m}}} + \frac{1}{2}\right). \tag{2.148}$$

Equation (2.148) in conjunction with Equation (2.144b) reveal, that the oscillator at zero temperature and in absence of any other noise is driven by its *intrinsic* zero point fluctuations. Even more important, the last contribution (Equation (2.144c)) of the noise spectrum $\bar{S}_{\hat{x}_{\mathrm{m}},\hat{x}_{\mathrm{m}}}(\omega)$ contains the spectrum $\bar{S}_{\hat{\mathcal{F}}_{\mathrm{sig}},\hat{\mathcal{F}}_{\mathrm{sig}}}(\omega)$ of the force to be measured.

The initially mentioned transduction factor $f_{\mathrm{transfer}}(\omega)$ is calculated as

$$f^{\theta,\Delta}_{\mathrm{transfer}}(\omega) = \Gamma_{\mathrm{meas}}(\Re\{\xi(\omega) - \mu(\omega)e^{2i\theta}\}) \tag{2.149}$$

with

$$\Gamma_{\mathrm{meas}} = \frac{g^2}{4\kappa} \tag{2.150}$$

$$\xi(\omega) = \kappa^2\left(|\chi_{\mathrm{cav}}(\omega)|^2 + |\chi_{\mathrm{cav}}(-\omega)|^2\right) \tag{2.151}$$

$$\mu(\omega) = 2\kappa^2\chi_{\mathrm{cav}}(\omega)\chi_{\mathrm{cav}}(-\omega)^* \tag{2.152}$$

and the cavity susceptibility $\chi_{\mathrm{cav}}(\omega)$

$$\chi_{\mathrm{cav}}(\omega) = \chi_{\mathrm{ampli}}(\omega) - i\chi_{\mathrm{phase}}(\omega) = \frac{1}{\frac{\kappa}{2} + i(\Delta - \omega)}\,. \tag{2.153}$$

The third contribution in Equation (2.143), $\bar{S}_{\mathrm{corr}}(\omega)$, of the output spectrum $\bar{S}_{\hat{\mathcal{X}}^{\theta,\mathrm{out}}_{\mathrm{om,L}},\hat{\mathcal{X}}^{\theta,\mathrm{out}}_{\mathrm{om,L}}}(\omega)$ arises due to correlation between imprecision noise[62] and the displacement fluctuations caused by quantum backaction noise. With the definition

$$\zeta(\omega) = 2\kappa^2\left(|\chi_{\mathrm{cav}}(\omega)|^2 - |\chi_{\mathrm{cav}}(-\omega)|^2\right) \tag{2.154}$$

the spectrum of the correlation reads

$$\bar{S}^{\theta,\Delta}_{\mathrm{corr}}(\omega) = \Gamma_{\mathrm{meas}}\left(\Re\{\chi_{\mathrm{eff}}\}\Im\{\mu(\omega)e^{2i\theta}\} + \Im\{\chi_{\mathrm{eff}}\}\Re\{\zeta(\omega)\}\right). \tag{2.155}$$

Inspecting Equation 2.143 shows, that the measured quadrature spectral density $\bar{S}^{\Delta}_{\hat{\mathcal{X}}^{\theta,\mathrm{out}}_{\mathrm{om,L}},\hat{\mathcal{X}}^{\theta,\mathrm{out}}_{\mathrm{om,L}}}(\omega)$ is calibrated into a displacement spectral density by

$$\bar{S}^{(\theta,\Delta),\mathrm{infer}}_{\hat{x}_{\mathrm{m}},\hat{x}_{\mathrm{m}}}(\omega) = \frac{\bar{S}^{\Delta}_{\hat{\mathcal{X}}^{\theta,\mathrm{out}}_{\mathrm{om,L}},\hat{\mathcal{X}}^{\theta,\mathrm{out}}_{\mathrm{om,L}}}(\omega)}{f^{\theta,\Delta}_{\mathrm{transfer}}(\omega)}\,. \tag{2.156}$$

As the name suggests, from $\bar{S}^{(\theta,\Delta),\mathrm{infer}}_{\hat{x}_{\mathrm{m}},\hat{x}_{\mathrm{m}}}(\omega)$ the position spectral density $\hat{S}_{\hat{x}_{\mathrm{m}},\hat{x}_{\mathrm{m}}}$ of the mechanical oscillator is inferred.

[61] $\bar{S}^{\Delta}_{\mathrm{intr}}(\omega)$ depends on Δ as $\chi_{\mathrm{eff}}(\omega)$ is a function of Δ (see Equation (2.122) - (2.123)).

[62] The term imprecision noise will be introduced in the next section.

In conjunction with Equation (2.85), the inferred displacement spectral density $\bar{S}^{(\theta,\Delta),\text{infer}}_{\hat{x}_\text{m},\hat{x}_\text{m}}(\omega)$ is calibrated to an inferred force spectral density $\bar{S}^{(\theta,\Delta),\text{infer}}_{\hat{\mathcal{F}},\hat{\mathcal{F}}}(\omega)$[63] as

$$\bar{S}^{(\theta,\Delta),\text{infer}}_{\hat{\mathcal{F}},\hat{\mathcal{F}}}(\omega) = \frac{\bar{S}^{(\theta,\Delta),\text{infer}}_{\hat{x}_\text{m},\hat{x}_\text{m}}(\omega)}{\gamma_\text{m}|\chi_\text{eff}|^2} = \frac{\bar{S}^{\Delta}_{\hat{\mathcal{X}}^{\theta,\text{out}}_\text{om,L},\hat{\mathcal{X}}^{\theta,\text{out}}_\text{om,L}}(\omega)}{f^{\theta,\Delta}_\text{transfer}(\omega)\gamma_\text{m}|\chi_\text{eff}|^2}\,. \tag{2.157}$$

Within this section the general description of the optical output quadrature spectral density $\bar{S}^{\Delta}_{\hat{\mathcal{X}}^{\theta,\text{out}}_\text{om,L},\hat{\mathcal{X}}^{\theta,\text{out}}_\text{om,L}}(\omega)$ (Equation (2.143)) of an optomechanical system and how to infer its displacement and and force spectral density $\bar{S}^{(\theta,\Delta),\text{infer}}_{\hat{x}_\text{m},\hat{x}_\text{m}}(\omega)$ and $\bar{S}^{(\theta,\Delta),\text{infer}}_{\hat{\mathcal{F}},\hat{\mathcal{F}}}(\omega)$ (Equation (2.156) and (2.157)) were discussed. Hence, in the next two subsection, the quadrature spectral density $\bar{S}^{\Delta}_{\hat{\mathcal{X}}^{\theta,\text{out}}_\text{om,L},\hat{\mathcal{X}}^{\theta,\text{out}}_\text{om,L}}(\omega)$ (Equation (2.143)) for two distinct cases, namely $\bar{S}^{\theta,\Delta}_\text{corr}(\omega) = 0$ and $\bar{S}^{\theta,\Delta}_\text{corr} \neq 0$ will be investigated. For these two cases the inferred displacement $\bar{S}^{(\theta,\Delta),\text{infer}}_{\hat{x}_\text{m},\hat{x}_\text{m}}(\omega)$ and force sensitivity $\bar{S}^{(\theta,\Delta),\text{infer}}_{\hat{\mathcal{F}},\hat{\mathcal{F}}}(\omega)$ will also be derived. The derivation for $\bar{S}^{\theta,\Delta}_\text{corr}(\omega) = 0$ will lead to the standard quantum limit (SQL) and the definition of the quantum backaction cooperativity C_QBA (Section 2.5.7), while the derivation for $\bar{S}_\text{corr} \neq 0$ will lead to ponderomotive squeezing (Section 2.5.8).

2.5.7 Quantum backaction cooperativity C_QBA and standard quantum limit

To deduce the displacement spectrum $\bar{S}_{\hat{x}_\text{m},\hat{x}_\text{m}}$ conventionally a measurement of the phase quadrature $\hat{Y}^\text{out}_\text{om,L}$ ($\theta = \pi/2$)[64] for a cavity tuned to resonance ($\Delta = 0$) is performed. The reasoning is that under these settings, the information of the displacement $\hat{x}_\text{m}$ is solely in the output phase quadrature $\hat{Y}_\text{out,L}$ (as seen from Equation (2.114b)). The restriction $\Delta = 0$ and $\theta = \frac{\pi}{2}$ leads to a vanishing correlation term ($\bar{S}^{\theta=\frac{\pi}{2},\Delta=0}_\text{corr}(\omega) = 0$) in Equation (2.143).

Thereby, the spectral density of the phase quadrature output

$$\bar{S}_{\hat{Y}^\text{out}_\text{om,L},\hat{Y}^\text{out}_\text{om,L}}(\omega) = \bar{S}^{\Delta}_{\hat{\mathcal{X}}^{\theta,\text{out}}_\text{om,L},\hat{\mathcal{X}}^{\theta,\text{out}}_\text{om,L}}(\omega)\Big|_{\substack{\theta=\pi/2\\ \Delta=0}}$$

reads

$$\bar{S}_{\hat{Y}^\text{out}_\text{om,L},\hat{Y}^\text{out}_\text{om,L}}(\omega) = \frac{1}{2} + f^{\theta=\frac{\pi}{2},\Delta=0}_\text{transfer}(\omega)|\chi_\text{m}(\omega)|^2\left(2\Gamma^{\Delta=0}_\text{QBA}(\omega) + \gamma_\text{m}\{\bar{S}_{\hat{\mathcal{F}}_\text{th},\hat{\mathcal{F}}_\text{th}} + \bar{S}_{\hat{\mathcal{F}}_\text{sig},\hat{\mathcal{F}}_\text{sig}}(\omega)\}\right) \tag{2.158}$$

$$= \frac{1}{2} + G_\text{om}(\omega)|\chi_\text{m}(\omega)|^2\left(\frac{G_\text{om}(\omega)}{2} + \gamma_\text{m}\{\bar{S}_{\hat{\mathcal{F}}_\text{th},\hat{\mathcal{F}}_\text{th}} + \bar{S}_{\hat{\mathcal{F}}_\text{sig},\hat{\mathcal{F}}_\text{sig}}(\omega)\}\right) \tag{2.159}$$

where the optomechanical measurement strength

$$G_\text{om}(\omega) = f^{\theta=\frac{\pi}{2},\Delta=0}_\text{transfer}(\omega) = g^2\kappa\frac{1}{\frac{\kappa^2}{4}+\omega^2} \tag{2.160}$$

[63] For improved readability $\bar{S}^{(\theta,\Delta),\text{infer}}_{\hat{\mathcal{F}},\hat{\mathcal{F}}}(\omega) \overset{\text{def}}{=} \bar{S}^{(\theta,\Delta),\text{infer}}_{\hat{\mathcal{F}}_\text{ext},\hat{\mathcal{F}}_\text{ext}}(\omega)$.

[64] For $\theta = \frac{\pi}{2}$ a measurement of the phase quadrature $\hat{Y}^\text{out}_\text{om,L}$ follows, as $\hat{\mathcal{X}}^{\theta,\text{out}}_\text{om,L} \to \hat{Y}^\text{out}_\text{om,L}$ (Equation (2.133)).

and the quantum backaction rate (for a tuned cavity $\Delta = 0$)

$$\Gamma_{\mathrm{QBA}}^{\Delta=0}(\omega) = \frac{G_{\mathrm{om}}(\omega)}{4}\,, \tag{2.161}$$

have been introduced. As explained in Section 2.5, the displacement spectral density is transferred via $f_{\mathrm{transfer}}^{\theta=\frac{\pi}{2},\Delta=0}(\omega)$ to the measured output optical quadrature. Therefore, from the optical phase quadrature $\bar{S}_{\hat{Y}_{\mathrm{om,L}}^{\mathrm{out}},\hat{Y}_{\mathrm{om,L}}^{\mathrm{out}}}(\omega)$ the measured displacement spectral density $\bar{S}^{\mathrm{infer}}_{\hat{x}_{\mathrm{m}},\hat{x}_{\mathrm{m}}}$ for a tuned cavity is calculated as (see Equation (2.156))[65]

$$\bar{S}^{\mathrm{infer}}_{\hat{x}_{\mathrm{m}},\hat{x}_{\mathrm{m}}}(\omega) = \bar{S}^{(\theta,\Delta)\mathrm{infer}}_{\hat{x}_{\mathrm{m}},\hat{x}_{\mathrm{m}}}(\omega)\Big|_{\substack{\theta=\pi/2\\ \Delta=0}} = \left.\frac{\bar{S}^{\Delta}_{\hat{X}^{\theta,\mathrm{out}}_{\mathrm{om,L}},\hat{X}^{\theta,\mathrm{out}}_{\mathrm{om,L}}}(\omega)}{f^{\theta,\Delta=0}_{\mathrm{transfer}}(\omega)}\right|_{\substack{\theta=\pi/2\\ \Delta=0}} = \frac{\bar{S}^{\Delta=0}_{\hat{Y}^{\mathrm{out}}_{\mathrm{om,L}},\hat{Y}^{\mathrm{out}}_{\mathrm{om,L}}}(\omega)}{f^{\theta=\frac{\pi}{2},\Delta=0}_{\mathrm{transfer}}(\omega)} \tag{2.162a}$$

$$= \bar{S}^{\theta=\frac{\pi}{2},\Delta=0}_{\mathrm{imp}}(\omega) + |\chi_{\mathrm{m}}(\omega)|^2 \bar{S}^{\Delta=0}_{\hat{\mathcal{F}}_{\mathrm{ext}},\hat{\mathcal{F}}_{\mathrm{ext}}}(\omega) \tag{2.162b}$$

$$= \frac{1}{2G_{\mathrm{om}}(\omega)} + |\chi_{\mathrm{m}}(\omega)|^2 \left(2\Gamma^{\Delta=0}_{\mathrm{QBA}}(\omega) + \gamma_{\mathrm{m}}\{\bar{S}_{\hat{\mathcal{F}}_{\mathrm{th}},\hat{\mathcal{F}}_{\mathrm{th}}} + \bar{S}_{\hat{\mathcal{F}}_{\mathrm{sig}},\hat{\mathcal{F}}_{\mathrm{sig}}}(\omega)\}\right)\,, \tag{2.162c}$$

with the imprecision noise $\bar{S}^{\theta=\frac{\pi}{2},\Delta=0}_{\mathrm{imp}}(\omega)$, generally defined as

$$\bar{S}^{\theta,\Delta}_{\mathrm{imp}}(\omega) = \frac{1}{2f^{\theta,\Delta}_{\mathrm{transfer}}(\omega)}\,. \tag{2.163}$$

Sorting Equation (2.162) into noise and signal contribution leads to the displacement noise spectral density $\bar{S}^{\mathrm{noise}}_{\hat{x}_{\mathrm{m}}\hat{x}_{\mathrm{m}}}(\omega)$[66] given by

$$\bar{S}^{\mathrm{noise}}_{\hat{x}_{\mathrm{m}},\hat{x}_{\mathrm{m}}}(\omega) = \frac{1}{2G_{\mathrm{om}}(\omega)} + |\chi_{\mathrm{m}}(\omega)|^2\frac{G_{\mathrm{om}}(\omega)}{2} + |\chi_{\mathrm{m}}(\omega)|^2 \underbrace{2\gamma_{\mathrm{m}}(\bar{n}+\frac{1}{2})}_{\bar{S}_{\hat{\mathcal{F}}_{\mathrm{th}},\hat{\mathcal{F}}_{\mathrm{th}}}} \tag{2.164}$$

$$= \underbrace{\bar{S}^{\theta=\frac{\pi}{2},\Delta=0}_{\mathrm{imp}}(\omega) + |\chi_{\mathrm{m}}(\omega)|^2 S^{\Delta=0}_{\mathrm{qba}}(\omega)}_{\bar{S}^{\mathrm{add}}_{\hat{x}_{\mathrm{m}},\hat{x}_{\mathrm{m}}}} + \underbrace{|\chi_{\mathrm{m}}(\omega)|^2 2\gamma_{\mathrm{m}}\left(\frac{k_{\mathrm{B}}T}{\hbar\omega_{\mathrm{m}}}+\frac{1}{2}\right)}_{\bar{S}^{\Delta=0}_{\mathrm{intr}}(\omega)} \tag{2.165}$$

where the backaction noise is generally given by

$$\bar{S}^{\Delta}_{\mathrm{qba}}(\omega) = 2\Gamma^{\Delta}_{\mathrm{QBA}}(\omega)\,. \tag{2.166}$$

Without backaction noise ($\bar{S}_{\mathrm{qba}}(\omega) = 2\Gamma_{\mathrm{QBA}}(\omega) = 0$), the imprecision noise $\bar{S}^{\theta=\frac{\pi}{2},\Delta=0}_{\mathrm{imp}}(\omega)$ remains and fundamentally limits the achievable precision of the optomechanical system. Therefore $\bar{S}^{\theta,\Delta}_{\mathrm{imp}}(\omega) = \frac{1}{2f^{\theta,\Delta}_{\mathrm{transfer}}(\omega)}$ is named imprecision noise. So, the displacement noise spectral density $S^{\mathrm{noise}}_{\hat{x}_{\mathrm{m}}\hat{x}_{\mathrm{m}}}(\omega)$ given in Equation (2.164) reveals that measuring with light adds noise to the imprecision noise $S_{\mathrm{impr}}(\omega)$. Thereby, the measurement itself adds noise to the intrinsic noise $\bar{S}^{\Delta=0}_{\mathrm{intr}}(\omega)$[67] of the

[65] For $\bar{S}^{\Delta=0}_{\hat{\mathcal{F}}_{\mathrm{ext}},\hat{\mathcal{F}}_{\mathrm{ext}}}(\omega)$ in Equation ((2.162b)) see footnote 60.

[66] Remark to the notation: $\bar{S}^{\mathrm{noise}}_{\hat{x}_{\mathrm{m}},\hat{x}_{\mathrm{m}}}(\omega) \overset{\mathrm{def}}{=} \bar{S}^{(\theta,\Delta),\mathrm{noise}}_{\hat{x}_{\mathrm{m}},\hat{x}_{\mathrm{m}}}(\omega)\Big|_{\substack{\theta=\pi/2\\ \Delta=0}}$.

[67] $\bar{S}^{\Delta=0}_{\mathrm{intr}}(\omega)$ (definition in Equation (2.147)) is proportional to $|\chi_{\mathrm{m}}(\omega)|^2$ as $|\chi^{\Delta=0}_{\mathrm{eff}}(\omega)|^2 = |\chi_{\mathrm{m}}(\omega)|^2$ (see Section 2.5.2).

system, and hence the added noise spectral density $\bar{S}^{\text{add}}_{\hat{x}_\text{m},\hat{x}_\text{m}}(\omega)$[68] for $\Delta = 0$ and $\theta = \pi/2$ is defined as (see Equation (2.165))

$$\begin{aligned}\bar{S}^{\text{add}}_{\hat{x}_\text{m},\hat{x}_\text{m}}(\omega) &= \bar{S}^{\text{noise}}_{\hat{x}_\text{m}\hat{x}_\text{m}}(\omega) - \bar{S}^{\Delta=0}_{\text{intr}}(\omega) \\ &= \bar{S}^{\Delta=0}_{\text{qba}}(\omega) + \bar{S}^{\theta=\frac{\pi}{2},\Delta=0}_{\text{imp}}(\omega)\,.\end{aligned} \tag{2.167}$$

Before taking a closer look at the minimisation of the added noise spectral density, an important figure of merit for quantum optomechanical force sensors, the so called quantum backaction cooperativity C_QBA and the effective optomechanical cooperativity $|C_\text{eff}|$, will be derived.

Quantum Backaction Cooperativity C_QBA

From the displacement noise $\bar{S}^{\text{noise}}_{\hat{x}_\text{m}\hat{x}_\text{m}}$ it is straightforward to see that an optomechanical system is limited by quantum backaction noise if $\bar{S}^{\Delta=0}_{\text{qba}}(\omega) > \bar{S}_{\hat{\mathcal{F}}_\text{th},\hat{\mathcal{F}}_\text{th}}$ (Equation (2.165)). This condition leads to quantum backaction cooperativity

$$C_\text{QBA} = \frac{\bar{S}^{\Delta=0}_{\text{qba}}(\omega=0)}{\bar{S}_{\hat{\mathcal{F}}_\text{th},\hat{\mathcal{F}}_\text{th}}} = \frac{g^2\hbar}{\kappa k_\text{B} T} Q \gg 1\,, \tag{2.168}$$

which is the ratio of the optomechanical measurement strength to the thermal decoherence rate. With respect to the C_QBA, quantum backaction limited sensors can be ensured by a stronger decoupling of the mechanical oscillator from the thermal bath (increasing $Q = \frac{\omega_\text{m}}{\gamma_\text{m}}$), by decreasing the temperature T and/or increasing the light enhanced coupling strength g.

Remark On Effective Phonon Number n_eff

Rewriting Equation (2.164) with the effective optomechanical cooperativity $|C_\text{eff}(\omega)| = \frac{G_\text{om}(\omega)}{4\gamma_\text{m}}$[69] and $\bar{S}_{\hat{\mathcal{F}}_\text{th},\hat{\mathcal{F}}_\text{th}} = 2(\bar{n}+\frac{1}{2})$ to

$$\bar{S}^{\text{noise}}_{\hat{x}_\text{m}\hat{x}_\text{m}}(\omega) = \frac{1}{8|C_\text{eff}(\omega)|\gamma_\text{m}} + 2\gamma_\text{m}|\chi_\text{m}(\omega)|^2 \underbrace{\left(\bar{n}+\frac{1}{2}+|C_\text{eff}(\omega)|\right)}_{\bar{n}_\text{eff}} \tag{2.169}$$

reveals that on resonance, the mechanical oscillator is heated due to quantum radiation pressure noise, as stated in Section 2.5.3. Equation (2.169) shows that the phonon number is effectively altered due to the optomechanical interaction and is given by $\bar{n}_\text{eff} = \bar{n} + \frac{1}{2} + |C_\text{eff}(\omega)|$.

Standard Quantum Limit

As seen in Equation (2.167) the added displacement noise spectral density $\bar{S}^{\text{add}}_{\hat{x}_\text{m},\hat{x}_\text{m}}$ is described by an interplay between imprecision $\bar{S}^{\theta=\frac{\pi}{2},\Delta=0}_{\text{imp}}(\omega)$ and quantum backaction

[68] Remark to the notation: $\bar{S}^{\text{add}}_{\hat{x}_\text{m},\hat{x}_\text{m}}(\omega) \overset{\text{def}}{=} \bar{S}^{(\theta,\Delta),\text{add}}_{\hat{x}_\text{m},\hat{x}_\text{m}}(\omega)\Big|_{\substack{\theta=\pi/2\\ \Delta=0}}$.

[69] For direct comparison of $|C_\text{eff}| = \frac{g^2\kappa}{4\gamma_\text{m}}\frac{1}{\frac{\kappa^2}{4}+\omega^2}$ given in Section 2.5.3:

$$|C_\text{eff}(\omega)| = \frac{G_\text{om}(\omega)}{4\gamma_\text{m}} \overset{\text{Eq.(2.160)}}{=} \frac{g^2\kappa}{4\gamma_\text{m}}\frac{1}{\frac{\kappa^2}{4}+\omega^2}.$$

noise $\bar{S}_{\mathrm{qba}}^{\Delta=0}(\omega)$

$$\bar{S}_{\hat{x}_\mathrm{m},\hat{x}_\mathrm{m}}^{\mathrm{add}}(\omega) = \bar{S}_{\mathrm{imp}}^{\theta=\frac{\pi}{2},\Delta=0}(\omega) + |\chi_\mathrm{m}(\omega)|^2 \bar{S}_{\mathrm{qba}}^{\Delta=0}(\omega) \tag{2.170a}$$

$$= \frac{1}{2G_\mathrm{om}(\omega)} + |\chi_\mathrm{m}(\omega)|^2 \frac{G_\mathrm{om}(\omega)}{2} \tag{2.170b}$$

$$= \frac{1}{2g^2\kappa|\chi_\mathrm{cav}^{\Delta=0}(\omega)|^2} + \frac{1}{2}|\chi_\mathrm{m}(\omega)|^2 g^2\kappa|\chi_\mathrm{cav}^{\Delta=0}(\omega)|^2 \tag{2.170c}$$

The spectral noise density $\bar{S}_{\hat{x}_\mathrm{m},\hat{x}_\mathrm{m}}^{\mathrm{add}}(\omega)$ and the resulting interplay of the noise contributions is depicted in Figure 2.14 for different coupling strength g. Together with Equation (2.170) and Figure 2.14, it is evident that for a weak coupling strength g or measurement strength $G_\mathrm{om}(\omega)$ imprecision noise dominates, whereas for strong coupling strengths g or measurement strength $G_\mathrm{om}(\omega)$ the backaction noise is the dominant noise source measured at the output.

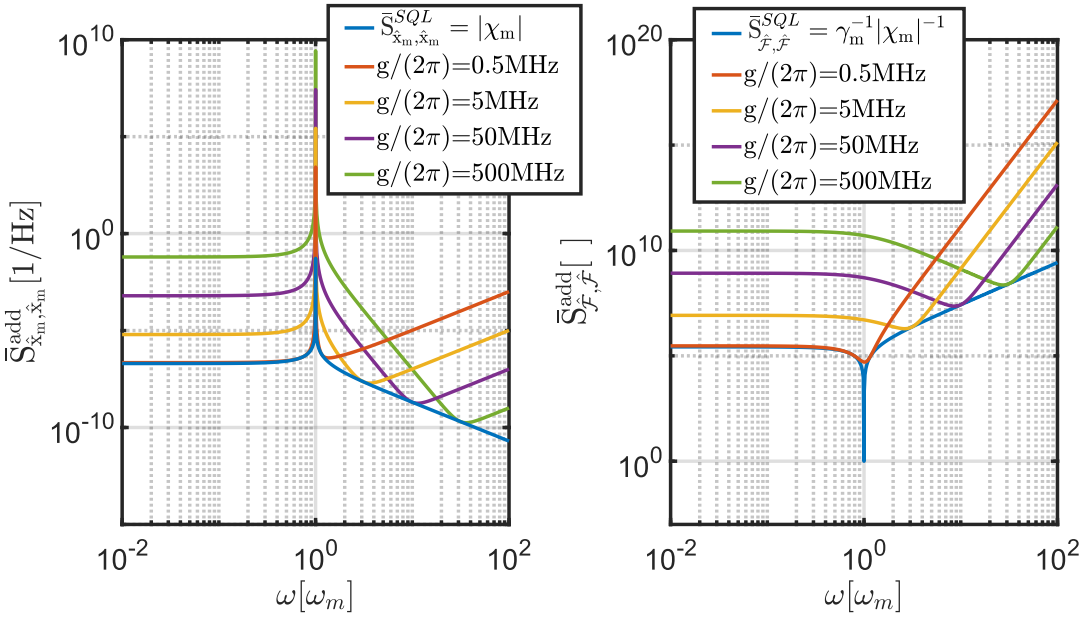

FIGURE 2.14: left: added displacement noise $\bar{S}_{\hat{x}_\mathrm{m},\hat{x}_\mathrm{m}}^{\mathrm{add}}(\omega)$ for different light-enhanced coupling strengths g together with the standard quantum limit $\bar{S}_{\hat{x}_\mathrm{m},\hat{x}_\mathrm{m}}^{\mathrm{SQL}}$
right: added force noise $\bar{S}_{\hat{\mathcal{F}},\hat{\mathcal{F}}}^{\mathrm{add}}(\omega)$ for different light-enhanced coupling strengths g together with the standard quantum limit $\bar{S}_{\hat{\mathcal{F}},\hat{\mathcal{F}}}^{\mathrm{SQL}}$ of force sensing.
Parameters for both graphs are: $\kappa/(2\pi) = 2\,\mathrm{MHz}$, $\Delta = 0\,\mathrm{Hz}$, $\omega_\mathrm{m}/(2\pi) = 800\,\mathrm{kHz}$ and $\gamma_\mathrm{m}/(2\pi) = 3\,\mathrm{Hz}$.

For a fixed coupling strength g and for frequencies below the mechanical resonance frequency ($\omega < \omega_\mathrm{m}$), quantum backaction noise[70] dominates because the susceptibility of χ_m of the mechanical oscillator to driving noise is constant for frequencies far below ω_m. For frequencies above the mechanical resonance $\omega > \omega_\mathrm{m}$ imprecision noise dominates because the susceptibility of the oscillator to the quantum radiation pressure noise decays with $1/(\omega^2)$. Near and at the mechanical resonance, the added displacement noise increases as the mechanical oscillator becomes more

[70] Quantum radiation pressure noise transfers momentum to the mechanical oscillator, which causes a displacement and by that quantum backaction noise onto the light field.

susceptible to amplitude fluctuations. The minimum added displacement sensitivity $\bar{S}^{\mathrm{add}}_{\hat{x}_\mathrm{m}\hat{x}_\mathrm{m}}(\omega)$ for a given coupling strength g is reached at a particular frequency at which the imprecision and backaction noise contributions are equal. Minimising $\bar{S}^{\mathrm{add}}_{\hat{x}_\mathrm{m}\hat{x}_\mathrm{m}}$ (Equation (2.170)) with respect to G_om by $G_\mathrm{om}(\omega) = |\chi_\mathrm{m}(\omega)|^{-1}$ leads to the displacement standard quantum limit

$$\bar{S}^{\mathrm{SQL}}_{\hat{x}_\mathrm{m},\hat{x}_\mathrm{m}}(\omega) = |\chi_\mathrm{m}(\omega)|. \tag{2.171}$$

The corresponding added force noise spectral density $\bar{S}^{\mathrm{add}}_{\hat{F},\hat{F}}(\omega)$ depicted on the right in Figure 2.14 is derived by multiplying the displacement noise spectral density $\bar{S}^{\mathrm{noise}}_{\hat{x}_\mathrm{m}\hat{x}_\mathrm{m}}$ (Equation (2.164)) with $\gamma_\mathrm{m}^{-1}|\chi_\mathrm{m}(\omega)|^{-2}$ as [71]

$$\bar{S}^{\mathrm{SQL}}_{\hat{F},\hat{F}}(\omega) = \gamma_\mathrm{m}^{-1}|\chi_\mathrm{m}(\omega)|^{-1}\,. \tag{2.172}$$

The force standard quantum limit $\bar{S}^{\mathrm{SQL}}_{\hat{F},\hat{F}}(\omega)$ in Figure 2.14 shows that the optomechanical system is most sensitive to weak signals at the mechanical resonance frequency ω_m. With this, the section devoted to deriving and explaining the displacement and force standard quantum limit is completed. The following two sections will focus on surpassing the standard quantum limit.

In the scheme presented in Section 2.5.8, the restriction of setting the quadrature angle $\theta = \frac{\pi}{2}$ is lifted, leading to a sub-SQL sensitivity within a certain frequency band.

The second approach, presented in this thesis (Section 2.6), explains the theory of a coherent quantum noise cancellation experiment which was first suggested by [TC10]. The concept of this approach is to cancel the quantum backaction noise $\bar{S}^{\Delta=0}_{\mathrm{qba}}(\omega)$ so that the imprecision noise $\bar{S}^{\theta=\frac{\pi}{2},\Delta=0}_{\mathrm{impr}}$ in Equation (2.170) can be made arbitrarily small, causing a broadband sub-SQL sensitivity.

[71] Relation $\bar{S}^{\mathrm{SQL}}_{\hat{F},\hat{F}}(\omega) = \frac{\bar{S}^{\mathrm{SQL}}_{\hat{x}_\mathrm{m},\hat{x}_\mathrm{m}}(\omega)}{\gamma_\mathrm{m}|\chi_\mathrm{m}(\omega)|^2}$ can be inferred from Equation (2.157).

2.5.8 Ponderomotive squeezing

In Section 2.5.7 a phase quadrature measurement ($\theta = \frac{\pi}{2}$) for a tuned cavity ($\Delta = 0$) and the resulting SQL was investigated. For the SQL the term $\bar{S}_{\text{corr}}^{\theta=\frac{\pi}{2},\Delta=0}(\omega)$ in Equation (2.143) vanishes. However, if one restricts the measurement not to be done at $\Delta = 0$ and $\theta = \frac{\pi}{2}$, the correlation term $\bar{S}_{\text{corr}}^{\theta,\Delta}(\omega)$ becomes non-zero. In this case, a squeezed output state defined by $\bar{S}^{\Delta=0,\text{noise}}_{\hat{\mathcal{X}}^{\theta,\text{out}}_{\text{om,L}},\hat{\mathcal{X}}^{\theta,\text{out}}_{\text{om,L}}}(\omega)$[72]$< \frac{1}{2}$ (see Section 2.2.3 and Figure 2.7b) could be measured. As the squeezed output state is generated by optomechanical interaction, it is named ponderomotive squeezing [BM15]. Due to the reduced optical noise properties of the output, sub-SQL sensitivity could be generated within a certain frequency band, as shown in the following. For simplicity, ponderomotive squeezing and its effect on displacement and force sensitivity will be explained for a setup with non-fixed quadrature (homodyne) angle $\theta \neq \frac{\pi}{2}$ and a fixed detuning of $\Delta = 0$. Assuming a lossless single-sided cavity ($\kappa_{\text{L}} = \kappa$) the optical output quadrature $\bar{S}^{\Delta=0}_{\hat{\mathcal{X}}^{\theta,\text{out}}_{\text{om,L}},\hat{\mathcal{X}}^{\theta,\text{out}}_{\text{om,L}}}(\omega)$ in Equation (2.143) is calculated as

$$\begin{aligned}
\bar{S}^{\Delta=0}_{\hat{\mathcal{X}}^{\theta,\text{out}}_{\text{om,L}},\hat{\mathcal{X}}^{\theta,\text{out}}_{\text{om,L}}}(\omega) &= \frac{1}{2} + f^{\theta,\Delta=0}_{\text{transfer}}(\omega) \times \{\bar{S}_{\hat{x}_{\text{m}},\hat{x}_{\text{m}}}\} + \bar{S}^{\theta,\Delta=0}_{\text{corr}}(\omega) \\
&= \frac{1}{2} + \underbrace{G_{\text{om}}(\omega)\sin(\theta)^2}_{f^{\theta,\Delta=0}_{\text{transfer}}(\omega)} \times \\
&\quad \Bigg\{ |\chi_{\text{m}}(\omega)|^2 \underbrace{\frac{G_{\text{om}}(\omega)}{2}}_{2\Gamma^{\Delta=0}_{\text{QBA}}} + |\chi_{\text{m}}(\omega)|^2 \underbrace{2\gamma_{\text{m}}\left(\bar{n}+\frac{1}{2}\right)}_{\bar{S}_{\hat{f}_{\text{th}},\hat{f}_{\text{th}}}} + \gamma_{\text{m}}|\chi_{\text{m}}(\omega)|^2 \bar{S}_{\hat{f}_{\text{sig}},\hat{f}_{\text{sig}}} \Bigg\} \\
&\quad \underbrace{-\frac{G_{\text{om}}(\omega)}{4}\left(\chi_{\text{m}}(\omega) + \chi^*_{\text{m}}(\omega)\right)\sin(2\theta)}_{\bar{S}^{\theta,\Delta=0}_{\text{corr}}(\omega)},
\end{aligned} \tag{2.173}$$

where the fourth line in Equation (2.173) is the correlation term $\bar{S}^{\theta,\Delta=0}_{\text{corr}}(\omega)$. Also, Equation (2.173) suggests that the optical noise spectral density $\bar{S}^{\Delta=0,\text{noise}}_{\hat{\mathcal{X}}^{\theta,\text{out}}_{\text{om,L}},\hat{\mathcal{X}}^{\theta,\text{out}}_{\text{om,L}}}(\omega)$[73]

$$\bar{S}^{\Delta=0,\text{noise}}_{\hat{\mathcal{X}}^{\theta,\text{out}}_{\text{om,L}},\hat{\mathcal{X}}^{\theta,\text{out}}_{\text{om,L}}}(\omega) = \frac{1}{2} + \underbrace{G_{\text{om}}(\omega)\sin(\theta)^2}_{f^{\theta,\Delta=0}_{\text{transfer}}(\omega)} \times \tag{2.174}$$

$$\Bigg\{ |\chi_{\text{m}}(\omega)|^2 \underbrace{\frac{G_{\text{om}}(\omega)}{2}}_{2\Gamma^{\Delta=0}_{\text{QBA}}} + \underbrace{|\chi_{\text{m}}(\omega)|^2 \overbrace{2\gamma_{\text{m}}\left(\bar{n}+\frac{1}{2}\right)}^{\bar{S}_{\hat{f}_{\text{th}},\hat{f}_{\text{th}}}}}_{\bar{S}^{\Delta=0}_{\text{intr}}(\omega)} \Bigg\} \tag{2.175}$$

$$\underbrace{-\frac{G_{\text{om}}(\omega)}{4}\left(\chi_{\text{m}}(\omega) + \chi^*_{\text{m}}(\omega)\right)\sin(2\theta)}_{\bar{S}^{\theta,\Delta=0}_{\text{corr}}(\omega)} \tag{2.176}$$

[72] $\bar{S}^{\Delta=0,\text{noise}}_{\hat{\mathcal{X}}^{\theta,\text{out}}_{\text{om,L}},\hat{\mathcal{X}}^{\theta,\text{out}}_{\text{om,L}}}(\omega)$ describes only noise and has thereby no signal information, hence $\bar{S}^{\Delta=0,\text{noise}}_{\hat{\mathcal{X}}^{\theta,\text{out}}_{\text{om,L}},\hat{\mathcal{X}}^{\theta,\text{out}}_{\text{om,L}}}(\omega) = \bar{S}^{\Delta=0}_{\hat{\mathcal{X}}^{\theta,\text{out}}_{\text{om,L}},\hat{\mathcal{X}}^{\theta,\text{out}}_{\text{om,L}}}(\omega) - \gamma_{\text{m}}|\chi_{\text{m}}(\omega)|^2 \bar{S}_{\hat{f}_{\text{sig}},\hat{f}_{\text{sig}}}\sin(\theta)^2$.

[73] See footnote 72.

describes a squeezed state $\left(\bar{S}^{\Delta=0,\text{noise}}_{\hat{X}^{\theta,\text{out}}_{\text{om,L}},\hat{X}^{\theta,\text{out}}_{\text{om,L}}}(\omega) < \frac{1}{2}\right)$, if

$$|\chi_\text{m}(\omega)|^2 \left(2\gamma_\text{m}\left(\bar{n}+\frac{1}{2}\right)+\frac{1}{2}G_\text{om}(\omega)\right)\sin^2(\theta) - \frac{1}{4}\left(\chi_\text{m}(\omega)+\chi^*_\text{m}(\omega)\right)\sin(2\theta) < 0\,. \tag{2.177}$$

This condition (Equation (2.177)) also entails that a quantum cooperativity of $C_\text{QBA} \geq 1$ (see Equation (2.168)) is necessary to obtain a squeezed output state, as otherwise thermal noise masks the squeezed output. Hence a measurement of ponderomotive squeezing indicates if the experiment is in a quantum backaction noise limited regime ($C_\text{QBA} \geq 1$) or not. Minimising the optical output noise spectrum $\bar{S}^{\Delta=0,\text{noise}}_{\hat{X}^{\theta,\text{out}}_{\text{om,L}},\hat{X}^{\theta,\text{out}}_{\text{om,L}}}(\omega)$ with respect to the quadrature angle θ results in a frequency dependent optimal angle

$$\theta^{\text{optical}}_{\text{opt}}(\omega) = \frac{1}{2}\arctan\left(\frac{2(\omega^2_\text{m}-\omega^2)}{G_\text{om}(\omega)+4\gamma_\text{m}(\bar{n}+\frac{1}{2})}\right)\,. \tag{2.178}$$

A plot of the optical output noise spectral density $\bar{S}^{\Delta=0,\text{noise}}_{\hat{X}^{\theta,\text{out}}_{\text{om,L}},\hat{X}^{\theta,\text{out}}_{\text{om,L}}}(\omega)$ for certain angles and for the optimal angle $\theta^{\text{optimal}}_{\text{opt}}(\omega)$ can be seen in Figure 2.15.

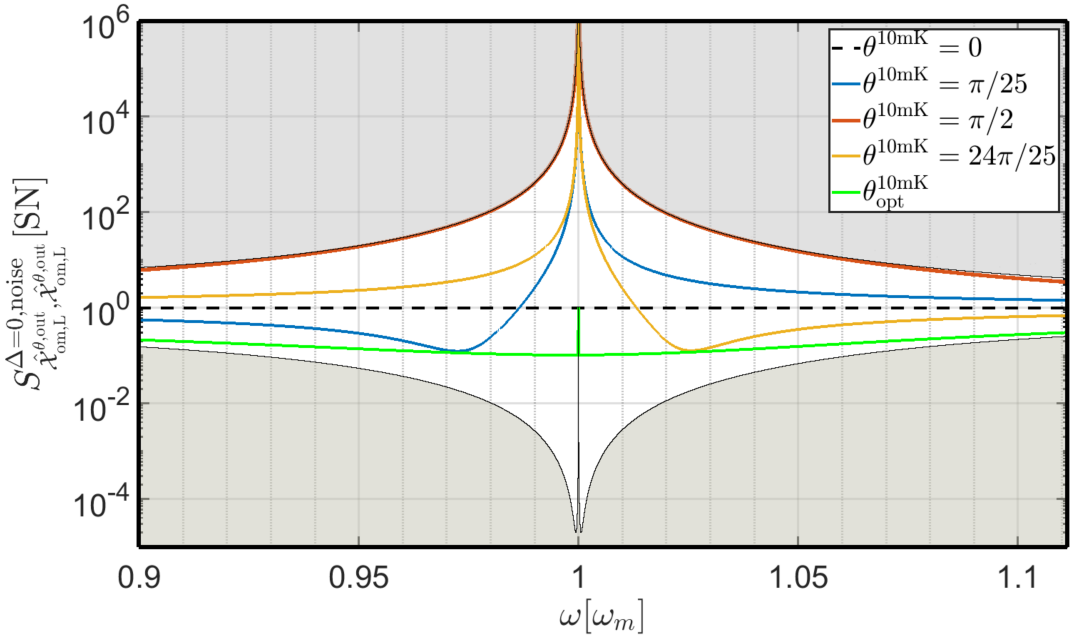

FIGURE 2.15: To shotnoise (SN) normalized optical output spectrum $\bar{S}^{\Delta=0,\text{noise}}_{\hat{X}^{\theta,\text{out}}_{\text{om,L}},\hat{X}^{\theta,\text{out}}_{\text{om,L}}}(\omega)$ for various quadrature angles θ at a temperature of $T = 10\,\text{mK}$. The shaded grey area represents the sensitivity bounds. The lower bound is given by the optimal angle $\theta^{\text{optimal}}_{\text{opt}}(\omega)$ at $T = 0\,\text{K}$ and the upper bound by $\theta = \pi/2$ at $T = 0\,\text{K}$ (Equation (2.178)). Other parameters are given by: $\kappa/(2\pi) = 2\,\text{MHz}$, $\omega_\text{m}/(2\pi) = 800\,\text{kHz}$, $\gamma_\text{m} = 3\,\text{Hz}$ and $g/(2\pi) = 500\,\text{kHz}$.

Figure 2.15 illustrates the optical output spectrum $\bar{S}^{\Delta=0,\text{noise}}_{\hat{X}^{\theta,\text{out}}_{\text{om,L}},\hat{X}^{\theta,\text{out}}_{\text{om,L}}}(\omega)$[74] for various

[74]Reminder: $\bar{S}^{\Delta}_{\hat{X}^{\theta,\text{out}}_{\text{om,L}},\hat{X}^{\theta,\text{out}}_{\text{om,L}}}(\omega)\Big|_{\substack{\theta=\pi/2\\ \Delta=0}} = \bar{S}_{\hat{Y}^{\text{out}}_{\text{om,L}},\hat{Y}^{\text{out}}_{\text{om,L}}}(\omega)$.

quadrature angles θ, normalized to shot noise [SN], considering a thermal bath temperature of $T = 10\,\mathrm{mK}$. The shaded grey area represents the sensitivity bounds for $T = 0\,\mathrm{K}$. The lower bound corresponds to the optimal squeezing angle $\theta_{\mathrm{opt}}^{\mathrm{optical}}(\omega)$ as defined in Equation (2.178),while the upper bound corresponds to the optical noise spectral density $\bar{S}^{\Delta=0,\mathrm{noise}}_{\hat{X}^{\theta,\mathrm{out}}_{\mathrm{om,L}},\hat{X}^{\theta,\mathrm{out}}_{\mathrm{om,L}}}(\omega)$ with $\theta = \theta_{\mathrm{opt}}^{\mathrm{optical}}(\omega) + \frac{\pi}{2}$. Notably, except for the mechanical resonance frequency $\omega = \omega_{\mathrm{m}}$, a squeezed output state ($\bar{S}^{\Delta=0,\mathrm{noise}}_{\hat{X}^{\theta,\mathrm{out}}_{\mathrm{om,L}},\hat{X}^{\theta,\mathrm{out}}_{\mathrm{om,L}}}(\omega) < SN$) can be measured at all frequencies by selecting the optimal frequency-dependent quadrature angle $\theta_{\mathrm{opt}}^{\mathrm{optical}}(\omega)$. Furthermore, Figure 2.15 demonstrates the dependence of squeezing performance on the temperature T. Consequently, by observing a ponderomotive squeezed output state, one can verify that the optomechanical system is limited by quantum backaction noise (Equation (2.177)).

The following will show how the squeezed optical output noise of the light improves the displacement and force detection with respect to the SQL. For this purpose, the added displacement noise spectral density $\bar{S}^{\theta,\mathrm{add}}_{\hat{x}_{\mathrm{m}},\hat{x}_{\mathrm{m}}}(\omega)$[75] is derived by using the same approach as in Section 2.5.7. Hence, $\bar{S}^{\theta,\mathrm{add}}_{\hat{x}_{\mathrm{m}},\hat{x}_{\mathrm{m}}}(\omega)$ contains only contributions that are not associated with intrinsic noise nor the signal and is deduced from Equation (2.176) as

$$\bar{S}^{\theta,\mathrm{add}}_{\hat{x}_{\mathrm{m}},\hat{x}_{\mathrm{m}}}(\omega) = \frac{\bar{S}^{\Delta=0,\mathrm{noise}}_{\hat{X}^{\theta,\mathrm{out}}_{\mathrm{om,L}},\hat{X}^{\theta,\mathrm{out}}_{\mathrm{om,L}}}(\omega)}{f^{\theta,\Delta=0}_{\mathrm{transfer}}} - \bar{S}^{\Delta=0}_{\mathrm{intr}}(\omega) \tag{2.179}$$

$$= \frac{1}{2G_{\mathrm{om}}\sin(\theta)^2} + |\chi_{\mathrm{m}}(\omega)|^2\frac{G_{\mathrm{om}}}{2} \tag{2.180}$$

$$- \frac{\chi_{\mathrm{m}}(\omega) + \chi^*_{\mathrm{m}}(\omega)}{2\tan(\theta)}. \tag{2.181}$$

Minimising the added displacement noise spectral density $\bar{S}^{\theta,\mathrm{add}}_{\hat{x}_{\mathrm{m}},\hat{x}_{\mathrm{m}}}(\omega)$ with respect to the homodyne angle θ gives the optimal homodyne angle $\theta_{\mathrm{opt}}^{\mathrm{disp}}(\omega)$ for displacement measurements,

$$\theta_{\mathrm{opt}}^{\mathrm{disp}}(\omega) = \arctan\left(\frac{2}{G_{\mathrm{om}}(\omega)\left(\chi_{\mathrm{m}}(\omega) + \chi^*_{\mathrm{m}}(\omega)\right)}\right). \tag{2.182}$$

The added displacement noise sensitivity $\bar{S}^{\theta,\mathrm{add}}_{\hat{x}_{\mathrm{m}},\hat{x}_{\mathrm{m}}}$ and added force noise sensitivity $\bar{S}^{\theta,\mathrm{add}}_{\hat{F},\hat{F}} = \gamma_{\mathrm{m}}^{-1}\chi_{\mathrm{m}}^{-1}\bar{S}^{\theta,\mathrm{add}}_{\hat{x}_{\mathrm{m}},\hat{x}_{\mathrm{m}}}$ is plotted for different quadrature angles and the optimal angle $\theta_{\mathrm{opt}}^{\mathrm{disp}}$ in Figure 2.16. Also depicted in this figure are the noise ellipses of the optical output state in the phase-space representation, which will be investigated more thoroughly in Figure 2.17.

[75] Remark to the notation: $\bar{S}^{\theta,\mathrm{add}}_{\hat{x}_{\mathrm{m}},\hat{x}_{\mathrm{m}}}(\omega) = \bar{S}^{(\theta,\Delta),\mathrm{add}}_{\hat{x}_{\mathrm{m}},\hat{x}_{\mathrm{m}}}(\omega)\Big|_{\Delta=0}$.

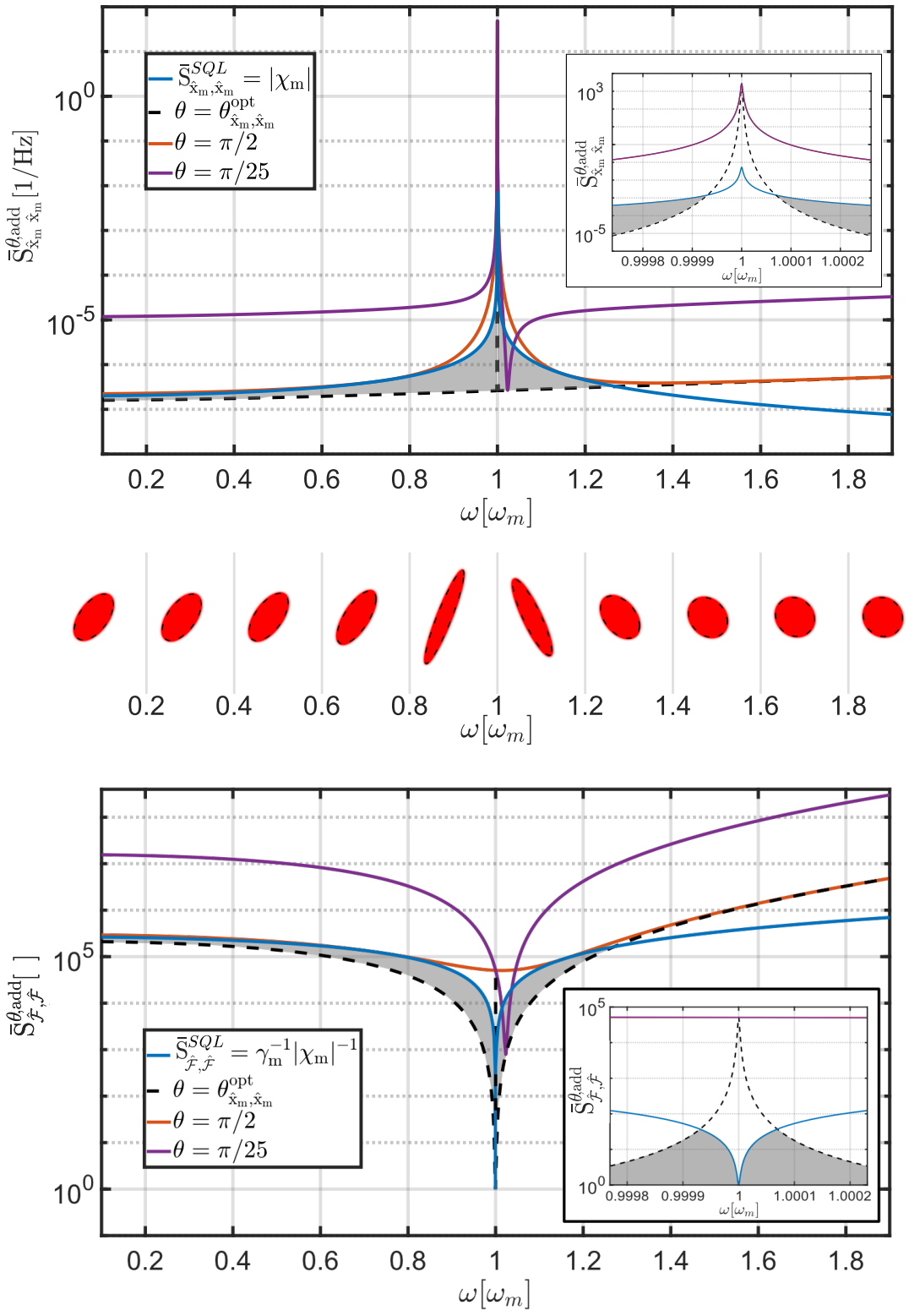

FIGURE 2.16: **Upper panel**: Displacement spectral density $\bar{S}^{\theta,\text{add}}_{\hat{x}_m,\hat{x}_m}$ for different quadrature angles θ. Black dashed line is $\bar{S}^{\theta,\text{add}}_{\hat{x}_m,\hat{x}_m}$ for the optimal homodyne angle $\theta^{\text{opt}}_{\text{disp}}$ (Equation (2.182)). Grey area indicates improvement with respect to the SQL sensitivity $\bar{S}^{\text{SQL}}_{\hat{x}_m,\hat{x}_m}$.
Middle panel: Noise ellipses in the phase-space representation, detailed description in figure of the optical output state in phase space representation [Ste19], detailed description in Figure 2.17.
Lower panel: Force spectral density $\bar{S}^{\theta,\text{add}}_{\hat{F},\hat{F}}$ for different quadrature angles θ. Black dashed line is $\bar{S}^{\theta,\text{add}}_{\hat{F},\hat{F}}$ for the optimal homodyne angle $\theta^{\text{opt}}_{\text{disp}}$ (Equation (2.182)). Gray area indicates improvement with respect to the SQL sensitivity $\bar{S}^{\text{SQL}}_{\hat{F},\hat{F}}$.
Used parameters are given by: $\kappa/(2\pi) = 2\,\text{MHz}$, $\omega_m/(2\pi) = 800\,\text{kHz}$, $\gamma_m = 3\,\text{Hz}$ and $g/(2\pi) = 500\,\text{kHz}$

Basically, the lower and upper panels in Figure 2.16 show that the corresponding displacement and force SQL is surpassed in a small frequency band due to ponderomotive squeezing. A more intuitive explanation of the sensitivity improvement due to ponderomotive squeezing will be given, based on one noise ellipse depicted in the middle panel of Figure 2.16, in the following Figure 2.17.

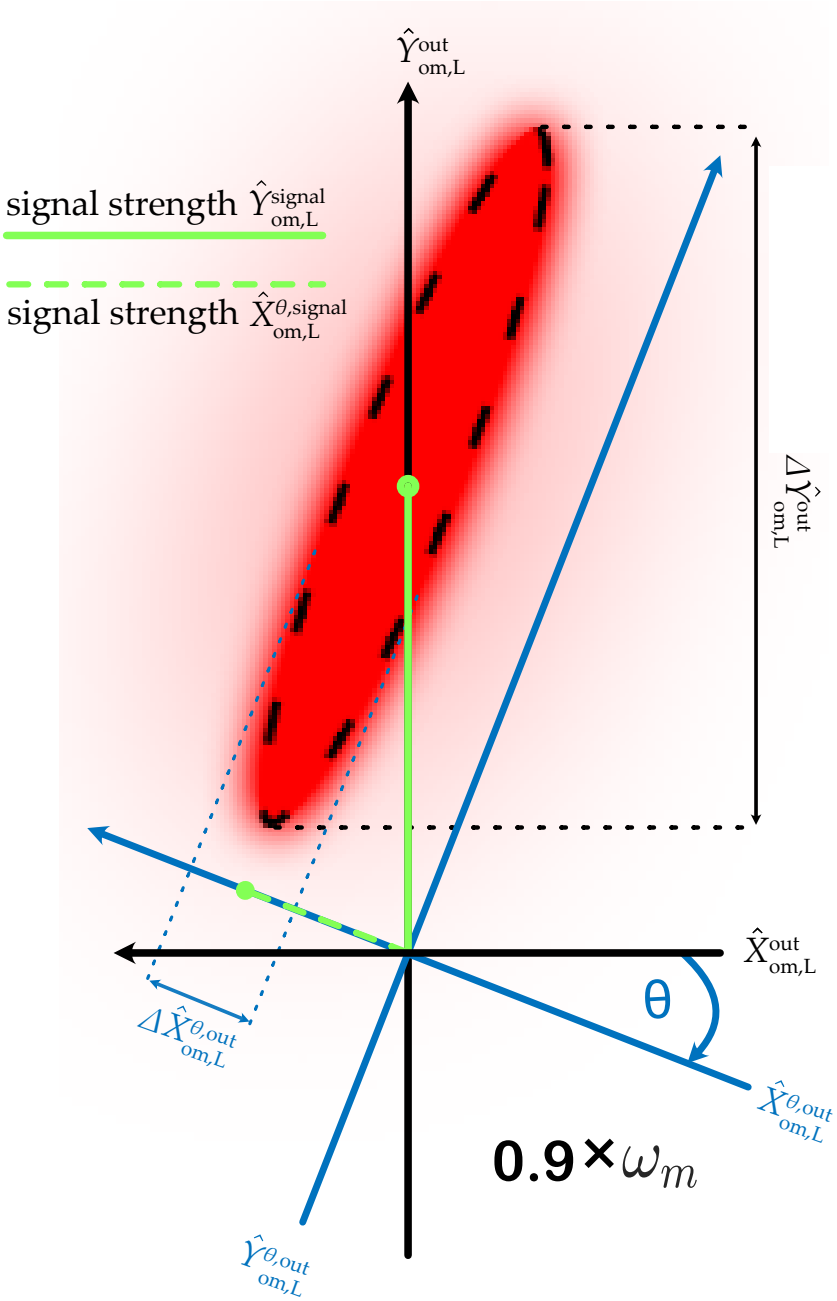

FIGURE 2.17: Noise ellipse of ponderomotive squeezing at $\omega = 0.9\omega_m$ taken from Figure 2.16. The projection of the corresponding quadrature axis represents the measurement of noise and signal in that (arbitrary) quadrature. The black coordinate system represents the amplitude and phase quadrature $\hat{Y}^{\theta,\text{out}}_{\text{om,i}}$ and $\hat{X}^{\theta,\text{out}}_{\text{om,i}}$, whereas the blue coordinate system represents the arbitrary amplitude and phase quadrature $\hat{Y}^{\theta,\text{out}}_{\text{om,L}}$ and $\hat{X}^{\theta,\text{out}}_{\text{om,L}}$ of the by θ rotated coordinated system (See Equation (2.133)). The blue axes are rotated by θ such that the smallest fluctuations of the squeezed state $\Delta\hat{Y}^{\theta,\text{out}}_{\text{om,L}}$ is measured on the rotated amplitude quadrature axis $\hat{X}^{\theta,\text{out}}_{\text{om,L}}$. More information is in the text.

Figure 2.17 shows the signal $\hat{Y}^{\text{signal}}_{\text{om,L}}$ in the phase quadrature $\hat{Y}^{\text{out}}_{\text{om,L}}$ (solid green

line)[76] and the noise ellipse due to ponderomotive squeezing for the particular measurement frequency $\omega = 0.9\omega_m$. Also shown is the rotated[77] coordinate system (blue) of the arbitrary quadrature, which axes are defined as $\hat{X}^{\theta,\text{out}}_{\text{om,L}} = \hat{X}^{\text{out}}_{\text{om,i}} \cos(\theta) + \hat{Y}^{\text{out}}_{\text{om,i}} \sin(\theta)$ and $\hat{Y}^{\theta,\text{out}}_{\text{om,L}} = \hat{X}^{\text{out}}_{\text{om,i}} \cos(\theta + \frac{\pi}{2}) + \hat{Y}^{\text{out}}_{\text{om,i}} \sin(\theta + \frac{\pi}{2})$ (see Equation (2.133)). The projection of the displaced squeezed state onto the amplitude quadrature axis $\hat{X}^{\theta,\text{out}}_{\text{om,L}}$ represents a measurement of the signal $\hat{X}^{\theta,\text{signal}}_{\text{om,L}}$ (dashed green line) and noise $\Delta\hat{X}^{\theta,\text{out}}_{\text{om,L}}$ at an arbitrary quadrature angle θ. Hence, Figure 2.17 reveals that measuring the signal $\hat{Y}^{\text{signal}}_{\text{om,L}}$ under a quadrature angle different from $\theta = \frac{\pi}{2}$ leads to a measurement of smaller signal strength $\hat{X}^{\theta,\text{signal}}_{\text{om,L}}$ (dashed green line) and a smaller noise contribution $\Delta\hat{X}^{\theta,\text{signal}}_{\text{om,L}}$ (compared to the SQL with $\hat{Y}^{\text{signal}}_{\text{om,L}}$ and $\Delta\hat{Y}^{\text{out}}_{\text{om,L}}$ where $\theta = \pi/2$ and $\Delta = 0$ (black coordinate system)). Fortunately, due to ponderomotive squeezing, for some quadrature angles θ, the measured reduced noise outweighs the signal loss and increases the signal-to-noise ratio at this particular quadrature angle. Therefore, as shown in Figure 2.16, the displacement and force SQL can be surpassed in a small frequency band by utilising the effect of ponderomotive squeezing.

As the SQL is only surpassed in a small frequency band by ponderomotive squeezing, an experiment in which the SQL is surpassed in a broad frequency range, namely the coherent quantum noise cancellation experiment (CQNC), will be introduced in the next section. This CQNC experiment is the main motivation for the experimental work done within the scope of this thesis. However, in this thesis, CQNC will only be briefly introduced, as in [Sch+22; Sch23] a detailed theoretical description, also with respect to losses, can be found.

2.6 Coherent quantum noise cancellation

In Section 2.5.8, the presence of frequency-dependent ponderomotive squeezing induced by optomechanical coupling was discussed. As an consequence of ponderomotive squeezing, the measured noise in the phase quadrature changes across different frequencies. It was noted that the quantum backaction noise observed in phase quadrature measurements can be understood as a consequence of ponderomotive squeezing. Consequently, a backaction-free measurement can be described by back-squeezing and -rotating the quadrature uncertainties, as mentioned in [Ste19].

Another concept for comprehending backaction cancellation is the introduction of an "effective" negative mass oscillator [PH15], which is solely susceptible to the quantum radiation pressure noise and not to the signal force measured by the mechanical oscillator. In this scenario, the *effective* negative mass (where the acceleration $\ddot{x}_m$ of a negative mass is opposite to its force $F = (-m)\ddot{x}_m$) moves in the opposite direction to the mechanical oscillator due to quantum radiation pressure. When the quantum back-action noise interacts with the positive and "effective" negative mass oscillator, the net displacement excited by quantum radiation pressure noise becomes zero and, therefore, is cancelled.

The following discussion outlines the approach followed by our group to achieve backaction cancellation (undoing ponderomotive squeezing) by the realisation of an "effective" negative mass oscillator, based on the idea proposed by Tsang and Caves [TC10]. As the *effective* negative mass, an ancilla cavity, containing a beamsplitter and

[76] Because $\Delta = 0$ the signal is solely in the phase quadrature $\hat{Y}^{\text{out}}_{\text{om,L}}$.

[77] Rotated by θ with respect to coordinate system of the arbitrary phase and amplitude quadrature $\hat{Y}^{\text{out}}_{\text{om,L}}$ and $\hat{X}^{\text{out}}_{\text{om,L}}$

a non-linear crystal, is suggested and depicted in Figure 2.18. The rationale behind selecting the ancilla cavity lies in the optomechanical interaction Hamiltonian $\hat{H}_{\mathrm{int}}$ (Equation (2.98)), which can be expressed by utilising $\hat{a} \to \alpha + \delta\hat{a}$ and $\hat{x}_{\mathrm{m}} \to \hat{b} + \hat{b}^\dagger$, as

$$H_{\mathrm{int}} \approx \alpha g_0 (\hat{a} + \hat{a}^\dagger)(\hat{b} + \hat{b}^\dagger) \tag{2.183}$$

$$\propto \underbrace{\hat{b}\hat{a} + \hat{b}^\dagger\hat{a}^\dagger}_{\mathrm{TMS}} + \underbrace{\hat{b}\hat{a}^\dagger + \hat{b}^\dagger\hat{a}}_{\mathrm{BS}}. \tag{2.184}$$

Writing the interaction Hamiltonian in this fashion reveals that the optomechanical interaction is described as a combination of a two-mode squeezing process (TMS) and a beamsplitter process (BS), where particles are created or annihilated in each mode, and two quanta are exchanged, respectively. Since the realisation of the *effective* negative mass relies on optical components, this scheme is referred to as a all-optical coherent quantum noise cancellation (CQNC) experiment. It is worth noting that alternative non-all-optical schemes have also been implemented, such as using an atomic spin oscillator as the effective negative mass oscillator [Moe+17].

The primary focus of this thesis is to investigate the optomechanical interaction within the context of the CQNC experiment. Therefore, only a brief overview of the CQNC theory will be provided to examine the necessary parameters. More comprehensive information on the negative mass oscillator, its realization, and investigation can be found in the work [Ste19]. Additionally, further details about the CQNC scheme, particularly how losses and imperfections degrade sensitivity, can be found in the papers and theses by my former colleagues [Wim+14; Ste19; Sch+22; Sch23]. It should be noted that, unlike in these works, this thesis considers the inclusion of thermal noise, which imposes stricter requirements on CQNC. Consequently, Section 2.6.4 will investigate a scheme utilising an additional beam to induce sideband cooling of the mechanical oscillator.

Figure 2.18 illustrates the proposed CQNC scheme schematically, as presented in [Ste19; Sch+22; Sch23].

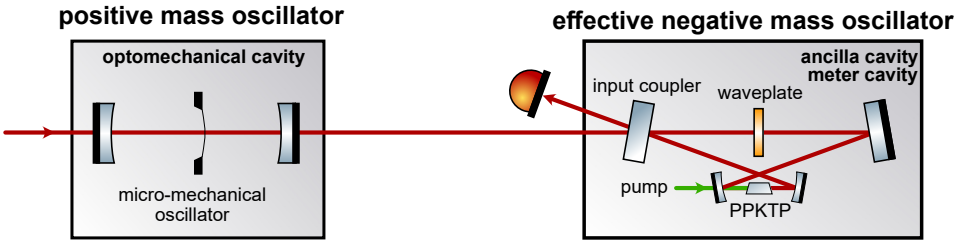

FIGURE 2.18: The cascaded scheme for an all optical CQNC experiment proposed by our group. The left cavity is essentially a cavity with an optomechanical device in it (further investigated in 4.2.3) whereas the ancilla cavity contains a wave-plate coupling two optical modes of orthogonal polarisations (beamsplitter process) and a non-linear (PPKTP)-crystal) exemplifying the two mode process.

Figure 2.18 illustrates the configuration where the output light from the optomechanical system, which is sensitive to quantum radiation pressure noise, is directed into the ancilla cavity. As mentioned, this cavity is designed to counteract the back-action effects by undoing the ponderomotive squeezing. System matrices based on the equations of motion are used to accurately determine the output phase quadratures and their spectral densities for the cascaded system. The calculation method for obtaining the output quadratures and their spectral densities in linear quantum

systems, as described in [Sch+22] will be briefly introduced in the following section. This calculation approach will be applied in Section 2.6.2 to analyse the CQNC system depicted in Figure 2.18.

2.6.1 Calculation of noise spectral densities using a matrix formalism

The following description is based on [Ste19; Sch+22]. The input-output relation of a linear quantum system with n system variables and k input and outputs can be written as [78]

$$x_{\mathrm{sys}}^{\mathrm{out}} = \left(K_{\mathrm{sys}}^{\mathrm{in}}\right)^{T} x_{\mathrm{sys}} - x_{\mathrm{sys}}^{\mathrm{in}} \tag{2.185}$$

with x_{sys} containing n system variables and $x_{\mathrm{sys}}^{\mathrm{in}}$ and $x_{\mathrm{sys}}^{\mathrm{out}}$ each containing k system input and output variables. Consequently, the driving matrix $K_{\mathrm{sys}}^{\mathrm{in}}$ is an $n \times k$-dimensional matrix.
The system parameters x_{sys} are described by their equations of motion

$$\dot{x}_{\mathrm{sys}}(t) = M_{\mathrm{sys}} x_{\mathrm{sys}}(t) + K_{\mathrm{sys}}^{\mathrm{in}} x_{\mathrm{sys}}^{\mathrm{in}}(t) + K_{\mathrm{sys}}^{\mathrm{bath}} x_{\mathrm{sys}}^{\mathrm{bath}}(t) \tag{2.186}$$

where M_{sys} describes the system matrix defined by the equations of motion of the system variables and $K_{\mathrm{sys}}^{\mathrm{bath}} x_{\mathrm{sys}}^{\mathrm{bath}}$ describes the noise of an external bath coupled into the system. The set of equations of motion can be solved in the Fourier domain and the solution reads

$$x_{\mathrm{sys}} = (i\omega - M_{\mathrm{sys}})^{-1} (K_{\mathrm{sys}}^{\mathrm{in}} x_{\mathrm{sys}}^{\mathrm{in}} + K_{\mathrm{sys}}^{\mathrm{bath}} x_{\mathrm{sys}}^{\mathrm{bath}}) \tag{2.187}$$

Plugging in Equation (2.185), the output can be written as

$$\begin{aligned} x_{\mathrm{sys}}^{\mathrm{out}} &= \left(K_{\mathrm{sys}}^{\mathrm{in}}\right)^{T} x_{\mathrm{sys}} - x_{\mathrm{sys}}^{\mathrm{in}} \\ &= \left(\left(K_{\mathrm{sys}}^{\mathrm{in}}\right)^{T} (i\omega - M_{\mathrm{sys}})^{-1} K_{\mathrm{sys}}^{\mathrm{in}} - 1 \right) x_{\mathrm{sys}}^{\mathrm{in}} \\ &\quad + \left(K_{\mathrm{sys}}^{\mathrm{in}}\right)^{T} (i\omega - M_{\mathrm{sys}})^{-1} K_{\mathrm{sys}}^{\mathrm{bath}} x_{\mathrm{sys}}^{\mathrm{bath}} \\ &= T_{\mathrm{sys}}^{\mathrm{in}} x_{\mathrm{sys}}^{\mathrm{in}} + T_{\mathrm{sys}}^{\mathrm{bath}} x_{\mathrm{sys}}^{\mathrm{bath}} \\ &= \mathcal{T} \tilde{x}_{\mathrm{sys}}^{\mathrm{in}} \end{aligned} \tag{2.188}$$

with

$$\tilde{x}_{\mathrm{sys}}^{\mathrm{in}} = \begin{pmatrix} x_{\mathrm{sys}}^{\mathrm{in}} \\ x_{\mathrm{sys}}^{\mathrm{bath}} \end{pmatrix} \tag{2.189}$$

$$\mathcal{T} = (T_{\mathrm{sys}}^{\mathrm{in}}, T_{\mathrm{sys}}^{\mathrm{bath}}) \tag{2.190}$$

[78] For clarity: Subscripts denote the system (optomechanical system, ancilla cavity or meter cavity), whereas superscripts denote the output (out), the input drive (in) or the external bath/noise (bath) of the system.

The (symmetrised[79]) spectral density $\bar{S}^{\text{out}}_{\text{sys}}(\omega)$ of the system output $(\boldsymbol{x}^{\text{out}}_{\text{sys}})$ is derived by

$$\begin{aligned}\delta(\omega-\omega')\bar{S}^{\text{out}}_{\text{sys}}(\omega) &= \frac{1}{2}\langle \boldsymbol{x}^{\text{out}}_{\text{sys}}(\omega)\boldsymbol{x}^{\text{out}^\dagger}_{\text{sys}}(\omega')\rangle + c.c \\ &= \frac{1}{2}\langle \boldsymbol{\mathcal{T}}(\omega)\tilde{\boldsymbol{x}}^{\text{in}}_{\text{sys}}\tilde{\boldsymbol{x}}^{\text{in}\ \dagger}_{\text{sys}}\boldsymbol{\mathcal{T}}(-\omega')\rangle + c.c \\ &= \frac{1}{2}\langle \boldsymbol{\mathcal{T}}(\omega)S^{\text{in}}_{\text{sys}}\boldsymbol{\mathcal{T}}(-\omega')\rangle + c.c\end{aligned} \tag{2.191}$$

with $S^{\text{in}}_{\text{sys}}$ being the input spectral density matrix of the system input. Using the matrix formalism, the spectral density of the in Figure 2.18 depicted cascaded CQNC scheme will be calculated in the following.

2.6.2 Ideal CQNC

As by the CQNC scheme shown in Figure 2.18, the output of one system is fed into the other. Hence, one describes one system output and uses it as the input for the other system. The equations of motion and its solution for the optomechanical system will first be derived with the matrix formalism to see the correspondences between the matrix formalism and the derivations given in Section 2.5.7. Revisiting the equations of motion for a cavity tuned on resonance $\Delta = 0$ (see Equation (2.111)) for the optomechanical system[80,81],

$$\begin{aligned}\dot{\hat{X}}_{\text{om}} &= -\frac{\kappa}{2}\hat{X}_{\text{om}} + \Delta\hat{Y} + \sqrt{\kappa^{\text{in}}_{\text{om}}}\hat{X}^{\text{in}}_{\text{om}} + \sqrt{\kappa^{\text{bath}}_{\text{om}}}\hat{X}^{\text{bath}}_{\text{om}} \\ \dot{\hat{Y}}_{\text{om}} &= -\frac{\kappa}{2}\hat{Y}_{\text{om}} - \Delta\hat{X} - g_{\text{om}}\hat{x}_{\text{m}} + \sqrt{\kappa^{\text{in}}_{\text{om}}}\hat{X}^{\text{in}}_{\text{om}} + \sqrt{\kappa^{\text{bath}}_{\text{om}}}\hat{Y}^{\text{bath}}_{\text{om}} \\ \dot{\hat{x}}_{\text{m}} &= \omega_{\text{m}}\hat{p}_{\text{m}} \\ \dot{\hat{p}}_{\text{m}} &= -\omega_{\text{m}}\hat{x}_{\text{m}} - \gamma_{\text{m}}\hat{p}_{\text{m}} + \sqrt{\gamma_{\text{m}}}\hat{\mathcal{F}}_{\text{ext}} - g_{\text{om}}\hat{X}_{\text{om}}\end{aligned}$$

shows that they can be cast in matrix form with $\Delta = 0$ as

[79] Definition of spectra given in Appendix B.

[80] The subscript $_{\text{om}}$ at variables and $_{\text{OMS}}$ at matrices is used to clarify that these parameters belong to the optomechanical system (OMS) as later corresponding parameters for the eNMO will be introduced.

[81] Remark: Instead of the subscripts $_{\text{L}}$ and $_{\text{R}}$ (used in Equation (2.111)) the superscripts $^{\text{in}}$ and $^{\text{bath}}$ are used to denote the input port of the drive and the input port of the external bath (noise) respectively.

$$\underbrace{\begin{pmatrix} \dot{\hat{X}}_{\mathrm{om}} \\ \dot{\hat{Y}}_{\mathrm{om}} \\ \dot{\hat{x}}_{\mathrm{m}} \\ \dot{\hat{p}}_{\mathrm{m}} \end{pmatrix}}_{\dot{\boldsymbol{x}}_{\mathrm{OMS}}(t)} = \underbrace{\begin{pmatrix} -\frac{\kappa_{\mathrm{om}}}{2} & 0 & 0 & 0 \\ 0 & -\frac{\kappa_{\mathrm{om}}}{2} & 0 & -g_{\mathrm{om}} \\ 0 & 0 & 0 & \omega_{\mathrm{m}} \\ -g & 0 & -\omega_{\mathrm{m}} & -\gamma_{\mathrm{m}} \end{pmatrix}}_{\boldsymbol{M}_{\mathrm{OMS}}} \underbrace{\begin{pmatrix} \hat{X}_{\mathrm{om}} \\ \hat{Y}_{\mathrm{om}} \\ \hat{x}_{\mathrm{m}} \\ \hat{p}_{\mathrm{m}} \end{pmatrix}}_{\boldsymbol{x}_{\mathrm{OMS}}(t)} \tag{2.192a}$$

$$+ \underbrace{\begin{pmatrix} \sqrt{\kappa_{\mathrm{om}}^{\mathrm{in}}} & 0 \\ 0 & \sqrt{\kappa_{\mathrm{om}}^{\mathrm{in}}} \\ 0 & 0 \\ 0 & 0 \end{pmatrix}}_{\boldsymbol{K}_{\mathrm{OMS}}^{\mathrm{in}}} \underbrace{\begin{pmatrix} \hat{X}_{\mathrm{om}}^{\mathrm{in}} \\ \hat{Y}_{\mathrm{om}}^{\mathrm{in}} \end{pmatrix}}_{\boldsymbol{x}_{\mathrm{OMS}}^{\mathrm{in}}(t)} \tag{2.192b}$$

$$+ \underbrace{\begin{pmatrix} \sqrt{\kappa_{\mathrm{om}}^{\mathrm{bath}}} & 0 & 0 & 0 \\ 0 & \sqrt{\kappa_{\mathrm{om}}^{\mathrm{bath}}} & 0 & 0 \\ 0 & 0 & 0 & 0 \\ 0 & 0 & 0 & \sqrt{\gamma_{\mathrm{m}}} \end{pmatrix}}_{\boldsymbol{K}_{\mathrm{OMS}}^{\mathrm{bath}}} \underbrace{\begin{pmatrix} \hat{X}_{\mathrm{om}}^{\mathrm{bath}} \\ \hat{Y}_{\mathrm{om}}^{\mathrm{bath}} \\ 0 \\ \hat{\mathcal{F}}_{\mathrm{ext}} \end{pmatrix}}_{\boldsymbol{x}_{\mathrm{OMS}}^{\mathrm{bath}}(t)} . \tag{2.192c}$$

In the above equation and in the following, a single-sided cavity with no additional losses $\kappa_{\mathrm{om}}^{\mathrm{bath}} = 0$[82] is assumed for simplicity[83]. So, the phase and amplitude quadrature output of the optomechanical system $\hat{Y}_{\mathrm{om}}^{\mathrm{out}}(\omega)$ and $\hat{X}_{\mathrm{om}}^{\mathrm{out}}(\omega)$ are calculated by using the procedure described in Section 2.6.1 as[84]

$$\hat{X}_{\mathrm{om}}^{\mathrm{out}}(\omega) = e^{i\phi_{\mathrm{om}}} \hat{X}_{\mathrm{om}}^{\mathrm{in}} \tag{2.193a}$$

$$\begin{aligned} \hat{Y}_{\mathrm{om}}^{\mathrm{out}}(\omega) =& e^{i\phi_{\mathrm{om}}} \hat{Y}_{\mathrm{om}}^{\mathrm{in}} + \kappa_{\mathrm{om}} \chi_{\mathrm{m}} g_{\mathrm{om}}^2 \chi_{\mathrm{c}}^2 \hat{X}_{\mathrm{om}}^{\mathrm{in}} \\ & - \chi_{\mathrm{m}} \sqrt{\kappa_{\mathrm{om}}} g_{\mathrm{om}} \chi_{\mathrm{om}} \sqrt{\gamma_{\mathrm{m}}} \hat{\mathcal{F}}_{\mathrm{ext}} , \end{aligned} \tag{2.193b}$$

with $e^{i\phi_{\mathrm{om}}} = \frac{\kappa_{\mathrm{om}}/2 - i\omega}{\kappa_{\mathrm{om}}/2 + i\omega}$, $\chi_{\mathrm{om}} = \frac{1}{\kappa_{\mathrm{om}}/2 + i\omega}$[85] and the mechanical susceptibility χ_{m}

$$\chi_{\mathrm{m}} = \frac{\omega_{\mathrm{m}}}{\omega_{\mathrm{m}}^2 - \omega^2 + i\gamma_{\mathrm{m}}\omega} . \tag{2.194}$$

Following Section 2.6.1 together with $\bar{S}^{\mathrm{in}} = \frac{1}{2}\mathrm{diag}(1, 1, 0, 2\bar{S}_{\hat{\mathcal{F}}_{\mathrm{ext}}, \hat{\mathcal{F}}_{\mathrm{ext}}})$ the output noise spectral density matrix reads[86]

$$\bar{S}_{\mathrm{OMS}}^{\mathrm{out}} = \frac{1}{2} \begin{pmatrix} 1 & -2G_{\mathrm{om}} \Re(\chi_{\mathrm{m}}) \\ -2G_{\mathrm{om}} \Re(\chi_{\mathrm{m}}) & 1 + G_{\mathrm{om}}^2 |\chi_{\mathrm{m}}|^2 + 2G_{\mathrm{om}} \gamma_{\mathrm{m}} |\chi_{\mathrm{m}}|^2 (\bar{S}_{\hat{\mathcal{F}}_{\mathrm{th}}, \hat{\mathcal{F}}_{\mathrm{th}}} + \bar{S}_{\hat{\mathcal{F}}_{\mathrm{sig}}, \hat{\mathcal{F}}_{\mathrm{sig}}}) \end{pmatrix} . \tag{2.195}$$

The general quadrature output spectrum $\bar{S}^{\Delta=0}_{\hat{X}_{\mathrm{om,L}}^{\theta,\mathrm{out}}, \hat{X}_{\mathrm{om,L}}^{\theta,\mathrm{out}}}$ (for the tuned case) from the matrix spectral density $\bar{S}_{\mathrm{OMS}}^{\mathrm{out}}$ can be obtained by using the rotation matrix

[82] Because of no additional losses $\kappa_{\mathrm{om}}^{\mathrm{in}} \to \kappa_{\mathrm{om}}$.

[83] A detailed analysis, including losses can be found in [Sch+22].

[84] As in Section 2.5.7 the output is taken at the input port of the drive, but is not indicated here by the subscript $_{\mathrm{L}}$ (in Section 2.5.7 the drive input is left ($_{\mathrm{L}}$)), e.g $\hat{Y}_{\mathrm{om,L}}^{\mathrm{out}} \to \hat{Y}_{\mathrm{om}}^{\mathrm{out}}(\omega)$.

[85] χ_{om} is the cavity susceptibility for $\Delta = 0$ of the optomechanical system (om) (see Equation (2.153)).

[86] $\bar{S}_{\hat{\mathcal{F}}_{\mathrm{ext}}, \hat{\mathcal{F}}_{\mathrm{ext}}} = \bar{S}_{\hat{\mathcal{F}}_{\mathrm{sig}}, \hat{\mathcal{F}}_{\mathrm{sig}}} + \bar{S}_{\hat{\mathcal{F}}_{\mathrm{th}}, \hat{\mathcal{F}}_{\mathrm{th}}}$.

$$R(\theta) \;=\; (\cos\theta, \sin\theta)^\top$$

$$\bar{S}^{\Delta=0}_{\hat{X}^{\theta,\mathrm{out}}_{\mathrm{om}},\hat{X}^{\theta,\mathrm{out}}_{\mathrm{om}}} = R(\theta)^\top \bar{S}^{\mathrm{out}}_{\mathrm{OMS}} R(\theta). \tag{2.196}$$

As CQNC should surpass the SQL without using ponderomotive squeezing, it follows that the phase quadrature output spectrum ($\theta = \pi/2$) $\bar{S}_{\hat{Y}^{\mathrm{out}}_{\mathrm{om}},\hat{Y}^{\mathrm{out}}_{\mathrm{om}}}(\omega)$ is given by

$$\begin{aligned}\bar{S}_{\hat{Y}^{\mathrm{out}}_{\mathrm{om}},\hat{Y}^{\mathrm{out}}_{\mathrm{om}}}(\omega) \;&=\; \bar{S}^{\Delta}_{\hat{X}^{\theta,\mathrm{out}}_{\mathrm{om}},\hat{X}^{\theta,\mathrm{out}}_{\mathrm{om}}}(\omega)\Big|_{\substack{\theta=\pi/2\\ \Delta=0}} = R\left(\pi/2\right)^\top \bar{S}^{\mathrm{out}}_{\mathrm{OMS}} R\left(\pi/2\right) \\ &= \frac{1}{2} + G_{\mathrm{om}}(\omega)|\chi_{\mathrm{m}}(\omega)|^2 \left(\frac{G_{\mathrm{om}}(\omega)}{2} + \gamma_{\mathrm{m}}(\bar{S}_{\hat{\mathcal{F}}_{\mathrm{th}},\hat{\mathcal{F}}_{\mathrm{th}}} + \bar{S}_{\hat{\mathcal{F}}_{\mathrm{sig}},\hat{\mathcal{F}}_{\mathrm{sig}}})\right) .\end{aligned} \tag{2.197}$$

So far, only the equation of the phase quadrature readout of the tuned cavity from Equation (2.159) has been recapitulated. Before feeding the output of the optomechanical system (OMS) into the *effective* negative mass oscillator (eNMO), the output phase quadrature and the spectral density matrix of the latter will be derived in the following. Based on the interaction Hamiltonian $\hat{H}_{\mathrm{anc}}$ of the ancilla and meter cavity (the eNMO-system) [Wim+14; Sch+22]

$$\hat{H}_{\mathrm{anc}} = \hbar g_{\mathrm{DC}} \left(\hat{a}\hat{c} + \hat{a}^\dagger\hat{c}^\dagger\right) + \hbar g_{\mathrm{BS}} \left(\hat{a}\hat{c}^\dagger + \hat{a}^\dagger\hat{c}\right) , \tag{2.198}$$

the equations of motion of the *effective* negative mass system are given by [87]

$$\underbrace{\begin{pmatrix} \dot{\hat{X}}_{\mathrm{c}} \\ \dot{\hat{Y}}_{\mathrm{c}} \\ \dot{\hat{X}}_{\mathrm{a}} \\ \dot{\hat{Y}}_{\mathrm{a}} \end{pmatrix}}_{\dot{\boldsymbol{x}}_{\mathrm{eNMO}}(t)} = \underbrace{\begin{pmatrix} -\frac{\kappa_{\mathrm{c}}}{2} & \Delta_{\mathrm{c}} & 0 & g_{\mathrm{Bs}} - g_{\mathrm{DC}} \\ -\Delta_{\mathrm{c}} & -\frac{\kappa_{\mathrm{c}}}{2} & 0 & -(g_{\mathrm{Bs}} + g_{\mathrm{DC}}) \\ 0 & g_{\mathrm{Bs}} - g_{\mathrm{DC}} & -\frac{\kappa_{\mathrm{a}}}{2} & \Delta_{\mathrm{a}} \\ -(g_{\mathrm{Bs}} + g_{\mathrm{DC}}) & 0 & -\Delta_{\mathrm{a}} & -\frac{\kappa_{\mathrm{a}}}{2} \end{pmatrix}}_{\boldsymbol{M}_{\mathrm{eNMO}}} \underbrace{\begin{pmatrix} \hat{X}_{\mathrm{c}} \\ \hat{Y}_{\mathrm{c}} \\ \hat{X}_{\mathrm{a}} \\ \hat{Y}_{\mathrm{a}} \end{pmatrix}}_{\boldsymbol{x}_{\mathrm{eNMO}}(t)} \tag{2.199a}$$

$$+ \underbrace{\begin{pmatrix} \sqrt{\kappa^{\mathrm{in}}_{\mathrm{c}}} & 0 \\ 0 & \sqrt{\kappa^{\mathrm{in}}_{\mathrm{c}}} \\ 0 & 0 \\ 0 & 0 \end{pmatrix}}_{\boldsymbol{K}^{\mathrm{in}}_{\mathrm{eNMO}}} \underbrace{\begin{pmatrix} \hat{X}^{\mathrm{in}}_{\mathrm{c}} \\ \hat{Y}^{\mathrm{in}}_{\mathrm{c}} \end{pmatrix}}_{\boldsymbol{x}^{\mathrm{in}}_{\mathrm{eNMO}}(t)} \tag{2.199b}$$

$$+ \underbrace{\begin{pmatrix} \sqrt{\kappa^{\mathrm{bath}}_{\mathrm{c}}} & 0 & 0 & 0 \\ 0 & \sqrt{\kappa^{\mathrm{bath}}_{\mathrm{c}}} & 0 & 0 \\ 0 & 0 & \sqrt{\kappa_{\mathrm{a}}} & 0 \\ 0 & 0 & 0 & \sqrt{\kappa_{\mathrm{a}}} \end{pmatrix}}_{\boldsymbol{K}^{\mathrm{bath}}_{\mathrm{eNMO}}} \underbrace{\begin{pmatrix} \hat{X}^{\mathrm{bath}}_{\mathrm{c}} \\ \hat{Y}^{\mathrm{bath}}_{\mathrm{c}} \\ \hat{Y}^{\mathrm{bath}}_{\mathrm{a}} \\ \hat{X}^{\mathrm{bath}}_{\mathrm{a}} \end{pmatrix}}_{\boldsymbol{x}^{\mathrm{bath}}_{\mathrm{eNMO}}(t)} . \tag{2.199c}$$

The eNMO-system contains two modes which are coupled via a beamsplitter coupling g_{BS} and a downconversion process g_{DC}[88]. The first mode, $\hat{c}$, with resonance frequency ω_{c}, is the mode of the driving field and is referred to as the meter cavity, while the second mode, $\hat{a}$, is referred to the ancilla cavity with resonance frequency ω_{a}. Their corresponding detunings are $\Delta_{\mathrm{c,a}} = \omega_{\mathrm{c,a}} - \omega_0$. As only the meter cavity is driven and

[87] Remark to the notation of κ: The superscripts $^{\mathrm{in}}$ and $^{\mathrm{bath}}$ are used to denote the input port of the drive and the input port of the external bath (noise) of the system, respectively.

[88] Downconversion process is the process which generates, in this case, two-mode squeezing.

the ancilla cavity only couples to the bath, the ancilla cavity input noise fields are incorporated into $\boldsymbol{K}^{\text{bath}}_{\text{eNMO}}\boldsymbol{x}^{\text{bath}}_{\text{eNMO}}(t)$[89]. For the driving field, $\kappa_{\text{c}}^{\text{in}}$ describes the rate at which the drive couples in, while $\kappa_{\text{c}}^{\text{bath}}$ describes the rate at which noise couples in via the remaining ports[90] into the mode $\hat{c}$. Comparison of the two system matrices $\boldsymbol{M}_{\text{OMS}}$ and $\boldsymbol{M}_{\text{eNMO}}$ in Equation (2.192) and (2.199) reveals that the effective negative mass imitates the radiation pressure interaction if $g_{\text{BS}} = g_{\text{DC}} = \frac{1}{2}g_{\text{anc}}$, where g_{anc} is the effective coupling strength of the ancilla cavity[91]. Assuming no additional loss for the driving field, $\kappa_{\text{c}}^{\text{bath}} = 0$, and $\Delta_{\text{c}} = 0$[92] the quadrature outputs reads

$$\hat{X}_{\text{c}}^{\text{out}}(\omega) = e^{i\phi_{\text{c}}}\hat{X}_{\text{c}}^{\text{in}} \tag{2.200a}$$

$$\begin{aligned}\hat{Y}_{\text{c}}^{\text{out}}(\omega) =& e^{i\phi_{\text{c}}}\hat{Y}_{\text{c}}^{\text{in}} + \kappa_{\text{c}}\chi_{\text{a}}g_{\text{anc}}^2\chi_{\text{c}}^2\hat{X}_{\text{c}}^{\text{in}} \\ &- \chi_{\text{a}}\sqrt{\kappa_{\text{c}}}g_{\text{anc}}\chi_{\text{c}}\sqrt{\kappa_{\text{a}}}\left(\frac{\kappa_{\text{a}}/2 + i\omega}{\Delta_a}\hat{X}_{\text{a}}^{\text{in}} + \hat{Y}_{\text{a}}^{\text{in}}\right),\end{aligned} \tag{2.200b}$$

with $e^{i\phi_{\text{c}}} = \frac{\kappa_{\text{c}}/2 - i\omega}{\kappa_{\text{c}}/2 + i\omega}$. Also the susceptibilities for the meter χ_{c} and ancilla χ_{a} cavity are given by

$$\chi_{\text{c}} = \frac{1}{\kappa_{\text{c}}/2 + i\omega}, \quad \chi_{\text{a}} = \frac{\Delta_a}{(\Delta_{\text{a}}^2 - \omega^2 + \kappa_{\text{a}}^2/4) + i\kappa_{\text{a}}\omega}, \tag{2.201}$$

while the measurement strength of the *effective* negative mass oscillator (eNMO) is

$$G_{\text{anc}}(\omega) = \kappa_{\text{c}}|\chi_{\text{c}}|^2 g_{\text{anc}}^2. \tag{2.202}$$

Together with the input noise matrix $S_{\text{eNMO}}^{\text{in}} = \frac{1}{2}\text{diag}\,(1,1,1,1)$ of the eNMO system, its spectral density matrix can be written as

$$\bar{S}_{\text{eNMO}}^{\text{out}} = \frac{1}{2}\begin{pmatrix} 1 & -2G_{\text{anc}}\Re\left(\chi_{\text{m}}\right) \\ -2G_{\text{anc}}\Re\left(\chi_{\text{m}}\right) & 1 + G_{\text{anc}}^2|\chi_{\text{a}}|^2 + 2G_{\text{anc}}|\chi_{\text{a}}|^2\kappa_{\text{a}}^2\left(\frac{\omega^2 + \kappa_{\text{a}}^2/4 + \Delta_{\text{a}}^2}{\Delta_{\text{a}}^2}\right) \end{pmatrix}. \tag{2.203}$$

As stated at the beginning of this section, for coherent quantum noise cancellation the output quadratures of the optomechanical system (Equation (2.193)) are used as the input of the eNMO-system. This is done by setting $X_{\text{c}}^{\text{in}} = X_{\text{om}}^{\text{out}}$ and $Y_{\text{c}}^{\text{in}} = Y_{\text{om}}^{\text{out}}$ or by $X_{\text{om}}^{\text{in}} = X_{\text{c}}^{\text{out}}$ and $Y_{\text{om}}^{\text{in}} = Y_{\text{c}}^{\text{out}}$, if they are cascaded in the opposite order. After cascading the subsystems, the phase quadrature spectral density is given as

$$\bar{S}^{\text{total}}_{\hat{Y}^{\text{out}},\hat{Y}^{\text{out}}} = G_{\text{om}}\gamma_{\text{om}}|\chi_{\text{m}}|^2\bar{S}^{\text{in}}_{\hat{\mathcal{F}}\hat{\mathcal{F}}} \tag{2.204}$$

$$+ \frac{G_{\text{anc}}^2|\chi_{\text{a}}|^2}{2} + \frac{G_{\text{om}}^2|\chi_{\text{m}}|^2}{2} + G_{\text{anc}}G_{\text{om}}\Re\left(\chi_{\text{m}}\chi_{\text{a}}^*\right) \tag{2.205}$$

$$+ \frac{1}{2} + \frac{G_{\text{anc}}\kappa_{\text{a}}|\chi_{\text{a}}|^2}{2}\left(\frac{\omega^2 + \kappa_{\text{a}}^2/4 + \Delta_{\text{a}}^2}{\Delta_{\text{a}}^2}\right). \tag{2.206}$$

[89] Also, $\kappa_{\text{a}}^{\text{bath}} = \kappa_{\text{a}}$, as there is no external drive for the ancilla cavity.

[90] E.g., losses due to i additional mirrors different from the input coupler and absorption, $\kappa_{\text{c}}^{\text{bath}} = \kappa_{\text{c}}^{\text{absor}} + \kappa_{\text{c}}^{\text{i}}$.

[91] Also more precisely: Only the ancilla cavity (anc) with mode $\hat{a}$ can be seen as the eNMO if coupled to the meter cavity (mode $\hat{c}$) in the same way but with opposite sign as the mechanical mode $\hat{b}$ is coupled to the driving field ($\hat{c}$) of the optomechanical cavity. However, as in [Sch+22], the eNMO contains the ancilla and meter cavity and their couplings.

[92] Again to imitate the OMS system.

As in Equation (2.157) and in Section 2.5.7, the output $S^{\text{total}}_{\hat{Y}_{\text{out}},\hat{Y}_{\text{out}}}$ is divided by[93] $G_{\text{om}}\gamma_{\text{om}}|\chi_{\text{m}}|^2$ to get the force noise spectral density $\bar{S}^{\text{noise}}_{\hat{\mathcal{F}},\hat{\mathcal{F}}}$, given by[94]

$$\bar{S}^{\text{noise}}_{\hat{\mathcal{F}},\hat{\mathcal{F}}} = \left(\frac{K_{\text{B}}T}{\hbar\omega_{\text{m}}} + \frac{1}{2}\right) \tag{2.207a}$$

$$+ \frac{G^2_{\text{anc}}|\chi_{\text{a}}|^2 + G^2_{\text{om}}|\chi_{\text{m}}|^2 + 2G_{\text{anc}}G_{\text{om}}\Re\left(\chi_{\text{m}}\chi^*_{\text{a}}\right)}{2G_{\text{om}}\gamma_{\text{om}}|\chi_{\text{m}}|^2} \tag{2.207b}$$

$$+ \frac{1}{2G_{\text{om}}\gamma_{\text{om}}|\chi_{\text{m}}|^2} + \frac{G_{\text{anc}}\kappa_{\text{a}}|\chi_{\text{a}}|^2}{2G_{\text{om}}\gamma_{\text{om}}|\chi_{\text{m}}|^2}\left(\frac{\omega^2 + \kappa^2_{\text{a}}/4 + \Delta^2_{\text{a}}}{\Delta^2_{\text{a}}}\right). \tag{2.207c}$$

The first term in Equation (2.207a) contains thermal noise and the zero point fluctuations, while Equation (2.207b) contains backaction noise of the positive and *effective* negative mass oscillator and its interplay ($2G_{\text{anc}}G_{\text{om}}\Re\left(\chi_{\text{m}}\chi^*_{\text{a}}\right)$). Equation (2.207c) contains imprecision noise due to the optomechanical system and noise coupled into the system due to the ancilla cavity. Equation (2.207b) reveals that by assuming a quantum backaction noise limited system (Equation (2.168))

$$C_{\text{qba}} = \frac{\hbar g^2_{\text{om}}}{\kappa_{\text{om}}k_{\text{B}}T}Q \gg 1 \tag{2.208}$$

under the following conditions backaction noise is cancelled [95]

$$G_{\text{om}} = G_{\text{anc}}\,, \tag{2.209}$$

$$\chi_{\text{m}} = -\chi_{\text{a}}\,. \tag{2.210}$$

$$\tag{2.211}$$

In detail, the condition $G_{\text{om}} = G_{\text{anc}}$ reads[96]

$$G_{\text{anc}} = \frac{g^2_{\text{anc}}\kappa_{\text{c}}}{\kappa^2_{\text{c}} + \omega^2} = \frac{g^2_{\text{om}}\kappa_{\text{om}}}{\kappa^2_{\text{om}} + \omega^2} = G_{\text{om}}\,, \tag{2.212}$$

and shows that a mismatch between the coupling strengths G_{anc} and G_{om} can be compensated by a mismatch in the linewidths κ_{om} and κ_{c}.

The the third condition $\chi_{\text{m}} = -\chi_{\text{a}}$ with

$$\chi_{\text{m}} = \frac{\omega_{\text{m}}}{\omega^2_{\text{m}} - \omega^2 + i\gamma_{\text{m}}\omega} \quad \text{and} \quad \chi_{\text{a}} = \frac{\Delta_{\text{a}}}{(\Delta^2_{\text{a}} - \omega^2 + \kappa^2_{\text{a}}/4) + i\kappa_{\text{a}}\omega} \tag{2.213}$$

leads to the following restrictions:

1. The detuning of the ancialla cavity has to fulfil

$$\Delta_{\text{a}} = -\omega_{\text{m}}\,, \tag{2.214}$$

as in this case the ancilla cavity acts as an *effective* negative mass oscillator.

2. The positive mechanical oscillator and the *effective* negative one should

[93] $G_{\text{om}}(\omega) = f^{\theta=\frac{\pi}{2},\Delta=0}_{\text{transfer}}(\omega)$ (see Equation (2.160)).
[94] Here all contribution, except the signal are included.
[95] One should keep in mind, that $g_{\text{BS}} = g_{\text{DC}} = \frac{1}{2}g_{\text{anc}}$ is assumed.
[96] G_{om} as introduced in Section 2.5.

have the same linewidth

$$\kappa_a = \gamma_m. \tag{2.215}$$

3. To decrease the only remaining difference in the denominator of the susceptibilities of χ_m and χ_a, which is due to a different coupling of the subsystems to their bath,

$$\omega_m \gg \kappa_a\,, \tag{2.216}$$

has to be fulfilled., containing the imprecision noise , The last two requirements imply the use of a high-Q mechanical resonator:

$$Q = \frac{\omega_m}{\gamma_m} \gg 1. \tag{2.217}$$

If these conditions are fulfilled, the quantum backaction noise in Equation (2.207b) of the positive and effective negative mass cancel each other, and for a quantum backaction noise limited case, the noise density reads by neglecting thermal noise ($Q_{qba} \gg 1$),

$$\bar{S}^{\text{add, CQNC}}_{\hat{\mathcal{F}},\hat{\mathcal{F}}} = \frac{1}{2\gamma_m G_{om}|\chi_m(\omega)|^2} + \frac{1}{2}\frac{\omega^2 + \gamma_m^2/4 + \omega_m^2}{\omega_m^2}\,. \tag{2.218}$$

In Equation (2.218) the second term describes noise that is coupled into the system due to the ancilla cavity. The input noise, due to the ancilla cavity sets the sensitivity limit as the first term, proportional to the imprecision noise $S_{\text{impr}}^{\theta=\frac{\pi}{2},\Delta=0}(\omega)$ (Equation (2.160)), can be made arbitrarily small by increasing the optomechanical measurement strength G_{om}. Thereby, the fundamental limit of CQNC, assuming a high mechanical quality factor ($Q \gg 1$), is given as [Sch+22]

$$\bar{S}^{\text{add,ideal CQNC}}_{\hat{\mathcal{F}},\hat{\mathcal{F}}} = \bar{S}^{\text{SQL}}_{\hat{\mathcal{F}},\hat{\mathcal{F}}} \times \begin{cases} 1 & \text{on resonance } \omega = \omega_m \\ 1/(2Q) & \text{off resonance } \omega \neq \omega_m \end{cases} \tag{2.219}$$

where the $\bar{S}^{\text{SQL}}_{\hat{\mathcal{F}},\hat{\mathcal{F}}}$ evaluated in Equation (2.172) is used.

Equation (2.219) reveals that the SQL of the force sensitivity is surpassed at all frequencies ω by a factor of $2Q$ except at ω_m where the sensitivities are equal. Thereby Equation (2.219) shows that a high mechanical quality factor (Q) is desirable in an ideal CQNC experiment. Additionally, a high mechanical quality factor is also needed to achieve a quantum backaction noise-limited optomechanical system[97], as for this the quantum backaction cooperativity $C_{qba} = \frac{\hbar g_{om}^2}{\kappa_{om} k_B T} Q \gg 1$ has to be satisfied (Section 2.5.7 and Equation (2.208)).

2.6.3 Non-ideal CQNC with $\kappa_a \ll \gamma_m$

For CQNC, a high Q-factor contradicts in an experiment with the condition $\kappa_a = \gamma_m$, given in Equation (2.215). Typically the cavity linewidth κ_a is order of magnitudes higher than the linewidth γ_m of the mechanical oscillators[98]. Because $C_{QBA} \propto Q \gg 1$ has to be to fulfilled to be quantum backaction noise limited, the condition $\gamma_m = \kappa_a$ is changed to $\gamma_m \ll \kappa_a$. According to the analysis in [Sch+22] in this case ($\gamma_m \ll \kappa_a$)

[97] This was already one assumption made at the beginning (Equation (2.208)).

[98] For CQNC, the in [Sch+22] proposed cavity linewidth κ_a is in the kHz regime, whereas the mechanical linewidth is in the mHz regime.

the resulting spectral force density is given by

$$S_{\hat{\mathcal{F}},\hat{\mathcal{F}}}^{\mathrm{CQNC},\gamma_\mathrm{m}\ll\kappa_\mathrm{a}} = \frac{\kappa_\mathrm{a}}{2\omega_\mathrm{m}} \times S_{\hat{\mathcal{F}},\hat{\mathcal{F}}}^{\mathrm{SQL}}\,. \tag{2.220}$$

Equation (2.220) demonstrates that even for $\gamma_\mathrm{m} \ll \kappa_\mathrm{a}$, the force SQL is surpassed in a CQNC experiment by a factor of $\frac{2\omega_\mathrm{m}}{\kappa_\mathrm{a}}$[99,100]. Hence, Equation (2.220) suggests a linewidth κ_a that should be as small as possible to increase the sensitivity.

Figure 2.19 illustrates the spectral noise sensitivity for ideal CQNC (black) (Equation (2.219)), the SQL for force sensitivity (blue) (Equation (2.172)), and non-ideal CQNC (red) (Equation (2.207)). For the non-ideal CQNC force spectral density $\bar{S}_{\hat{\mathcal{F}},\hat{\mathcal{F}}}^{\mathrm{noise},\gamma_\mathrm{m}\ll\kappa_\mathrm{a}}$ a temperature of 4 K was assumed. Note that the spectral densities for the SQL $\bar{S}_{\hat{\mathcal{F}},\hat{\mathcal{F}}}^{\mathrm{SQL}}$ and ideal CQNC $\bar{S}_{\hat{\mathcal{F}},\hat{\mathcal{F}}}^{\mathrm{add,\ ideal\ CQNC}}$ represent added noise densities and do not include intrinsic noise sources, like thermal noise.

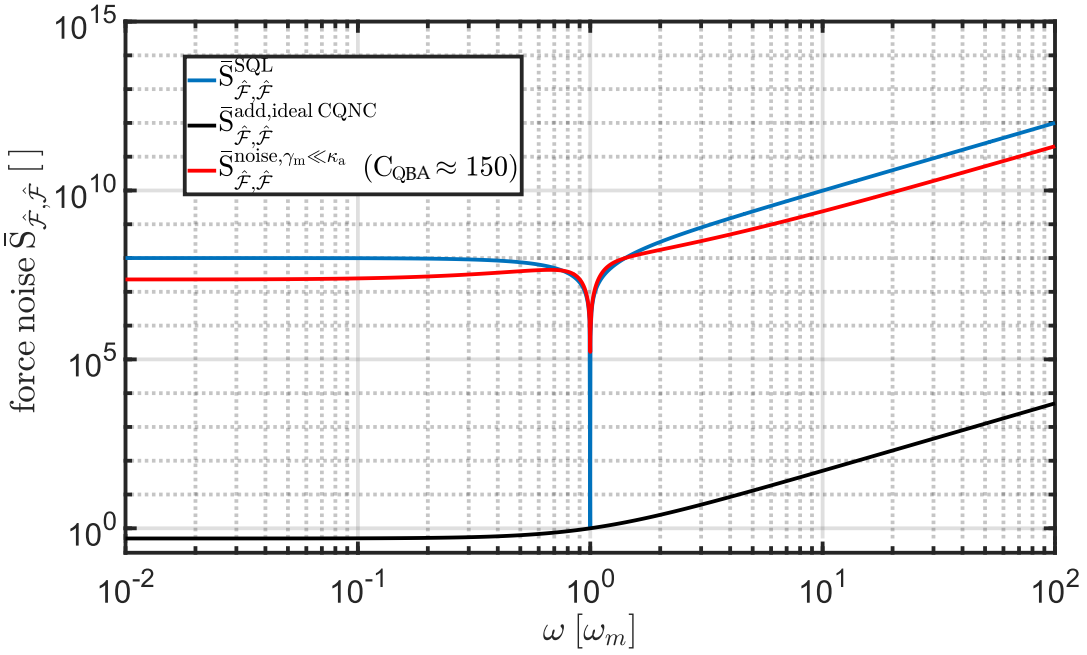

FIGURE 2.19: CQNC performance and SQL: The black line shows the force sensitivity for ideal CQNC $\bar{S}_{\hat{\mathcal{F}},\hat{\mathcal{F}}}^{\mathrm{add,ideal\ CQNC}}$, the blue line the force spectra density $\bar{S}_{\hat{\mathcal{F}},\hat{\mathcal{F}}}^{\mathrm{SQL}}$ of the SQL and the red line the spectral density $\bar{S}_{\hat{\mathcal{F}},\hat{\mathcal{F}}}^{\mathrm{noise},\gamma_\mathrm{m}\ll\kappa_\mathrm{a}}$.
Used parameters: $g_\mathrm{DC} = g_\mathrm{BS} = \frac{1}{2}g_\mathrm{anc}$, $g_\mathrm{om} = G_\mathrm{anc}$, $g_\mathrm{om}/(2\pi) = 500\,\mathrm{kHz}$, $\omega_\mathrm{m}/(2\pi) = 500\,\mathrm{kHz}$, $\gamma_\mathrm{m}/(2\pi) = 10^{-8}\omega_\mathrm{m}$, $\kappa_\mathrm{om}/(2\pi) = \kappa_\mathrm{c}/(2\pi) = 2\,\mathrm{MHz}$ and $\kappa_\mathrm{a}/(2\pi) = 200\,\mathrm{kHz}$.

Figure 2.19 shows first that by using a CQNC experiment, indeed, the SQL is surpassed across all frequencies, except at the mechanical resonance frequency ($\omega = \omega_\mathrm{m}$). The increase in noise for ideal CQNC above the resonance frequency is due to the noise penalty introduced by the ancilla cavity (Equation (2.207c)). Secondly, if the condition $\gamma_\mathrm{m} = \kappa_\mathrm{a}$ is not fulfilled, still assuming $\gamma_\mathrm{m} \ll \kappa_\mathrm{a}$, the SQL is surpassed below and above the resonance frequency ω_m. The sensitivity of $\bar{S}_{\hat{\mathcal{F}},\hat{\mathcal{F}}}^{\mathrm{noise},\gamma_\mathrm{m}\ll\kappa_\mathrm{a}}$ is limited by the temperature contribution in Equation (2.207a) and hence can be improved by going to lower temperatures. Specifically, at the resonance frequency ω_m the sensitivity

[99] The sensitivity is enhanced if the values of the resulting spectral density is smallest.
[100] As long as $\kappa_\mathrm{a} \ll \omega_\mathrm{m}$ Equation (2.216) is satisfied.

of $\bar{S}^{\text{noise},\gamma_m \ll \kappa_a}_{\hat{\mathcal{F}},\hat{\mathcal{F}}}(\omega_m)$ is given by $\frac{K_B T}{\hbar \omega_m} + \frac{1}{2}$. In summary, the sensitivity $\bar{S}^{\text{noise},\gamma_m \ll \kappa_a}_{\hat{\mathcal{F}},\hat{\mathcal{F}}}$ for a non-ideal CQNC experiment with $\kappa_a \ll \omega_m$ can be improved by engineering an ancilla cavity with a linewidth κ_a as small as possible and by decreasing the temperature T.

Additional losses

So far, no parameters, like propagation losses or coupling efficiencies, have been assumed. Such a study can be found in [Sch+22; Sch23]. The outcome of this case study is, that a CQNC experiment is feasible, even if losses are treated and mismatches of the requirements given in Equation (2.210) to Equation (2.216) are present. The values proposed by [Sch+22] for a feasible CQNC experiment can be seen in Table 2.1

Symbol	Parameter	Value
ω_m	mechanical resonance frequency	500 kHz
γ_m	mechanical linewidth	5 mHz
g_{om}	optomechanical coupling strength	500 kHz
κ_{om}	optomechanical cavity linewidth	1.98 MHz
Δ_a	ancilla cavity detuning	−495 kHz
κ_c	meter cavity linewidth	2 MHz
κ_a	ancilla cavity linewidth	200 kHz
g_{BS}	beam-splitter coupling strength	253 kHz
g_{DC}	down-conversion coupling strength	243 kHz
η^{esc}_{om}	escape efficiency OMS	90 %
η^{esc}_{c}	escape efficiency eNMO	90 %
η_{prop}	propagation efficiency	97 %
κ_a	ancilla cavity linewidth	200 kHz
η_{det}	detection efficiency	97 %
T	temperature	4 K

TABLE 2.1: Set of parameters proposed by [Sch+22] for a realisation of a CQNC experiment. Parameters highlighted in red will be experimentally investigated within Part II.

In Table 2.1 $\eta^{esc}_{om,c}$ describes the coupling efficiency of the optomechanical system (om) and the meter cavity (c), given by $\eta^{esc}_{om,c} = \frac{\kappa^{in}_{om,c}}{\kappa^{in}_{om,c}+\kappa^{bath}_{om,c}} = \frac{\kappa^{in}_{om,c}}{\kappa_{om,c}}$.

As mentioned, this work focuses explicitly on an optomechanical system designed for a CQNC experiment. In Chapter 4, the optomechanical system is constructed to meet the specified values highlighted in Table 2.1. Ultimately, the setup served as a proof of concept, since the actual values were not met with the available optomechanical oscillator. However, the following section will discuss an idea of how the CQNC setup can be improved by an additional beam introducing sideband cooling before showing the actual optomechanical setup.

2.6.4 CQNC with sideband cooling

In the previous Section 2.6.3 it was shown, that a realistic treatment of $\gamma_m \ll \kappa_a$ leads to a degradation of CQNC performance. One idea to mitigate the degradation originating from the mismatch of the linewidth is the introduction of an independent beam, which induces sideband cooling. Hence, for a red detuned beam the mechanical linewidth γ_m is broadened to γ_{eff} (Section 2.5.2). Therefore, the introduced beam is denoted in the following as the cooling beam. The benefit of using a cooling beam is a broadening of the effective linewidth and thus an approach to the condition ($\gamma_{eff} \approx \kappa_a$)[101], which leads to a CQNC sensitivity improvement. Not only the (effective) mechanical linewidth changes, but also an additional noise term, due to backaction noise of the cooling beam, is introduced to the system. However, it will be explained within this section, that under the right circumstances the effect of the alteration of the mechanical linewidth outweighs the additional backaction noise contribution of the cooling beam. In the following, the additional cooling beam is depicted in blue in Figure 2.20.

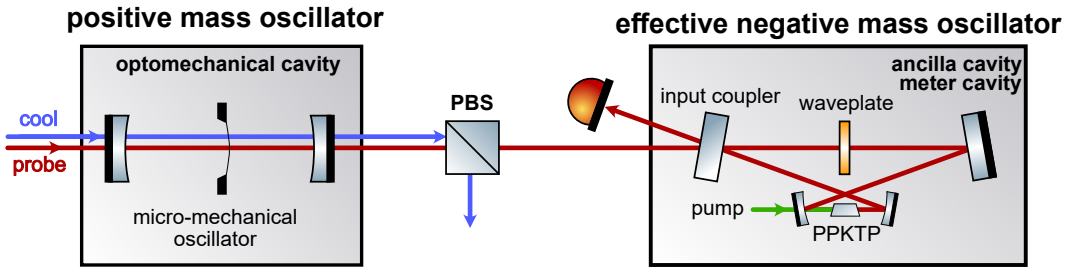

FIGURE 2.20: Proposed cascaded scheme for an all optical CQNC experiment, including an additional cooling beam (blue). The cooling beam is only seen by the optomechanical cavity, as it is separated by a PBS from the effective negative mass oscillator (eNMO). The right cavity, as shown in Figure 2.18, represents the eNMO.

For the derivations, the probe beam is assumed to be resonant with the optomechanical system, as in the previous section, whereas the cooling beam is detuned by Δ_{cool} to the cavity resonance frequency. Also the optomechanical coupling strength of the cooling beam is denoted as g_{cool}, whereas the linewidths of the cooling beam and the probe beam are the same.

As the cooling beam couples into the OMS cavity from the same port as the probe beam, but is assumed to be independent[102] of the probe beam, the equations of motion of the OMS system are given by

[101] Originally the condition is given as $\gamma_m = \kappa_a$.

[102] In an experiment achieved by orthogonal polarisations and/or different frequencies of the probe and cooling beam.

$$\dot{\hat{X}}_{\mathrm{om}} = -\frac{\kappa}{2}\hat{X}_{\mathrm{om}} + \sqrt{\kappa_{\mathrm{om}}^{\mathrm{in}}}\hat{X}_{\mathrm{om}}^{\mathrm{in}} + \sqrt{\kappa_{\mathrm{om}}^{\mathrm{bath}}}\hat{X}_{\mathrm{om}}^{\mathrm{bath}}$$

$$\dot{\hat{Y}}_{\mathrm{om}} = -\frac{\kappa}{2}\hat{Y}_{\mathrm{om}} - g_{\mathrm{om}}\hat{x}_{\mathrm{m}} + \sqrt{\kappa_{\mathrm{om}}^{\mathrm{in}}}\hat{Y}_{\mathrm{om}}^{\mathrm{in}} + \sqrt{\kappa_{\mathrm{om}}^{\mathrm{bath}}}\hat{Y}_{\mathrm{om}}^{\mathrm{bath}}$$

$$\dot{\hat{X}}_{\mathrm{cool}} = -\frac{\kappa_{\mathrm{om}}}{2}\hat{x}_{\mathrm{cool}} + \Delta_{\mathrm{cool}}\hat{p}_{\mathrm{cool}} + \sqrt{\kappa_{\mathrm{om}}^{\mathrm{in}}}\hat{X}_{\mathrm{cool}}^{\mathrm{in}} + \sqrt{\kappa_{\mathrm{om}}^{\mathrm{bath}}}\hat{X}_{\mathrm{cool}}^{\mathrm{bath}}\,, \tag{2.221}$$

$$\dot{\hat{Y}}_{\mathrm{cool}} = -\frac{\kappa_{\mathrm{om}}}{2}\hat{Y}_{\mathrm{cool}} - \Delta_{\mathrm{cool}}\hat{X}_{\mathrm{cool}} - g_{\mathrm{cool}}\hat{x}_{\mathrm{m}} + \sqrt{\kappa_{\mathrm{om}}^{\mathrm{in}}}\hat{Y}_{\mathrm{cool}}^{\mathrm{in}} + \sqrt{\kappa_{\mathrm{om}}^{\mathrm{bath}}}\hat{Y}_{\mathrm{cool}}^{\mathrm{bath}}\,, \tag{2.222}$$

$$\dot{\hat{x}}_{\mathrm{m}} = \omega_{\mathrm{m}}\hat{p}_{\mathrm{m}}\,, \tag{2.223}$$

$$\dot{\hat{p}}_{\mathrm{m}} = -\omega_{\mathrm{m}}\hat{x}_{\mathrm{m}} - g\hat{X}_{\mathrm{om}} - g_{\mathrm{cool}}\hat{X}_{\mathrm{cool}} - \gamma_{\mathrm{m}}\hat{p}_{\mathrm{m}} + \sqrt{\gamma_{\mathrm{m}}}\hat{\mathcal{F}}_{\mathrm{ext}}\,. \tag{2.224}$$

As in Section 2.6.2 the equations of motion are written in matrix form as

$$\underbrace{\begin{pmatrix} \dot{\hat{X}}_{\mathrm{om}} \\ \dot{\hat{Y}}_{\mathrm{om}} \\ \dot{\hat{X}}_{\mathrm{cool}} \\ \dot{\hat{Y}}_{\mathrm{cool}} \\ \dot{\hat{x}}_{\mathrm{m}} \\ \dot{\hat{p}}_{\mathrm{m}} \end{pmatrix}}_{\dot{\mathbf{x}}_{\mathrm{OMS}}(t)} = \underbrace{\begin{pmatrix} -\frac{\kappa_{\mathrm{om}}}{2} & 0 & 0 & 0 & 0 & 0 \\ 0 & -\frac{\kappa_{\mathrm{om}}}{2} & 0 & 0 & -g_{\mathrm{om}} & 0 \\ 0 & 0 & -\frac{\kappa_{\mathrm{om}}}{2} & \Delta_{\mathrm{cool}} & 0 & 0 \\ 0 & 0 & -\Delta_{\mathrm{cool}} & -\frac{\kappa_{\mathrm{om}}}{2} & -g_{\mathrm{cool}} & 0 \\ 0 & 0 & 0 & 0 & 0 & \omega_{\mathrm{m}} \\ -g_{\mathrm{om}} & 0 & -g_{\mathrm{cool}} & 0 & -\omega_{\mathrm{m}} & -\gamma_{\mathrm{m}} \end{pmatrix}}_{\mathrm{M_{sys}}} \underbrace{\begin{pmatrix} \hat{X}_{\mathrm{om}} \\ \hat{Y}_{\mathrm{om}} \\ \hat{X}_{\mathrm{cool}} \\ \hat{Y}_{\mathrm{cool}} \\ \hat{x}_{\mathrm{m}} \\ \hat{p}_{\mathrm{m}} \end{pmatrix}}_{\mathbf{x}_{\mathrm{OMS}}(t)}. \tag{2.225}$$

$$+ \underbrace{\begin{pmatrix} \sqrt{\kappa_{\mathrm{om}}} & 0 & 0 & 0 \\ 0 & \sqrt{\kappa_{\mathrm{om}}} & 0 & 0 \\ 0 & 0 & \sqrt{\kappa_{\mathrm{om}}} & 0 \\ 0 & 0 & 0 & \sqrt{\kappa_{\mathrm{om}}} \\ 0 & 0 & 0 & 0 \\ 0 & 0 & 0 & 0 \end{pmatrix}}_{\mathrm{K_{OMS}^{in}}} \underbrace{\begin{pmatrix} \hat{X}_{\mathrm{om}}^{\mathrm{in}} \\ \hat{Y}_{\mathrm{om}}^{\mathrm{in}} \\ \hat{X}_{\mathrm{om}}^{\mathrm{cool}} \\ \hat{Y}_{\mathrm{om}}^{\mathrm{cool}} \end{pmatrix}}_{\mathbf{x}_{\mathrm{OMS}}^{\mathrm{in}}(t)}, \tag{2.226}$$

$$+ \underbrace{\begin{pmatrix} \cancelto{0}{\sqrt{\kappa_{\mathrm{om}}^{\mathrm{bath}}}} & 0 & 0 & 0 & 0 & 0 \\ 0 & \cancelto{0}{\sqrt{\kappa_{\mathrm{om}}^{\mathrm{bath}}}} & 0 & 0 & 0 & 0 \\ 0 & 0 & \cancelto{0}{\sqrt{\kappa_{\mathrm{om}}^{\mathrm{bath}}}} & 0 & 0 & 0 \\ 0 & 0 & 0 & \cancelto{0}{\sqrt{\kappa_{\mathrm{om}}^{\mathrm{bath}}}} & 0 & 0 \\ 0 & 0 & 0 & 0 & 0 & 0 \\ 0 & 0 & 0 & 0 & 0 & \sqrt{\gamma_{\mathrm{m}}} \end{pmatrix}}_{\mathrm{K_{OMS,bath}}} \underbrace{\begin{pmatrix} \hat{X}_{\mathrm{om}}^{\mathrm{bath}} \\ \hat{Y}_{\mathrm{om}}^{\mathrm{bath}} \\ \hat{X}_{\mathrm{cool}}^{\mathrm{bath}} \\ \hat{Y}_{\mathrm{cool}}^{\mathrm{bath}} \\ 0 \\ \hat{\mathcal{F}}_{\mathrm{ext}} \end{pmatrix}}_{\mathbf{x}_{\mathrm{OMS,bath}}(t)}. \tag{2.227}$$

Using the same procedure, as in Section 2.6.1, the quadrature output of phase $\hat{Y}^{\text{out}}_{\text{om}}(\omega)$ and amplitude $\hat{X}^{\text{out}}_{\text{om}}(\omega)$ of the optomechanical system are calculated as

$$\hat{Y}^{\text{out}}_{\text{om}}(\omega) = e^{i\phi_{\text{om}}}\hat{Y}^{\text{in}}_{\text{om,L}} + \kappa_{\text{om}}\chi_{\text{eff}}g^2_{\text{om}}\chi^2_{\text{om}}\hat{X}^{\text{in}}_{\text{om}} \tag{2.228a}$$

$$- \chi_{\text{eff}}\sqrt{\kappa_{\text{om}}}g_{\text{om}}\chi_{\text{om}}\sqrt{\gamma_{\text{m}}}\hat{F}_{\text{ext}} \tag{2.228b}$$

$$- g_{\text{om}}g_{\text{cool}}\kappa_{\text{om}}\chi_{\text{cool}}\chi_{\text{om}}\chi_{\text{eff}}(\hat{Y}^{\text{in}}_{\text{cool}} + \frac{\chi_{\text{c}}^{-1}}{\Delta_{\text{cool}}}\hat{X}^{\text{in}}_{\text{cool}}) \tag{2.228c}$$

$$\hat{X}^{\text{out}}_{\text{om}}(\omega) = e^{i\phi_{\text{om}}}\hat{X}^{\text{in}}_{\text{om}} \tag{2.229}$$

with

$$\chi_{\text{cool}} = \frac{\Delta_{\text{cool}}}{\omega^2 - \Delta^2_{\text{cool}} - i\kappa_{\text{om}}\omega - \kappa^2_{\text{om}}/4}, \tag{2.230}$$

$$\chi_{\text{eff}} = \frac{\omega_{\text{m}}}{\omega^2_{\text{eff}} - \omega^2 + i\omega\gamma_{\text{eff}}}. \tag{2.231}$$

The phase quadrature spectral density, for an added cooling beam, using $S_{\text{in}} = \frac{1}{2}\text{diag}(1,1,1,1,0,2\bar{S}_{\hat{\mathcal{F}}_{\text{ext}},\hat{\mathcal{F}}_{\text{ext}}})$ (Section 2.6.1) is derived as

$$\bar{S}^{\text{added, cool}}_{\hat{Y}^{\text{out}}_{\text{om}},\hat{Y}^{\text{out}}_{\text{om}}} = \frac{1}{2} + 2G_{\text{om}}|\chi_{\text{eff}}|^2\left(\Gamma^{\text{probe},\Delta=0}_{\text{QBA}} + \Gamma^{\text{cool}}_{\text{QBA}}\right) + G_{\text{om}}\gamma_{\text{eff}}|\chi_{\text{eff}}|^2\bar{S}_{\hat{\mathcal{F}}_{\text{ext}},\hat{\mathcal{F}}_{\text{ext}}} \tag{2.232a}$$

$$= \frac{1}{2} + G_{\text{om}}|\chi_{\text{eff}}(\omega)|^2\left(\frac{G_{\text{om}}}{2} + \gamma_{\text{m}}(\bar{S}_{\hat{\mathcal{F}}_{\text{th}},\hat{\mathcal{F}}_{\text{th}}} + \bar{S}_{\hat{\mathcal{F}}_{\text{sig}},\hat{\mathcal{F}}_{\text{sig}}})\right) \tag{2.232b}$$

$$+ 2G_{\text{om}}|\chi_{\text{eff}}(\omega)|^2\Gamma^{\text{cool},\Delta}_{\text{QBA}}, \tag{2.232c}$$

with

$$\Gamma^{\text{probe},\Delta=0}_{\text{QBA}} = \frac{g^2_{\text{om}}\kappa_{\text{om}}}{4}\frac{1}{\frac{\kappa^2_{\text{om}}}{4} + \omega^2} = \frac{G_{\text{om}}}{4} \tag{2.233}$$

and

$$\Gamma^{\text{cool},\Delta}_{\text{QBA}} = \frac{g^2_{\text{cool}}\kappa_{\text{om}}}{4}\frac{\Delta^2_{\text{cool}} + \frac{\kappa^2_{\text{om}}}{4} + \omega^2}{\Delta^4_{\text{cool}} + 2\Delta^2_{\text{cool}}(\frac{\kappa^2_{\text{om}}}{4} - \omega^2) + (\frac{\kappa^2_{\text{om}}}{4} + \omega^2)^2} \tag{2.234}$$

being the quantum backaction rate of the probe and the cooling beam, respectively (Equation (2.146)).

A comparison of the phase quadrature output spectrum $\bar{S}_{\hat{Y}^{\text{out}}_{\text{om,L}},\hat{Y}^{\text{out}}_{\text{om,L}}}$ (Equation (2.197)) and the one with the added cooling beam $\bar{S}^{\text{added, cool}}_{\hat{Y}^{\text{out}}_{\text{om,L}},\hat{Y}^{\text{out}}_{\text{om,L}}}$ reveals, that due to the dynamical backaction of the cooling beam, not only the mechanical susceptibility is altered ($\chi_{\text{m}} \rightarrow \chi_{\text{eff}}$), but also the noise is increased by $2G_{\text{om}}|\chi_{\text{eff}}(\omega)|^2\Gamma^{\text{cool},\Delta}_{\text{QBA}}$. The additional noise originates from the quantum backaction of the cooling beam, coupling via the optomechanical oscillator to the phase quadrature output (see Equation (2.232a)).

To see how the cooling beam influences the overall CQNC performance, the phase and amplitude quadrature output $\hat{X}^{\text{out}}_{\text{om,L}}(\omega)$ and $\hat{Y}^{\text{out}}_{\text{om,L}}(\omega)$ (Equation (2.228) and (2.228c)) of the optomechanical system are used as inputs $\hat{X}^{\text{in}}_{\text{c}}$ and $\hat{Y}^{\text{in}}_{\text{c}}$ of the eNMO (Equation (2.200)). After cascading the two subsystems in this way, the total output phase quadrature spectral density $\bar{S}^{\text{total, added cool}}_{\hat{Y}^{\text{out}},\hat{Y}^{\text{out}}}$ becomes

$$\bar{S}^{\text{total, added cool}}_{\hat{Y}^{\text{out}},\hat{Y}^{\text{out}}} = G_{\text{om}}\gamma_{\text{om}}|\chi_{\text{eff}}|^2 \overbrace{\left(\bar{S}_{\hat{\mathcal{F}}_{\text{th}},\hat{\mathcal{F}}_{\text{th}}} + \bar{S}_{\hat{\mathcal{F}}_{\text{sig}},\hat{\mathcal{F}}_{\text{sig}}}\right)}^{\bar{S}^{\text{in}}_{\hat{\mathcal{F}},\hat{\mathcal{F}}}} \tag{2.235a}$$

$$+ \frac{G^2_{\text{anc}}|\chi_{\text{a}}|^2}{2} + \frac{G^2_{\text{om}}|\chi_{\text{eff}}|^2}{2} + G_{\text{anc}}G_{\text{om}}\Re\left(\chi_{\text{m}}\chi^*_{\text{a}}\right) \tag{2.235b}$$

$$+ \frac{1}{2} + \frac{G_{\text{anc}}\kappa_{\text{a}}|\chi_{\text{a}}|^2}{2}\left(\frac{\omega^2 + \kappa^2_{\text{a}}/4 + \Delta^2_{\text{a}}}{\Delta^2_{\text{a}}}\right) + 2G_{\text{om}}|\chi_{\text{eff}}(\omega)|^2\Gamma^{\text{cool},\Delta}_{\text{QBA}}\,. \tag{2.235c}$$

As implied in Section 2.5.7 the output $S^{\text{total, added cool}}_{\hat{Y}^{\text{out}},\hat{Y}^{\text{out}}}$ has to be divided by the prefactor $G_{\text{om}}\gamma_{\text{eff}}|\chi_{\text{m}}|^2$ of the force spectral density $\bar{S}^{\text{noise, added cool}}_{\hat{\mathcal{F}},\hat{\mathcal{F}}}$, to infer the force noise spectral density $\bar{S}^{\text{noise, added cool}}_{\hat{\mathcal{F}},\hat{\mathcal{F}}}$ (Equation (2.157)), which calculates as[103]

$$\bar{S}^{\text{noise, added cool}}_{\hat{\mathcal{F}},\hat{\mathcal{F}}} = \left(\frac{K_{\text{B}}T}{\hbar\omega_{\text{m}}} + \frac{1}{2}\right) \tag{2.236a}$$

$$+ \frac{G^2_{\text{anc}}|\chi_{\text{a}}|^2 + G^2_{\text{om}}|\chi_{\text{eff}}|^2 + 2G_{\text{anc}}G_{\text{om}}\Re\left(\chi_{\text{eff}}\chi^*_{\text{a}}\right)}{2G_{\text{om}}\gamma_{\text{m}}|\chi_{\text{eff}}|^2} \tag{2.236b}$$

$$+ \frac{1}{2G_{\text{om}}\gamma_{\text{m}}|\chi_{\text{eff}}|^2} + \frac{G_{\text{anc}}\kappa_{\text{a}}|\chi_{\text{a}}|^2}{2G_{\text{om}}\gamma_{\text{m}}|\chi_{\text{eff}}|^2}\left(\frac{\omega^2 + \kappa^2_{\text{a}}/4 + \Delta^2_{\text{a}}}{\Delta^2_{\text{a}}}\right) + \frac{2\Gamma^{\text{cool},\Delta}_{\text{QBA}}}{\gamma_{\text{m}}}\,. \tag{2.236c}$$

A comparison of the force noise spectral densities $S^{\text{total, added cool}}_{\hat{Y}^{\text{out}},\hat{Y}^{\text{out}}}$ and $S^{\text{noise}}_{\hat{Y}^{\text{out}},\hat{Y}^{\text{out}}}$ (Equation (2.207)), suggests that the temperature contribution $\left(\frac{K_{\text{B}}T}{\hbar\omega_{\text{m}}} + \frac{1}{2}\right)$ is not altered by sideband cooling (Section (2.5.3)). Regarding Equation (2.235a) the effective susceptibility χ_{eff} affects the thermal noise $\bar{S}_{\hat{\mathcal{F}}_{\text{th}},\hat{\mathcal{F}}_{\text{th}}}$ and signal $\bar{S}_{\hat{\mathcal{F}}_{\text{sig}},\hat{\mathcal{F}}_{\text{sig}}}$ in the same way, in that the thermal noise and the signal are altered equally. Concerning force detection, sideband cooling does not change the thermal contribution in the force noise spectral density[104].

However, the introduction of a cooling beam to the CQNC setup leads to a modification of the mechanical linewidth γ_{eff}. By using a red-detuned cooling beam, the linewidth is broadened $(\gamma_{\text{eff}} > \gamma_{\text{m}})$, which shows promising progress towards achieving the condition $\gamma_{\text{eff}} = \kappa_{\text{a}}$[105]. But it is important to consider the trade-offs involved. Although fulfilling the condition $\gamma_{\text{eff}} = \kappa_{\text{a}}$ may be accomplished, the cooling beam introduces an additional challenge due to its quantum backaction noise $\frac{2\Gamma^{\text{cool},\Delta}_{\text{QBA}}}{\gamma_{\text{m}}}$ (Equation (2.236c)).

Therefore, next the condition for backaction cancellation for CQNC with an additional cooling beam will be discussed. As can be inferred from Equation (2.236) all backaction contributions are cancelled if

$$\frac{G^2_{\text{anc}}|\chi_{\text{a}}|^2 + G^2_{\text{om}}|\chi_{\text{eff}}|^2 + 2G_{\text{anc}}G_{\text{om}}\Re\left(\chi_{\text{eff}}\chi^*_{\text{a}}\right)}{2G_{\text{om}}\gamma_{\text{m}}|\chi_{\text{eff}}|^2} + \frac{2\Gamma^{\text{cool},\Delta}_{\text{QBA}}}{\gamma_{\text{m}}} = 0\,. \tag{2.237}$$

Due to the vast parameter space involved, finding an analytical solution for the

[103] In the force noise spectral density all contribution, except the signal are included.

[104] Force noise spectral density can be understood as a measure of signal to noise ratio.

[105] Originally the requirement, without the cooling beam, is $\gamma_{\text{m}} = \kappa_{\text{a}}$ (Equation (2.215)) .

backaction cancellation condition in Equation (2.237) is not straightforward. To narrow the parameter space and for reasons of comparability, similar conditions as for non ideal CQNC (Section 2.6.3) are assumed, which are

$$g_{\mathrm{BS}} = g_{\mathrm{DC}} = \frac{g_{\mathrm{anc}}}{2}\,, \tag{2.238a}$$

$$G_{\mathrm{anc}} = \frac{g_{\mathrm{anc}}^2 \kappa_{\mathrm{c}}}{\kappa_{\mathrm{c}}^2 + \omega^2} = \frac{g_{\mathrm{om}}^2 \kappa_{\mathrm{om}}}{\kappa_{\mathrm{om}}^2 + \omega^2} = G_{\mathrm{om}}\,, \tag{2.238b}$$

$$g = g_{\mathrm{anc}}\,, \tag{2.238c}$$

$$\kappa_{\mathrm{om}} = \kappa_{\mathrm{c}}\,, \tag{2.238d}$$

$$\chi_{\mathrm{a}} = -\chi_{\mathrm{eff}}\,, \tag{2.238e}$$

$$\kappa_{\mathrm{a}} \ll \omega_{\mathrm{m}}\,. \tag{2.238f}$$

Explicitly the condition in Equation (2.238e) reads

$$\frac{\Delta_{\mathrm{a}}}{(\omega^2 - (\Delta_{\mathrm{a}}^2 + \kappa_{\mathrm{a}}^2/4) - i\kappa_{\mathrm{a}}\omega)} = \frac{-\omega_{\mathrm{m}}}{\omega^2 - \omega_{\mathrm{eff}}^2(\Delta_{\mathrm{cool}}, g_{\mathrm{cool}}) - i\omega\gamma_{\mathrm{eff}}(\Delta_{\mathrm{cool}}, g_{\mathrm{cool}})}\,. \tag{2.239}$$

To further reduce the parameter space, one more restriction is introduced. Using Equation (2.126) the detuning Δ_{cool} is fixed to Δ_{opt}, at which the linewidth γ_{eff} reaches its maximum, while being proportional to g_{cool}^2. With this and the aforementioned conditions the remaining free parameters are given by g and g_{cool}.

In the unresolved sideband regime ($\omega_{\mathrm{m}} \ll \kappa_{\mathrm{om}}$) there is no combination of g and g_{cool} that improves the CQNC sensitivity, as the condition in Equation (2.239) is never perfectly matched. Even without perfect matching of the susceptibilities (Equation (2.239)) , the quantum backaction of the cooling beam increases, which outweighs a potential improvement caused by better matching.

The situation changes drastically in the resolved sideband regime ($\omega_{\mathrm{m}} \gg \kappa_{\mathrm{om}}$) in that the condition in Equation (2.239) reads (for $\Delta_{\mathrm{cool}} = \Delta_{\mathrm{opt}}$)

$$\frac{\Delta_{\mathrm{a}}}{(\omega^2 - (\Delta_{\mathrm{a}}^2 + \kappa_{\mathrm{a}}^2/4) - i\kappa_{\mathrm{a}}\omega)} = \frac{-\omega_{\mathrm{m}}}{\omega^2 - \omega_{\mathrm{m}}^2 - i\omega\gamma_{\mathrm{eff}}}\,. \tag{2.240}$$

Perfect matching of the susceptibilities in (Equation (2.239)) can be reached[106] by increasing g_{cool}. However, an increase in g_{cool} simultaneously amplifies the additional backaction contribution $\frac{2\Gamma_{\mathrm{QBA}}^{\mathrm{cool},\Delta}}{\gamma_{\mathrm{m}}}$(Equation (2.236c)) introduced by the cooling beam. As this additional noise (Equation (2.234)) and the improvement of the matching condition (Equation (2.240)) both depend linearly on g_{cool}^2, a trade-off between these exists, which limits the improvement of the CQNC sensitivity.

In contrast to Figure 2.19, where a fixed value for the optomechanical coupling strength g was used, in Figure 2.21 the spectral force noise sensitivity $\bar{S}_{\hat{\mathcal{F}},\hat{\mathcal{F}}}^{\mathrm{noise},\gamma_{\mathrm{m}}\ll\kappa}$ (red) without an additional cooling beam is minimised with respect to g[107]. The, in Figure 2.21 depicted, spectral force noise spectral density $\bar{S}_{\hat{\mathcal{F}},\hat{\mathcal{F}}}^{\mathrm{noise,\ added\ cool}(\Delta_{\mathrm{opt}}=\Delta_{\mathrm{opt}})}$(green) of a CQNC scheme with an additional cooling beam is minimised with respect to g and g_{cool}. Other fixed plot parameters are given in the caption of Figure 2.21. For comparison, the force noise spectral density of the SQL $\bar{S}_{\hat{\mathcal{F}},\hat{\mathcal{F}}}^{\mathrm{SQL}}$ (blue) and ideal CQNC $\bar{S}_{\hat{\mathcal{F}},\hat{\mathcal{F}}}^{\mathrm{ideal\ CQNC}}$ (black) are shown.

[106] Still assuming $\kappa_{\mathrm{a}} \ll \omega_{\mathrm{m}}$.

[107] Assuming the conditions given in Section 2.6.3.

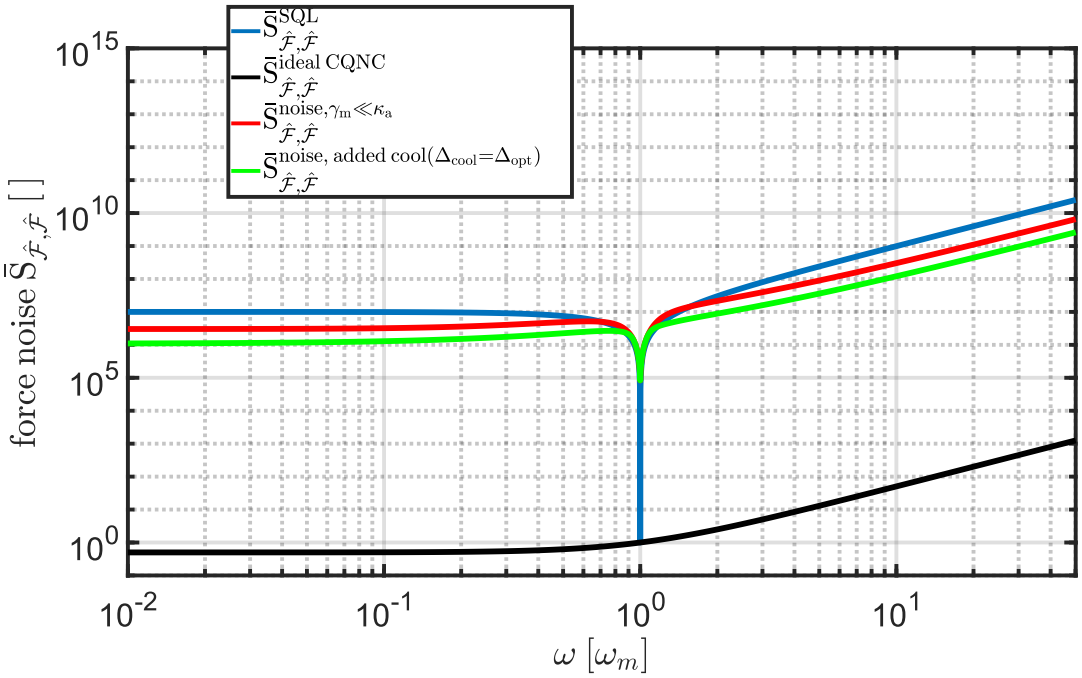

FIGURE 2.21: CQNC performance and SQL: The black line shows the force sensitivity for ideal CQNC $\bar{S}^{\mathrm{add,ideal\ CQNC}}_{\hat{\mathcal{F}},\hat{\mathcal{F}}}$, the blue line the force spectral density $\bar{S}^{\mathrm{SQL}}_{\hat{\mathcal{F}},\hat{\mathcal{F}}}$ of the SQL (Equation (2.172)), and the red line the spectral density $\bar{S}^{\mathrm{noise},\gamma_m \ll \kappa_a}_{\hat{\mathcal{F}},\hat{\mathcal{F}}}$ which is observed if $\gamma_m \ll \kappa_a$ (Equation (2.218)). The green line shows the force spectral density for CQNC with an additional cooling beam $\bar{S}^{\text{noise, added cool}(\Delta_{\mathrm{cool}}=\Delta_{\mathrm{opt}})}_{\hat{\mathcal{F}},\hat{\mathcal{F}}}$ which is minimised with respect to g and g_{cool}.
Used parameters: $g_{\mathrm{DC}} = g_{\mathrm{BS}} = \frac{1}{2}G_{\mathrm{eNMO}}$, $g_{\mathrm{om}} = G_{\mathrm{eNMO}}$,
$\omega_m/(2\pi) = 1.5\,\mathrm{MHz}$, $\gamma_m/(2\pi) = 10^{-7}\omega_m$,
$\kappa_{\mathrm{om}}/(2\pi) = \kappa_c/(2\pi) = 300\,\mathrm{kHz}$, $\kappa_a/(2\pi) = 500\,\mathrm{kHz}$ and $T = 4\,\mathrm{K}$.

Figure 2.21 demonstrates, that an additional cooling beam used in an CQNC experiment can lead to a force sensitivity improvement, as its force spectral density $\bar{S}^{\text{noise, added cool}(\Delta_{\mathrm{cool}}=\Delta_{\mathrm{opt}})}_{\hat{\mathcal{F}},\hat{\mathcal{F}}}$ (green) surpasses the force spectral density $\bar{S}^{\mathrm{noise},\gamma_m \ll \kappa}_{\hat{\mathcal{F}},\hat{\mathcal{F}}}$ (red) accomplished without the additional cooling beam.

A cooling beam supported CQNC scheme only shows an improvement of the sensitivity in the resolved sideband regime, if one restricts the detuning of the cooling beam to $\Delta_{\mathrm{cool}} = \Delta_{\mathrm{opt}}$. A real case study, including losses and no restriction in the detuning Δ_{cool} still remains open. The parameters provided in Table 2.1, proposed by [Sch+22], for a feasible CQNC experiment do not consider the resolved sideband regime. In this case, adding an additional cooling beam does not lead to an improvement in sensitivity.

In the subsequent chapter, the focus lies on examining an optomechanical system specifically tailored for conducting a CQNC experiment. The construction of this optomechanical system is based on the parameters outlined in Table 2.1 (proposed by [Sch+22]).

Part II

Experiment

This part of the thesis is devoted to the experimental generation of shot noise limited light and to the development and its characterisation of an optomechanical system suitable for CQNC. Therefore the experimental part is divided into the two following chapters.

In Chapter 3 the laser light preparation is discussed. Like during the derivations for CQNC (Section 2.6.2), shot noise limited input light and a probe beam independent cooling beam were assumed. The first Section 3.1 of this chapter shows how a shot noise limited probe beam is created, while the second Section 3.2 explains how the independent[108] cooling beam is generated from the shot noise limited probe beam.

In Chapter 4 the centrepiece of this thesis and one of two main features of CQNC[109], namely the optomechanical system will be introduced. This optomechanical system composed of, as already depicted in Figure 2.18, a Fabry-Pérot cavity with a mechanical oscillator between its mirrors. For this reason Section 4.1 gives the theoretical background of silicon nitride (SiN) square membranes as these are used within this thesis as mechanical oscillators. Subsequently in Section 4.2.1 the aforementioned optomechanical system is theoretically investigated. This investigation entails that the SIN membrane within a cavity can be traced back to the canonical[110] optomechanical system depicted in Figure 2.9. The advantage of the membrane between two mirrors with respect to the canonical system, in which one end mirror acts as the optomechanical oscillator, is that the optical and mechanical properties of the mechanical oscillator are separated. In the canonical system the oscillator should have a high reflectivity to enhance the intracavity power and by that the optomechanical coupling strength g[111]. This typically goes in hand with an increase of the mechanical oscillator mass[112], reducing its Q-factor. In the membrane within a cavity scheme the cavity end mirrors ensure a high intracavity field which is coupled to the low reflective and high-Q single layer SiN membrane which represents the mechanical oscillator. Hence in the latter scheme the optical and mechanical properties are separated. It will be shown in Section 4.2.1 that the coupling strength g for the membrane within a cavity is two times higher than in the canonical system if the reflectivity R_m of the membrane is close to one ($R_\mathrm{m} \rightarrow 1$) . Based on the discussion in Section 4.2.1, Section 4.2.2 introduces the designed optomechanical cavity, its requirements and its assembling. Once the assembling is done, the optical properties of the optomechanical cavity, depending on the membrane position within the cavity, are characterised (Section 4.2.3). This characterisation reveals the membrane position at which, for a given input power, the optomechanical coupling strength g is highest.

After setting the membrane closely to this position two measurement principles to deduce the optomechanical coupling strength g, are performed in Section 4.3. First, in Section 4.3.1 the results of the OMIT experiment, for several mechanical resonance frequencies and its corresponding coupling strength g, are shown. For this measurement the MZI theoretically described in Section 2.1.3 was used. Shown

[108] From the probe beam independent.

[109] The other centerpiece of CQNC is the *effective* negative mass oscillator, which experimental investigations are covered in [Ste19].

[110] Canonical - "simplest representative of a class".

[111] From now on the optomechanical coupling strength is denoted by g (in Section 2.6 also $g_\mathrm{om} = g$ was used).

[112] In the beginning a high reflective mechanical oscillator was ensured by a Bragg mirror, a multilayer dielectric mirror, embedded on SiN supporting structure as in [Ste19].

in Section 4.3.1 is how the beam position on the membrane can be inferred from the OMIT measurement. The second measurement principle discussed in 4.3.2 is based on the consequences of dynamical backaction (see Section 2.5). The results presented in section 4.3.2 show the measured mechanical frequency shift $\delta\omega_m$, the effective mechanical linewidth γ_{eff} induced by dynamical backaction and the optomechanical coupling strength g, deduced from this measurements. The dynamical backaction in this measurements was induced by a (second) cooling beam (generated in Section 3.2), whereas the mechanical properties were measured by a probe beam[113].

[113]The probe beam induces no dynamical backaction as it is tuned on resonance. Additionally its power is much weaker compared to the cooling beam power

Chapter 3

Laser light preparation

The derivations and explanations for the CQNC experiment in Section 2.6.2 were based on the assumption of a shot noise-limited input beam. In Section 2.6.4, an additional independent cooling beam was introduced to investigate the CQNC performance under the influence of an in situ changeable effective mechanical linewidth γ_{eff}. Therefore, the origin and generation of these two beams will be discussed in the subsequent sections.

3.1 Laser light and noise

The laser source for all subsequently generated beams is a non-planar ring oscillator (NPRO) (Coherent Mephisto). To be suitable for a CQNC experiment, the amplitude noise of the laser should be dominated by shot noise. For this purpose, the amplitude noise, typically far above shot noise at low frequencies, is suppressed with a double pass filter cavity, depicted in Figure 3.1. This cavity configuration is based on the design rules presented in [MN18].

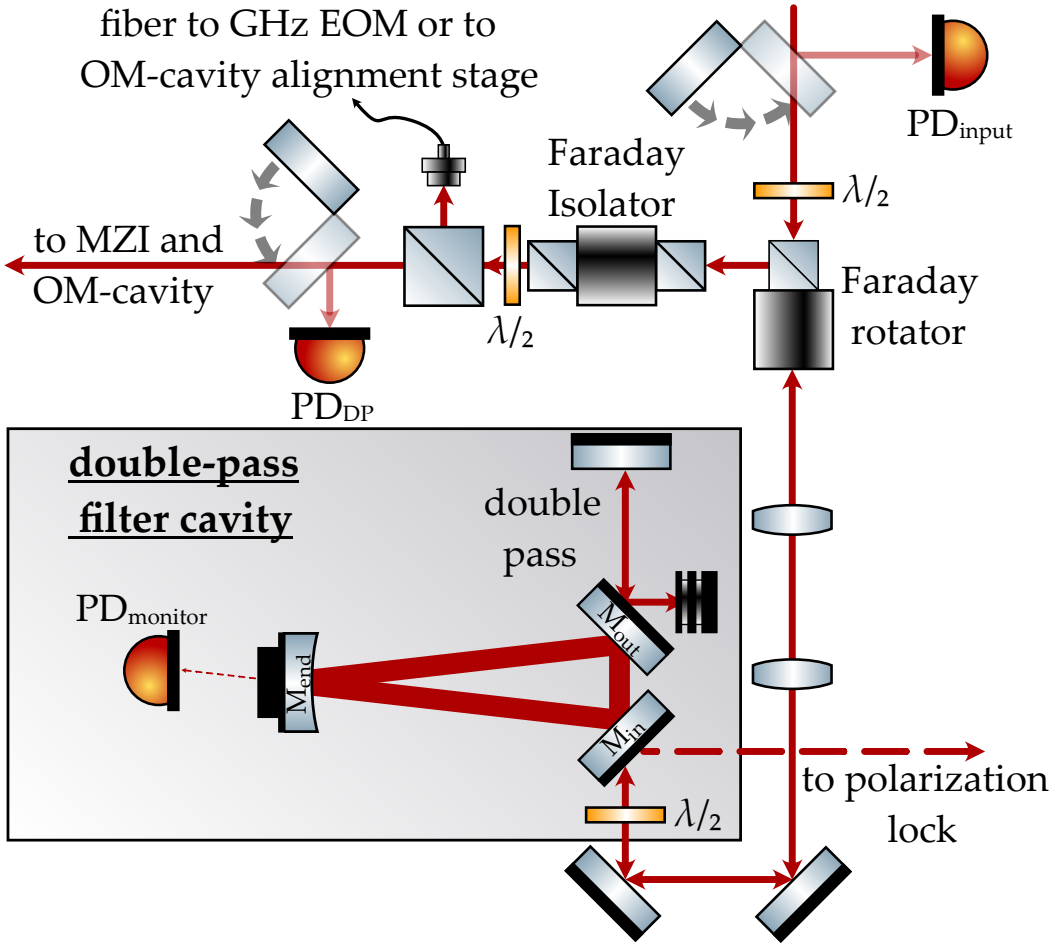

FIGURE 3.1: Schematic of the double-pass filter cavity. Shown are the filter cavity together with a Faraday rotator and Faraday isolator used as a pick of of filtered light and used to prevent damage due to unwanted back-reflections, respectively. Use of other components is explained in main text.

In Figure 3.1 the double-pass filter cavity, together with other components, which will be explained in the following, are shown. Before the linearly polarised light of the laser is send to the filter cavity, it passes through a Faraday rotator which prevents laser damage due to back-reflected light. In addition, the Faraday rotator serves as a pick of for the amplitude noise-suppressed light field originating from the double-pass filter cavity.

The double-pass filter cavity in depicted is a three-mirror triangular cavity that can be treated as a Fabry-Pèrot cavity and hence can be described as a low-pass filter (see Section 2.1.4). In this setup, the filter cavity is locked on resonance ($\Delta = 0$), to ensure that no laser frequency or phase fluctuations will be converted into amplitude noise by the filter cavity. For the lock, a polarisation-based homodyne locking scheme is used [Heu+10; HC80]. On resonance, the corner frequency of the low-pass filter cavity is given by its line width κ_{DP} (see Equation (2.35)). The double-pass configuration is used to enhance the low-pass filter effect and therefore the amplitude noise suppression of the filter cavity. This means that light leaking out of the filter cavity at the output mirror M_{out} is directly sent back into the cavity through this mirror. Hence, the filter cavity is used twice and acts as a second-order low-pass filter. After the light has passed the cavity a second time and leaves through the input mirror M_{input} it reaches the Faraday rotator again, which rotates the linearised

polarisation by 90 deg with respect to the input polarisation. Due to this rotation, the amplitude-filtered light can be separated from the input light. The (from the input light) separated beam is sent through a Faraday isolator before it is split again by a polarisation beam splitter into two paths. One path goes to the optomechanical cavity (OM-cavity). The other path leads to a fiber-coupled GHz electro-optic modulator (GHz-EOM), which output can be connected to an alignment stage for the OM-cavity (Section 4.2.2) or to the cooling beam generation stage (discussed in Section 3.2). To ensure that the amplitude noise filtered light is shot noise (SN) limited at frequencies ω around the mechanical resonance frequency ω_m the filter cavity line width κ_DP has to be as small as possible at low frequencies as the laser amplitude noise is far above shot noise (see Figure 3.2))

The following will discuss the linewidth and other parameters of the filter cavity. Due to the different reflectivities of the double-pass filter cavity mirrors for s- and p-polarised light, the filter cavity exhibits two different cavity line widths $\kappa_\mathrm{DP}^\mathrm{p\text{-}pol}$ and $\kappa_\mathrm{DP}^\mathrm{s\text{-}pol}$. To switch between the resulting low finesse (for p-polarisation) and high finesse (s-polarisation) operation of the cavity, a $\lambda/2$-waveplate is placed (as depicted in Figure 3.1) in front of the input mirror M_in. The exact parameters of the filter cavity and its resulting linewidths κ_DP are summarised in the following Table 3.1.

Parameter	Symbol	Value
Power Reflectivities	$R_\mathrm{in,out}$	s-pol:99.5%, p-pol:99.985%
	R_end	99.995%
Cavity linewidth	$\kappa_\mathrm{DP}^\mathrm{p\text{-}pol}$	1.14 MHz
	$\kappa_\mathrm{DP}^\mathrm{s\text{-}pol}$	40 kHz
Radius of curvature	RoC_end	1 m
Round trip length	L_DP	42 cm
Free Spectral Range	$FSR_{\delta\mathrm{f}}$	357 MHz

TABLE 3.1: Nominal values of the filter cavity.

Apart from the parameters in Table 3.1, the spacer material upon which the mirrors are clamped should be chosen to have low (thermal) length fluctuations ΔL at room temperature. This should be ensured because length fluctuations ΔL of the cavity length L leads to frequency fluctuations Δf given by [Bro99]

$$\Delta f = \frac{\Delta L}{L} f_\mathrm{laser}\,. \tag{3.1}$$

For this reason, the spacer is monolithic and made of Invar[1] which has a relative thermal expansion coefficient of $\alpha_\mathrm{th} \approx 1 \times 10^{-6}\,\mathrm{K}$. Additionally, the spacer is placed on a brass foot with an underlying rubber sheet to suppress the coupling of external vibrations to the cavity.

The resulting relative intensity noise RIN (explained in Appendix C) of the laser before and after passing through the double-pass filter cavity is depicted in Figure 3.2

[1] A nickel–iron alloy.

for p- and s- polarised input light. This relative intensity noise was measured via a direct detection scheme (see Section 2.3.1) in which the photodetector detected 10 mW for all measurements. The same photodiode was used to measure the RIN of the input light at position PD_{input}. In addition, this photodetector measured the double-pass filtered light at position P_{DP}, as depicted in Figure 3.1. The high-pass filtered photodetector[2] output was sent to a signal analyser[3] and in post-processing converted into relative intensity noise RIN. The conversion and how to extract the inferred relative intensity noise for other powers from a RIN measurement at 10 mW is explained in Appendix C.

In Figure 3.2 the RIN measurements are discussed for s- and p-polarised light in Figure 3.2, which reveals that the RIN is suppressed for both input polarisations due to the cavity's second-order low-pass filter characteristic.

[2]High-pass <1 kHz.
[3]Keysight N9010B.

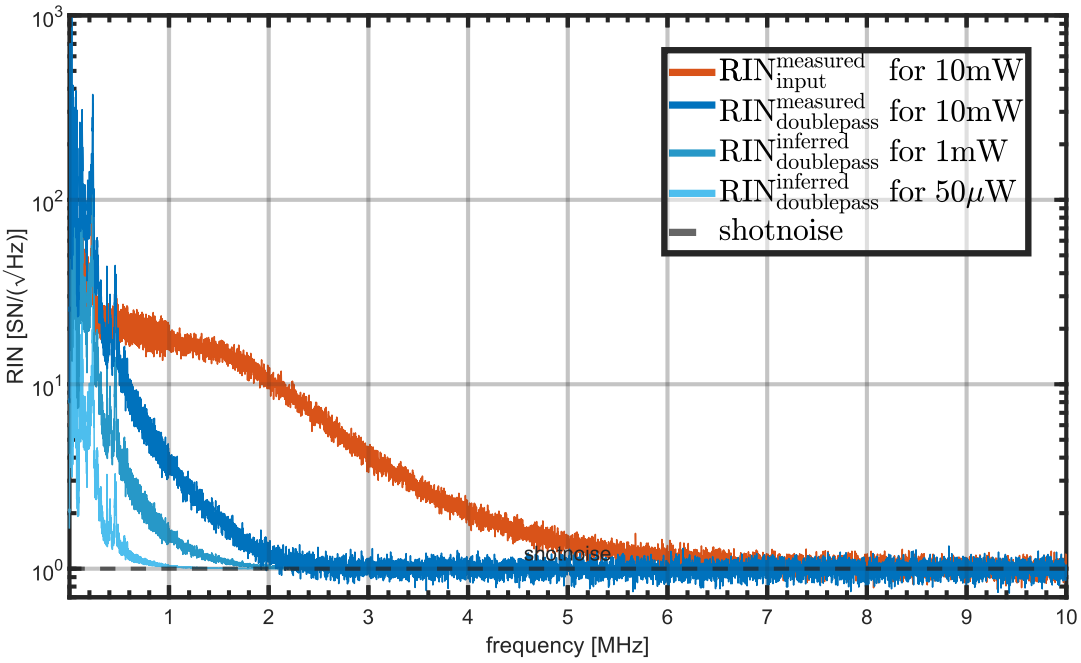

(a) Measured and inferred relative intensity noise RIN for p-polarised light normalised to shot noise (SN).

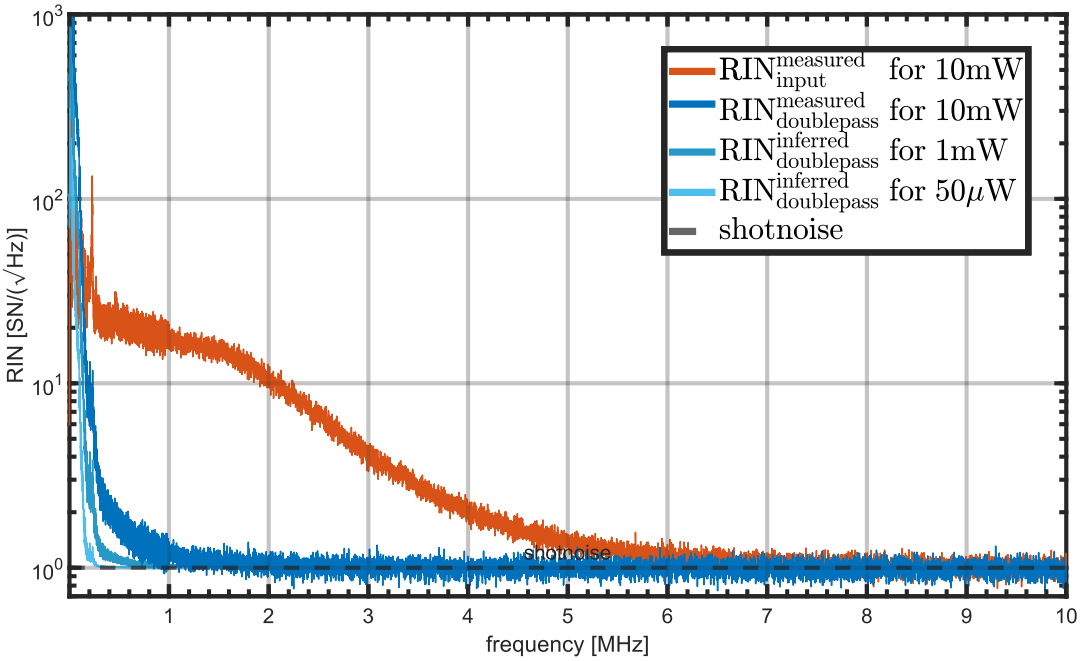

(b) Measured and inferred relative intensity noise RIN for s-polarised light normalised to shot noise (SN).

FIGURE 3.2: Relative intensity noise RIN normalised to shot noise (SN) for s- and p-polarised light (lower and upper plot, respectively).
Relative intensity noise $RIN^{measured}_{input}$ (red) measured in front of the cavity, whereas $RIN^{measured}_{double\ pass}$ was measured after the light passed twice through the filter cavity.
For both measurements the detected power was 10 mW.

Comparing the measured RIN for s- and p-polarised light (Figure 3.2b and 3.2a) reveals that the shot noise SN is reached at lower frequencies ω by using s-polarised light. This is expected considering the smaller line width of the double-pass filter cavity for s-polarised light ($\kappa^{s\text{-pol}}_{DP} \ll \kappa^{p\text{-pol}}_{DP}$) given in Table 3.1. Unfortunately, for

both polarisations, the amplitude noise below 200 kHz is increased with respect to the input amplitude fluctuations. One reason for this might be that the cavity is not perfectly locked on resonance. Hence, minor frequency or phase input fluctuations are converted by the filter cavity into amplitude fluctuations[4]. However, Figure 3.2b reveals that for a light power of 1 mW the shot noise level is reached for ≈ 1 MHz, whereas for 50 µW the shot noise is reached at ≈ 400 kHz. This is a good achievement because the s-polarised double-pass filtered beam can be used for the implementation of a CQNC experiment. It might be beneficial to investigate the origin[5] of the excess noise to suppress this or to pre-suppress the amplitude laser noise by an active feedback control to the laser.

Before discussing the optomechanical system and its characterisation in Chapter 4, the generation of a cooling beam will be explained in the following. This beam is used for the optical characterisation of the optomechanical system in Section 4.2.3, and in Section 4.3.2 to induce dynamical backaction.

3.2 Two color scheme

In Section 2.6.4, the CQNC scheme with an additional cooling beam was introduced. Therefore, this section will discuss the generation of this cooling beam, which will be used in the experiment described in Section 4.3.2, to induce dynamical backaction. The setup for the cooling beam generation is depicted in Figure 3.3.

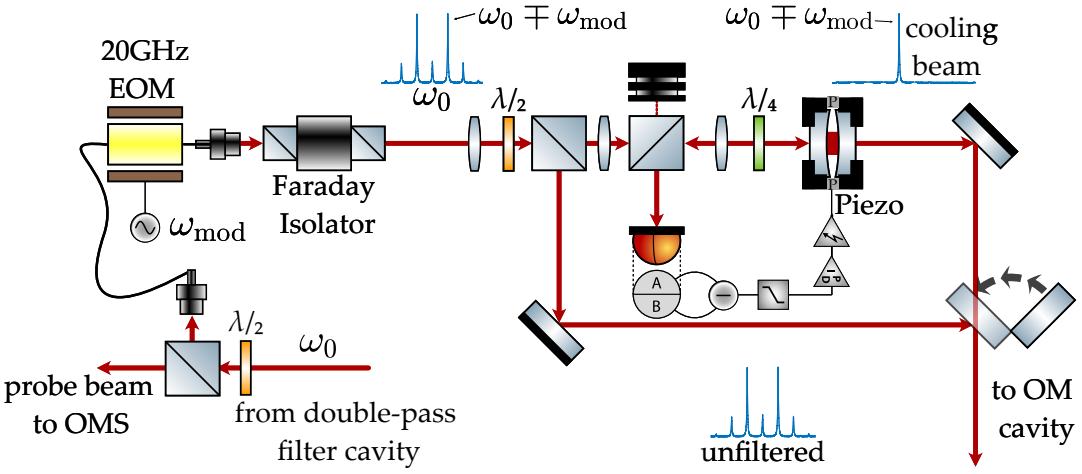

FIGURE 3.3: Setup used to generate a beam that is solely oscillating at frequency $\omega_0 \pm \omega_{mod}$. A portion of the beam coming from the double-pass filter cavity is phase modulated by a fiber-coupled GHz electro-optic modulator (GHz-EOM). The phase-modulated beam is sent to a cavity that transmits one sideband, if it is locked to the sideband frequency. The cavity lock is established by a modulation free tilt lock [SGM99].
The phase-modulated beam can bypass the filter cavity and can be sent (with all sidebands) for characterisation and calibration purposes to the optomechanical system (OMS).

[4]Coupling of input phase quadrature fluctuations Y_{in} and the amplitude quadrature fluctuations X_{om} for $\Delta \neq 0$ for an optical cavity ($g = 0$) can be inferred from intracavity field equations (see Equation 2.115c).

[5]Excess noise can steam from input laser frequency or phase fluctuations or it is induced by the filter cavity due to vibrations or a slight off-resonant lock $\Delta \neq 0$.

In Figure 3.3, one part of the light with frequency ω_0 coming from the double-pass filter cavity (Section 3.1) is sent to the optomechanical system, whereas the other part is sent to a fiber-coupled GHz electro-optic modulator (GHz-EOM). This GHz-EOM generates (by phase-modulation), depending on the modulation depth β, $m(m \in N)$ sidebands at frequency $\omega_0 \pm m \cdot \omega_{\mathrm{mod}}$ (see 2.1.1). The phase-modulated beam passes through a Faraday isolator[6] and is split into two paths by a polarisation beam splitter (PBS) in conjunction with a $\lambda/2$-wave plate. In reflection of the PBS, the unfiltered phase-modulated beam is sent directly to the optomechanical system (OMS) and is used for optical characterisation and calibration of the optomechanical system and its components[7]. In transmission of the PBS, the phase-modulated beam is sent to a linear filter cavity. This cavity separates the different phase-modulated sidebands by transmitting one phase-modulated sideband and reflecting the carrier and other sidebands.

The parameters of the filter cavity, which are partly determined in the following[8], are given in Table 3.2.

Parameter	Symbol	Value
Power Reflectivities	$R_{\mathrm{in,out}}$	$\approx$99.04%
Cavity linewidth	κ_{cool}	(119.69 ± 2.45) MHz
Radius of curvature[9]	$RoC_{\mathrm{in,out}}$	25 mm
Free Spectral Range	$FSR_{\delta\nu}$	38.84 GHz
Cavity length	L_{cool}	3.86 mm

TABLE 3.2: Parameters of the filter cavity for the cooling beam. All parameters are deduced by measurements explained in this section, except the radius of curvature RoC, which are given by the manufacturer.

The linear filter cavity is constructed with two equal (spherical) mirrors clamped from different sides to the same piezoelectric actuator, as depicted in Figure 3.4. The cavity length L is linearly changed to address different resonant frequencies by applying a ramp voltage to the piezoelectric actuator. As the length of the cavity defines its resonant frequency, the sidebands of frequencies $\omega_0 \pm \omega_{\mathrm{mod}}$ are resonant at different cavity lengths. This effect is observed by measuring the power transmitted through the cavity over time using a photodiode.

The subsequent description explains the measurement of the cavity's Free Spectral Range (FSR) and linewidth κ_{cool} of the filter cavity. These measurement principles are later also used in Section 4.2.3 to characterise the optomechanical system's FSR and linewidth κ. To extract the $FSR_{\delta\nu}$ of the cavity, the fiber-coupled GHz-EOM was driven at a frequency of $\omega_{\mathrm{mod}} = 9$ GHz with a high modulation depth β which resulted in second-order sidebands at $\omega_0 \pm 2\omega_{\mathrm{mod}}$ appearing. In Figure 3.4, a modulation frequency of $\omega_{\mathrm{mod}} = 9$ GHz has been used to emphasize that the lower and upper sideband of $\pm 2\omega_{\mathrm{mod}}$ of two consecutive resonant carrier frequencies ω_0 are almost overlapping. As introduced in Section 2.1.4, the distance between two consecutive resonances of an unmodulated beam is given by $FSR_{\delta\nu} = \frac{c}{2L}$. Hence, the Free

[6] Used to prevent back-reflections.

[7] Used to measure the linewidth and resonance frequency for different membrane positions and to calibrate piezo movements (see Section 4.2.3).

[8] Like the FSR and the cavity linewidth.

[9] The input (in) and output (out) mirror have the same radius of curvature, i.e. $RoC_{\mathrm{in}} = RoC_{\mathrm{out}} = RoC_{\mathrm{in,out}}$.

Spectral Range ($FSR_{\delta\nu}$) of the cavity is deduced from the frequency $\omega_{\text{mod}}^{\text{overlap}}$ at which the l-th-order sidebands of two consecutive resonant carrier frequencies overlap. The relationship between the $FSR\delta\nu$ and $\omega_{\text{mod}}^{\text{overlap}}$ is given by

$$FSR_{\delta\nu} = l \cdot \omega_{\text{mod}}^{\text{overlap}} . \tag{3.2}$$

Here, $FSR_{\delta\nu}$ represents the frequency difference between two consecutive resonant carrier frequencies, and $\omega_{\text{mod}}^{\text{overlap}}$ is the GHz-EOM driving frequency at which the l-th-order sidebands overlap. For the filter cavity, the second-order sideband $(l = 2)$ was overlapping at a frequency of $\omega_{\text{mod}} = 9.7\,\text{GHz}$, yielding $FSR_{\delta\nu}^{\text{cool}} = 38.8\,\text{GHz}$ (Equation (3.2)). This corresponds to a cavity length of 3.86 mm. One could also measure the $FSR_{\delta\nu}$ by overlapping the first-order sideband. However, the highest usable modulation frequency for the fiber-based EOM is specified to 20 GHz at which the used signal generator could not apply a suitable modulation depth.

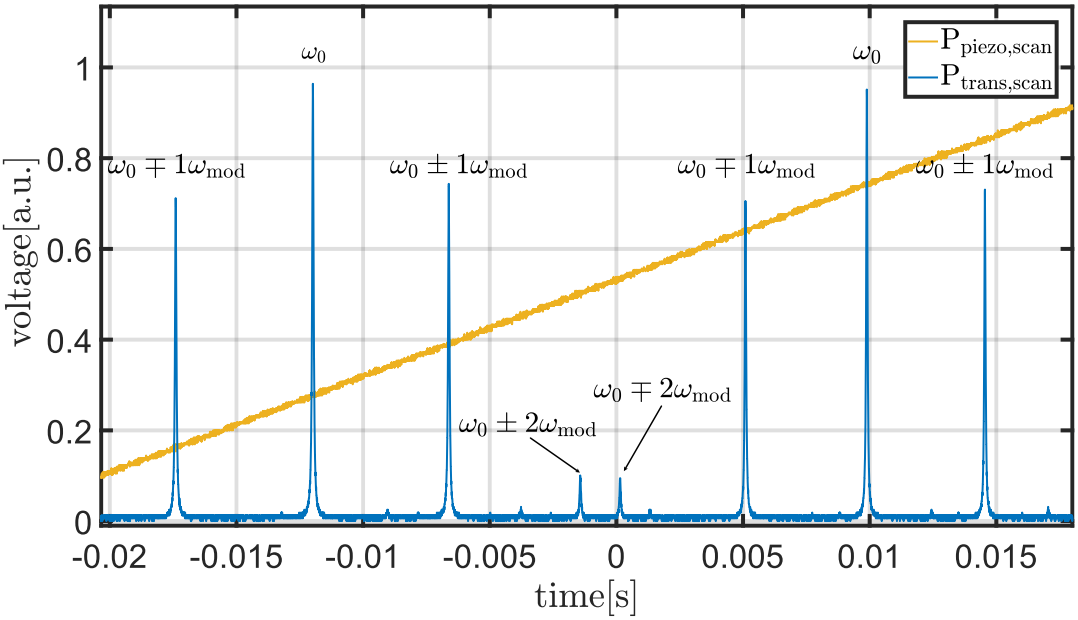

FIGURE 3.4: Measured transmitted power P_{trans} behind the linearly scanned cavity. The input beam is phase modulated with a frequency of $\omega_{\text{mod}} = 9.7\,\text{GHz}$. The $FSR_{\delta\nu}$ can be deduced from the overlap of upper and lower sidebands.

In the next Figure 3.5 a small modulation depth β at a modulation frequency $\omega_{\text{mod}} = 1\,\text{GHz}$ is used to extract the linewidth of the cavity, while the cavity length is changed linearly in time via the piezoelectric actuator.

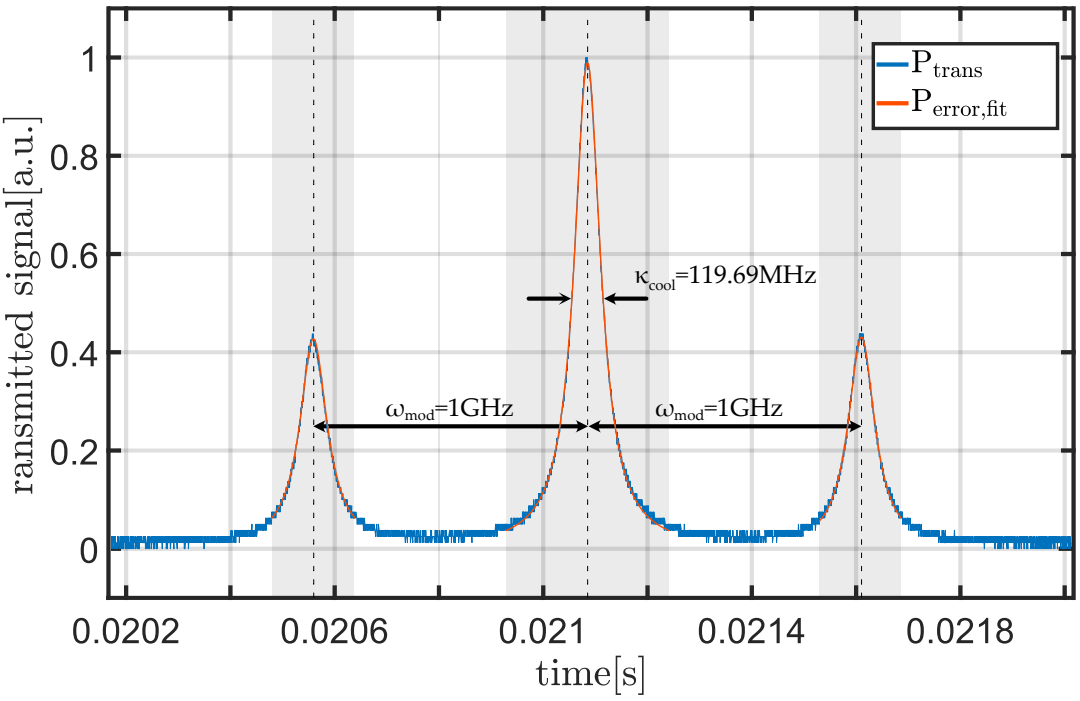

FIGURE 3.5: Measured transmitted power P_{trans} of phase modulated input behind the linearly scanned cavity. The modulation frequency of the input beam is $\omega_{\text{mod}} = 1\,\text{GHz}$. With the distance in frequency of the side-bands to the carrier the time axis is calibrated to a frequency axis. A Lorentzian fit to the data in the grey shaded area is used to extract the linewidth $\kappa_{\text{cool}} = (119.69 \pm 0.04)\,\text{MHz}$.

The resonances appearing at $\omega_0 \pm 1\,\text{GHz}$ are used to calibrate the time axis into frequency units. From a Lorentzian fit to the three resonances based on Equation (2.35) the linewidth was calculated as $\kappa_{\text{cool}} = (119.69 \pm 0.04)\,\text{MHz}$, where the error is given by the standard deviation.

Figure 3.6 shows the power of the sidebands measured by a photodetector in transmission and their corresponding error signals. This measurement is used to explain how one sideband is separated from the carrier and other sidebands. The error signal was generated with a tilt locking technique described in [SGM99]. The advantage of this scheme is that it is modulation free. In contrast, the disadvantage is that a slight misalignment of the input beam to the cavity axis, leading to spatial higher-order modes, is needed.

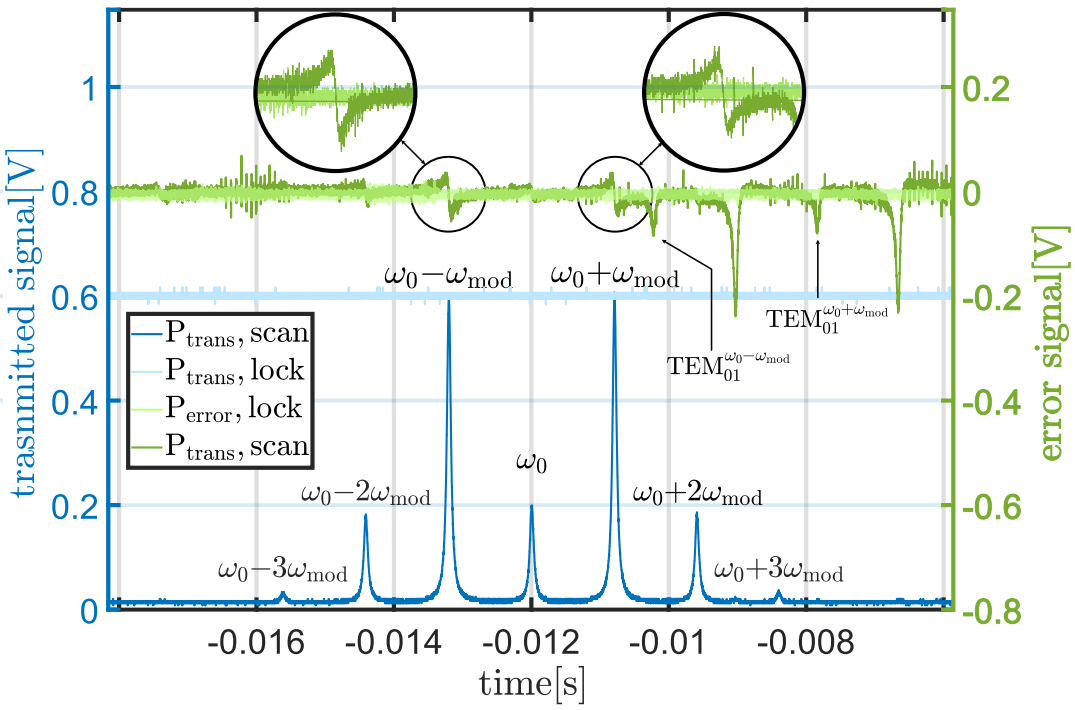

FIGURE 3.6: Measured transmitted power P_{trans} and reflected error signal P_{error} of a phase modulated input beam, while the cavity was linearly scanned (scan) or locked (lock). The input beam was phase modulated at a frequency of $\omega_{\mathrm{mod}} = 3\,\mathrm{GHz}$ and a modulation depth of $\beta \approx 1.8$. Also visible are higher order modes (TEM_{01}).

The aforementioned misalignment introduces a feature visible in the error signal[10] because the cavity decomposes the input field into the spatial TEM_{00} and TEM_{01}-mode. Using the values given in Table 3.2 the frequency difference of the $TEM_{01}^{\omega_0 \pm n\cdot\omega_{\mathrm{mod}}}$ to its corresponding carrier $TEM_{00}^{\omega_0 \pm n\cdot\omega_{\mathrm{mod}}}$ with frequency is calculated by [Bon+16]

$$\Delta TEM_{00\to 01} = \frac{\arccos(1 - \frac{L_{\mathrm{cool}}}{RoC_{\mathrm{in,out}}})}{\pi} FSR_{\delta\nu} = 6.96\,\mathrm{GHz}\,. \tag{3.3}$$

Other features visible in the scanned error signal are probably due to a mode mismatch. Ultimately, the cavity could be locked to a sideband with frequency $\omega_0 \pm \omega_{\mathrm{mod}}$. Figure 3.6 reveals that once the cavity is locked to one first-order sideband, for example with frequency $\omega + \omega_{\mathrm{mod}}$, only this sideband is transmitted. In contrast, the cavity reflects all other sidebands and higher-order spatial modes. Hence, in transmission, a beam solely oscillating with frequency $\omega_0 + \omega_{\mathrm{mod}}$ is isolated.

At a modulation frequency of $\omega_{\mathrm{mod}} = \frac{1}{2}\Delta TEM_{00\to 01}$ the higher order mode $TEM_{01}^{\omega_0-\omega_{\mathrm{mod}}}$ will overlap with the sideband at $\omega_0 + \omega_{\mathrm{mod}}$. In the experiment in Section 4.3.2 a modulation frequency of $\omega_{\mathrm{mod}} \approx 3.1\,\mathrm{GHz} \pm 30\,\mathrm{MHz}$ is needed.Based on Figure 3.6, using a modulation frequency $\omega_{\mathrm{mod}} \approx 3.1\,\mathrm{GHz} \pm 30\,\mathrm{MHz}$ is not problematic, as at this modulation frequency no sidebands or spatial modes overlap with each other.

Before using the discussed cooling beam, first, the mechanical oscillator (Section 4.1) and the optomechanical system (Section 4.2), described by a Fabry-Pèrot cavity with the mechanical oscillator in it will, be discussed.

[10] Of course it also visible in the transmitted power if one would zoom in.

Chapter 4

Optomechancial Setup

This chapter discusses the optomechanical system (OMS), described by a mechanical oscillator placed inside a Fabry-Pérot cavity[1]. This work uses a silicon nitride membrane embedded in a silicon frame (depicted in Figure 4.1) as a mechanical oscillator. The OMS is also called a membrane-at-the-edge system (MatE), as the membrane is placed close to one end mirror of the Fabry-Pérot cavity. Because a silicon nitride membrane is used as a mechanical oscillator, its mechanical oscillator properties, such as its mechanical resonance frequencies and quality factors, are described in Section 4.1.

Subsequently, in Section 4.2.1, it is shown how the membrane position x_{m} within the cavity alters the optical properties of the MatE system and how the optomechanical coupling strength $g \propto \frac{\partial \omega_{\mathrm{MatE}}}{\partial x_{\mathrm{m}}}$ is derived for this setup.

This description is followed by the actual design and adjustment procedure of the MatE-system described in Section 4.2.2. Afterwards, in Section 4.2.3, the measured optical properties of the MatE-system are presented. The membrane position with the highest coupling strength g is inferred from these measurements.

Finally, the optomechanical coupling strength g is measured utilising two independent experiments. Firstly, the coupling strength g is determined in 4.3.1 using an OMIT experiment, and secondly in Section 4.3.2 with an experiment using consequences of dynamical backaction (see Section 2.5).

4.1 Micro mechanical oscillators

The following sections will discuss the mechanical properties of the SiN membrane in use. The discussion starts with introducing the mechanical resonance frequencies and their displacement pattern (Section 4.1.1), followed by the description of the quality factor Q and the loss channels that limit the quality factor (Section 4.1.2).

4.1.1 Resonance frequencies and mode pattern of square membranes

In this thesis, the mechanical oscillator is a commercially available silicon nitride square membrane on top of a silicon (Si) supporting frame[2], which is shown together with a schematic of the top and side view, in Figure 4.1.

[1] Different to Figure 2.9, in that the mechanical oscillator is the output coupler of a Fabry-Pérot cavity.
[2] From Norcada Inc: www.norcada.com.

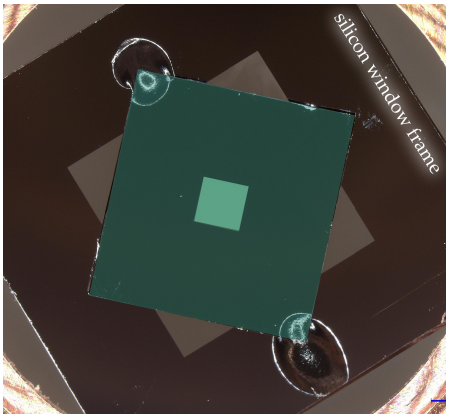

(a) Microscope picture of the utilised membrane. The bright green area illustrates the SiN membrane on top of the Si substrate. The Si substrate is glued to an additional silicon window frame clamped to a copper holder.

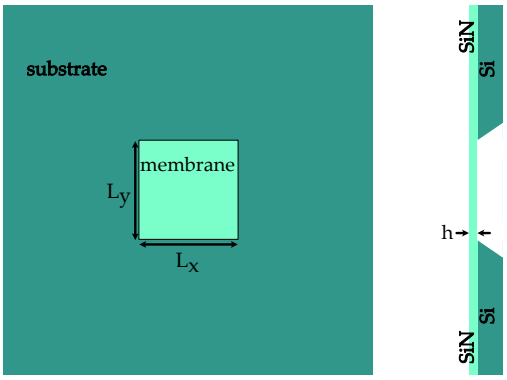

(b) Schematic top and side view of the SiN-membrane on top of a Si substrate. L_{text} and L_y denote the SiN-membrane sidelength and h the thickness of the SiN-membrane.

FIGURE 4.1: a) Photograph of the SiN-membrane and b) its schematic side and top view.

The shown membrane has a thickness of $h = 50\,\text{nm}$ and an approximate area of $1\,\text{mm} \times 1\,\text{mm}$. The substrate, where the membrane rests, is $500\,\mu\text{m}$ thick and measures $5\,\text{mm} \times 5\,\text{mm}$ in width.

The out-of-plane motion $u(x, y, t)$ of the rectangular membrane in the x-y plane is governed by the two-dimensional wave equation [SVR16].

$$\sigma \nabla^2 u - \rho \frac{\partial^2 u}{\partial t^2} = 0\,, \tag{4.1}$$

with σ being the tensile stress and ρ the mass density. As the membrane is fixed to the silicon frame, its zero displacements at the edges are used as the boundary condition. With this boundary condition the eigenfrequencies $\omega_{m,n}$ and their corresponding mode patterns are calculated as

$$u_{m,n}(x, y, t) = a_{m,n} \cos(\omega_{m,n} t) \sin(m\pi \frac{x}{L_x}) \sin(n\pi \frac{y}{L_y}) \tag{4.2}$$

$$\omega_{m,n} = \pi \sqrt{\frac{\sigma}{\rho} \left(\frac{m^2}{L_x^2} + \frac{n^2}{L_y^2} \right)}\,, \tag{4.3}$$

with L_x and L_y describing the side length of the membrane (see Figure 4.1b).

In Figure 4.2, the derived membrane mode patterns of different resonance frequencies $\omega_{m,n}$ are depicted and reveal that the mode index m and n are associated with the number of anti-nodes along their corresponding axis[3].

[3] According to Equation 4.2 m corresponds to the x- and n to y-axis.

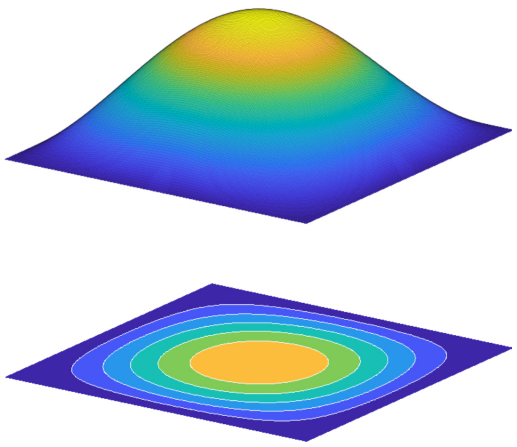

(a) Square membrane mode shapes of the (1,1)-membrane mode.

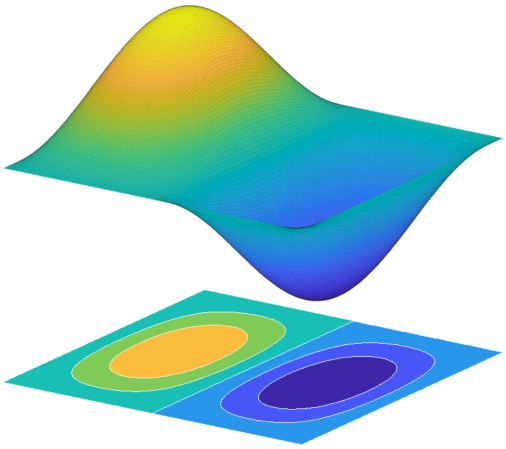

(b) Square membrane mode shapes of the (1,2)-membrane mode.

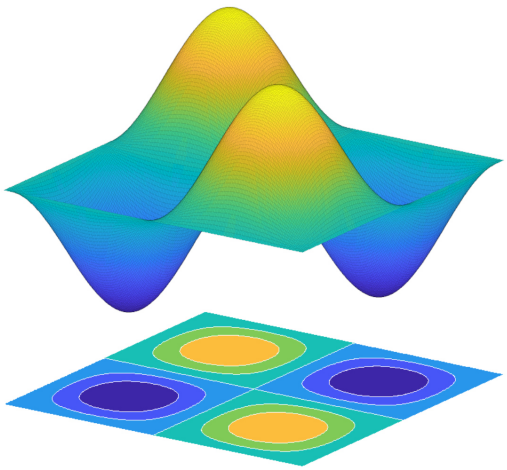

(c) Square membrane mode shapes of the (2,2)-membrane mode.

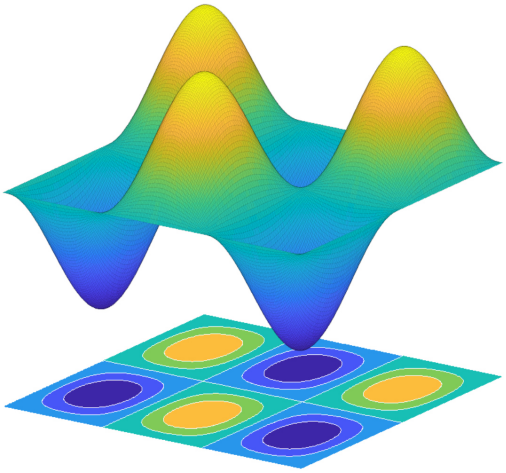

(d) Square membrane mode shapes of the (2,3)-membrane mode.

FIGURE 4.2: Square Membrane mode shapes $u_{\mathrm{m,n}}(x, y, t = \frac{2\pi}{\omega_{\mathrm{m,n}}})$ of four different resonance frequencies $\omega_{\mathrm{m,n}}$.

For the special case of a square membrane $L_{\mathrm{x}} = L_{\mathrm{y}} = L$ the eigenfrequencies are given by

$$\omega_{\mathrm{m,n}} = \omega_{1,1}\sqrt{\frac{m^2+n^2}{2}}\,. \tag{4.4}$$

A closer investigation shows that for a perfectly symmetric square membrane, two different mode shapes share the same eigenfrequency $\omega_{\mathrm{m,n}}$[4]. In this situation, the eigenfrequencies are called degenerate. In reality, perfect square membranes do not exist. This is taken into account by expressing $L_{\mathrm{x}} = L(1+\frac{\delta x}{2})$ and $L_{\mathrm{y}} = L(1-\frac{\delta x}{2})$ with $|\delta x| \ll 1$. With this an approximated solution for the eigenfrequency is calculated as [Hen22]

$$\omega_{\mathrm{m,n}} \approx \omega_{1,1}\sqrt{\frac{m^2+n^2}{2}}\left(1+\frac{m^2-n^2}{2(m^2+n^2)}|\delta x|\right)\,. \tag{4.5}$$

Equation (4.5) entails that the degeneracy of the eigenfrequencies is broken for a small side length difference ($|\delta x| \ll 1$). This degeneracy is also observed in the

[4]For example, the $\omega_{1,2} = \omega_{2,1}$, whereas $u_{1,2}(x, y, t) \neq u_{2,1}(x, y, t)$.

measurement discussed in Section 4.3.1 as the utilised membrane is not perfectly square.
For completeness, the effective mass of the membrane mode is introduced in the following. The effective mass of the membrane mode m_{eff} is derived by calculating the potential energy E_{pot} of the oscillating membrane as

$$E_{\mathrm{pot}} = \frac{1}{2}\omega_{\mathrm{m,n}}^2 \int u(x,y,t)dV \tag{4.6}$$

$$= \frac{1}{2}\underbrace{\frac{\rho L_{\mathrm{x}} L_{\mathrm{y}} h}{4}}_{m_{\mathrm{eff}}} \omega_{\mathrm{m,n}}^2 u^2(t)\,. \tag{4.7}$$

Comparing Equation (4.7) with the solution of a one-dimensional oscillator[5] reveals that the effective mass m_{eff} is independent of the mode shape and resonance frequency:

$$m_{\mathrm{eff}} = \frac{\rho L_{\mathrm{x}} L_{\mathrm{y}} h}{4} = \frac{m_{\mathrm{phys}}}{4}\,. \tag{4.8}$$

Here m_{phys} describes the physical mass of the membrane. Care has to be taken, as this result is only valid for a rectangular mode shape. In contrast, for other membrane topologies (e.g., circular membranes [SVR16]), the effective mass m_{eff} is, in general, not independent of the mode pattern and its resonance frequency.

4.1.2 Quality factor of square membranes

In order to conduct quantum optomechanical experiments, mechanical oscillators must possess high Q-factors to isolate them from the thermal environment. Mainly, achieving high Q-factors is essential since parameters of the optomechanical system must satisfy the quantum cooperativity ($C_{\mathrm{qba}} \propto Q \gg 1$) condition (as indicated in Equation (2.168)), to enable successful experimentation of quantum effects. For this reason, this section is devoted to investigate loss channels described by Q^{-1}, which effectively degrade the quality factor Q. In general, the quality factor Q is written as the sum of its dissipation mechanism obeying the equation [SVR16]

$$\frac{1}{Q} = \frac{1}{Q_{\mathrm{gas}}} + \frac{1}{Q_{\mathrm{clamping}}} + \frac{1}{Q_{\mathrm{intr}}} + \dots\,. \tag{4.9}$$

For membranes, the dissipation mechanisms denoted in Equation 4.9 are the main limiting contributions and will be discussed in the following. So, in the context of this thesis, only a small excerpt of the theory on quality factors is given. For more details, [Tsa19] and [SVR16] are highly recommended.

Gas damping loss

One of the most dominant external loss mechanisms arises under atmospheric pressure due to gas damping. Gas damping appears due to the interaction of gas molecules with the membrane. Therefore the experimental setup is placed in a vacuum environment at a pressure P of 10^{-7} mbar. This pressure is associated with the so-called ballistic regime [SVR16]. The ballistic regime is characterised by the fact that individual gas molecules do not interact with each other but only through elastic collisions with the membrane. Following [Bia+06; SVR16], the loss mechanism due to

[5] $E_{\mathrm{pot}} = \frac{1}{2}m\omega_{\mathrm{m}}^2$

gas damping is described by

$$Q_{\mathrm{gas}}^{-1} = \left[\frac{\rho h \omega_{\mathrm{m,n}}}{4}\sqrt{\frac{\pi}{2}}\sqrt{\frac{RT}{M_{\mathrm{m}}}}\frac{1}{P}\right]^{-1}, \tag{4.10}$$

where R is the gas constant, T the temperature in Kelvin and M_{m} the molar mass of the gas molecules. In Equation (4.10), the so-called squeeze-film damping is neglected. This effect describes air being squeezed out between the mechanical oscillator and a nearby surface due to the oscillator's motion. However, the presented experiments are not done within the boundary of squeeze-film damping, as the membrane is placed far enough away from other objects. Hence, the squeeze-film damping can be neglected. A rough estimation reveals that for experiments accomplished within this thesis, gas damping is not a dominating loss mechanism, as for $\omega_{\mathrm{m,n}} \approx 1\,\mathrm{MHz}$, $T = 300\,\mathrm{K}$ and $h = 100\,\mathrm{nm}$ the resulting Q factor Q_{gas} is in the order of 1×10^9.

Clamping loss

Clamping loss arises due to the loss of elastic energy from the membrane into its support structure. In literature different names for clamping loss, all describing the same loss mechanics, exist. These names are anchor loss, radiation loss, mounting loss, and phonon tunneling loss [Tsa19].
An equation describing the clamping loss of a general mechanical oscillator topology with resonance frequency ω_{res} is given by [WR+11; Tsa19]

$$\frac{1}{Q_{\mathrm{clamping}}} = \frac{\pi}{2\rho_{\mathrm{s}} 2\rho_{\mathrm{res}}\omega_{\mathrm{res}}^3}\int_{\mathrm{q}}\left|\int_{\mathrm{S}} d\bar{S}\cdot(\sigma_{\mathrm{q}}^{(0)}\cdot\bar{u}'_{\mathrm{res}} - \sigma'_{\mathrm{res}}\cdot\bar{u}_{\mathrm{q}}^{(0)})\right|^2 \delta(\omega_{\mathrm{res}} - \omega(q))\,, \tag{4.11}$$

where σ_{res}, u_{res} and ρ_{res} describes the stress, the displacement field and density of the resonator, whereas σ_{q}, u_{q} and ρ_{q} correspond to the substrate. In addition, $\omega(q)$ is the eigenfrequency of a corresponding substrate spatial mode, while ω_{res} describes the resonator eigenfrequency.

For a square membrane, Equation (4.11) can be solved analytically by assuming a coupling of membranes mode with free modes of a semi-infinite substrate. In this case, the clamping loss arises due to the coupling of substrate and membrane modes and is given for a semi-infinite substrate as [SVR16]

$$Q_{\mathrm{clamping}} \approx 1.5\frac{\rho_{\mathrm{s}}}{\rho_{\mathrm{res}}}\eta^3\frac{n^2m^2}{(n^2+m^2)^{\frac{3}{2}}}\frac{L}{h} \tag{4.12}$$

with the acoustic mismatch η between the substrate and resonator

$$\eta = \sqrt{\frac{E_{\mathrm{q}}\rho_{\mathrm{r}}}{\rho_{\mathrm{s}}\sigma}}\,. \tag{4.13}$$

Here E_{q} is the Young modulus of the substrate. The assumption of a semi-infinite structure is valid as the substrate is usually much larger than the membrane[6].

For the SiN membranes used in this thesis, the clamping loss is a significant contribution that limits the membrane quality factor Q. The Si chip on which the membrane is embedded was glued to an additional silicon window frame to ensure

[6] In a simulation software like ComSol, a semi-infinite structure can be modeled by a so-called perfectly matched layer (PML).

outside vibrations are coupled less to the membrane. Of course, this is a naive approach. A further sophisticated approach would rely on finding a topology that minimises the loss mechanism given in Equation (4.11). One of these topologies is a phonic bandgap crystal. In this topology, investigated in [Yu+14], the membrane is embedded in the middle of a silicon support structure that acts as a band gap for acoustic waves. Due to this bandgap, the coupling between membrane and non-membrane modes of the support structure is suppressed within a particular frequency band. Hence a specific membrane mode can be isolated from clamping losses.

Intrinsic loss

Intrinsic losses are generated by several loss mechanisms, such as thermal elastic damping [LR00] and phonon-phonon interaction. These and other loss mechanisms contributing are described in [SVR16; Tsa19].

However, these and other loss mechanisms associated with intrinsic loss will not be mentioned in the following as a phenomenological description [VS14] leads to a more compact equation for intrinsic loss.

For the description in [VS14], the quality factors of membranes with different sizes have been investigated. The results are, that the intrinsic loss Q_{intr}^{-1} can be divided into surface loss Q_{surf}^{-1} and volume loss Q_{vol}^{-1}, yielding

$$Q_{\text{intr}}^{-1} = Q_{\text{surf}}^{-1}(h) + Q_{\text{vol}}^{-1} \tag{4.14}$$

$$= (\alpha \cdot h)^{-1} + Q^{-}1_{\text{vol}}\,. \tag{4.15}$$

with $\alpha = (6 \pm 4) \times 10^{10}\,\text{m}^{-1}$ and $Q_{\text{vol}} = 28000 \pm 2000$ [VS14]. Due to the phenomenological investigation, the error bars are relatively large. Finally, as the name suggests, eliminating their source cannot reduce intrinsic losses. However, intrinsic losses can still be diluted, which is discussed next. Based on this dilution, the quality factor of a membrane reaches higher values than the intrinsic damping suggests.

Dissipation dilution

The stored versus lost energy ratio per oscillation describes the most general form of the quality factor Q. Therefore, the basic principle of dissipation dilution is to enhance the quality factor by introducing a conservative energy W_{i}[7], which is discussed in the following. In the most general form, the intrinsic quality factor Q_{intr} is given by

$$Q_{\text{intr}} = \sum_i \frac{W_i}{\Delta W_i} = \frac{W_{\text{bend}} + W_{\text{elong}}}{\Delta W_{\text{bend}} + \Delta W_{\text{elong}}}\,, \tag{4.16}$$

with W_i and ΔW_i describing the total stored energy and the dissipated energy associated with a process i. In this case, the processes are explicitly given as elongation and bending of the membrane during its motion. Hence, W_{elong} and ΔW_{elong} describe the stored and dissipated energy associated with the elongation of the membrane, and W_{bend} and ΔW_{bend} describe the stored and dissipated energy associated with bending of the membrane. Hence, a high tensile stress of the membrane is desirable, as the stored energy W_{tensil} is increased. For the membrane, this tensile stress arises due to the pre-stress of the membrane during the manufacturing process, as after depositing the SiN membrane on top of the Si substrate, the materials contract differently during

[7] Conservative energy describes the energy with no associated dissipation channel ($\Delta W_{\text{conservative}} = 0$).

cooldown [PM19]. Due to this different contraction, the membrane is pre-stressed, and a purely conservative energy term arises due to the higher tensile stress (first measured by [Ver+06]).

In theory the quality factor Q_{dilution} with the purely conservative stored energy W_{stress} reads [SVR16; Tsa19]

$$Q_{\text{dilution}} = \frac{W_{\text{tensile}} + W_{\text{bend}} + W_{\text{elong}}}{\Delta W_{\text{bend}} + \Delta W_{\text{elong}}} \tag{4.17}$$

$$= D_{\text{Q}} Q_{\text{intr}}\,, \tag{4.18}$$

where the dissipation dilution factor is defined as

$$D_{\text{Q}} = (1 + \frac{W_{\text{tensile}}}{W_{\text{bend}} + W_{\text{elong}}})\,. \tag{4.19}$$

Equation (4.17) reveals that for high tensile energy ($W_{\text{tensile}} \gg W_{\text{bend}}, W_{\text{elong}}$), the intrinsic noise is not reduced but diluted, by the added conservative energy term W_{tensile} [Cat22].

For a membrane, the dilution factor can be calculated as [SVR16]

$$D_{\text{Q}} = \left[\underbrace{\frac{\pi^2(n^2+m^2)}{12}\frac{E}{\sigma}\left(\frac{h}{L}\right)^2}_{\text{sine shape}} + \underbrace{\frac{1}{\sqrt{3}}\sqrt{\frac{E}{\sigma}\frac{h}{L}}}_{\text{edge shape}} \right]^{-1}. \tag{4.20}$$

A detailed investigation of equation (4.20) reveals that the dilution factor is limited by losses induced at the clamping point (edge). The reason is that at the edges, the mean curvature is higher than the ideal sinusoidal mode shape (Equation (4.2))), which is visualised in Figure 4.3.

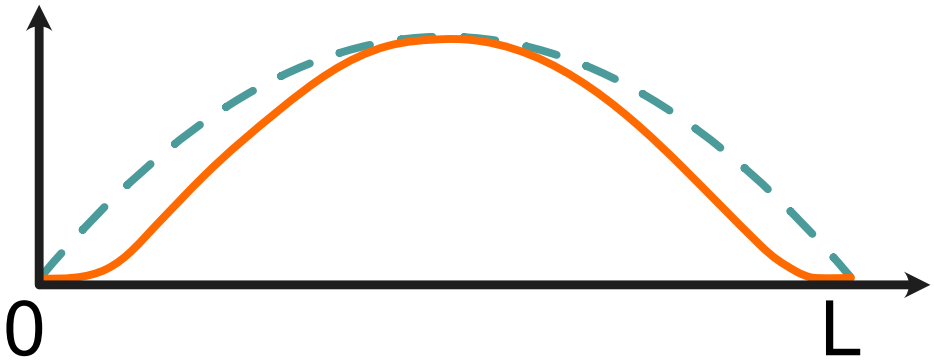

FIGURE 4.3: Ideal sinusoidal mode curvature of the fundamental mode of a square a membrane (grey dashed) together with the corresponding real curvature caused by bending (orange).

Hence, the dilution factor (see Equation (4.19)) [Tsa19; Cat22] is limited by bending loss ΔW_{bend}, which is described by the bending of the membrane at its edges.

The findings introduced in this Section 4.1.2 have been the motivation for the fabrication of so-called soft clamp membranes [Tsa19; Tsa+17]. For soft clamp membranes, the bending at the oscillating mode is reduced to enhance the dilution factor and, thus, the quality factor. Also, the soft clamp membrane mode is highly stressed

to boost the dilution factor D_Q even more. Additionally, a phononic bandgap further isolates the membrane mode from the outside and hence reduces clamping loss. With that strategy, optomechanical oscillators with a Q-factor of 10^9 were reached at a resonance frequency of $\omega_{res} = 1.135\,\mathrm{MHz}$ [Mas+19].

Within this thesis, the membranes show a quality factor of $Q \approx 5 \times 10^5$ and thus, even at 4 K, will be dominated by thermal and not by quantum backaction noise, as $C_{qba} \not> 1$. However, the SiN membranes are an excellent choice to characterise and investigate the optomechanical system concerning its stability and workability at 4 K. Once an optomechanical system with high stability and workability is established, devices with higher quality factors, e.g., other membrane topologies, can be used. Based on this, the next chapter introduces the optomechanical system and its assembling strategy.

4.2 Optomechanical cavity

4.2.1 Membrane at the Edge

The optomechanical setup used in this thesis is a Membrane at the edge (MatE) system, where a SiN membrane is positioned close to one end mirror. This configuration is based on the membrane in the middle (MiM) setup, first investigated in [Jay+08]. Both systems' theoretical description and comparison can be found in [Dum+19]. However, the subsequent discussion solely focuses on the MatE system utilised throughout this thesis.

More specifically, this section aims to establish the relationship between the resonance frequency ω_{MatE} of the MatE system and the membrane position x_m. Since the optomechanical coupling strength g depends on the derivative $\frac{\partial \omega_{MatE}}{\partial x_m}$ (Equation (2.112)), the membrane position x_m at which the highest optomechanical coupling occurs can be inferred from the function $\omega_{MatE}(x_m)$. Thus, the function $\omega_{MatE}(x_m)$ is derived in the following, based on the principle sketch of the MatE system depicted in Figure 4.4.

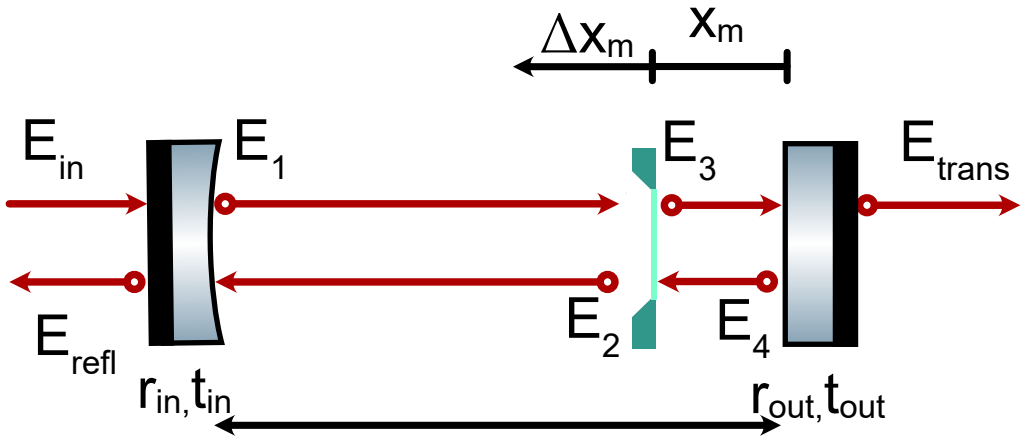

FIGURE 4.4: Principle layout of a MatE system consisting of two mirrors with power reflectivity R_i and transmissivity T_i. The distance between the mirrors is given by the length L, whereas x_m denotes the distance between the output mirror, and Δx_m a movement of the membrane.

As depicted in Figure 4.4 the MatE-system consists of an input mirror and an output mirror with amplitude reflectivity $r_{\text{in,out}}$ and transmissivity $t_{\text{in,out}}$. The distance between these end mirrors is denoted as L. In between these mirrors, a SiN-membrane (Section 4.1) is located close to the output mirror. The distance between the output mirror and the membrane is defined in the following as

$$x'_{\text{m}} = x_{\text{m}} + \Delta x_{\text{m}}\,, \tag{4.21}$$

where Δx_{m} describes the membrane displacement around its initial position x_{m}. Also as seen in Figure 4.4 the distance between the membrane and the output mirror is small compared to the cavity length L ($x'_{\text{m}} \ll L$). It is important to note, that a change in L does **not** alter the distance x'_{m} between the membrane and the output mirror. The distance x'_{m} is solely changed by moving the membrane by Δx_{m}, not the output coupler. Furthermore, the membrane is characterised as a dielectric slab with reflectivity r_{m} and transmissivity t_{m}, which is given by [Jay+08]

$$r_{\text{m}} = |r_{\text{m}}|^{i\phi_{\text{r}}} = \frac{(n^2-1)\sin(knh)}{2in\cos(knh) + (n^2+1)\sin(knh)}\,, \tag{4.22}$$

$$t_{\text{m}} = |t_{\text{m}}|^{i\phi_{\text{t}}} = \frac{2n}{2in\cos(knh) + (n^2+1)\sin(knh)}\,. \tag{4.23}$$

Here n is the index of refraction, h the thickness of the membrane, $k = \frac{2\pi}{\lambda}$[8] the wave vector of the light, ϕ_{r} the phase of the complex reflectivity r_{m} and ϕ_{t} the phase of the transmissivity, respectively. Together with this, the electric field in Figure 4.4 is given by

$$E_1 = it_{\text{in}}E_{\text{in}} + r_{\text{in}}E_2 e^{ik(L-x'_{\text{m}})} \tag{4.24a}$$

$$E_2 = ir_{\text{m}}E_{\text{in}}e^{ik(L-x'_{\text{m}})} + it_{\text{m}}E_4 e^{ikx'_{\text{m}}} \tag{4.24b}$$

$$E_3 = it_{\text{m}}E_1 e^{ik(L-x'_{\text{m}})} + r_{\text{m}}E_4 e^{ikx'_{\text{m}}} \tag{4.24c}$$

$$E_4 = r_{\text{out}}E_3 e^{ikx'_{\text{m}}} \tag{4.24d}$$

$$E_{\text{refl}} = it_{\text{in}}E_2 e^{ik(L-x'_{\text{m}})} + r_{\text{in}}E_{\text{in}} \tag{4.24e}$$

$$E_{\text{trans}} = it_{\text{out}}E_3 e^{ikx'_{\text{m}}}\,. \tag{4.24f}$$

From these equations the transmitted field E_{trans} is calculated as

$$E_{\text{trans}} = \frac{it_{\text{in}}t_{\text{m}}t_{\text{out}}}{e^{-ikL} - r_{\text{m}}\left(r_{\text{in}}e^{ik(L-2x'_{\text{m}})} + r_{\text{out}}e^{-ik(L-2x'_{\text{m}})}\right) + \left(r_{\text{m}}^2 + t_{\text{m}}^2\right)r_{\text{in}}r_{\text{out}}e^{ikL}}E_{\text{in}}\,. \tag{4.25}$$

As in the case of a non-single-sided Fabry-Pèrot cavity ($t_{\text{in}}, t_{\text{out}} > 0$), the resonance condition for the MatE system is satisfied when the power in the transmission reaches its maximum (also assuming $t_{\text{m}} > 0$). This condition is fulfilled if the denominator of Equation (4.25) is minimal. An approximate solution for this condition is derived assuming $r_{\text{in,out}} \to 1$ and a lossless membrane with $|r_{\text{m}}|^2 + |t_{\text{m}}|^2 = 1$[9] [Dum+19] and reads

$$\cos(2kL + \phi_{\text{r}}) + |r_{\text{m}}|\cos(2kx'_{\text{m}} - kL) = 0\,, \tag{4.26}$$

[8] λ is the wavelenght of the light

[9] Also $r_{\text{m}} = |r_{\text{m}}e^{i\phi_{\text{r}}}|$, $t_{\text{m}} = |t_{\text{m}}e^{i\phi_{\text{t}}}|$, $r_{\text{m}}t^*_{\text{m}} = -r^*_{\text{m}}t_{\text{m}}$ and $e^{2i(\phi_{\text{r}}-\phi_{\text{t}})} = -1$ [Dum+19].

with ϕ_r being the complex phase of the membrane reflectivity r_m. This equation is transformed to

$$\tan(kL) = \frac{\cos(\phi_r) + |r_m| \cos(2kx'_m)}{\sin(\phi_r) - |r_m| \sin(2kx'_m)} \tag{4.27}$$

which will be further approximated in the following.

For a cavity length $L \gg \lambda$ and considering that the membrane only changes the resonant wave vector $k_N = N\frac{\pi}{L}$[10] by a small amount Δk, the wavector k is expressed as [Dum+19]

$$k = k_N + \Delta k\,. \tag{4.28}$$

Also, kx'_m is further approximated, as the membrane is positioned close to the output mirror ($x'_m \ll \frac{L}{2}$), by

$$kx'_m = k_N x'_m + \Delta k x'_m \approx x'_m k_N\,. \tag{4.29}$$

Inserting Equation (4.29) into Equation (4.27) and solving for k results in the resonance condition expressed as

$$k = k_N + \Delta k = k_N + \frac{1}{L} \arctan\left[\frac{\cos(\phi_r) + |r_m| \cos(2k_N x'_m)}{\sin(\phi_r) - |r_m| \sin(2k_N x'_m)}\right], \tag{4.30}$$

where c is the speed of light. In terms of frequency Equation (4.30) is expressed as[11]

$$\omega_{MatE} = 2\pi N \cdot FSR_\nu + \frac{c}{L} \arctan\left[\frac{\cos(\phi_r) + |r_m| \cos(2k_N x'_m)}{\sin(\phi_r) - |r_m| \sin(2k_N x'_m)}\right]. \tag{4.31}$$

Equation (4.31) shows that the resonance frequency ω_{MatE} of the MatE system depends on the membrane position x_m. This dependency of the resonance frequency over membrane position is shown in Figure 4.5. In this figure, the membrane was displaced from its initial position x'_m to a new position $x_m + \Delta x_m$. Therefore the x-axis is denoted as Δx_m.

[10] $L = N\lambda/2$.

[11] $ck = \omega$ and $FSR_\nu = \frac{c}{2L}$.

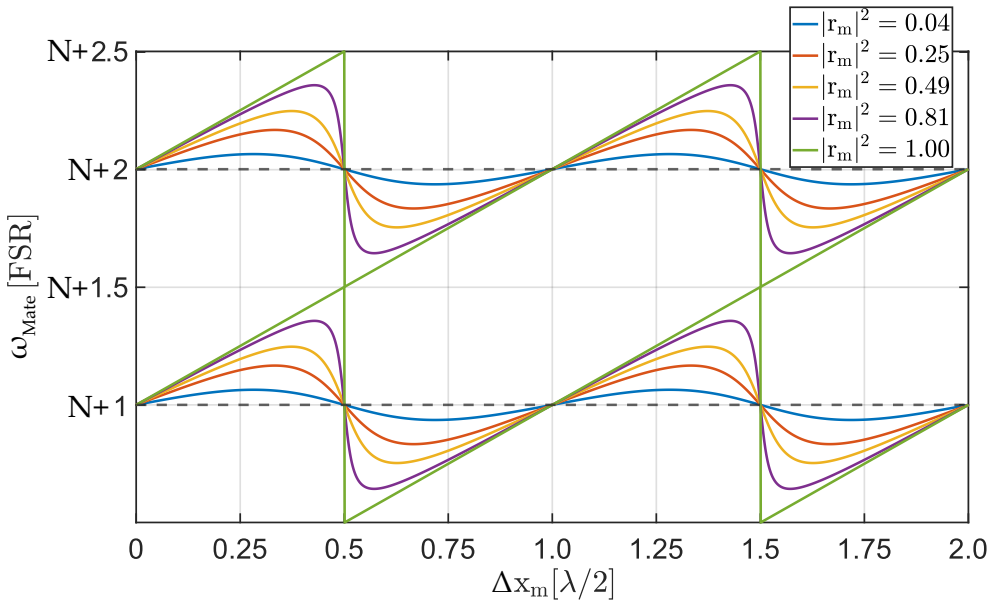

FIGURE 4.5: Resonant condition (Equation (4.31)) for the in Figure 4.4 depicted membrane at the edge system for different membrane reflectivities r_{m}. The initial membrane position x_{m} is change by Δx_{m} ($x'_{\mathrm{m}} = x_{\mathrm{m}} + \Delta x_{\mathrm{m}}$). For simplicity the phase ϕ_{r} in Equation (4.31) is set to zero.

Figure 4.5 and Equation (4.31) reveal that the resonance frequency ω_{MatE} of the MatE system depends on the membrane position, while the membrane reflectivity r_{m} defines how strong this dependency is. From Equation (4.31) the frequency change of ω_{MatE} depends on x_{m} and is given by [Dum+19]

$$\frac{\partial \omega_{\mathrm{MatE}}}{\partial x_{\mathrm{m}}} = \frac{2k_{\mathrm{N}}}{\pi} 2\pi FSR_{\nu} \frac{|r_{\mathrm{m}}|^2 + |r_{\mathrm{m}}|\cos(2k_{\mathrm{N}}x_{\mathrm{m}} + \phi_{\mathrm{r}})}{|r_{\mathrm{m}}|^2 + 2|r_{\mathrm{m}}|\cos(2k_{\mathrm{N}}x_{\mathrm{m}} + \phi_{\mathrm{r}}) + 1} \tag{4.32}$$

with $FSR_{\nu} = \frac{c}{2L}$.
As mentioned earlier, the optomechanical coupling strength g depends on the derivative $\frac{\partial \omega_{\mathrm{MatE}}}{\partial x'_{\mathrm{m}}}$ (Equation (2.112)). By investigating Figure 4.5 one can deduce the position x'_{m} for which the derivative $\frac{\partial \omega_{\mathrm{MatE}}}{\partial x'_{\mathrm{m}}}$ is highest from the position at which the slope is highest. This specific position is given in Figure 4.5 at $\Delta x_{\mathrm{m}} = 0.5\lambda/2$ and $\Delta x_{\mathrm{m}} = 1.5\lambda/2$. Since the derivations of the MatE system were primarily theoretical, the next chapter is dedicated to providing a more intuitive description of the relationship between the resonance frequency ω_{MatE} and the membrane position x_{m}. In the following intuitive explanation, it will also become apparent that the membrane is dissipatively coupled to the cavity light field. The cavity line width κ_{MatE} is influenced by the membrane position x_{m}. On the other hand, the previously introduced dependency of the resonance frequency ω_{MatE} on the membrane position x_{m} is referred to as dispersive coupling.

4.2.1.1 Intuitive description of MatE system

The intuitive description is based on describing the membrane and the output mirror as a sub-cavity. As depicted in Figure 4.6*a*, this sub-cavity is also denoted as a compound mirror[12].

[12] Due to its smaller length

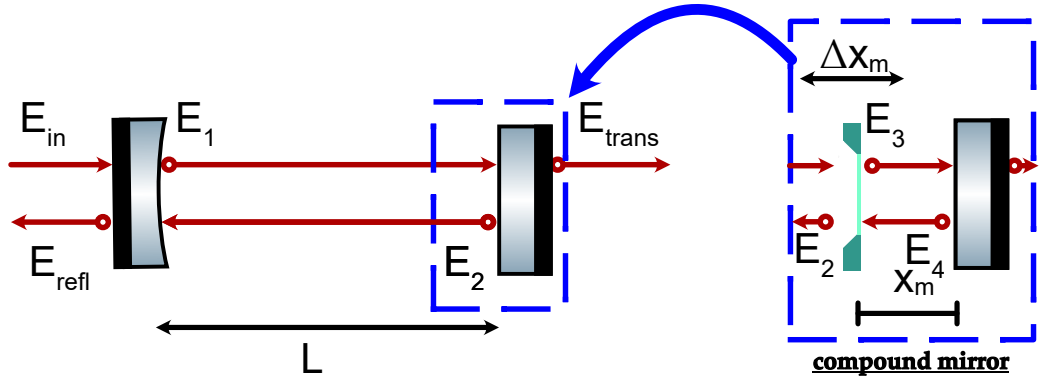

(a) The MatE system depicted in Figure 2.2 transformed to a canonical Fabry-Pèrot cavity by describing the membrane and output mirror as a compound mirror

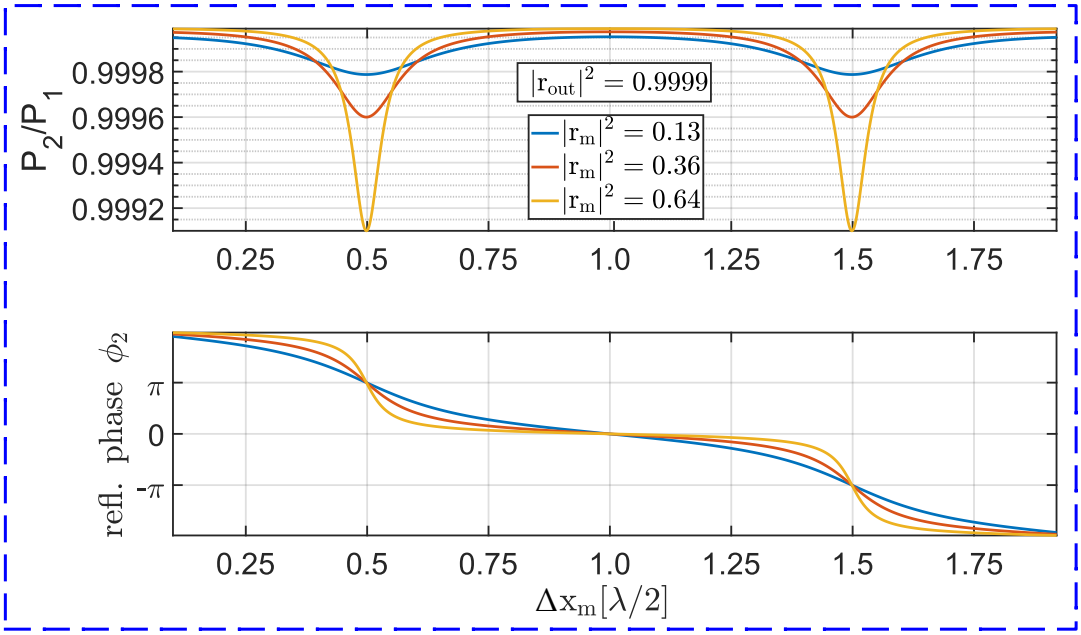

(b) Dependency of compound Mirror reflectivity $P_2/P1 = (|E_2|^2/|E_1|^2)$ and phase response ϕ_2 on membrane position Δx_m.

FIGURE 4.6: a) MatE system transformed to a canonical Fabry-Pèrot cavity by using a compound mirror and b) compound mirror reflectivity $P_2/P1$ and phase response.

By introducing the compound mirror, the MatE system can be effectively treated as a Fabry-Pérot cavity composed of the input mirror and the compound mirror. Also, as in the previous Figure 4.4, one should keep in mind that a change of the mirror distance L does **not** alter the length x_m between the membrane and the output mirror.

4.2.1.2 Dissipative coupling

The compound mirror reflectivity $R_\mathrm{compound}(x'_\mathrm{m}) = \frac{P_2}{P_1} = \frac{|E_2|^2}{|E_1|^2}$ ($E_{1,2}$ are depicted in Figure 4.6a) depends on the distance $x'_\mathrm{m} = x_\mathrm{m} + \Delta x_\mathrm{m}$ between the membrane and the output mirror, as the compound mirror can also be described by a Fabry-Pèrot cavity (see Figure 4.6b). Thereby, the line width κ_MatE of a lossless MatE system can be expressed with the transmissivity T_in of the input mirror (analogous to Equation

(2.30)) as

$$\kappa_{\mathrm{MatE}}(x'_{\mathrm{m}}) = \frac{T_{\mathrm{in}} + T_{\mathrm{compound}}(x'_{\mathrm{m}})}{\tau_{\mathrm{RT}}} \tag{4.33}$$

$$= \frac{T_{\mathrm{in}} + (1 - R_{\mathrm{compound}}(x_{\mathrm{m}}))}{\tau_{\mathrm{RT}}} . \tag{4.34}$$

Here τ_{RT} describes the round trip time between the compound and the input mirror. The exact expression of κ_{Mate} based on the compound mirror description can be found in [Dum+19]

$$\kappa_{\mathrm{MatE}} = \frac{(1 - |r_{\mathrm{m}}^2|)c|t_{\mathrm{in}}|^2 + (1 + 2|r_{\mathrm{m}}|\cos(2kx\mathrm{m} + \phi_{\mathrm{r}}) + |r_{\mathrm{m}}|^2)c|t_{\mathrm{out}}|^2}{2x'_{\mathrm{m}}(1 - |r_{\mathrm{m}}^2|) + 2(Lx'_{\mathrm{m}})(1 + 2|r_{\mathrm{m}}|\cos(2kx'_{\mathrm{m}} + \phi_{\mathrm{r}}) + |r_{\mathrm{m}}|^2)} . \tag{4.35}$$

Equation (4.33) and (4.35) reveal that the cavity linewidth κ_{MatE} depends on the membrane position, which is denoted as dissipative coupling.

4.2.1.3 Dispersive coupling

With reference to the phase response ϕ_2 depicted in Figure 4.6b, an explanation for the dispersive coupling (the perturbation of ω_{MatE} due to the membrane position x_{m}) will be given. First, it is important to note that the resonance frequency of an empty, non-single-sided Fabry-Pèrot cavity corresponds to the cavity length at which the intracavity power and hence the transmitted power are maximised (see Figure 2.6 or [Bon+16]).
Alternatively, the resonance condition is defined based on the phase relationship between the intra-cavity field E_1 (as described in Section 2.1.4) and the input field E_{input}, resulting in ϕ_1 being equal to $N \cdot 2\pi$, where N is an integer[13]. Considering that the compound mirror induces a membrane position-dependent phase shift ϕ_2 of its reflected field E_2 (see Figure 4.6b), it becomes evident that the resonance condition $\phi_1 = N \cdot 2\pi$ relies on the membrane position x'_{m}. When the compound mirror alters the phase ϕ_2 of its reflected light, the cavity length L must adjust accordingly to satisfy the resonance condition $\phi_1 = N \cdot 2\pi$[14]. Due to the non-linear relationship between the phase shift ϕ_2 and the membrane position x'_{m}, the resulting resonance frequency ω_{MatE} also exhibits a non-linear dependence on x'_{m} (refer to Figure 4.5). Additionally, Figure 4.5 indicates that the highest resonance frequency change $\frac{\partial \omega_{\mathrm{MatE}}}{\partial x'_{\mathrm{m}}}$ occurs when the compound mirror is on resonance ($\Delta x_{\mathrm{m}} = 0.5\frac{\lambda}{2}$). This is sensible as the response of reflected phase ϕ_2 of the compound mirror is also steepest at this membrane position.
For the CQNC experiment (Section 2.6), a suggested coupling strength of $g = 500\,\mathrm{kHz}$ is desired (see Table 2.1). To achieve this, the membrane should ideally be placed at a position where $\frac{\partial \omega_{\mathrm{MatE}}}{\partial x'_{\mathrm{m}}}$ and hence the optomechanical coupling strength g are maximised. However, directly accessing the frequency ω_{MatE} in the experiments is not possible. The reason is that only the input and output mirror positions are movable, while the absolute membrane position remains fixed at $\Delta x_{\mathrm{m}} = 0$ to avoid noise coupling directly to the membrane. To overcome these constraints and deduce the resonance frequency ω_{MatE} over x_{m}, a relative membrane position variation is

[13] For resonance, the phase of the light after completing one round trip must match the input field [Bon+16].

[14] This adjustment can be achieved by moving either the compound mirror or the input mirror since changing L does **not** affect x'_{m} (see Figure 4.6a).

employed by moving the input and output mirrors. The details of this approach are explained in the following section.

4.2.1.4 Deducing the resonance frequency in an experiment

Different from the setup in Figure 4.4, the membrane position x_m is fixed in MatE system utilised within this thesis. Only the position of the input mirror and the output mirror can be changed. The position change of the input and output mirror is denoted as Δx_{in} and Δx_{out} respectively, whereas distance L between the unaltered input and the output mirror is defined as

$$L = x_{out} - x_{in} \,. \tag{4.36}$$

Hence a lenght difference ΔL is described by

$$\Delta L = \Delta x_{out} - \Delta x_{in} \,. \tag{4.37}$$

Figure 4.7 shows a sketch of the in the experiments used MatE-system, in that also the distance are visualised. The Figure reveals that the membrane moves relatively towards to input coupler if the input and output mirror position is changed by the same amount $\Delta x_{in} = \Delta x_{out}$. In this case, the membrane position changes relatively to the input mirrors by

$$\Delta x_m = -\Delta x_{in} \,. \tag{4.38}$$

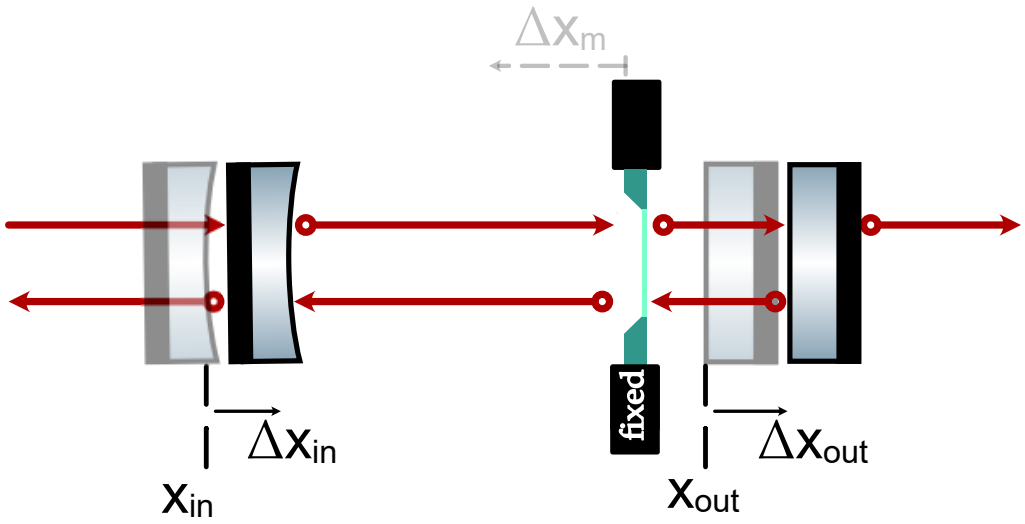

FIGURE 4.7: Sketch of the experimental realised MatE system. Different to the setup in Figure 2.2 the absolute membrane position is fixed. The membrane is relatively moved with Δx_m by moving the input and the output mirror. As in Figure 2.2 the input mirror is also moveable.

The relations, given in Equation (4.37) and (4.38) will be used later. First, a simulation of the transmitted power of a MatE system depicted in Figure 4.8 will be investigated. In Figure 4.8a the transmitted power $P_{trans}(\Delta x_{in}, \Delta x_{out})$ for the setup depicted in Figure 4.7 is shown for different position changes Δx_{out} and Δx_{in}. Whereas Figure 4.8b shows the simulated transmitted power over the swept input position Δx_{in} for a fixed output coupler position $\Delta x_{out} = \frac{3}{4}\frac{\lambda}{2}$ (indicated by red dashed line in Figure 4.8a)).

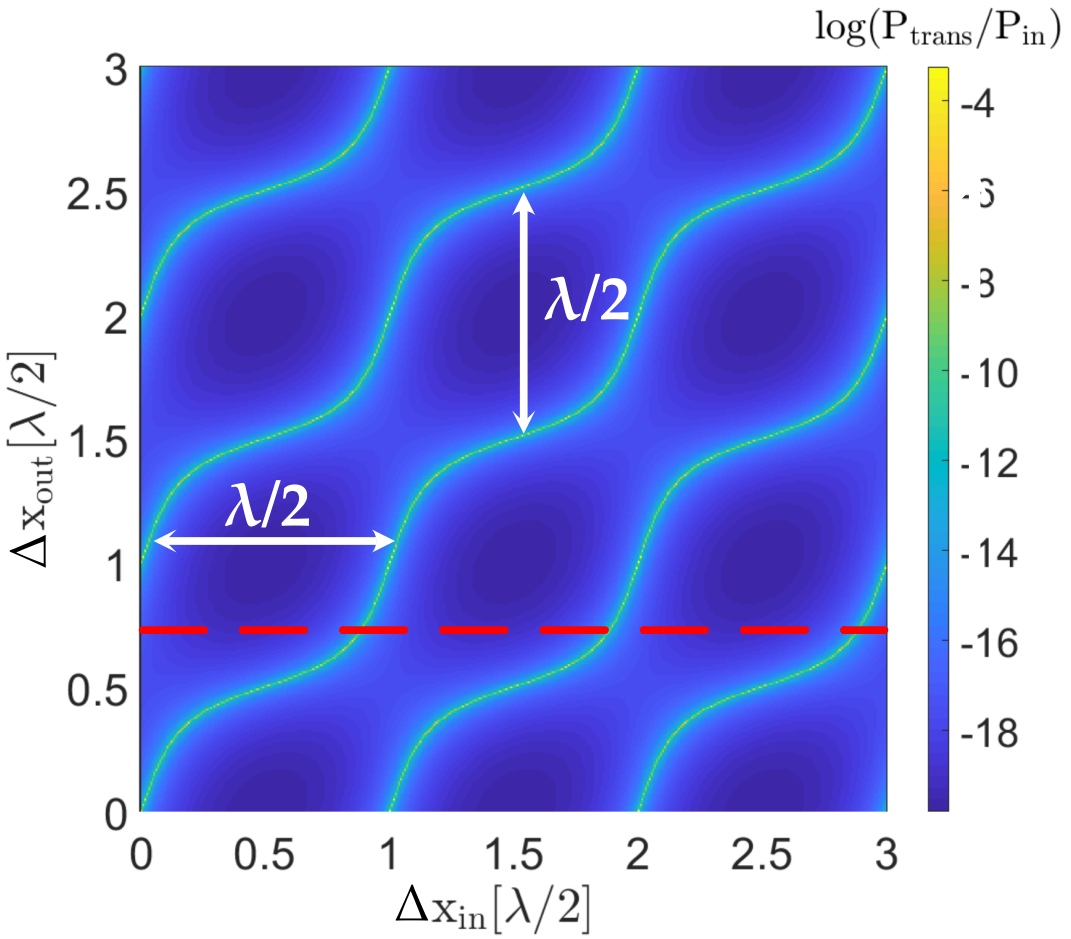

(a)

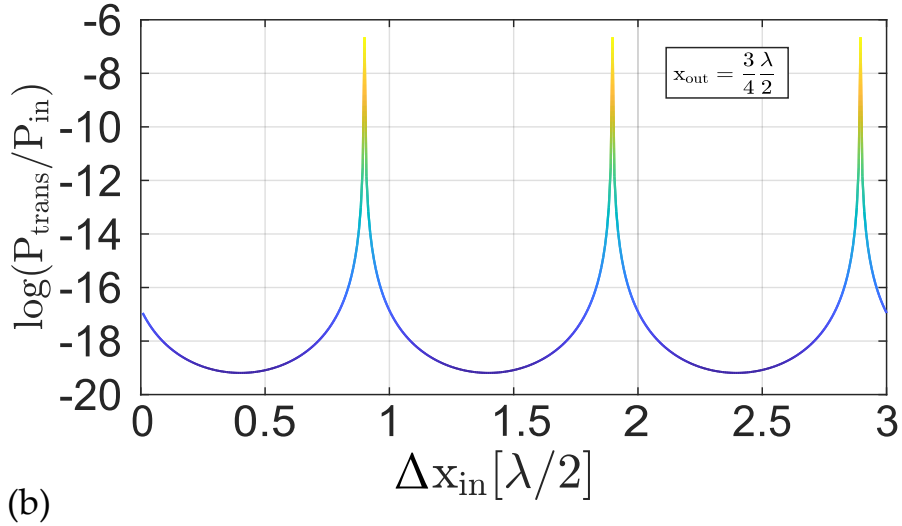

(b)

FIGURE 4.8: Upper Figure a: Simulated power $P_{\text{trans}}(\Delta x_{\text{in}}, \Delta x_{\text{out}})$ for various input coupler positions Δx_{in} and output coupler positions Δx_{out}.
Lower Figure : Simulated transmitted power $P_{\text{trans}}(\Delta x_{\text{in}}, \Delta x_{\text{out}} = \frac{3}{4}\frac{\lambda}{2})$ for fixed output mirror positions Δx_{out} over input mirror position Δx_{in}.

Figure 4.8a illustrates the simulated transmitted power $P_{\text{trans}}(\Delta x_{\text{in}}, \Delta x_{\text{out}})$ for various input coupler positions Δx_{in} and output coupler positions Δx_{out}.

Additionally, Figure 4.8b emphasizes the construction principle of Figure 4.8 by showing the transmitted power over the input position x_{in} for $x_{\text{out}} = \frac{3}{4}\frac{\lambda}{2}$ (indicated by the red dashed line in Figure 4.8a). Figure 4.8 highlights also the distance between consecutive resonances, denoted by $\lambda/2$. These successive resonances are precisely defined by

$$P_{\text{trans}}(\Delta x_{\text{in}}^{\text{res}}, \Delta x_{\text{out}}^{\text{res}}) = P_{\text{trans}}(\Delta x_{\text{in}}^{\text{res}} + j\frac{\lambda}{2}, \Delta x_{\text{out}}^{\text{res}} + l\frac{\lambda}{2}) \tag{4.39}$$

with $l, j \in \mathbb{Z}$ and $\Delta x_{\text{in,out}}^{\text{res}}$ being the position of the input and output mirror at which the resonance condition is fulfilled. The distance between the consecutive resonance of $\lambda/2$ is worth noting as it will be used in the real experiment to calibrate the piezoelectric actuator movement (see Section 4.2.3).

In the following it will be explained, how the resonance frequency ω_{MatE} over membrane position x_{m} can be extracted from the power $P_{\text{trans}}(\Delta x_{\text{in}}, \Delta x_{\text{out}})$ depicted in Figure 4.8a. In the utilised MatE system, the transmitted power $P_{\text{trans}}(\Delta x_{\text{in}}, \Delta x_{\text{out}})$ over the end mirror position alone does not provide direct access to the resonance frequency as a function of the membrane position x_{m}. The cavity length difference ΔL and the relative membrane motion can be calculated using Equations (4.37) and (4.38), which are derived from the input position and output mirror position changes Δx_{in} and Δx_{out}. By applying the transformations from Equations (4.37) and (4.38), the transmitted power $P_{\text{trans}}(\Delta x_{\text{in}}, \Delta x_{\text{out}})$ can be converted to $P_{\text{trans}}(\Delta x_{\text{m}}, \Delta\omega)$. This transformation process is depicted in Figure 4.9 and is based on this figure explained in the following.

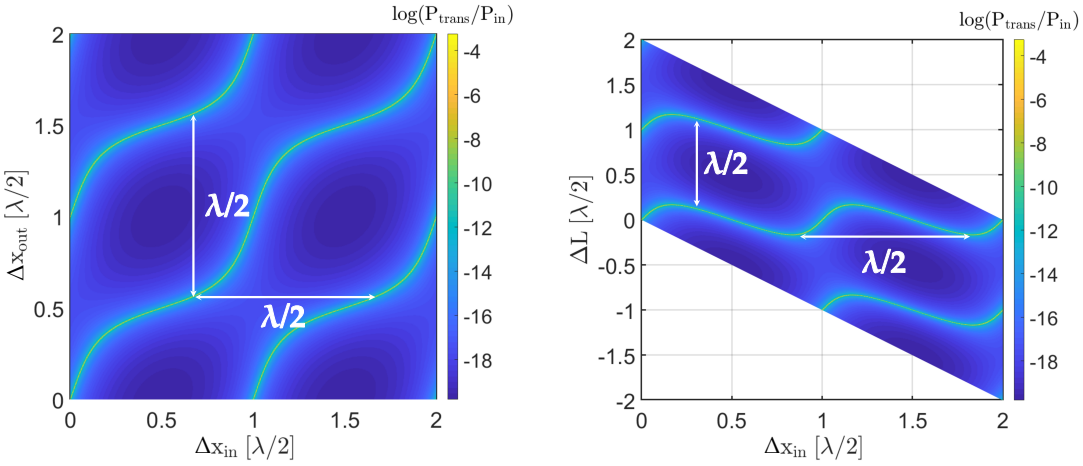

(a) Transmitted power $P_{\text{trans}}(\Delta x_{\text{in}}, \Delta x_{\text{out}})$.

(b) Transmitted power $P_{\text{trans}}(\Delta x_{\text{in}}, \Delta L)$.

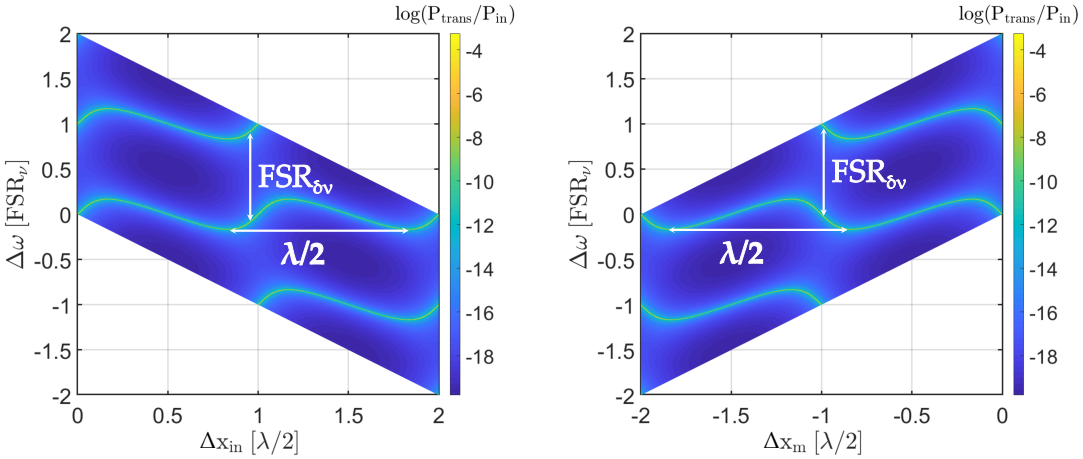

(c) Transmitted power $P(\Delta x_{\text{in}}, \Delta\omega)$.

(d) Transmitted power $P_{\text{trans}}(\Delta x_{\text{m}}, \Delta\omega)$.

FIGURE 4.9: Recipe to transform $P_{\text{trans}}(\Delta x_{\text{in}}, \Delta x_{\text{out}})$ to $P_{\text{trans}}(\Delta x_{\text{m}}, \Delta\omega)$. Following transformation or done in between: Figure a) to b) $P(\Delta x_{\text{in}}, \Delta x_{\text{out}}) \rightarrow P(\Delta x_{\text{in}}, \Delta L)$, Figure b) to c) $P(\Delta x_{\text{in}}, \Delta L) \rightarrow P(\Delta x_{\text{in}}, \Delta\omega)$ and Figure c) to d) $P(\Delta x_{\text{in}}, \Delta\omega) \rightarrow P(\Delta x_{\text{m}}, \Delta\omega)$. Further informations are in the text.

The transmitted power $P_{\text{trans}}(\Delta x_{\text{in}}, \Delta x_{\text{out}})$ shown in Figure 4.9a is first transformed to $P_{\text{trans}}(\Delta x_{\text{in}}, \Delta L)$ (Figure 4.9b) using $\Delta L = \Delta x_{\text{out}} - \Delta x_{\text{in}}$ (Equation ((4.37))). Since a cavity length change ΔL corresponds to a resonance frequency shift $\Delta\omega$, given by (Equation ((2.26)) and 2.27 Section 2.1.4)

$$\omega_{\text{cav}} + \Delta\omega = N \cdot 2\pi FSR_\nu + \Delta_\omega \equiv N \cdot FSR_\lambda + \Delta L = L_{\text{res}} + \Delta L \tag{4.40}$$

the cavity length change ΔL is used to further transform $P_{\text{trans}}(\Delta x_{\text{in}}, \Delta L)$ to $P_{\text{trans}}(\Delta x_{\text{in}}, \Delta\omega)$.

With the last transformation step (using Equation ((4.38))), it is shown that from a power measurement $P(\Delta x_{\text{in}}, \Delta x_{\text{out}})$ a power measurement $P(\Delta x_{\text{m}}, \Delta\omega)$ is deduced.

Hence, as depicted in Figure 4.9 from a measurement of the transmitted power $P(\Delta x_{\text{in}}, \Delta x_{\text{out}})$ (Figure 4.9a) the power $P(\Delta x_{\text{m}}, \Delta\omega)$ (Figure 4.9d) is deduced. Figure 4.9d shows the resonant condition of the MatE system for different membrane positions, and is used to deduce the position of the membrane x_{m} at which the membrane position modulates the resonance frequency ω_{MatE} most. Thereby, from

Figure 4.9d membrane position x_m at which the optomechanical coupling strength $g \propto \frac{\partial \omega_{MatE}}{\Delta x_m}$ is highest, can be deduced.

The next Section 4.2.2 addresses the design and assembling process of the utilised MatE system. The assembly is followed by Section 4.2.3, which discusses a measurement of $P(\Delta x_{in}, \Delta x_{out})$ and its transformation to $P(\Delta x_m, \Delta \omega)$.

4.2.2 Design and assembly of the MatE cavity

Following the investigation carried out in [Sch+22], resulting in the parameters given in Table 2.1, the optomechanical cavity's linewidth should be 2 MHz. To meet this criterion, the MatE-cavity parameters provided in Table 4.1 were chosen.

Parameter	Symbol	Value
Power Reflectivity	R_{in}	$\approx 99.6\,\%$
Radius of curvature	RoC_{in}	50 mm
Power Reflectivity	R_{out}	$\approx 99.9995\,\%$
Radius of curvature	RoC_{out}	∞
Cavity length	L_{MatE}	48.5 mm
Cavity linewidth	κ_{MatE}	≈ 2 MHz
Free Spectral Range	$FSR_{\delta\nu}$	≈ 3.1 GHz
Waist size	w_0	≈ 60 µm
Waist position	z_0	at flat output mirror
Membrane size	$L_x \times L_y$	≈ 1000 µm $\times$ 1000 µm
Membrane thickness	h	≈ 50 nm

TABLE 4.1: Parameters of the MatE-cavity.

Moreover, in order to prevent direct clamping of the membrane structure to its holder, the membrane chip was glued to a 10 mm×10 mm silicon window frame with an aperture size of 5 mm×5 mm (see Figure 4.12a).

To achieve a desirable high escape efficiency η_{om}^{esc} (Table 2.1) the reflectivity of the input mirror $R_{in} = 99.6\%$ and of the output mirror $R_{out} = 99.9995\%$ were selected (nominal escape efficiency $\eta_{om}^{esc} \approx 98\%$). Due to the radii of curvatures of the cavity mirrors, the waist position is on the flat output mirror and has a size of 60 µm. In order to avoid losses due to clipping and to minimise losses arising due to a mode-mismatch between the low-reflecting membrane and the curved input mirror, the membrane is set to a position near the waist w_0 (close to the output mirror). To prevent additional losses, it is important to ensure that the angular alignment of the membrane is orthogonal to the cavity axis. To facilitate this and further adjustments, a separate alignment stage, shown in Figure 4.10a has been set up. The alignment procedure, depicted in the following figures, is discussed next.

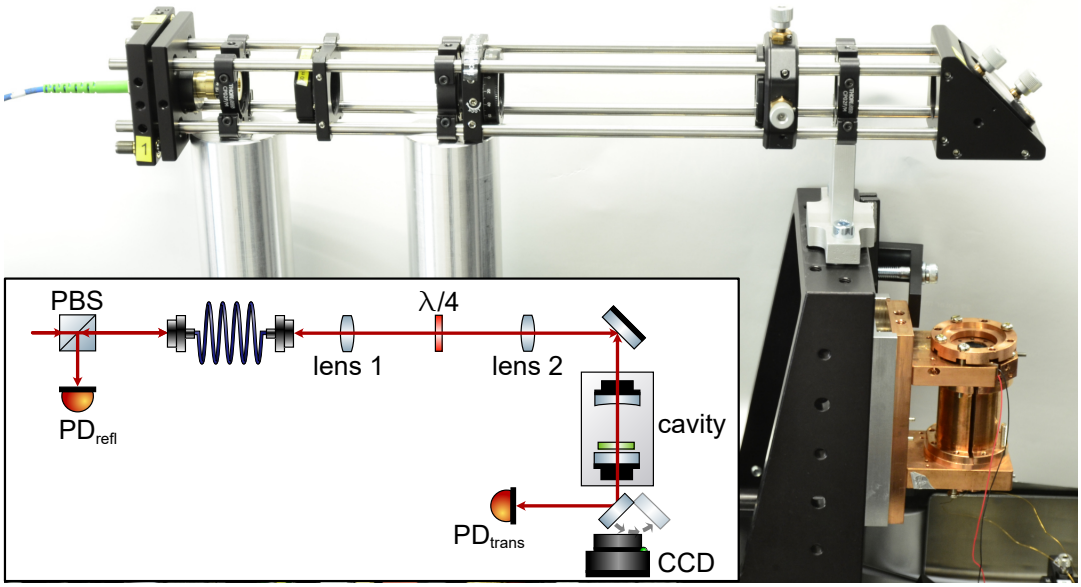

(a) Schematic and picture of the alignment stage for the optomechanical system.

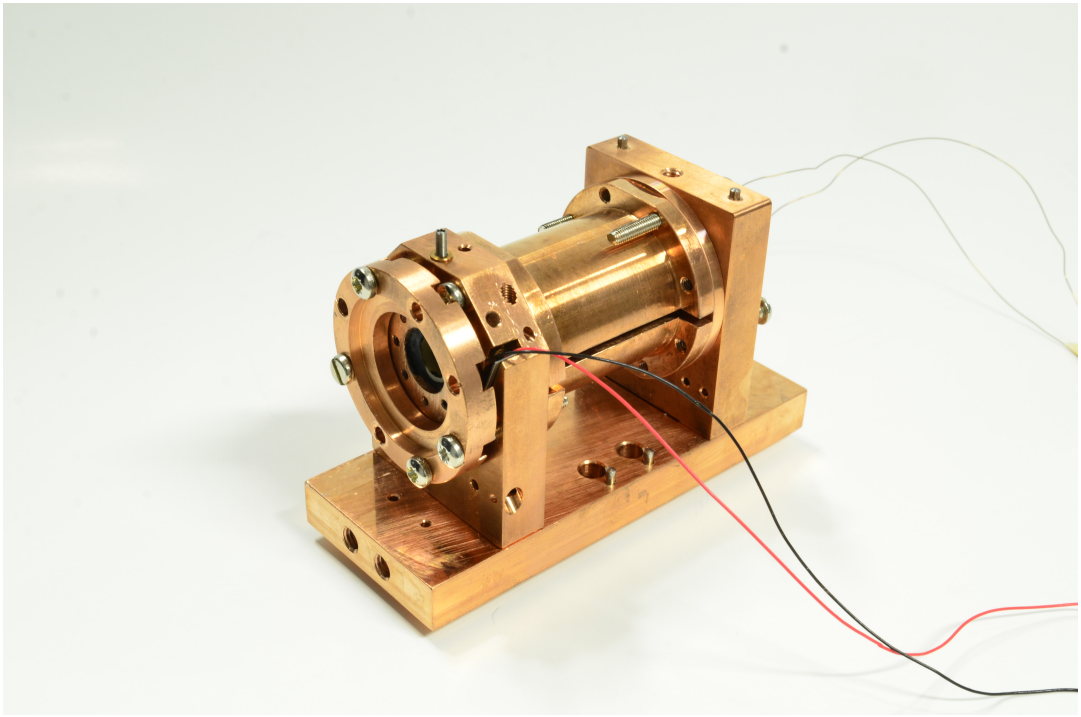

(b) Picture of the assembled optomechanical system

FIGURE 4.10: Picture of alignment stage (a) and the optomechanical system(b)

In Figure 4.10a the alignment stage which guides the beam to the optomechanical system can be seen. The light arrives via a fibre at input of the alignment stage (upper left. green). Two lenses are used for mode matching purposes, whereas the steering mirror in concordance with the tiltable fibre coupler are used to align cavity and optical axis.

Before starting with the alignment procedure, it is worth noting, that the optomechanical system, as depicted in Figure 4.10b, is made out of copper to ensure thermalisation in cryogenic environment. To ensure a tight fit of all connection, the screws are made of nickel-plated brass, as these contract slightly more than copper during cool-down.

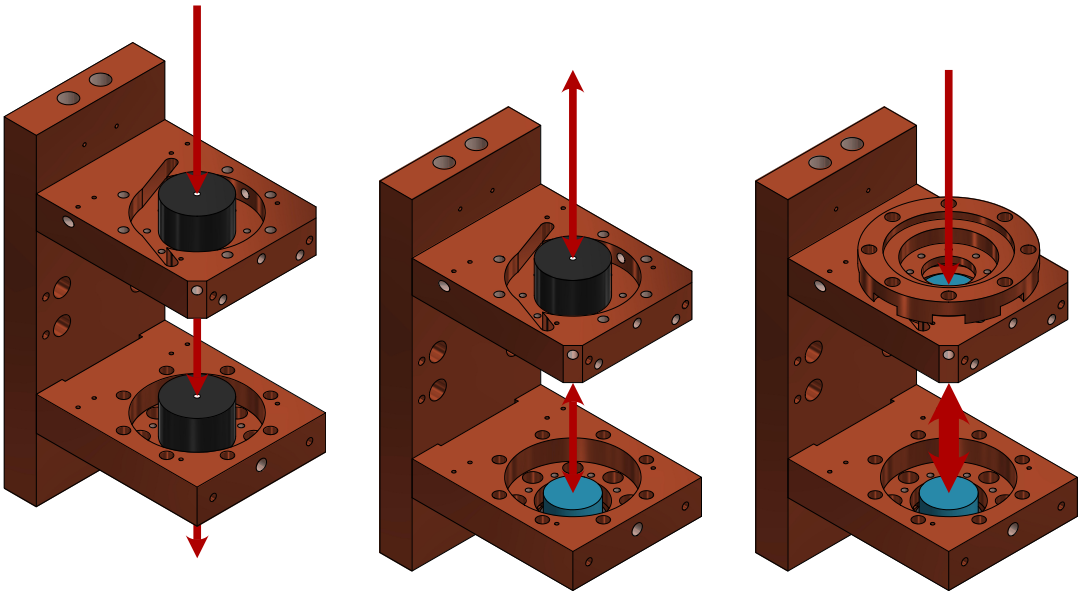

(a) Rough alignment of cavity and beam axis via apertures.

(b) Finer alignment of the beam axis.

(c) Alignment of bare cavity (without membrane).

In Figure 4.11a the first alignment step can be seen, in which two apertures are used to roughly align the beam to the cavity axis. Once this is achieved, the second aperture is replaced by the flat output mirror (Figure 4.11b) (glued to the piezoelectric actuator PZT_{out}), which reflects the light back to the fibre. A $\lambda/4$ wave plate, ensures that the reflected beam travelling back trough the fibre is detected at the photodiode PD_{refl}. Measuring of the maximal amount of the back-reflected light, entails that the beam axis is best aligned to the cavity axis. This alignment is done via fine adjustment of the steering mirror and the tiltable fibre coupler. Subsequently the remaining aperture is replaced by the curved mirror (glued to the piezoelectric actuator PZT_{in}). While ramping PZT_{out} the output power was monitored in transmission and the curved input mirror was moved in x-y direction[15]and the lenses (lens 1 and 2 in Figure 4.10a) were aligned in such a way, that only the TEM_{00} becomes visible. With this the bare[16] cavity is aligned. Once aligned the position of the lenses and the steering mirrors were fixed.

[15] z-direction given by the cavity axis.
[16] Without the membrane.

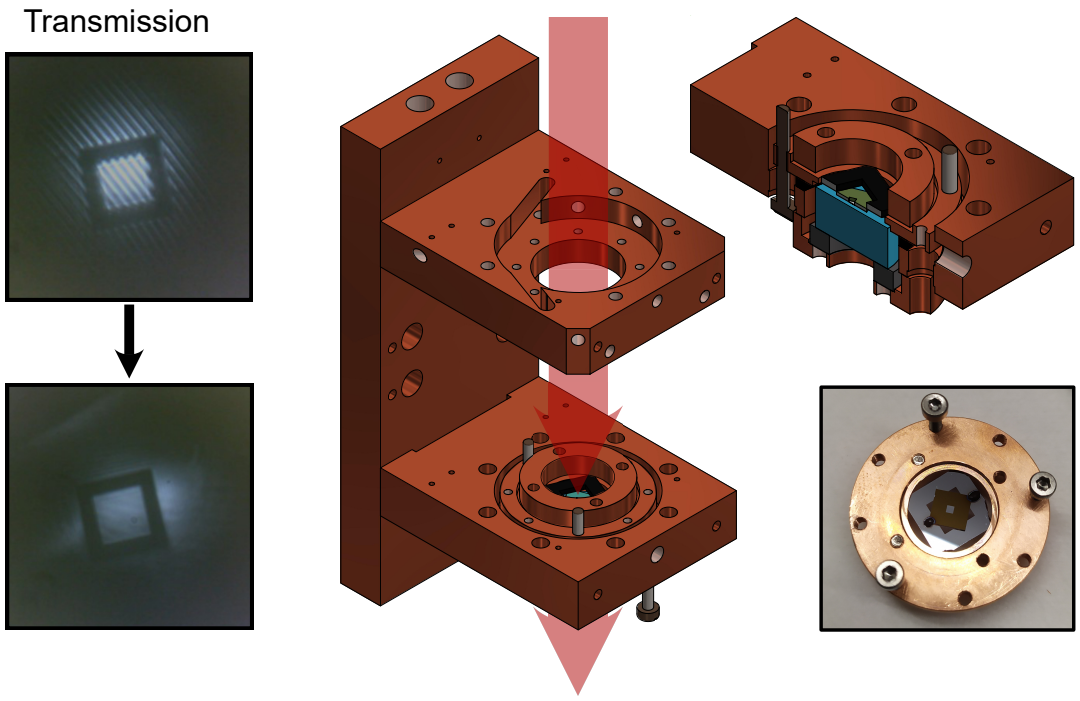

(a) Alignment of membrane to beam and cavity axis.

FIGURE 4.12: Alignment steps 1

The input mirror is removed within the next step (Figure 4.12a), and the membrane with its holder is inserted. To align the membrane to the cavity axis, an additional lens, widening the beam profile is inserted in front of the cavity. This allows clear imaging of the membrane and detection of the interference fringes arising due to the etalon build by the membrane and the flat output mirror (left in Figure 4.12a). The rubber ring between the membrane holder and the mirror allows for tilting the membrane holder with respect to the flat mirror by tightening/loosening the three screws shown in the right inset of Figure 4.12a. By Manipulating the screws, one can get rid of interference stripes originating from a tilt between the membrane and the flat mirror. Once the interference pattern is no longer visible, the membrane and mirror can be assumed to be parallel. With this, the membrane is also aligned orthogonal to the cavity axis.

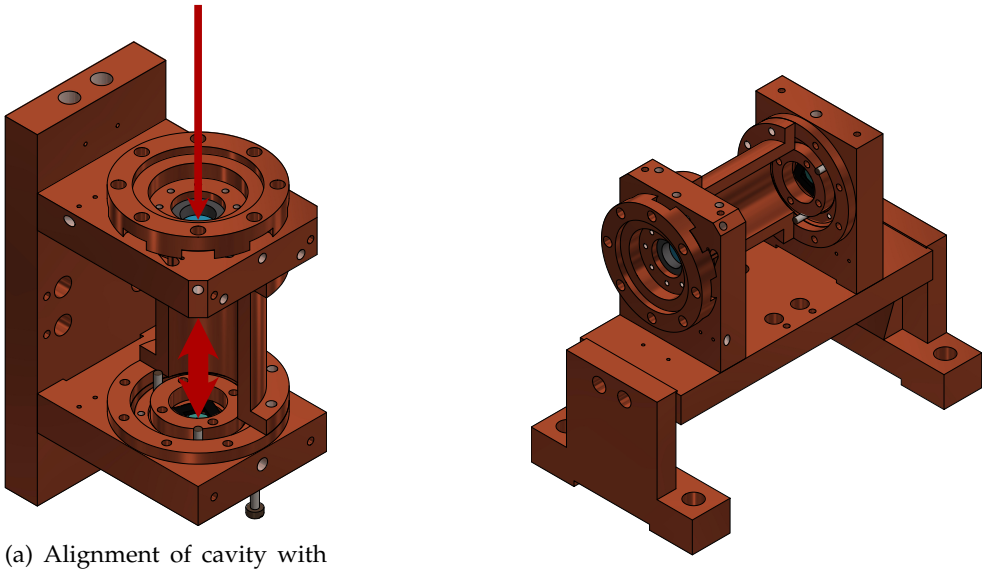

(a) Alignment of cavity with membrane inserted.

(b) Final aligned MatE-system

FIGURE 4.13: Alignment steps 2

Finally, after removing the widening lens, the input mirror is reinserted (Figure 4.13a), and moved to a position where cavity resonance appears once more in transmission while PZT_{out} is ramped. When the alignment process is successfully completed, copper feet are fixed to the cavity, which are used for mounting the entire optomechanical system to the cold plate of the cryostat. The membrane positioning along the cavity axis, to address the position of the highest optomechanical coupling g (theoretically explained in Section 4.2.1), is discussed in the following section.

4.2.3 Optical characterisation of MatE-system

This section will describe the optical characterisation of the MatE system. The aim is to determine the resonant frequency ω_{MatE} with respect to the membrane position x_{m}. As the optomechanical coupling strength g is proportional to $\left(\frac{\partial \omega_{\text{MatE}}}{\partial x_{\text{m}}}\right)$, the membrane position x_{m} at which the coupling strength g is highest is inferred from the measurement presented in this section.

For this purpose the setup depicted in Figure 4.14 is used. As shown, a probe beam, a calibration beam (calib.), the membrane-at-the-edge (MatE) cavity inside a cryostat, and photodiodes in the transmission of the OMS are used for the experiment. Also, a fiber-coupled GHz EOM and an oscilloscope connected to a computer are utilised. The purpose of these components will become apparent in the following. For the characterisation, the response of the probe beam with power $P_{\text{probe}} = 1\,\text{mW}$ for different mirror positions of the MatE-system is measured in transmission of the MatE system (described in Section 4.2.2), which is located within a cryostat. Unfortunately, no measurements at cryogenic temperatures were performed within this thesis, as it was not possible to lock the MatE system at cryogenic temperature. This is most likely caused by the dynamic range of the piezoelectric actuator, which drops to 10% at 4 K or it is caused by glue joints breaking during cool-down. Nevertheless, the MatE system is located in the cryostat because even at 300 K a pressure of 10^{-7} mbar was achieved. At this pressure, the quality factor of the membrane is not limited by gas damping (see Section 4.1).

During the characterisation measurements, the absolute position of the membrane remains fixed. In contrast, the relative motion of the membrane within the MatE cavity is adjusted by changing the positions x_{in} and x_{out} of the input and output mirror (as in Figure 4.7). An input mirror position change is in the following denoted as Δx_{in}. A position change Δx_{in} is induced by applying a driving voltage V_{in} to a piezoelectric actuator PZT_{in} attached to the input mirror. The driving voltage V_{in} is linearly swept over time between 32.5 V and 96.8 V with a frequency of 0.67 Hz. Throughout this linear sweep, the transmitted power $P_{\text{trans}}^{\text{probe}}$ measured by the photodetector $PD_{\text{trans}}^{\text{probe}}$ and the applied sweep voltage V_{in} (used as a trigger) is recorded using an oscilloscope.

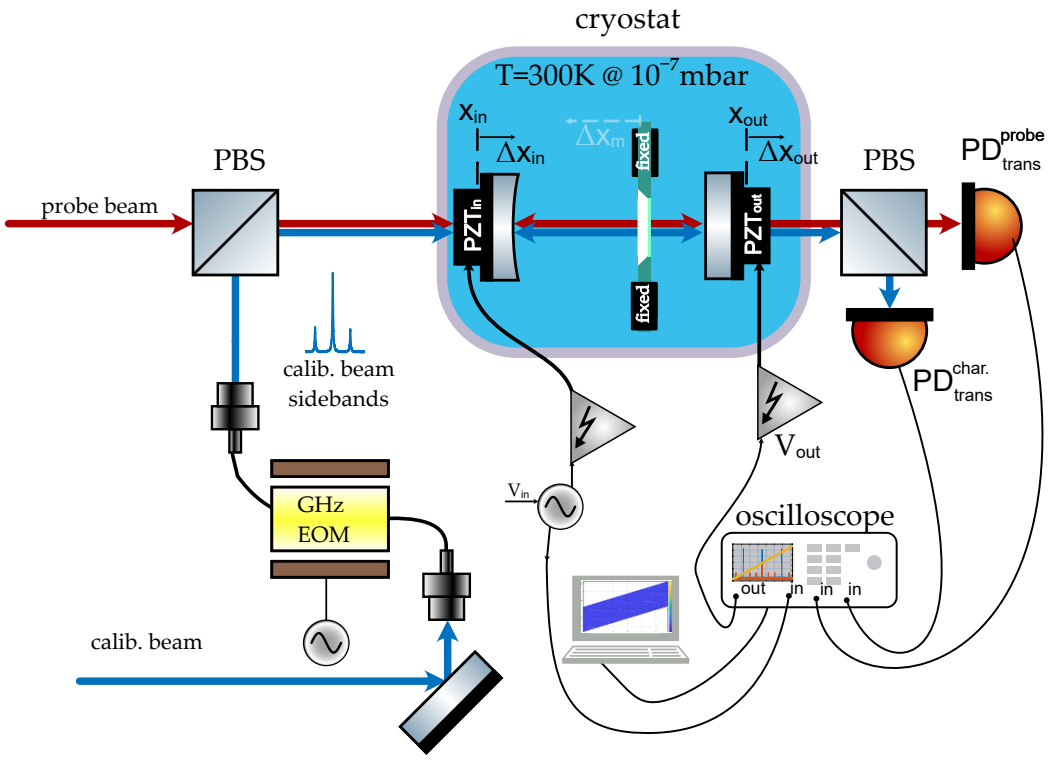

FIGURE 4.14: Setup to measure the power of the MatE-system for different combinations of input and output mirror position changes $\Delta x_{\text{in,out}}$.

The input mirror position sweep is done for different mirror positions $x_{\text{out}} + \Delta x_{\text{out}}$. Therefore, variations in output mirror position Δx_{out} are achieved, by using the piezoelectric actuator PZT_{out} attached to the output mirror. Differently from the input mirror position, the output mirror position was changed in steps. After one input mirror sweep at a fixed output mirror position, the measured transmitted power $P_{\text{trans}}^{\text{probe}}$ and the sweep voltage V_{in} are recorded on the oscilloscope, which sends the recorded data to a computer. After recording the data, the oscilloscope, in conjunction with an HV-amplifier, generates a step voltage of 0.27 V, that is applied to the PZT_{out} increasing Δx_{out} of the output mirror. The transmitted power $P_{\text{trans}}^{\text{probe}}$, is measured this way, for 240 voltage steps, corresponding to 240 output mirror positions Δx_{out}. For every measurement, the oscilloscope is triggered to the sweep voltage V_{in} that drives the input mirror position change Δx_{in}. Thereby, for 240 linearly increased output mirror positions, the transmitted power $P_{\text{trans}}^{\text{probe}}$ was measured while the input mirror position was linearly swept. In that manner, an array of 240×92000 data points was recorded. This recorded data of the transmitted probe power $P_{\text{trans}}^{\text{probe}}(V_{\text{in}}, V_{\text{out}})$ is presented in Figure 4.15.

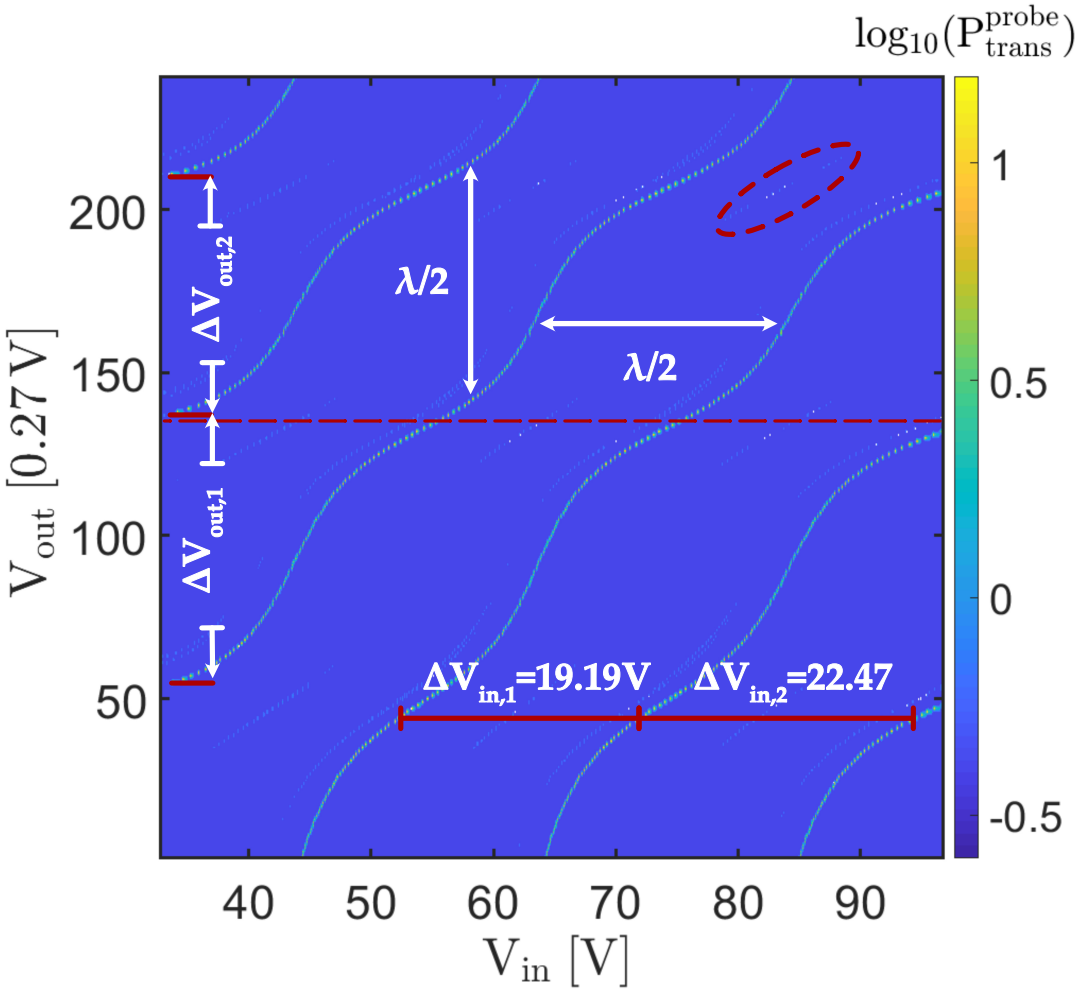

FIGURE 4.15: Measured transmitted power $P_{\text{trans}}^{\text{probe}}(V_{\text{in}}, V_{\text{out}})$ over the voltage $V_{\text{in,out}}$.

In Figure 4.15, some spatial higher-order modes are visible (one is marked by the red dashed ellipse). These are caused either by a slight misalignment of the membrane with respect to the fundamental mode of the cavity or by a mode mismatch or misalignment of the input beam to the cavity. The higher-order mode contributions are negligible for the optomechanical experiments within this thesis, as these are not overlapping with the fundamental mode and are comparably small. The red dashed line in Figure 4.15 marks the DC voltage $V_{\text{out}} = 135 \cdot 0.27\,\text{V} = 36.45\,\text{V}$ applied to the piezo PZT_{out}, which was used for measurement of the coupling strength g discussed in Section 4.3.1 and 4.3.2.

The measured data shows a distortion in V_{in}-axis compared to the theoretical model shown in Figure 4.8 caused by a non-linear PZT behaviour. A comparison of the measured transmitted power $P_{\text{trans}}^{\text{probe}}(V_{\text{in}}, V_{\text{out}})$ (Figure 4.15) with a simulated version $P_{\text{trans}}^{\text{probe}}(\Delta x_{\text{in}}, \Delta x_{\text{out}})$ (Figure 4.8) reveals that there is a high agreement. However, the measured power $P_{\text{trans}}^{\text{probe}}(V_{\text{in}}, V_{\text{out}})$ is distorted with respect to simulated power $P_{\text{trans}}^{\text{probe}}(\Delta x_{\text{in}}, \Delta x_{\text{out}})$. This distortion is best identified in Figure 4.15 by the red marked lines denoted by $\Delta V_{\text{in},1} = 19.19\,\text{V}$ and $\Delta V_{\text{in},2} = 22.47\,\text{V}$. These lines represent the distance between two consecutive resonances at a fixed output mirror position and have an unequal length. The voltage $\Delta V_{\text{in},1}$ and $\Delta V_{\text{in},2}$ would be equal (corresponding to $\lambda/2$), if the piezoelectric actuator's applied voltage V_{in} and V_{out} caused a linear displacement of its attached input and output mirror. Hence, the distortion is due

to the non-linear displacement response of the piezoelectric actuator to its applied voltage [LSP12].

To calibrate the position change Δx_{in} of the input mirror over the voltage V_{in} applied to PZT_{in} the calibration beam (calib.), depicted in Figure 4.14, is used. This characterisation beam is phase-modulated. The phase modulation allows to identify the FSR of the cavity and thereby is used to convert the PZT voltage into a length displacement. The generation of the calibration beam is explained in Section 3.2.

The carrier frequency of the calibration beam in the MatE-system spatially overlaps with the probe beam, but the polarisations of both beams are orthogonal. Hence they can be separated using polarisation beam splitters (PBSs). Additionally, interference and beating between the two beams is avoided due to their orthogonal polarisation. This orthogonality is essential, as both beams have the same carrier frequency ω_0. Due to their polarisation, their power $PD^{\text{probe}}_{\text{trans}}$ and $PD^{\text{char.}}_{\text{trans}}$ can be measured independently in transmission after the beams are spatially separated by a PBS.

For calibration purposes, the power $P^{\text{calib.}}_{\text{trans}}$ of the phase-modulated calibration beam is measured in transmission. At the same time, the output mirror position x_{out} is fixed, and the input mirror position is swept by applying the voltage V_{in} to PZT_{in}. For this configuration, the MatE-system's free spectral range FSR_ν is extracted by linearly changing the modulation frequency ω_{mod} of the fiber-EOM affecting the calibration beam. The modulation frequency ω_{mod} is increased linearly until the generated upper and lower sideband overlap in the measured transmitted signal detected at $PD^{\text{char.}}_{\text{trans}}$ (detailed explanation in Section 3.2 and Figure 3.4). With that, the FSR_ν for the MatE system is measured as $FSR_\nu = 3.1129\,\text{GHz}$. Once the FSR_ν is measured, the modulation frequency ω_{mod} of the phase modulation is set to $\omega_{\text{mod}} = \frac{1}{3} FSR_\nu$[17] to create sidebands at $\omega_0 \pm \frac{1}{3} FSR_\nu$. A time series of the detected power in transmission of the probe, the phase-modulated calibration beam and the sweep voltage V_{in} is depicted in Figure 4.16. As illustrated in Figure 4.16, the distance between the generated sidebands is $\frac{\lambda}{6}$[18].

[17] This is an arbitrary choice. Other ratios would also be possible.

[18] one FSR_ν corresponds to $\lambda/2$ (Section 2.1.4).

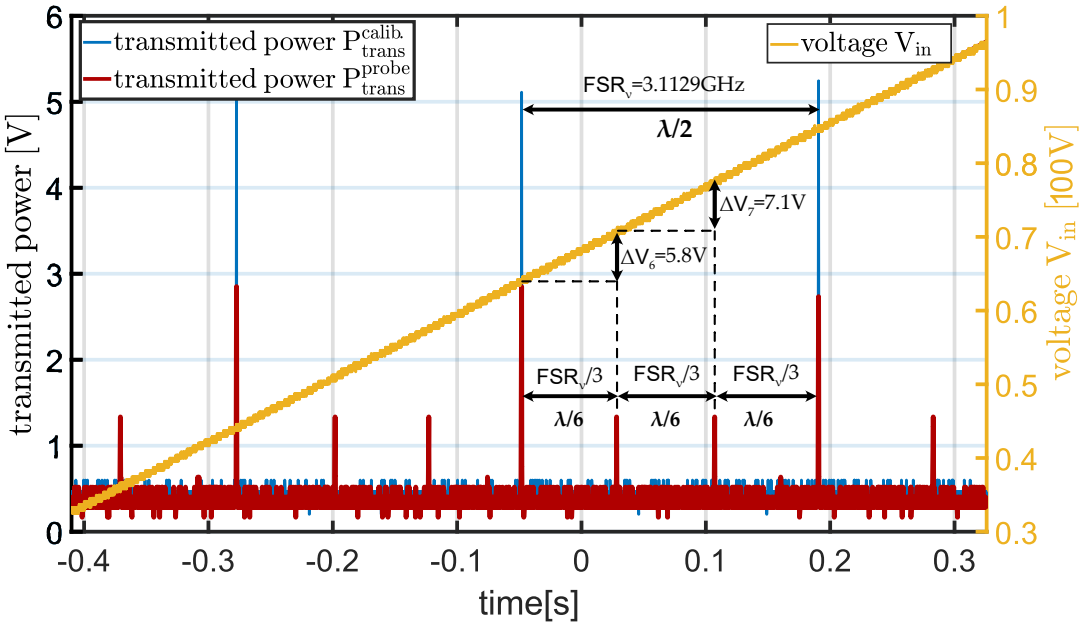

FIGURE 4.16: Transmitted probe $P_{\text{trans}}^{\text{probe}}$ (blue) and calibration beam power $P_{\text{trans}}^{\text{calib.}}$(red) at a fixed output mirror position x_{out} over time, while the voltage V_{in}(yellow) is swept linearly in time. The voltage V_{in} applied to the piezoelectric actuator PZT_{in} to sweep the input mirror position is shown in yellow. Also, as an example, some distances of the sidebands and the carrier (FSR and $FSR/3$) are depicted. The corresponding voltage between the fifth and sixth transmission peak ΔV_6 and between the sixth and seventh transmission peak ΔV_7 of the calibration beam is shown exemplarily. As depicted each voltage difference ΔV_6 and ΔV_7 corresponds to a input mirror movement movement of $\Delta x_{\text{in}} = \lambda/6$.

The voltage V_{in} applied to the piezoelectric actuator PZT changed the input mirror position, resulting in resonances at different positions for the carrier and sidebands of the calibration beam in the optomechanical system (as shown in Figure 4.16). By measuring the calibration peaks in transmission and analysing their non-linear temporal spacing, the measured voltage V_{in} can be calibrated in units of λ. For example, the voltage difference between the fifth and sixth transmission peaks ($V_6 = 5.8\,\text{V}$) corresponds to $\lambda/6$. Similarly, the voltage difference between the sixth and seventh transmission peaks ($\Delta V_7 = 7.1\,\text{V}$) also corresponds to $\lambda/6$. Therefore, by utilising the sidebands of the calibration beam, the non-linear response of the input mirror motion can be calibrated in terms of λ. The resulting calibration curve of the mirror displacement Δx_{in} in units of λ over the voltage V_{in} can be seen in Figure 4.17. This figure shows the extracted data points from Figure 4.16 and a polynomial fit of seventh order to this point. A seventh-order polynomial is selected based on its ability to resemble best the displacement over voltage dependency depicted in [LSP12].

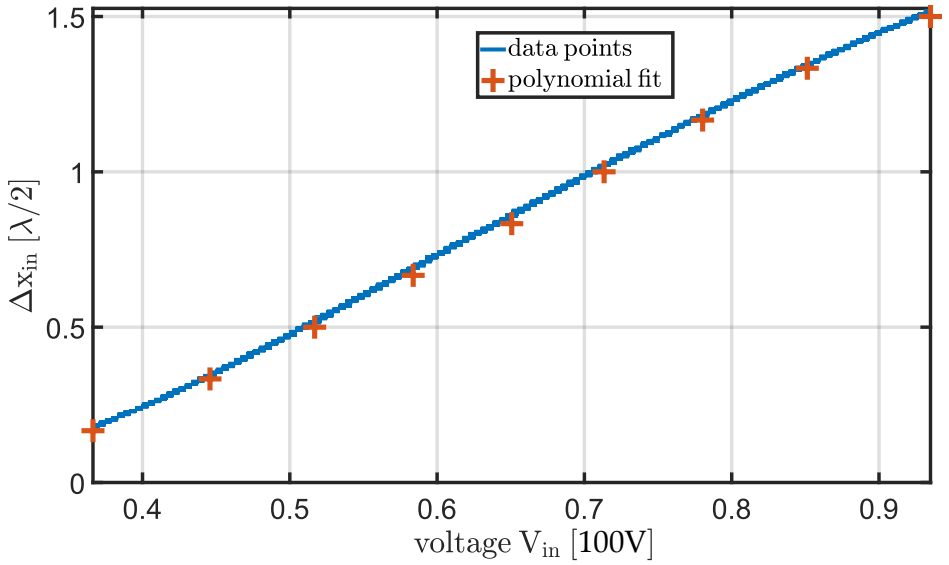

FIGURE 4.17: Calibration curve of the mirror displacement Δ_{in} in units of λ over the voltage V_{in} applied to the piezoelectric actuator attached to the input mirror.

As the output mirror is moved in steps (by applying 240 times a step voltage V_{out} of 0.27 V to PZT_{out}) and not linearly swept, the previously explained calibration procedure cannot be used. Hence the calibration of the displacement over voltage V_{out} is done more coarsely. Namely the vertical distance of consecutive resonances at $V_{in} = 32.5\,\mathrm{V}$, denoted as $\Delta V_{out,1}$ and $\Delta V_{out,2}$ in Figure 4.15 are used to transform V_{out} to Δx_{out}. Their voltages are given by $\Delta V_{out,1} = 22.68\,\mathrm{V}$ and $\Delta V_{out,2} = 19.71\,\mathrm{V}$. With these calibration the measured power $P^{probe}_{trans}(V_{in}, V_{out})$ can be transformed to $P^{probe}_{trans}(\Delta x_{in}, \Delta x_{out})$. Following the transformation procedure explained in Section 4.2.1 (Figure 4.9) the measured transmitted power $P^{probe}_{trans}(V_{in}, V_{out})$ can be converted into $P^{probe}_{trans}(x_m, \Delta\omega)$. The transmitted power $P^{probe}_{trans}(x_m, \Delta\omega)$ obtained from these transformations is depicted in Figure 4.18.

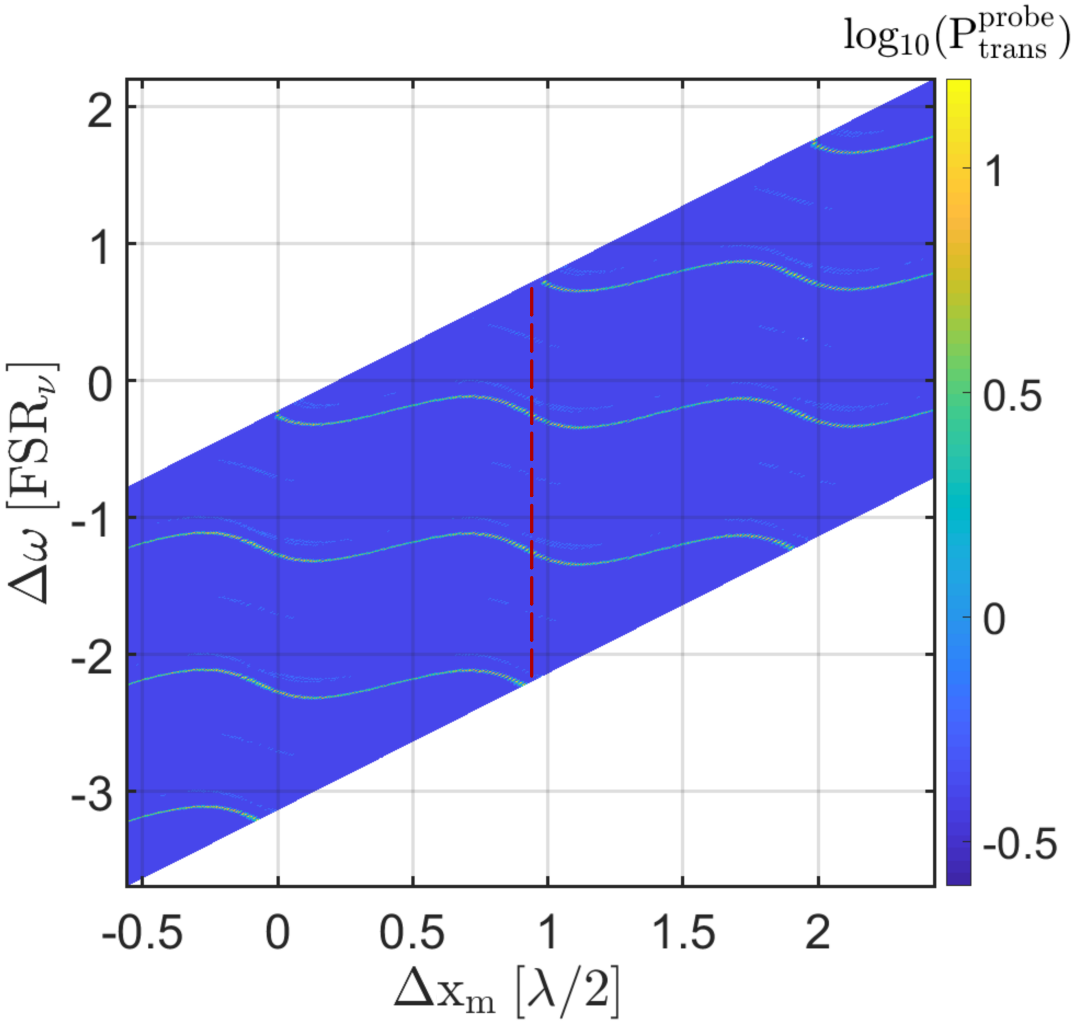

FIGURE 4.18: Transmitted power $P_{\mathrm{trans}}^{\mathrm{probe}}(\Delta x_{\mathrm{m}}, \Delta\omega)$ transformed from $P_{\mathrm{trans}}^{\mathrm{probe}}(V_{\mathrm{in}}, V_{\mathrm{out}})$ (Figure 4.15). The Figure is used to deduce the highest coupling strength g, as $g \propto \frac{\partial\omega_{\mathrm{MatE}}}{\partial x_{\mathrm{m}}}$.

From Figure 4.18 the membrane position x_{m} with the highest optomechanical coupling strength $g(g \propto \frac{\partial\omega_{\mathrm{MatE}}}{\partial x_{\mathrm{m}}})$ can be inferred. Also, the red dashed line transformed from Figure 4.15 is depicted. This dashed red line indicates the membrane position x_{m}, which is used during the coupling strength g measurements presented in Section 4.3.1 and 4.3.2. As seen in Figure 4.15, this relative membrane position x_{m} is attained by applying a DC voltage of $V_{\mathrm{out}} = 36.45\,\mathrm{V}$ to the output mirror piezoelectric actuator PZT_{out}. At this voltage, the resonance frequency ω_{MatE} is reached by locking the MatE cavity via the input mirror on resonance. Consequently, the dashed red line reveals that the membrane is positioned near the location with the highest optomechanical coupling strength $g(g \propto \frac{\partial\omega_{\mathrm{MatE}}}{\partial x_{\mathrm{m}}})$.

The indicated membrane position and resonance frequency is addressed during the subsequent experiments. These experiments are used to measure the optomechanical coupling g. Therefore, in Section 4.3.1, the optomechanical coupling strength is measured by using the OMIT effect (introduced in Section 2.5.5), whereas in Section 4.3.2 the effect of dynamical backaction (DBA) (introduced in Section 4.3.2.1) is used.

4.3 Measurement of optomechanical coupling strength g

In the two following sections, experiments for measuring the coupling strength g will be discussed. Section 4.3.1 focuses on the OMIT experiment, whose theory is outlined in Section 2.5.5. Almost all relevant parameters of an optomechanical system can be deduced from the OMIT experiment. This section is followed by Section 4.3.2, where the effect arising from dynamical backaction is used to measure the coupling strength g. The theory for dynamical backaction is discussed in Section 2.5.2.

4.3.1 OMIT measurement

This section discusses the experiment and the measurement of the OMIT effect (see Section 2.5.5).

As explained in Section 2.5.5 in an OMIT experiment, the phase modulation of an input field $\alpha_{\mathrm{L}}^{\mathrm{in}}$ is converted by the optomechanical system (OMS) into amplitude fluctuations $\delta X_{\mathrm{om,R}}^{\mathrm{out}}$ [19] in transmission. The resulting amplitude fluctuations $\delta X_{\mathrm{om,R}}^{\mathrm{out}}$ (Equation (2.140)) are expressed in terms of a complex transfer function as

$$H_{\mathrm{OMIT}}(\omega) = \frac{S_{\mathrm{trans}}(\omega)}{S_{\mathrm{reference}}(\omega)} \propto \frac{\delta X_{\mathrm{om,R}}^{\mathrm{out}}(\omega)}{\alpha_{\mathrm{L}}^{\mathrm{in}} \cdot \beta(\omega)} = C_{\mathrm{OMIT}} \frac{C(\omega)}{1 - M(\omega)} \,. \tag{4.41}$$

Here $\beta(\omega)$ describes the modulation depth of the input phase modulation, $\alpha_{\mathrm{L}}^{\mathrm{in}}$ the amplitude of the phase-modulated input field, C_{OMIT} a proportionality factor and $\frac{C(\omega)}{1-M(\omega)}$ the conversion of the phase modulated input field to the amplitude quadrature $\delta X_{\mathrm{om,R}}^{\mathrm{out}}$ in transmission. The conversion is driven by the detuned cavity, described by $C(\omega)$, and by the optomechanical interaction, described by $(1 - M(\omega))^{-1}$, respectively. As discussed in Section 2.5.5, from $\frac{C(\omega)}{1-M(\omega)}$ most relevant parameters of the optomechanical system can be deduced. Therefore within the presented OMIT experiment, a signal $S_{\mathrm{reference}}$ proportional to the modulation depth $\beta(\omega)$ and a signal S_{trans} proportional to the amplitude fluctuation $\delta X_{\mathrm{om,R}}^{\mathrm{out}}$ in transmission of the OMS is measured.

The experimental setup to achieve these measurements is depicted in the following Figure 4.19 and will be explained in two steps. First, the Mach-Zehnder interferometer (explained in Section 2.1.3) will be discussed, followed by a brief discussion of the optomechanical system in conjunction with the direct detection scheme in transmission.

[19] Subscript R indicates the right mirror (output mirror) at which the transmitted signal $\delta X_{\mathrm{om,R}}^{\mathrm{out}}$ leaks out.

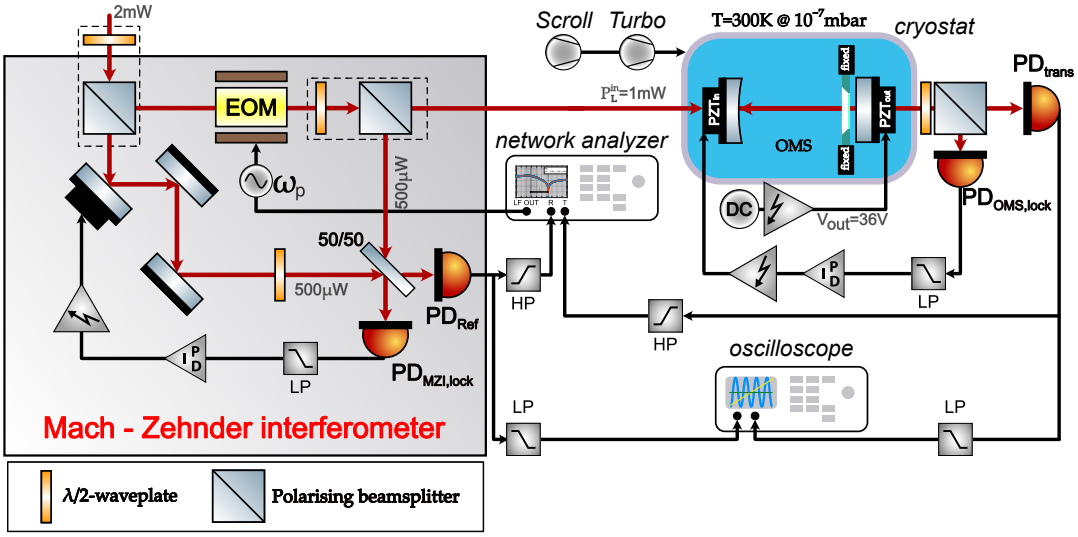

FIGURE 4.19: Sketch of the experimental OMIT setup, consisting of a Mach-Zehnder-interferometer, a cryostat (used as a vacuum chamber) containing the optomechanical system (OMS = MatE system), a network analyser, an oscilloscope and various photodiodes. The LF output of the photodiodes is used for locking or monitoring purposes, whereas the HP outputs are used as the inputs for the network analyser. Detailed description in the text.

The highlighted Mach-Zehnder interferometer (MZI) in Figure 4.19 is used to measure the signal $S_{\text{reference}}$ which is proportional to the modulation depth $\beta(\omega_p)$ and is theoretically described in Section 2.1.3. A broadband electro-optic-modulator[20] (EOM) is placed in one arm of the MZI. This EOM is driven at frequency ω_p via the LF output of the shown network analyser[21] and hence generates on its traversing light field due to phase modulation sidebands at $\pm\omega_p$ with a modulation depth $\beta(\omega_p)$. As emphasised in Section 2.1.3, the MZI consists of variable beamsplitters formed by $\lambda/2$ wave-plates in conjunction with polarising beamsplitters (indicated by dashed boxes in Figure 4.19). These tunable beamsplitters split the power such that 500 µW of the phase-modulated light interferes with 500 µW of the non-phase modulated light of the other MZI arm at the 50/50 power beamsplitters at the output of the MZI. Furthermore, 1 mW of the phase modulated light is sent as the input light α_L^{in}[22] to the OMS. As discussed in Section 2.1.3, the mid-fringe locked MZI measures a signal proportional to the phase modulation $\beta(\omega_p)$ generated by the EOM. Hence, the photodetector $PD_{\text{MZI, lock}}$ at one of its outputs is used to stabilise the MZI at mid-fringe[23]. At the other output of the locked MZI, the signal $S_{\text{reference}}$ proportional to the modulation depth $\beta(\omega_p)$ is measured by the photodetector PD_{ref}. The high-pass (cut-off frequency $\ll 1$ kHz) filtered output of the detected signal is sent to the network analyser, which uses the signal as the reference signal $S_{\text{refercnce}}$ for the transfer function (denominator of Equation (4.41)). The low-pass filtered output is sent to an oscilloscope and monitored to keep track of the MZI lock. With this, the reference signal of the transfer function $H_{\text{OMIT}}(\omega)$ is measured. The optomechanical system and the measured transmitted amplitude fluctuations $\delta X_{\text{om,R}}^{\text{out}}$ are explained in the following.

[20] QUBIG PSA2M-NIR.
[21] Agilent E5061B.
[22] Its power is denoted as P_L^{in} in Figure 4.19.
[23] The locking bandwidth is below 10 kHz.

As mentioned in the previous description, 1 mW of phase-modulated light is sent to the optomechanical system, which is placed inside a cryostat. The cryostat is used as a vacuum chamber in this experiment, as it was impossible to lock the cavity[24] at 4 K. The pressure at 300 K was detected as 10^{-7} mbar. As explained in Section 4.2.3, the membrane was positioned by the DC voltage $V_{\text{out}} = 36.45$ V applied to the PZT_{out}. The power in the transmission of the optomechanical system was measured by two photodetectors, both utilising a direct detection scheme (2.3.1). Hence, both photodiodes are generally susceptible to the transmitted amplitude quadrature fluctuations $\delta X^{\text{out}}_{\text{om,R}}$. However, the photodetector $PD_{\text{OMS, lock}}$ was used to lock the optomechanical system on the side at roughly $\Delta = \kappa/2$. The second photodetector PD_{trans} in transmission measured the signal S_{trans} proportional to $\delta X^{\text{out}}_{\text{om,R}}$. Also, in transmission, the high-pass filtered output of the photodetector PD_{trans} (cut-off frequency $\ll 1$ kHz) is sent to the network analyser. Additionally, the low-pass pass filtered output of PD_{tans} was sent to the oscilloscope to keep track of the optomechanical cavity lock.

For accomplishing the OMIT measurement, the network analyser generates an RF tone (10dbm)[25] which is sent to the EOM and thereby induces a phase modulation with modulation depth $\beta(\omega_{\text{p}})$ to the beam a^{in}_{L}. The frequency ω_{p} of the RF tone is swept while at the same time, the network analyser measures the transfer function $\frac{C(\omega)}{1-M(\omega)}$ using the reference signal $S_{\text{reference}}$ and the transmitted signal S_{trans} as inputs. First, the measured transfer function of a broad frequency sweep (200 kHz to 8 MHz), which is depicted in Figure 2.12, will be discussed.

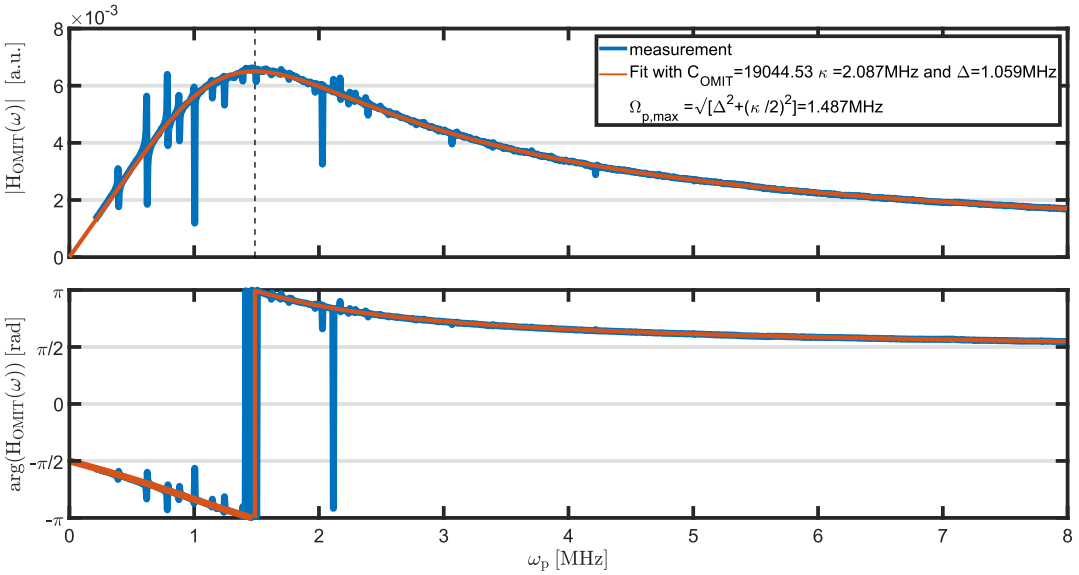

FIGURE 4.20: Magnitude $|H_{\text{OMIT}}(\omega)|$ and phase response $arg(H_{\text{OMIT}}(\omega))$ of OMIT response $H_{\text{OMIT}}(\omega)$ in a broad frequency range (from 200 kHz-8 MHz).

In Figure 4.20 the magnitude and phase of the transfer function $H_{\text{OMIT}} = \frac{C(\omega)}{1-M(\omega)}$ over the modulation frequency ω_{p} are shown. The dip-peak features due to the OMIT effect (explained in Section 2.5.5) will be discussed separately in the next figure.

Hence, first, the use of the transfer function H_{OMIT} over a broad frequency range (Figure 4.21 is explained first. The theoretical OMIT response over a broad frequency

[24] Probably due to the dynamic range of the piezo, which drops to 10% at 4 K or due to broken gluing joints during cooldown.

[25] This creates a small modulation depth $\beta(\omega_{\text{p}})$, as a nonresonant EOM is used.

range (200 kHz to 8 MHz) depicted in Figure 2.12 is used to deduce the optical parameters of the optomechanical system, as the broadband response entails mainly the cavity transduction $C(\omega)$ (apart from the peak-dip features). Hence, by globally[26] fitting the measured magnitude and the phase response of the OMIT response $H_{\mathrm{OMIT}}(\omega)$ over a broad frequency range with a least-square fit [27] to $C(\omega)$, the constant C_{OMIT}, the detuning Δ and the linewidth κ of the optomechanical system are deduced. These parameters are given as

$$\kappa/(2\pi) = (2.09 \pm 0.08)\,\mathrm{MHz} \tag{4.42a}$$
$$\Delta/(2\pi) = (1.06 \pm 0.05)\,\mathrm{MHz} \tag{4.42b}$$
$$C_{\mathrm{OMIT}} = (1.90 \pm 0.11)\,\mathrm{MHz}\,. \tag{4.42c}$$

Here the error indicates the 95% confidence interval. After measuring the transfer function H_{OMIT} over a broad frequency range, the sweep range of the modulation frequency is changed to a narrower range near a peak-dip feature, which is also visible in Figure 4.20. For instance, in Figure 4.21, the sweep range was set to 392 kHz-394 kHz.

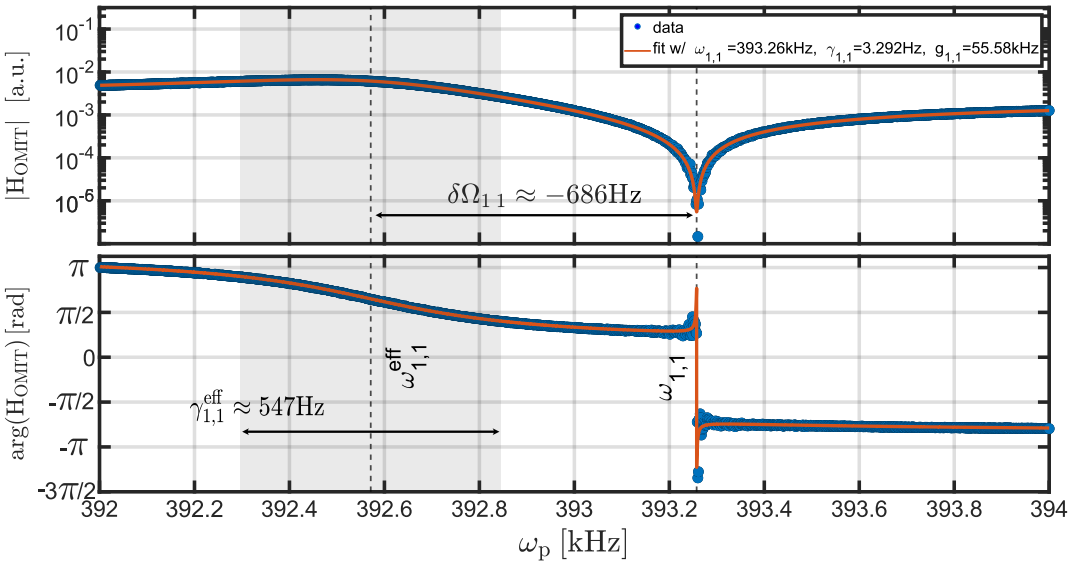

FIGURE 4.21: Magnitude $|H_{\mathrm{OMIT}}(\omega)|$ and phase response $arg(H_{\mathrm{OMIT}}(\omega))$ of OMIT response $H_{\mathrm{OMIT}}(\omega)$ in a narrow frequency range around the resonance frequency $\omega_{1,1}$.

Figure 4.21 illustrates the OMIT transfer function $H_{\mathrm{OMIT}}(\omega)$ in a narrow frequency range around the resonance frequency $\omega_{1,1}$. Also depicted in Figure 4.21 is the fit result to the data and the, from the fit extracted, mechanical linewidth $\gamma_{1,1}$, resonance frequency $\omega_{1,1}$ and the coupling strengths $g_{1,1}$.

In the following, the fit procedure is outlined. The mechanical resonance frequency $\omega_{1,1}$, linewidth $\gamma_{1,1}$, and mechanical coupling strength $g_{1,1}$ of the (1,1) membrane mode are determined by globally fitting the magnitude and phase response of the transfer function H_{OMIT} to the measured data. The fit was accomplished by a least-square method, which uses initial guessed values for κ, Δ, and C_{OMIT}, obtained from

[26] Globally refers to the simultaneous fitting of multiple datasets, which share the same parameters.
[27] Done with MATLAB - The Math Works, Inc. MATLAB. Version 2019a, The Math Works, Inc., 2020. Computer Software.

the fit to the broad OMIT-response (equation (4.42) and Figure 4.20). Remarkably[28], the fit values for κ, Δ, and C_{OMIT} extracted from the narrow transfer function H_{OMIT} and the phase response $arg(H_{\mathrm{OMIT}}(\omega))$ around the mechanical features (e.g., Figure 4.21) are found to be consistent with the initial estimates, falling within their confidence intervals.

The extracted values are presented in Figure 4.21 and Table 4.2. Additionally, the effective linewidth $\gamma_{1,1}^{\mathrm{eff}} = \gamma_{\mathrm{m}} + \Gamma_{\mathrm{opt}}$ and frequency shift $\delta\Omega_{1,1} = \omega_{1,1} - \omega_{1,1}^{\mathrm{eff}}$ are depicted in Figure 4.21. These values are calculated using the fit values according to Equation (2.123).

The measurement principle and fit process are repeated for 13 membrane modes (dip-peak features), and detailed data and fits are provided in Appendix D. Table 4.2 presents the extracted parameters of these measurements. The extracted values for κ, Δ, and C_{OMIT} remain consistent with the initial estimates for all fits; therefore, they are not included in Table 4.2.

modenumber	$\omega_{\mathrm{m,n}}/(2\pi)$	$\gamma_{\mathrm{m,n}}/(2\pi)$	$g_{\mathrm{m,n}}/(2\pi)$	$Q_{\mathrm{m,n}}[10^5]$
1,1	393.2 kHz	(3.2 ± 0.4) Hz	(55.58 ± 1.04) kHz	1.22 ± 0.15
1,2	622.9 kHz	(5.0 ± 1.7) Hz	(77.1 ± 0.8) kHz	1.24 ± 0.42
2,1	621.0 kHz	(2.6 ± 1.2) Hz	(21.9 ± 0.2) kHz	2.39 ± 1.10
2,2	787.7 kHz	(2.0 ± 0.6) Hz	(62.2 ± 0.3) kHz	3.94 ± 1.18
1,3	881.1 kHz	(1.6 ± 0.3) Hz	(47.0 ± 0.8) kHz	5.51 ± 1.03
3,1	-	-	-	-
2,3	1004.3 kHz	(4.4 ± 1.2) Hz	(44.58 ± 0.65) kHz	2.28 ± 0.62
3,2	1001.5 kHz	(7.4 ± 1.7) Hz	(15.82 ± 0.23) kHz	1.35 ± 0.31
3,3	1180.1 kHz	(1.5 ± 0.2) Hz	(6.6 ± 0.5) kHz	7.87 ± 1.05
1,4	1148.9 kHz	(8.7 ± 0.2) Hz	(13.3 ± 0.3) kHz	1.32 ± 0.03
4,1	1145.0 kHz	(6.0 ± 0.2) Hz	(28.3 ± 0.7) kHz	1.91 ± 0.06
2,4	1245.4 kHz	(5.2 ± 2.9) Hz	(17.7 ± 0.5) kHz	2.40 ± 1.34
4,2	1242.6 kHz	(4.1 ± 2.4) Hz	(38.9 ± 0.1) kHz	3.03 ± 1.48
3,4	1392.6 kHz	(6.1 ± 2.2) Hz	(44.6 ± 0.7) kHz	2.28 ± 0.82
4,3	1388.94 kHz	(4.6 ± 1.8) Hz	(29.0 ± 0.7) kHz	2.28 ± 0.82
4,4	1573.36 kHz	(1.5 ± 0.5) Hz	(8.0 ± 0.4) kHz	10.49 ± 3.50

TABLE 4.2: From OMIT measurement extracted resonance frequency $\omega_{\mathrm{m,n}}$, mechanical linewidth $\gamma_{\mathrm{m,n}}$ and coupling strengt $g_{\mathrm{m,n}}$ of 13 different membrane modes. Due to a measurement error, it was not possible to determine the parameters for the (3,1)-mode.

The errors in Table 4.1 indicate the 95% confidence interval of the fit values. The uncertainty of the deduced different membrane mode resonance frequencies ω_{m} is not given, as it lies in the sub-Hz regime. Contrary, the uncertainty of the mechanical linewidth $\gamma_{\mathrm{m,n}}$ is relatively large. This could be improved by taking additional measurements around the resonance frequencies $\omega_{\mathrm{m,n}}$ with higher resolution bandwidth.

[28] Remarkably also, because all fit functions used unbounded fit parameters.

However, the measurement time for each resonance was already approximately 15 min. From the different membrane mode resonance frequencies $\omega_{m,n}$ given in table 4.1, one can infer that the membrane is not perfectly square, as, for example, the (2,1) and (1,2)-mode frequency $\omega_{1,2}$ and $\omega_{2,1}$ are not degenerate (explained in 4.1).

Also, Table 4.2 reveals varying coupling strengths $g_{m,n}$ between different membrane modes of resonance frequency $\omega_{m,n}$. This variation arises from the different spatial overlaps between the Gaussian beam profile of the intracavity field and the membrane mode profiles (Figure 4.2), which is discussed next. The spatial overlap integral $\eta_{m,n}$, is defined as follows [Nie+17]:

$$\eta_{m,n}(x,y) = exp\left[-\frac{w_0(x_m)^2}{8}(m^2k_x^2 + n^2k_y^2)\right]\sin(mk_x x)\sin(nk_y y)\,, \tag{4.43}$$

where $k_{x,y} = \frac{\pi}{L_{x,y}}$, and $L_{x,y}$ represent the sidelengths in the x and y directions, respectively. The parameter $w_0(x_m)$ corresponds to the waist size of the beam at the membrane position x_m [KL66]. The coordinates x and y denote the beam position on the membrane, with the origin $(0,0)$ located at the middle of the membrane ($L_x/2$ and $L_y/2$).

Considering the overlap-integral, the optomechanical coupling strength $g_{m,n}$ given by (compare with Equation (2.112))

$$g = \sqrt{2}\frac{\delta\omega_{MatE}}{\partial x_m}x_{zpf}\alpha \rightarrow g_{m,n} = \sqrt{2}\eta_{m,n}(x,y)\frac{\delta\omega_{MatE}}{\partial x_m}x_{zpf}\alpha\,. \tag{4.44}$$

Hence, due to the overlap integral, the coupling strength $g_{m,n}$ of different membrane modes m,n differs.

By employing a likelihood function, the beam position on the membrane can be estimated based on the varying coupling strengths $g_{m,n}$. The detailed procedure is outlined in [Nie+17]. Figure 4.22 presents the result in this context. For the calculation, shown in Figure 4.22 a waist size of $w_0(x_m) = 56\,\mu m$ and a side length of $L_x = L_y = 1050\,\mu m$ has been used[29].

[29] Inferred from a microscope picture.

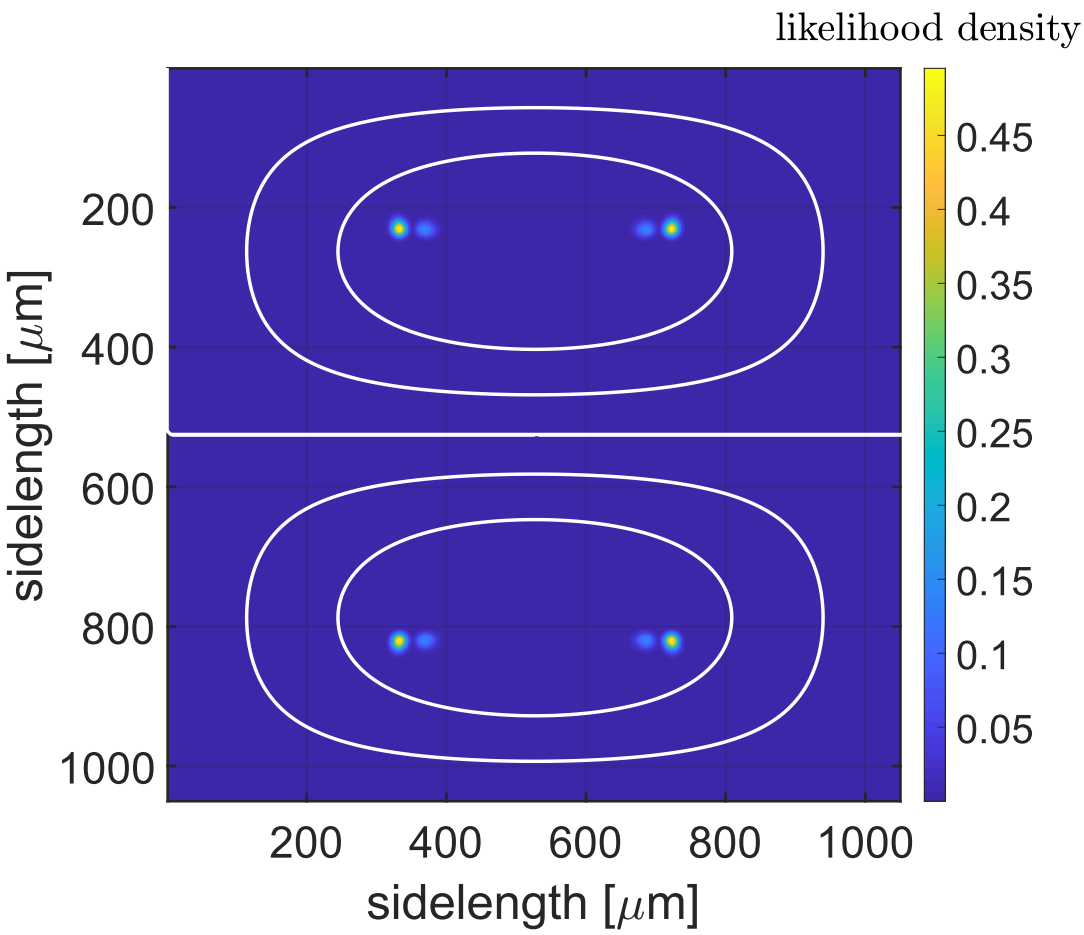

FIGURE 4.22: Estimated beam position. White contour shows the (1,2)-mode displacement pattern pattern.

Figure 4.22, shows the estimated beam position (bright spots), suggested by the likelihood function used from [Nie+17], together with the mode-pattern of the (1,2) - mode. It shows that the beam incident is close to the (1,2)-mode of the membrane. The membrane was intentionally coarsely adjusted to this position, as more modes could be measured at this position due to the overlap.

In summary, this section explained the OMIT measurement. It revealed that the OMIT measurement enables quick and fast access to the most relevant optomechanical parameters, especially to the light-enhanced coupling strength $g_{\mathrm{m,n}}$. The coupling strength g will be measured in the next section by measuring the consequences of the dynamical backaction.

Before describing the dynamical backaction experiment, it is important to note that the membrane's usability for quantum backaction noise-limited experiments is inadequate. All values in Table 4.2 and the cavity linewidth κ (Equation (4.42)), assuming a temperature of 4 K, result in a quantum cooperativity (Equation (2.168)) $C_{\mathrm{qba}}^{m,n} = \frac{\hbar g_{m,n}^2}{k_{\mathrm{B}} T \kappa} Q_{m,n} \not> 1$. This indicates that the membranes are unsuitable for a quantum backaction limited experiment at 4 K. However, this thesis investigates only this membrane to demonstrate that the characterisation and measurement principles work. For future quantum backaction limited experiments, one should consider replacing the membrane with a high-Q mechanical oscillator, similar to the one used in [Mas+19].

4.3.2 Dynamical backaction measurements

Within this section dynamical backaction (DBA) is used, to deduce the optomechanical coupling strength g. Therefore, the experimental setup, depicted in Figure 4.23, is used and will be explained in the following.

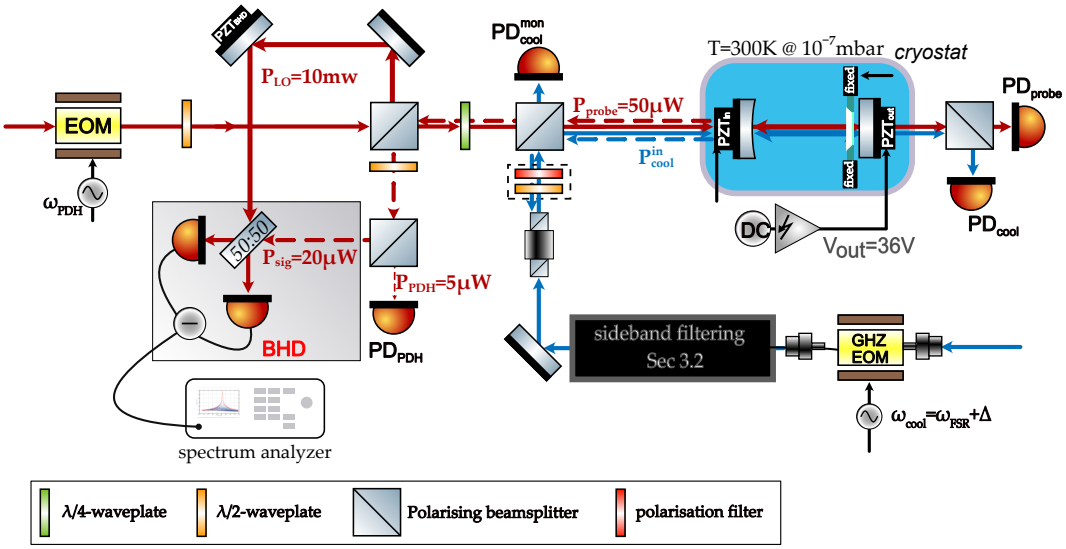

FIGURE 4.23: Sketch of the experimental DBA measurement setup, consisting of a balanced homodyne detector (BHD), a cryostat (used as a vacuum chamber) containing the MatE system and the probe and cooling beam send to the MatE system. Dashed lines indicating the reflected field of the MatE system. The black box indicates the generation of the cooling beam (described in Section 3.2).

The optomechanical system (OMS), shown in Figure 4.23, is placed inside a cryostat. Since it was not possible to lock the cavity at 4 K[30], the cryostat was used as a vacuum chamber, which at 300 K ensured a pressure of 10^{-7} mbar. As explained in Section 4.2.3, the membrane position was set by the DC voltage $V_{\text{out}} = 36.45\,\text{V}$ applied to the PZT_{out}. As depicted in Figure 4.23, within the DBA experiment three beams are used: The local oscillator beam (LO) (red), a probe beam (red), and a cooling beam (blue). The utility of these beams is explored next, commencing with the probe beam and LO beam.

The probe beam, with a power of $P_{\text{probe}} = 50\,\mu\text{W}$, originates from the same source as the local oscillator field, which has a power of $P_{\text{LO}} = 10\,\text{mW}$. Hence, as the name suggests, the local oscillator is used within the balanced homodyne detection scheme (theory in Section 2.3.2), whereas the probe beam is used to probe the membrane's dynamics and to establish an on-resonance lock ($\Delta = 0$) for the optomechanical system. Also, the probe field in reflection of the OMS, from the optomechanical cavity is split into two parts: one part, containing most of the power, is sent to the homodyne detector as the signal field (Section 2.3.2), as it contains information on the membrane dynamics in its phase quadrature[31]. The other part is detected by the detector PD_{PDH} to generate a Pound-Drever-Hall (PDH) error signal [Dre+83] to lock the optomechanical system. The PDH error signal is fed to the piezoelectric actuator PZT_{in} attached to the OMS input mirror to establish the lock on resonance.

[30] Probably due to the dynamic range of the piezo, which drops to 10% at 4 K or due to broken glueing joints during cooldown.

[31] Still assuming the optomechanical system is locked on resonance.

In the following, the spectrum measured by the balanced homodyne detector, in the absence of the cooling beam, will be discussed . After locking the cavity using the PDH technique, the balanced homodyne detector (BHD) angle θ needs to be adjusted to measure the phase quadrature spectrum $\bar{S}_{\hat{Y}^{\text{out}}_{\text{om,L}},\hat{Y}^{\text{out}}_{\text{om,L}}}(\omega)$ (Equation (2.74)).

For a homodyne angle of $\theta = \frac{\pi}{2}$, the measured homodyne spectrum $S_{\text{VV}}^{\theta=\frac{\pi}{2}}(\omega)$ is proportional to the phase quadrature spectrum $\bar{S}_{\hat{Y}^{\text{out}}_{\text{om,L}},\hat{Y}^{\text{out}}_{\text{om,L}}}(\omega)$[32] and thus serves as a measure of the membrane's dynamics (see Equation (2.162c)). Hence, in the DBA experiment, the homodyne angle is locked to $\theta = \frac{\pi}{2}$, facilitated by the piezoelectric-actuated mirror PZT_{BHD}. Once the homodyne detector (BHD) and the optomechanical system (by PHD errors signal) are locked, the resulting measured BHD spectrum $S_{\text{VV}}^{\theta=\frac{\pi}{2}}(\omega)$ of the probe beam is sent to a spectrum analyser[33], which measures a spectrum in units of V^2/Hz.

Before discussing the cooling beam, it is explained how the mechanical resonance frequency ω_{m} and linewidth γ_{m} are deduced from the measured BHD spectrum $S_{\text{VV}}^{\theta=\frac{\pi}{2}}(\omega)$. Explicitly, the measured phase quadrature $\theta = \pi/2$ is given by $\bar{S}_{\hat{Y}^{\text{out}}_{\text{om,L}},\hat{Y}^{\text{out}}_{\text{om,L}}}(\omega)$ (Equation (2.158))

$$S_{\text{VV}}^{\theta=\frac{\pi}{2}}(\omega) = C \cdot \bar{S}_{\hat{Y}^{\text{out}}_{\text{om,L}},\hat{Y}^{\text{out}}_{\text{om,L}}}(\omega) \tag{4.45}$$

$$= C \cdot \left(\frac{1}{2} + G_{\text{om}}(\omega)|\chi_{\text{m}}(\omega)|^2 \left(\frac{G_{\text{om}}(\omega)}{2} + \gamma_{\text{m}}\{\bar{S}_{\hat{\mathcal{F}}_{\text{th}},\hat{\mathcal{F}}_{\text{th}}} + \bar{S}_{\hat{\mathcal{F}}_{\text{sig}},\hat{\mathcal{F}}_{\text{sig}}}\}\right)\right) \tag{4.46}$$

$$\approx C \cdot \left(\frac{1}{2} + |\chi_{\text{m}}(\omega)|^2 \underbrace{G_{\text{om}}(\omega_{\text{m}})\bar{S}^{\Delta=0}_{\hat{\mathcal{F}}_{\text{ext}},\hat{\mathcal{F}}_{\text{ext}}}(\omega)}_{\text{const.}}\right) . \tag{4.47}$$

In the last step (Equation (4.47))[34], the generally frequency-dependent optomechanical measurement strength $G_{\text{om}}(\omega)$[35] is treated as frequency-independent in the vicinity (the measurement range) of the mechanical resonance frequency $\omega_{\text{m,n}}$. A measurement of the spectrum $S_{\text{VV}}^{\theta=\frac{\pi}{2}}(\omega)$ in the absence of the cooling beam is depicted in Figure 4.24. This measurement and the following measurement in Section 4.3.2.1 and 4.3.2.2 are in a frequency range around the resonance frequency $\omega_{1,3}$ of the (1,3)-mode of the membrane. Thus within the presented DBA measurements in Section 4.3.2.1 and Section 4.3.2.2, only the (1,3)-mode and its coupling strength $g_{1,3}$ is investigated.

[32] Proportional to the power of the LO (see Equation (2.74)) and the gain of the photodetector.
[33] Keysight N9010B.
[34] $\bar{S}^{\Delta=0}_{\hat{\mathcal{F}}_{\text{ext}},\hat{\mathcal{F}}_{\text{ext}}}$ given in Equation (2.162). General expression given in footnote 60.
[35] $G_{\text{om}} = \frac{g^2\kappa}{\frac{\kappa^2}{4}+\omega^2}$ (Equation (2.160)).

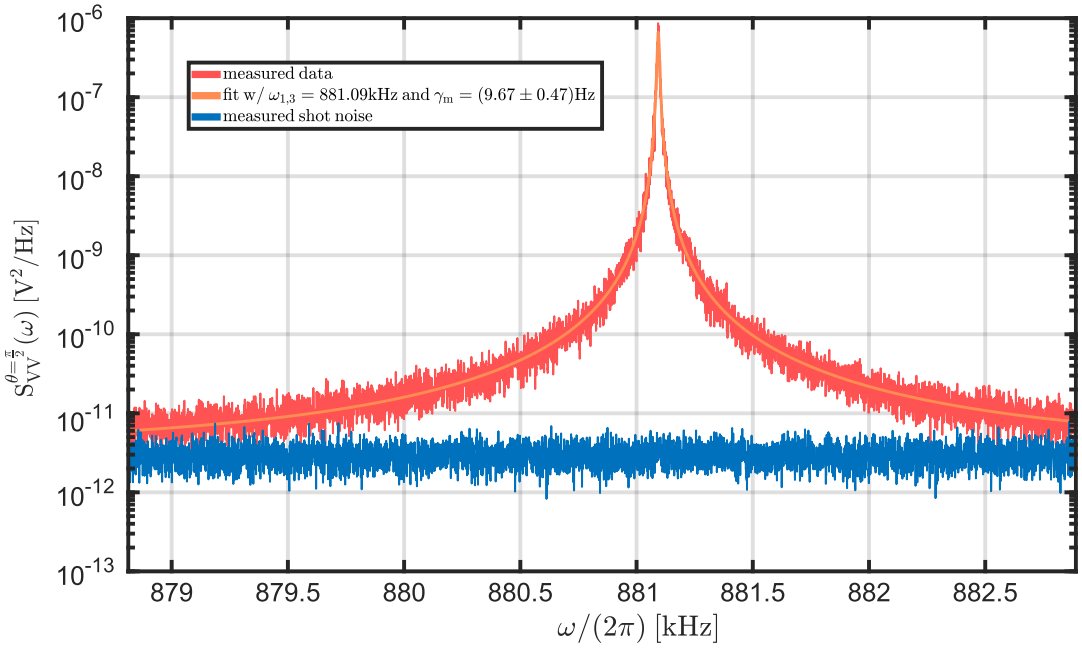

FIGURE 4.24: Measured homodyne spectrum $S_{VV}^{\theta=\frac{\pi}{2}}(\omega)$ and the measured shot noise detected at the balanced homodyne detector. The orange line represents the Lorentzian fit, from which the mechanical resonance frequency $\omega = \omega_{1,3} = 881.09\,\text{kHz}$ and linewidth $\gamma_m = (9.67 \pm 0.47)\,\text{Hz}$ of the 1,3-membrane mode is deduced.

Figure 4.24 shows a measurement of the shot noise (SN), for which the signal path was blocked[36]. After subtraction of the uncorrelated shot noise from $S_{VV}^{\theta=\frac{\pi}{2}}(\omega)$ (Equation (4.47)), the remaining spectrum is expressed by

$$\begin{aligned} S_{VV}^{\theta=\frac{\pi}{2},\,-SN}(\omega) &= C \cdot |\chi_m(\omega)|^2 G_{om}(\omega_m) \bar{S}^{\Delta=0}_{\hat{\mathcal{F}}_{ext},\hat{\mathcal{F}}_{ext}}(\omega) \\ &= C_{fit} |\chi_m(\omega)|^2 , \end{aligned} \tag{4.48}$$

with the newly defined constant $C_{fit} = C \cdot \bar{S}^{\Delta=0}_{\hat{\mathcal{F}}_{ext},\hat{\mathcal{F}}_{ext}}(\omega)$. The right side of Equation (4.48) explicitly reads

$$C_{fit} \cdot |\chi_m(\omega)|^2 = C_{fit} \cdot \frac{\omega_m^2}{(\omega_m^2 - \omega^2)^2 + \gamma_m^2 \omega^2} \tag{4.49}$$

and reveals that with a fit the mechanical resonance frequency ω_m and linewidth γ_m are deduced. Using a least square fit, the mechanical resonance frequency ω_m and linewidth γ_m is given by

$$\omega_{1,3}/(2\pi) = 881.09\,\text{kHz} \text{ and } \gamma_m/(2\pi) = (9.67 \pm 0.47)\,\text{Hz}\,, \tag{4.50}$$

where the error indicates the 95% confidence interval. No error is given for resonance frequency ω_m as this error is in the sub-Hz range.

In the following, the cooling beam will be introduced, which alters the mechanical susceptibility $\chi_m(\omega)$ due to dynamical backaction (Section 2.5.2). As discussed in Section 2.5.2 and visualised in Figure 2.11, a resonantly locked field, like the probe beam, does not alter the mechanical susceptibility χ_m. However, the susceptibility

[36] Note: The shot noise is also well above electronic noise.

is altered if the cavity is detuned with respect to the light field. For example, if the cavity is red-detuned[37] ($\Delta_{\text{cool}} > 0$), the dynamical backaction causes an increase of the effective linewidth $\gamma_{\text{eff}} > \gamma_{\text{m}}$, which effectively cools the membrane (see Section 2.5.3). As the name suggests, the cooling beam only generates cooling, as it remains within the DBA experiment red-tuned with respect to the cavity resonance frequency.

Next, the creation of the cooling beam detuning Δ_{cool} is briefly outlined. The detuning $\Delta_{\text{cool}} = \omega_{\text{cav}} - \omega_{\text{cool}}$ of the cooling beam to the optomechanical cavity resonance frequency ω_{cav} is accomplished by changing the frequency ω_{cool} of the cooling beam. The frequency of the cooling beam ω_{cool} is generated by a fiber-coupled GHz-EOM, which is driven at a frequency ω_{mod} in conjunction with a filter cavity (black box in Figure 4.23 and explained in Section 3.2). The filter cavity isolates a sideband solely oscillating at $\omega_0 + \omega_{\text{mod}}$ or $\omega_0 - \omega_{\text{mod}}$ from a phase-modulated field, which serves then as the cooling beam for the DBA experiment. Thereby, the frequency of the cooling beam can be altered by changing the modulation frequency ω_{mod} of the GHz-EOM.

How the cooling beam is explicitly used within the experiment and how the measurement of the altered susceptibility $\chi_{\text{eff}}(\omega)$ is done is outlined in the following. In the presented DBA experiment, the cavity is locked on resonance with respect to the probe beam, with frequency $\omega_0 = \omega_{\text{cav}} = N\omega_{\text{FSR}}$. Here ω_{cav} is the resonance frequency of the optomechanical system[38] (Section 4.2.1), ω_{FSR} the free spectral range in angular units and $N \in \mathbb{Z}$. The frequency of the cooling beam is then shifted with respect to the probe beam. The frequency of the cooling beam is hence given by $\omega_{\text{cool}} = \omega_0 + \omega_{\text{mod}}$. During the measurement presented in Section 4.3.2.1 and Section 4.3.2.2 the frequency of the cooling beam is set to $\omega_{\text{cool}} = \omega_0 + \omega_{\text{FSR}} + \Delta_{\text{cool}}$ [39]. Here, the FSR is $\omega_{\text{FSR}} = 3.112\,90\,\text{GHz}$ and its measurement is explained in Section 4.2.3. Hence, the cooling beam is detuned by Δ_{cool} to the cavity resonance $\omega_{\text{cav}} + \omega_{\text{FSR}}$ and alters the mechanical susceptibility due to dynamical backaction.

As the cooling beam and probe beam are independent of each other (different frequency and orthogonal polarisation), the probe beam probes the change of the mechanical susceptibility solely induced by the dynamical backaction of the cooling beam. To avoid dynamical backaction contributions of the probe beam, due to an unintentional small detuning, its power is also only $P_{\text{probe}} = 50\,\mu\text{W}$. On the other hand, the power of the cooling beam can be changed by the attenuator in the form of a polarisation filter in conjunction with a $\lambda/2$ wave plate[40] (dashed box in Figure 4.23), whereas the detuning Δ_{cool} can be changed by the modulation frequency of the GHz-EOM. For the measurements of dynamical backaction, the input power of the cooling beam $P_{\text{cool}}^{\text{in}}$ was calibrated with the photodetector $PD_{\text{cool}}^{\text{mon}}$. Its calibration curve used for the experiment in Section 4.3.2.1 is shown in Figure 4.25. The light power $P_{\text{cool}}^{\text{in}}$ measured in this calibration curve (red crosses) also denotes the power which is used in the DBA measurement in Section 4.3.2.1. Also, for the experiment described in Section 4.3.2.2, the power $PD_{\text{cool}}^{\text{mon}}$ is monitored to keep track of the input cooling power $P_{\text{cool}}^{\text{in}}$.

[37] Detuning is generally defined in this thesis by $\Delta = \omega_{\text{cav}} - \omega_0$, with ω_{cav} being the resonance frequency of the cavity and ω_0 being the laser frequency.

[38] For readability ω_{cav} is written. However as the optomechanical system is the MatE-system described in Section 4.2.1: $\omega_{\text{cav}} = \omega_{\text{MatE}}$.

[40] The polarising filter also "cleans" the polarisation of the cooling beam.

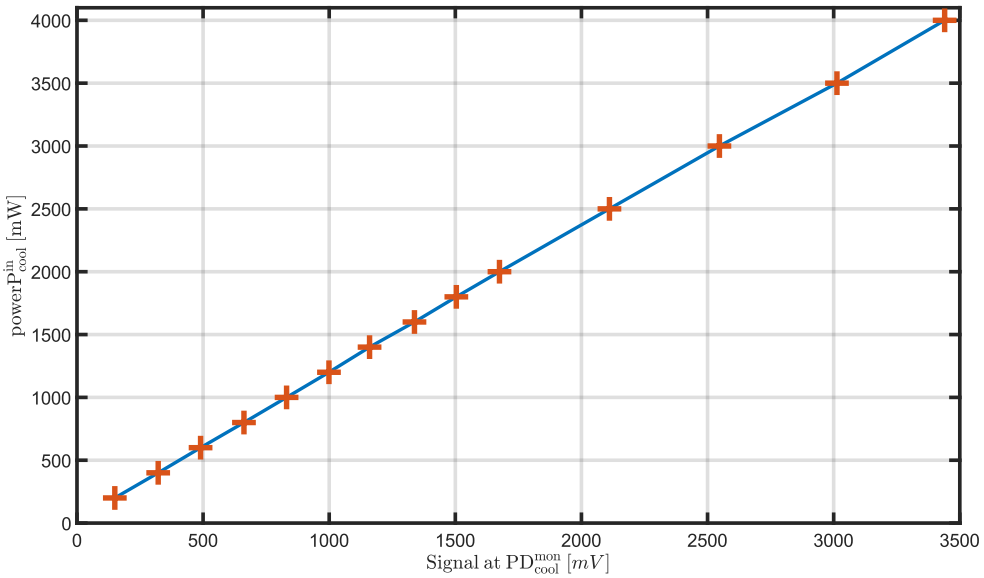

FIGURE 4.25: Input power P^{in}_{cool} of the cooling beam over measured voltage of photodetector PD^{mon}_{cool}

To keep track of the resonance condition of the optomechanical system, the power of the cooling and probe beam is monitored separately in transmission via PD_{cool} and PD_{probe}, respectively. As the probe beam probes the membrane dynamics altered solely by the cooling beam ($\chi_m \rightarrow \chi_{eff}$), the measured BHD quadrature spectrum $S^{\theta=\frac{\pi}{2}}_{VV}(\omega)$ becomes (compare Equation (4.47))

$$S^{\theta=\frac{\pi}{2}}_{VV}(\omega) \approx C \cdot \left(\frac{1}{2} + |\chi_{eff}(\omega)|^2 \underbrace{G_{om}(\omega_m) \bar{S}^{total}_{\hat{\mathcal{F}}_{ext},\hat{\mathcal{F}}_{ext}}(\omega)}_{\text{const.}} \right) , \tag{4.51}$$

[41] with (see Equation (2.122))

$$|\chi_{eff}(\omega)|^2 = \frac{\omega_m^2}{(\omega_{eff}^2(\Delta_{cool}, g_{cool}) - \omega^2)^2 + \gamma_{eff}^2(\Delta_{cool}, g_{cool})\omega^2} . \tag{4.52}$$

Hence, as in the case with no cooling beam, after subtraction of the uncorrelated shot noise from $S^{\theta=\frac{\pi}{2}}_{VV}(\omega)$, the resulting spectrum is given by

$$S^{\theta=\frac{\pi}{2},\,-SN}_{VV}(\omega) = C_{fit}|\chi_{eff}(\omega)|^2 . \tag{4.53}$$

Thus, by fitting the measured data to $S^{\theta=\frac{\pi}{2},\,-SN}_{VV}(\omega)$, the effective mechanical resonance frequency ω_{eff} and effective mechanical linewidth γ_{eff} is inferred.

As suggested by (4.52) the effective resonance frequency $\omega_{eff}(\Delta_{cool}, g_{cool})$ and linewidth $\gamma_{eff}(\Delta_{cool}, g_{cool})$ depends on the detuning Δ_{cool} and coupling strength g_{cool}

[41] $\bar{S}^{total}_{\hat{\mathcal{F}}_{ext},\hat{\mathcal{F}}_{ext}}(\omega)$ contains also quantum backaction noise from the probe $\left(\bar{S}^{probe,\Delta=0}_{qba} = 2\Gamma^{probe,\Delta=0}_{QBA}\right)$ and cooling beam $\left(\bar{S}^{probe,\Delta=0}_{qba} = 2\Gamma^{cool,\Delta}_{QBA}\right)$ (see Section 2.6.4, especially Equation (2.232) - (2.234)).

(Equation (2.123). Described in Equation (2.112) and (2.105a), the coupling strength g_{cool} depends on the input power $P_{\mathrm{cool}}^{\mathrm{in}}$ of the cooling beam. Therefore, by measuring the alteration induced by the cooling beam of the mechanical susceptibility the coupling strength g_{cool} can be deduced. This is done in the following by employing two different experiments. In Section 4.3.2.1 the detuning Δ_{cool} of the cooling beam is fixed, while its power $P_{\mathrm{cool}}^{\mathrm{in}}$ is changed, whereas in Section 4.3.2.2 the power $P_{\mathrm{cool}}^{\mathrm{in}}$ is fixed, but the detuning Δ_{cool} is changed.

4.3.2.1 Dynamical backaction - power series

In this section the spectrum $S_{VV}^{\theta=\frac{\pi}{2}}$ is measured for various power levels P_{cool}^{in}, while the cooling beam frequency remains fixed at $\omega_{cool} = \omega_0 + \omega_{FSR} + \frac{\kappa}{2}$[42]. As mentioned previously, the various used power levels P_{cool}^{in} are shown as red crosses in Figure 4.25. The measured, and, for representation, smoothed spectra[43] for these power levels are illustrated in blue in Figure 4.26. Here the shades of blue intensify to indicate increasing cooling power P_{cool}^{in}, while the red-coloured spectra are measured in the absence of the cooling beam (also depicted in Figure 4.24).

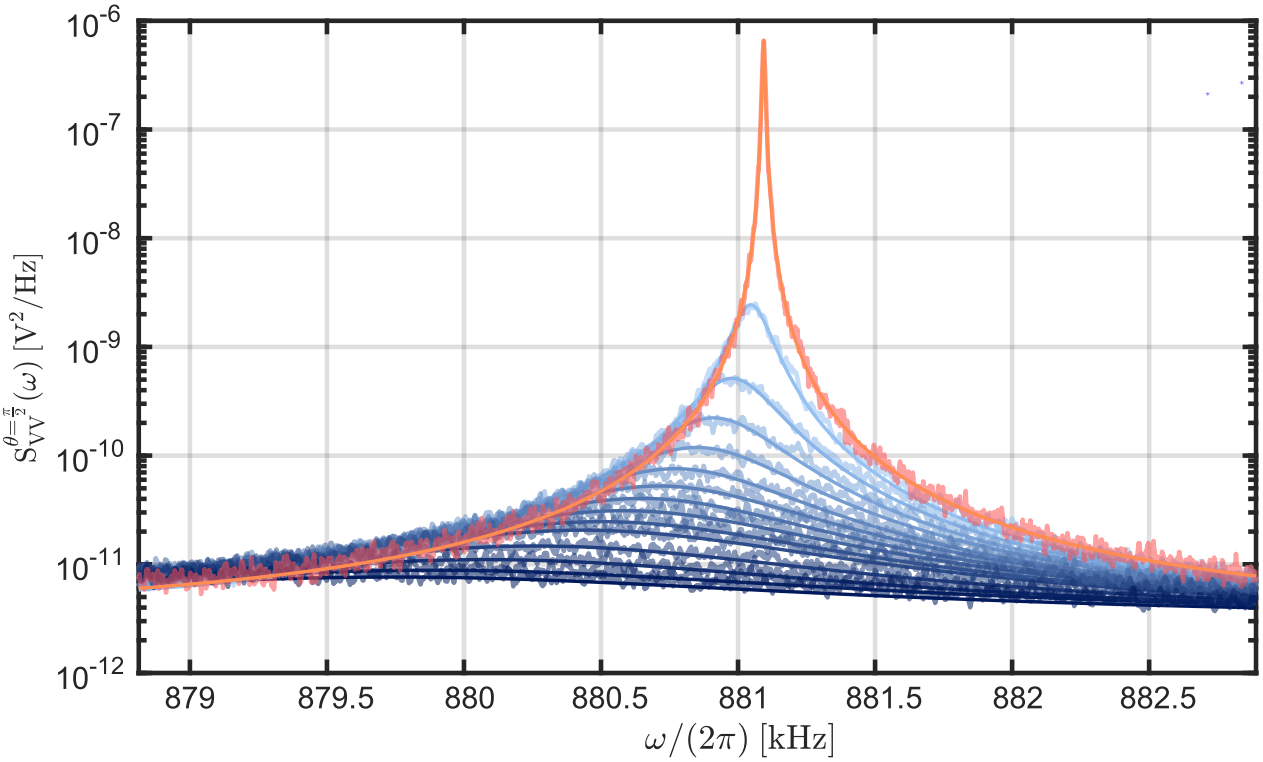

FIGURE 4.26: Measured homodyne spectra $S_{VV}^{\theta=\frac{\pi}{2}}(\omega)$ of the probe beam for different cooling beam powers P_{cool}^{in}. Shades of blue intensify to indicate increasing cooling power P_{cool}^{in}, while the red-coloured spectra are measured in the absence of the cooling beam.

From the blue spectra, the effects of sideband cooling and the frequency shift become visible, as the effective mechanical linewidth $\gamma_{eff,(1,3)}$ and the effective resonance frequency $\omega_{eff,(1,3)}$ of the (1,3)-membrane mode decreases with increasing cooling power P_{cool}^{in}. This behaviour is also supported by the theory in Equation (2.123) and Figure 2.11. Using a least square fit, as discussed in Section 4.3.2, the unaltered resonance frequency $\omega_{1,3}$ and linewidth $\gamma_{1,3}$ and the input power P_{cool}^{in} depended altered resonance frequency $\omega_{eff,(1,3)}$ and linewidth $\gamma_{eff,(1,3)}$ are deduced. From these values, the frequency shift $\delta\Omega_{1,3}$ and the optomechanical damping rate $\Gamma_{opt(1,3)}$

$$\delta\Omega_{1,3} = \omega_{eff,(1,3)} - \omega_m \quad \text{and} \quad \Gamma_{opt(1,3)} = \gamma_{eff(1,3)} - \gamma_{1,3}\,, \tag{4.54}$$

[42] $\kappa/2$ as the detuning Δ_{cool} was chosen to later compare DBA results with OMIT results (Section 4.3.1).

[43] Data is smoothed by a moving average filter. However, all presented least square fits are done to the non-smoothed data.

are extracted. The frequency shift $\delta\Omega_{1,3}$ and the optomechanical damping rate $\Gamma_{\text{opt},(1,3)}$ extracted from the spectra shown in Figure 4.26, for various cooling powers, are depicted in Figure 4.27.

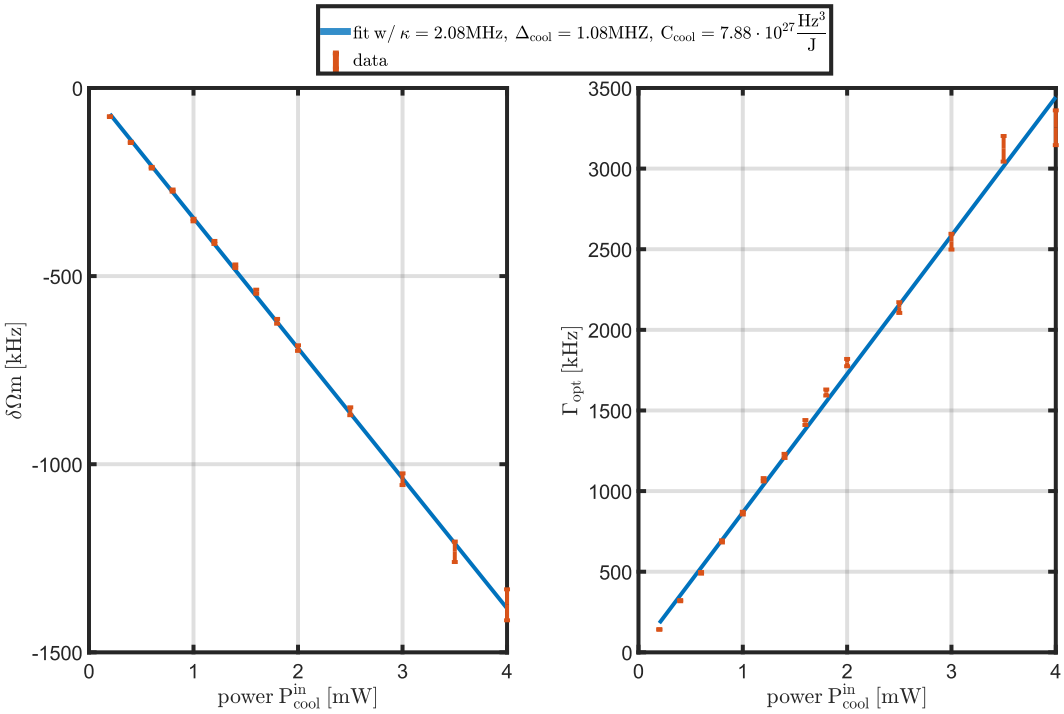

FIGURE 4.27: Left: Measured resonance frequency shift $\Delta_{1,3}$ (red) together with a least-square fit (blue) for different cooling beam power $P^{\text{in}}_{\text{cool}}$.
Right: Measured optomechanical damping rate $\Gamma_{\text{opt},(1,3)}$ (red) together with a least-square fit (blue) for different cooling beam power $P^{\text{in}}_{\text{cool}}$.

The deduced values of $\delta\Omega_{1,3}$ and $\Gamma^{\text{opt}}_{1,3}$ are depicted including errorbars, which indicate the 95% confidence interval.

The blue line is a fit to the data, which is explained in the following. As described in Section 2.5.2, the frequency shift $\delta\Omega_{1,3}$ and the optomechanical damping rate $\Gamma_{\text{opt},(1,3)}$, originating from DBA, are given by

$$\delta\Omega_{\text{m}} \approx -\frac{g^2_{\text{cool}}}{4}\left(\frac{\Delta_{\text{cool}}+\omega_{\text{m}}}{(\Delta_{\text{cool}}+\omega_{\text{m}})^2+\frac{\kappa^2}{4}}+\frac{\Delta_{\text{cool}}-\omega_{\text{m}}}{(\Delta_{\text{cool}}-\omega_{\text{m}})^2+\frac{\kappa^2}{4}}\right) \tag{4.55}$$

$$\Gamma_{\text{opt},(1,3)} \approx \frac{g^2_{\text{cool}}}{4}\left(\frac{\kappa}{(\Delta_{\text{cool}}-\omega_{\text{m}})^2+\frac{\kappa^2}{4}}-\frac{\kappa}{(\Delta_{\text{cool}}+\omega_{\text{m}})^2+\frac{\kappa^2}{4}}\right). \tag{4.56}$$

By using the definition of the optomechanical coupling strength g (Equation (2.112) and the intracavity field solution (2.105a), $g^2_{\text{cool}}(P^{\text{in}}_{\text{cool}})$ becomes,

$$g^2_{\text{cool}}(P^{\text{in}}_{\text{cool}}) = 2g^2_{\text{cool},0}|\alpha^{\text{cav}}_{\text{cool}}|^2 = \frac{C_{\text{cool}}}{\frac{\kappa^2}{4}+\Delta^2_{\text{cool}}}\cdot P^{\text{in}}_{\text{cool}} \tag{4.57}$$

with $g_{\text{cool},0}$ denoting the vacuum optomechanical coupling and $|\alpha^{\text{cav}}_{\text{cool}}|^2 = P^{\text{cav}}_{\text{cool}}$ the intracavity power of the cooling beam, and C_{cool} denoting a constant, containing also the input rates $\kappa^{\text{in}}_{\text{L}}$ (see Equation (2.105a)). Inserting Equation (4.57) into Equation (4.55) and (4.56) the cooling power depended resonance shift $\delta\Omega_{1,3}$ and the

optomechanical damping rate $\Gamma^{\text{opt}}1,3$ are expressed as

$$\delta\Omega_{1,3}(P^{\text{in}}_{\text{cool}}) \approx \frac{1}{4} \cdot \underbrace{\frac{C_{\text{cool}}}{\frac{\kappa^2}{4} + \Delta^2_{\text{cool}}} \cdot P^{\text{in}}_{\text{cool}}}_{g^{\text{cool}}_{1,3}} \cdot \left(\frac{\Delta_{\text{cool}} + \omega_{1,3}}{(\Delta_{\text{cool}} + \omega_{1,3})^2 + \frac{\kappa^2}{4}} - \frac{\Delta_{\text{cool}} - \omega_{1,3}}{(\Delta_{\text{cool}} - \omega_{1,3})^2 + \frac{\kappa^2}{4}} \right) \tag{4.58}$$

$$\Gamma^{\text{opt}}_{1,3}(P^{\text{in}}_{\text{cool}}) \approx \frac{1}{4} \cdot \underbrace{\frac{C_{\text{cool}}}{\frac{\kappa^2}{4} + \Delta^2_{\text{cool}}} \cdot P^{\text{in}}_{\text{cool}}}_{g^{\text{cool}}_{1,3}} \cdot \left(\frac{\kappa}{(\Delta_{\text{cool}} + \omega_{1,3})^2 + \frac{\kappa^2}{4}} - \frac{\kappa}{(\Delta_{\text{cool}} + \omega_{1,3})^2 + \frac{\kappa^2}{4}} \right) . \tag{4.59}$$

Equation (4.58) and (4.59) are used for a global least square fit to the measured values of the frequency shift $\delta\Omega_{1,3}(P^{\text{in}}_{\text{cool}})$ and the optomechanical damping rate $\Gamma_{\text{opt},(1,3)}(P^{\text{in}}_{\text{cool}})$ (see Figure 4.27). The resulting values, together with their 95% confidence interval, are given by

$$\kappa/(2\pi) = (2.08 \pm 0.04)\,\text{MHz} \tag{4.60}$$

$$\Delta_{\text{cool}}/(2\pi) = (1.08 \pm 0.06)\,\text{MHz} \tag{4.61}$$

$$C_{\text{cool}} = (7.88 \pm 0.01) \times 10^{27}\,\frac{\text{Hz}^3}{\text{J}} . \tag{4.62}$$

The inferred coupling strength $g^{\text{cool,infer}}_{1,3}(P^{\text{in}}_{\text{cool}})$ of the (1,3)-mode for different arbitrary input powers $P^{\text{in}}_{\text{cool}}$ is calculated by inserting the mean values of the extracted data into Equation (4.57) and are shown in Figure 4.28 (blue).

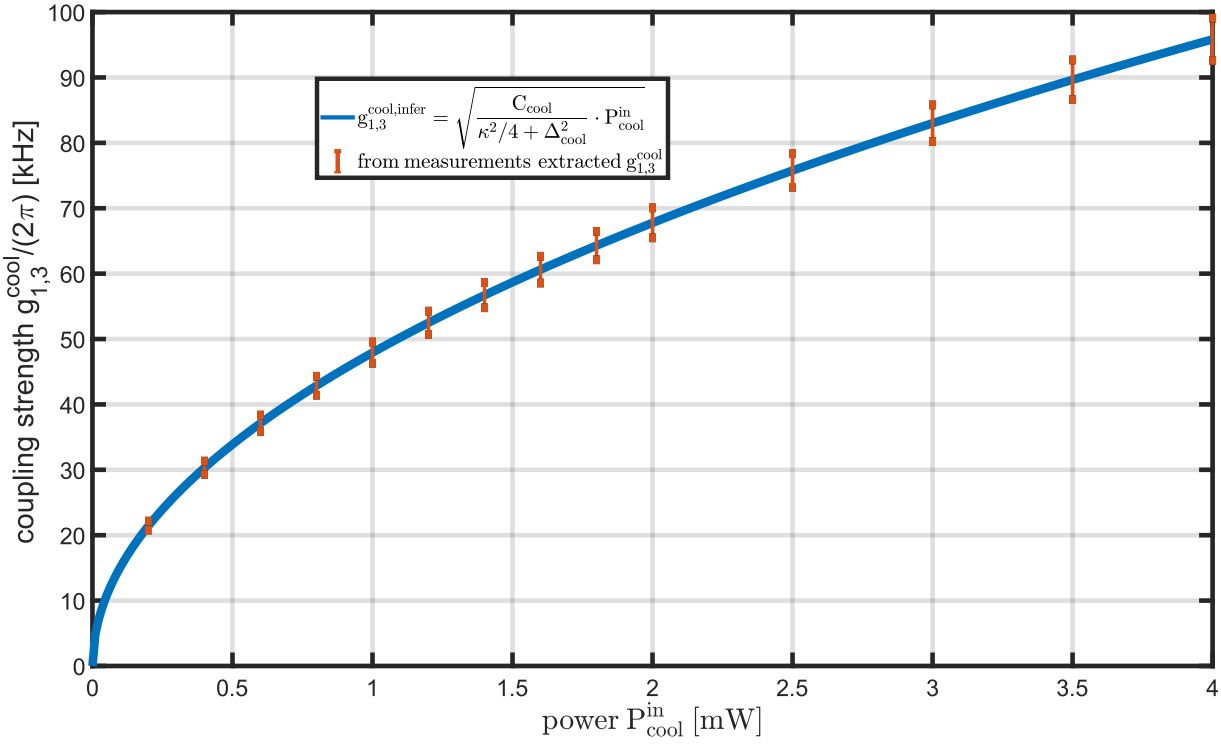

FIGURE 4.28: Optomechanical coupling strength g inferred from DBA measurement with fixed cooling beam detuning Δ_{cool} and varying cooling beam power $P^{\text{in}}_{\text{cool}}$.

Figure 4.28 also presents the coupling strength $g_{1,3}^{\text{cool}}$ calculated for the various powers used in this experiment, along with their corresponding errors (red). These errors are determined by propagation of uncertainties and lead to a relative error of $\pm 3.3\%$ for the coupling strength $g_{1,3}^{\text{cool}}$.

Comparing the extracted linewidth κ and the detuning Δ, reveals they agree with the values measured by the OMIT measurement (Equation (4.42)), when considering their uncertainties. Therefore, for the same input power, the coupling strengths $g_{1,3}^{\text{cool}}$ of the (1,3)-mode measured by this DBA experiment should be equal to the coupling strength deduced $g_{1,3}$ by the OMIT experiment (given in Table 4.2). For an input power of 1 mW the two coupling strength are given by

$$g_{1,3}^{\text{OMIT}}/(2\pi) = (47.0 \pm 0.8)\,\text{kHz} \tag{4.63}$$

$$g_{1,3}^{\text{cool,power}}/(2\pi) = (47.9 \pm 1.6)\,\text{kHz}\,. \tag{4.64}$$

Thus it is shown that the same coupling strengths from the DBA and the OMIT experiment are deduced for the (1,3)-mode of the membrane, and thereby, both techniques are useable to measure the coupling strength g. In the next Section 4.3.2.2, the DBA experiment is done with a different setting, in that the input power $P_{\text{cool}}^{\text{in}}$ remains constant and the detuning Δ_{cool} is changed.

4.3.2.2 Dynamical backaction - detuning series

In this section the spectrum $S_{\text{VV}}^{\theta=\frac{\pi}{2}}$ around the (1,3)-mode of the membrane is measured for various detunings Δ_{cool} of the cooling beam ($\omega_{\text{cool}} = \omega_0 + \omega_{\text{FSR}} + \Delta_{\text{cool}}$), while its power $P_{\text{cool}}^{\text{in}}$ is fixed to 1 mW. The fixed cooling beam power $P_{\text{cool}}^{\text{in}}$ was monitored on $PD_{\text{cool}}^{\text{mon}}$ to make sure, that the input power $P_{\text{cool}}^{\text{in}}$ remains constant, and to monitor, that the filter cavity (black box in Figure 4.23) does not fall out of lock, while the detuning Δ_{cool} is changed. During the experiment, the detected power on filter cavity remained constant while the detuning Δ_{cool} was changed, indicating that the filter cavity remained locked.

Spectra measurements, as described in Section 4.3.2, were taken for 40 different cooling beam detunings Δ_{cool}. After shot noise subtraction (Equation (4.53)) from the measured spectra, the effective resonance frequency ω_{eff} and the linewidth γ_{eff} were deduced by a least square fit (see Section 4.3.2). From these values the frequency shift $\delta\Omega_{1,3}$ and optomechanical damping rate $\Gamma_{\text{opt,(1,3)}}$ (Equation (4.50)) are calculated[44].

The measurement of the frequency shift $\delta\Omega_{1,3}$ and optomechanical damping rate $\Gamma_{1,3}^{\text{opt}}$ over the detuning Δ_{cool} is shown Figure 4.29

[44] $\omega_{1,3}$ and $\gamma_{1,3}$ given in Equation (4.50).

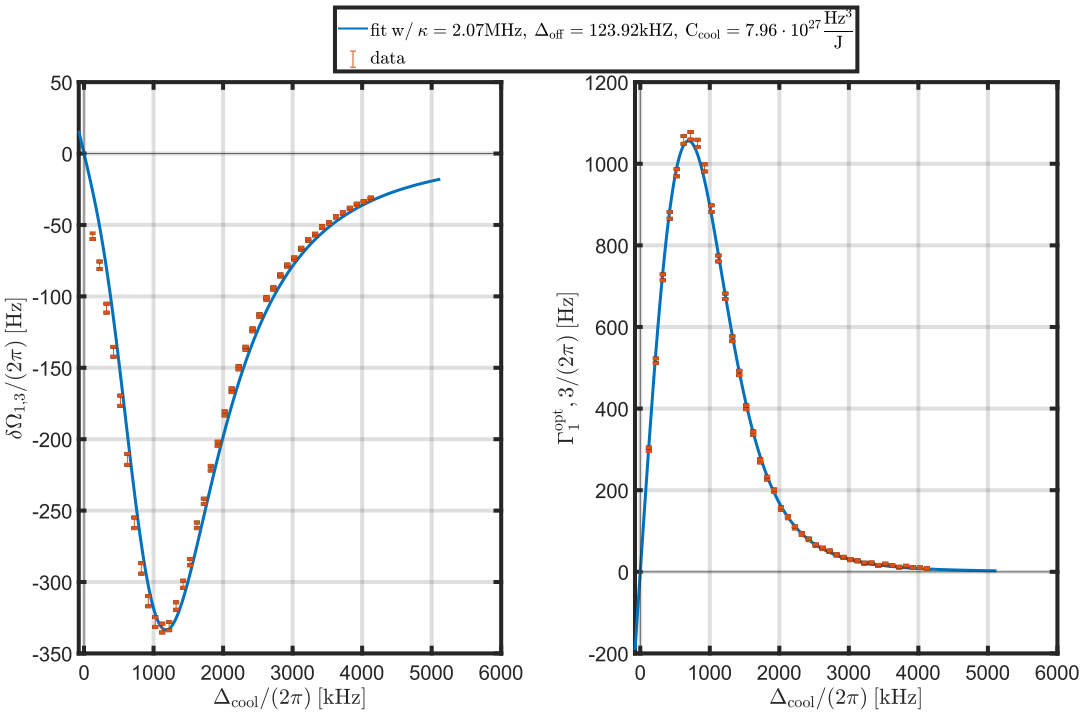

FIGURE 4.29: Left: Measured resonance frequency shift $\Delta_{1,3}$ (red) together with a least-square fit (blue) for different cooling beam detunings Δ_{cool}.
Right: Measured optomechanical damping rate $\Gamma_{opt,(1,3)}$ (red) together with a least-square fit (blue) for different cooling beam detunings Δ_{cool}.

In Figure 4.29, the measured frequency shift $\delta\Omega_{1,3}$ and optomechanical damping rate $\Gamma_{opt,(1,3)}$ are shown by red bars, which length indicates the 95% confidence interval. Also, a least-square fit (blue) to the measured data is shown, which is discussed in the following.

Different to Section 4.3.2.1, the detuning Δ_{cool} instead of the cooling power P_{cool}^{in} is changed. Thus the fit function of frequency shift $\delta\Omega_{1,3}$ and optomechanical damping rate $\Gamma_{opt,(1,3)}$ depends on the detuning and is given by (compare with Equation (4.58) and (4.59))

$$\delta\Omega_{1,3}(\Delta_{cool}) \approx \frac{1}{4} \cdot \underbrace{\frac{C_{cool}}{\frac{\kappa^2}{4} + (\Delta_{cool} + \Delta_{off})^2} \cdot P_{cool}^{in}}_{g_{1,3}^{cool}} \times \left(\frac{(\Delta_{cool} + \Delta_{off}) + \omega_{1,3}}{((\Delta_{cool} + \Delta_{off}) + \omega_{1,3})^2 + \frac{\kappa^2}{4}} - \frac{(\Delta_{cool} + \Delta_{off}) - \omega_{1,3}}{((\Delta_{cool} + \Delta_{off}) - \omega_{1,3})^2 + \frac{\kappa^2}{4}} \right) \tag{4.65}$$

$$\Gamma_{1,3}^{opt}(\Delta_{cool}) \approx \frac{1}{4} \cdot \underbrace{\frac{C_{cool}}{\frac{\kappa^2}{4} + (\Delta_{cool} + \Delta_{off})^2} \cdot P_{cool}^{in}}_{g_{1,3}^{cool}} \times \left(\frac{\kappa}{((\Delta_{cool} + \Delta_{off}) + \omega_{1,3})^2 + \frac{\kappa^2}{4}} - \frac{\kappa}{(\Delta_{cool} + \Delta_{off} + \omega_{1,3})^2 + \frac{\kappa^2}{4}} \right). \tag{4.66}$$

Here the value Δ_{off} takes an offset of the assumed detuning Δ_{cool} with respect to

the resonance frequency $\omega_{\text{cav}} + \omega_{\text{FSR}}$ into account. The resulting least-square fit parameters are

$$\kappa/(2\pi) = (2.07 \pm 0.07)\,\text{MHz} \tag{4.67}$$

$$\Delta_{\text{off}}/(2\pi) = (123.92 \pm 12.21)\,\text{kHz} \tag{4.68}$$

$$C_{\text{cool}} = (7.96 \pm 0.01) \times 10^{27}\,\frac{\text{Hz}^3}{\text{J}}\,. \tag{4.69}$$

As revealed by Equation (4.65) and Equation (4.66) the coupling strength is given by

$$\frac{C_{\text{cool}}}{\frac{\kappa^2}{4} + (\Delta_{\text{cool}} + \Delta_{\text{off}})^2} \cdot P_{\text{cool}}^{\text{in}}\,. \tag{4.70}$$

Hence, by using the extracted fit values (Equation (4.69)) the coupling strength can be calculated. The obtained coupling strengths are depicted in Figure 4.30.

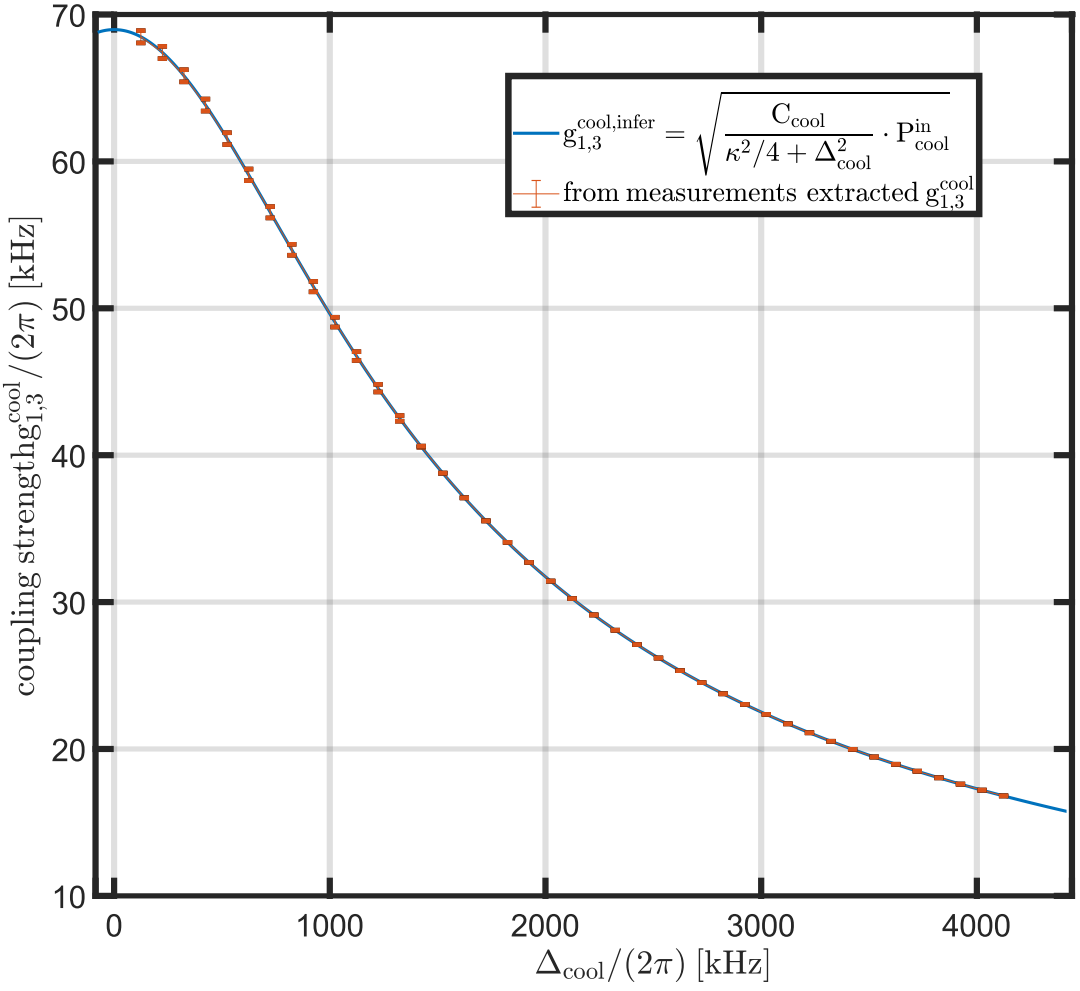

FIGURE 4.30: Optomechanical coupling strength g inferred from DBA measurement with fixed cooling beam power $P_{\text{cool}}^{\text{in}}$ and varying cooling beam detuning Δ_{cool}

Figure 4.28 presents the coupling strength $g_{1,3}^{\text{cool}}$ calculated for the various detuning Δ_{cool} in this experiment, along with their corresponding errors (red). These errors are determined by the propagation of uncertainties and lead to a relative error of $\pm 1\%$ for the coupling strength $g_{1,3}^{\text{cool}}$. The blue line indicates the coupling strength $g_{1,3}$, calculated with the extracted fit values (Equation (4.69)), for arbitrary detunings Δ_{cool}.

In conclusion, the DBA measurements presented in Section 4.3.2.1 and 4.3.2.2, reveal that it is possible to extract the coupling strength g of the optomechanical device. Also the DBA measurements imply, that an independent cooling beam can be created to alter the mechanical properties and which can thereby by used for an CQNC experiment with an additional cooling beam 2.6.4 Before Chapter 4 is closed, in the following, a brief comparison of the measured coupling strengths is discussed.

4.3.3 Comparison of coupling strength measurements

In the following, the coupling strengths $g_{1,3}$ measured within the OMIT experiment (Section 4.3.1) and measured by the DBA experiment at a detuning of$\Delta \approx 1\,\mathrm{MHz}$ and an input power of 1 mW are compared. With these settings used in all three experiments, the basic condition should be equal, allowing for a comparison of the results. The coupling strengths measured under these settings in the various experiments are given in Equation (4.71).

$$\begin{aligned} g_{1,3}^{\mathrm{OMIT}}/(2\pi) &= (47.0 \pm 0.8)\,\mathrm{kHz} \\ g_{1,3}^{\mathrm{cool,power}}/(2\pi) &= (47.9 \pm 1.6)\,\mathrm{kHz} \\ g_{1,3}^{\mathrm{cool,detuning}}/(2\pi) &= (49.05 \pm 0.50)\,\mathrm{kHz} \end{aligned} \tag{4.71}$$

Here $g_{1,3}^{\mathrm{OMIT}}$ denotes the measured coupling strength given in the OMIT experiment (Section 4.3.1), $g^{\mathrm{cool,power}}$ measured the coupling strength given in the DBA experiment with various cooling beam powers (Section 4.3.2.1) and $g^{\mathrm{cool,detuning}}$ the measured coupling strength for different cooling beam detunings Δ_{cool} within Section 4.3.2.2. By comparing the values given in Equation (4.71), it becomes apparent that the coupling strength measured in the last Section 4.3.2.2 differs slightly from the coupling strengths derived by the other experiments. Using the upper and lower bound of the coupling strengths given in Equation (4.71) the coupling strength $g_{1,3}^{\mathrm{all}}$ is given by $g_{1,3}^{\mathrm{all}} = (47.85 \pm 1.65)\,\mathrm{kHz}$. Thereby, it is shown that the measured coupling strength is almost the same for all three experiments and hence reveals that all of these techniques can be used to deduce the coupling strength g of the optomechanical system.

Chapter 5

Summary and outlook

This thesis focused on constructing and characterising an optomechanical system (OMS) with the aim of enabling all-optical coherent quantum noise cancellation (CQNC), first suggested by [TC10]. Initially, the fundamental principles of a coherent quantum noise cancellation scheme were outlined, and a theoretical investigation explored the potential benefits of using a second beam to modify the mechanical oscillator's dynamics in the OMS through dynamical backaction. The findings suggest that such modifications may be advantageous mainly in the resolved sideband regime. Due to the vast parameter space involved, further investigations were deemed necessary. Nevertheless, it is demonstrated, based on a case study by Schweer [Sch+22], that all-optical CQNC can be achieved without altering the optomechanical oscillator's dynamics by a second beam.

In the context of an all-optical CQNC experiment proposed in [Sch+22], the probe beam was assumed to be shot noise limited. To meet this condition experimentally, a filter cavity was set up in a double pass configuration to suppress amplitude noise. The results showed that the amplitude noise in transmission is shot noise limited above frequencies of 1 MHz at a power of 1 mW. Depending on the resonance frequency, of the mechanical oscillator in use, this is beneficial for a CQNC experiment. To decrease amplitude noise of the probe light further, a traditional active laser power stabilizing scheme can be implemented [KWD11].

The primary objective of this thesis was the development and characterisation of an optomechanical system as a subsystem of the Coherent Quantum Noise Cancellation experiment. The development of the optomechanical system was guided by realistic requirements and a parameter space proposed in a previous studies [Sch+22; Sch23; Ste19; Wim+14]. Consequently, special attention was given to achieving a high coupling efficiency between light and a silicon nitride membrane, representing a mechanical oscillator. Experimental investigations were carried out to determine the optimal position within the optomechanical system, at which the coupling strength g is highest. To determine g, two experiments were conducted. So far, measurements at cryogenic temperatures, a requirement for the OMS to be quantum backaction noise limited, could not be performed due to technical challenges related to locking the optomechanical system. These issue was possibly caused by the piezoelectric actuator's reduced dynamic range at 4K or broken glue joints during cool-down. Thus, operating the optomechanical oscillator in a cryogenic environment remains a pending task.

Nevertheless, even at room temperature and at a pressure of 10^{-7} mbar the measurements to characterise the optomechanical system were successfully performed. In the first experiment, the optomechanically-induced-transparency effect (OMIT) was employed to investigate the optical linewidth of the OMS and the resonance frequencies, quality factors, and optomechanical coupling strengths of thirteen resonating modes the membrane. The cavity's linewidth was found to satisfy the proposed value

of 2 MHz. However, the membrane proved unsuitable for an all-optical CQNC due to its quality factors in the order of $10^5 - 10^6$. These values do not meet the quantum backaction cooperativity requirement, even at 4K, suggesting that the system is limited by thermal noise rather than quantum backaction noise. As such, a promising oscillator candidate for CQNC should possess a high quality factor with a resonance frequency near 1 MHz [Sch+22] to be quantum backaction noise-limited at 4K.

Although the utilised membranes were unsuitable for CQNC, they were a valuable choice for characterising optomechanical cavity measurement techniques. The second experiment, making use of dynamical backaction (DBA), also provides crucial values relevant to CQNC. More precisely, it was demonstrated that both the DBA and OMIT measurements yielded consistent results for the linewidth and coupling strength. However, the dynamical backaction experiment was more time-consuming compared to OMIT, explaining the investigation of only one membrane mode as opposed to thirteen via OMIT measurements.

To address the uncertainty in the extracted linewidth from OMIT and DBA measurements, it is recommended to employ a ring-down measurement in the future. This allows for the extraction of quality factors with higher precision, especially for CQNC experiments that require higher quality factors, ensured by smaller mechanical linewidth [Jay+12]. Once cryogenic measurements become feasible, appropriate strategies should be employed to accurately measure the membrane's temperature, as it may differ from the cryostat temperature readings. Techniques like displacement calibration of the measured spectrum [Gor+10] and ponderomotive squeezing in the quantum backaction limited regime hold promise for achieving accurate temperature measurements. An additional technique, once the backaction limited regime is reached is given by quantum noise thermometry [Mas+19].

The determination of optical losses in the cavity remains a relevant task, which has not been addressed in this thesis. Accessible ponderomotive squeezing can be utilised to infer the losses' impact, as it is highly influenced by them.

In conclusion, the developed optomechanical system holds promise for realizing an all-optical CQNC experiment once optomechanical oscillators with higher quality factors are used, and cryogenic temperature operation becomes feasible.

Appendix A

Fourier transformation

This appendix deals with the used definition of the Fourier transform and its connection to the spectral density. Within this thesis the Fourier transformation for any time varying signal or operator $\hat{s}(t)$ is defined as (like in [Sch23])

$$s(\omega) = \mathcal{F}[s(t)](\omega) \equiv \frac{1}{\sqrt{2\pi}} \int_{-\infty}^{\infty} s(t) e^{-i\omega t} dt \tag{A.1}$$

$$s^{\dagger}(\omega) = \mathcal{F}[s(t)^{\dagger}](\omega) \equiv \frac{1}{\sqrt{2\pi}} \int_{-\infty}^{\infty} s(t) e^{-i\omega t} dt \tag{A.2}$$

$$= (\hat{s}(-\omega))^{\dagger}, \tag{A.3}$$

Wherever equation of motion are solved in Fourier space the important following relation for time derivates is useful

$$\frac{d}{dt}\hat{s}(t) = \frac{d}{dt}\mathcal{F}^{-1}[\hat{s}(\omega)](t) = \mathcal{F}^{-1}[i\omega \cdot \hat{s}(\omega)](t) \tag{A.4}$$

$$\therefore \mathcal{F}[\frac{d}{dt}\hat{s}(t)] = i\omega \cdot \hat{s}(\omega) \tag{A.5}$$

Appendix B

Power spectral density

The spectral density $S_{\hat{x}_\mathrm{m},\hat{x}_\mathrm{m}}$, for example of the position $\hat{x}_\mathrm{m}$, is given by the Fourier transform of the autocorrelation function (Wiener-Kinchin theorem)

$$S_{\hat{x}_\mathrm{m},\hat{x}_\mathrm{m}}(\omega) = \langle \hat{x}_\mathrm{m}(\omega)\hat{x}_\mathrm{m}(\omega')\rangle \tag{B.1}$$

$$= \frac{1}{2\pi}\int d\tau \,\langle \hat{x}_\mathrm{m}(t)\hat{x}_\mathrm{m}(t+\tau)\rangle \, e^{-i\omega\tau} \tag{B.2}$$

$$= \frac{1}{2\pi}\int d\tau C(\tau) e^{-i\omega\tau}\,. \tag{B.3}$$

with C being the auto correlation function.
Within this thesis the symmetrized spectrum is used [1], which reads

$$\bar{S}_{\hat{x}_\mathrm{m},\hat{x}_\mathrm{m}} = \frac{1}{2}(S_{\hat{x}_\mathrm{m},\hat{x}_\mathrm{m}}(-\omega) + S_{\hat{x}_\mathrm{m},\hat{x}_\mathrm{m}}(\omega)) \tag{B.4}$$

$$= \frac{1}{2\pi}\int d\tau \,\langle \hat{x}_\mathrm{m}(0)\hat{x}_\mathrm{m}(t)\hat{x}_\mathrm{m}(\tau) + \hat{x}_\mathrm{m}(\tau)\hat{x}_\mathrm{m}(t)\hat{x}_\mathrm{m}(0)\rangle \, e^{-i\omega\tau} \tag{B.5}$$

[1] Denoted by the bar above the S

Appendix C

Relative intensity noise measurements

In section 3.1 the relative intensity noise RIN measured before and behind a filter cavity is shown. In this appendix it will be explained how these measurements were done and how the inferred relative intensity noise RIN^{infere} for different light powers were from these measurements. The in section 3.1 discussed amplitude noise measurement was measured by detecting a 10 mW laser power with a photodetector. Its highpass-filtered output[1] was sent to a signal analyser (SA) to measure the amplitude noise $A_{\text{noise}}^{\text{measured}}(\omega)$ over frequency ω. From the amplitude noise measurement $A_{\text{noise}}^{\text{measured}}(\omega)$ (in units of V) the measured relative intensity noise $RIN^{\text{measured}}(\omega)$ is calculated via

$$RIN^{\text{measured}}(\omega) = \frac{A_{\text{noise}}^{\text{measured}}(\omega)}{\sqrt{RBW}U_{\text{DC}}} \tag{C.1}$$

where RBW is the resolution bandwidth of the signal analyser and $U_{\text{DC}}^{\text{meas}}$ is the DC voltage measured by the photodetector proportional to the measured light power P_{meas}.
As the measured amplitude noise $A_{\text{measured}}^{\text{noise}}(\omega)$ is a combination of classical and uncorrelated shot noise $A_{\text{classical}}^{\text{noise}}(\omega)$ and $A^{\text{SN}}(\omega)$ the measured relative intensity noise $RIN^{\text{measured}}(\omega)$ can be written as

$$RIN^{\text{measured}}(\omega) = \sqrt{\left(RIN^{\text{classical}}\right)^2 + \left(RIN^{\text{SN}}\right)^2} = \sqrt{\left(\frac{A_{\text{noise}}^{\text{classical}}(\omega)}{\sqrt{RBW}U_{\text{DC}}}\right)^2 + \underbrace{\left(\frac{\sqrt{2e}}{I_0}\right)^2}_{\propto \frac{1}{U_{\text{DC}}^{\text{meas}}}}}. \tag{C.2}$$

In Equation (C.2) $RIN^{\text{classical}}$ describes the classical noise contribution and RIN^{SN} the shot noise contribution of the measured RIN^{measured}, with e being the elementary charge and I_0 the output current of the photodetector. Because the classical amplitude noise $A_{\text{noise}}^{\text{classical}}$ is proportional to the light power P_{light} and hence also to the measured voltage $U_{\text{DC}}^{\text{meas}}$ Equation (C.2) can be written with $A_{\text{noise}}^{\text{classical}}(\omega) = C(\omega)U_{\text{DC}}^{\text{meas}}$ and

[1] highpass at 11 kHz to prevent damage to the signal analyser.

$I_0 = \frac{U_{\mathrm{DC}}^{\mathrm{meas}}}{R_0}$ [2] as

$$\begin{aligned} RIN^{\mathrm{measured}}(\omega) &= \sqrt{\left(\frac{C(\omega)\cdot U_{\mathrm{DC}}^{\mathrm{meas}}}{\sqrt{RBW}U_{\mathrm{DC}}^{\mathrm{meas}}}\right)^2 + \left(\frac{\sqrt{2e}}{\frac{U_{\mathrm{DC}}^{\mathrm{meas}}}{R_0}}\right)^2} \\ &= \sqrt{\left(\frac{C(\omega)}{\sqrt{RBW}}\right)^2 + \left(\frac{R_0\sqrt{2e}}{U_{\mathrm{DC}}^{\mathrm{meas}}}\right)^2}, \end{aligned} \tag{C.2a}$$

where $C(\omega)$ is a frequency dependent proportionality factor and R_0 is the transimpedance resistor of the photodetector. Equations (C.2a) reveal that the classical relative intensity noise $RIN^{\mathrm{classical}}(\omega)$ is independent of U_{DC}, whereas the shot noise contribution R^{SN} depends on U_{DC}.

Hence, from the measured relative intensity noise $RIN^{\mathrm{measured}}(\omega)$ at light power P_{meas} the relative intensity noise $RIN^{\mathrm{infer}}(\omega)$ (depicted in Figure 3.2) of an arbitrary light power P_{infere} can be deduced via[3]

$$RIN^{\mathrm{infer}}(\omega) = \sqrt{\left(\frac{A_{\mathrm{noise}}^{\mathrm{classical}}(\omega)}{\sqrt{RBW}U_{\mathrm{DC}}^{\mathrm{meas}}}\right)^2 + \left(\frac{R_0\sqrt{2e}}{U_{\mathrm{DC}}^{\mathrm{meas}}\frac{P_{\mathrm{infere}}}{P_0}}\right)^2}. \tag{C.3}$$

Important

In practice the input impedance of the signal analyser and the input impedance of the oscilloscope (used to measure $U_{\mathrm{DC}}^{\mathrm{meas}}$) and the output impedance of the photodetector are generally not equal and therefore have to be taken into account.

[2] Ohm's law.

[3] The transimpedance resistor R_0 and the DC voltage $U_{\mathrm{DC}}^{\mathrm{meas}}$ have to be measured.

Appendix D

OMIT measurements

Depicted are the measurements with their corresponding fits, from which the values in Table 4.2 have been extracted

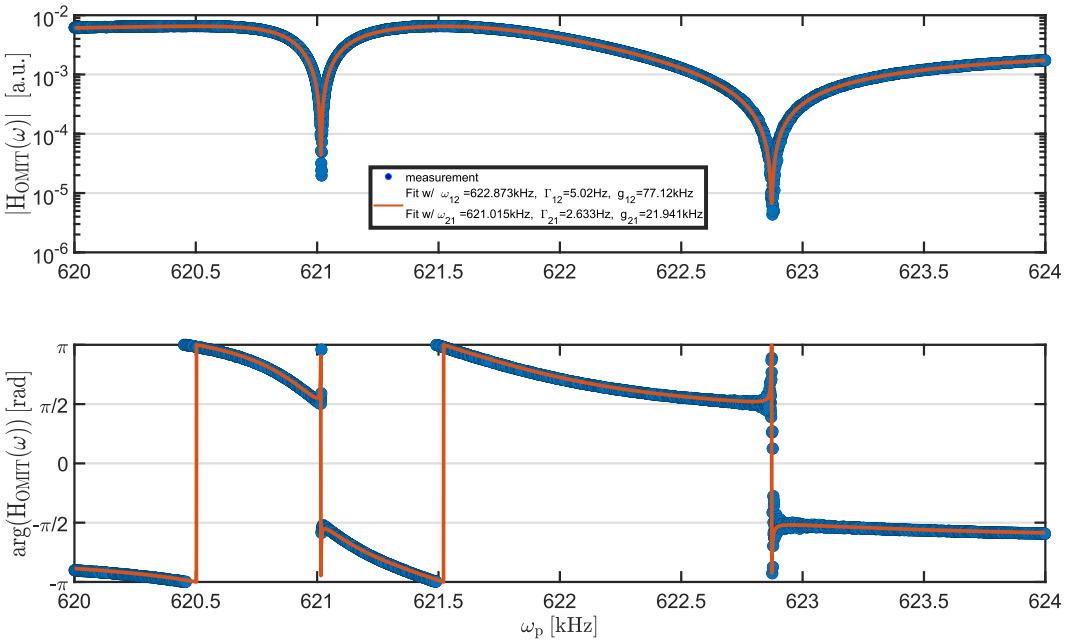

FIGURE D.1: OMIT measurement of $\omega_{1,2}$ and $\omega_{1,2}$

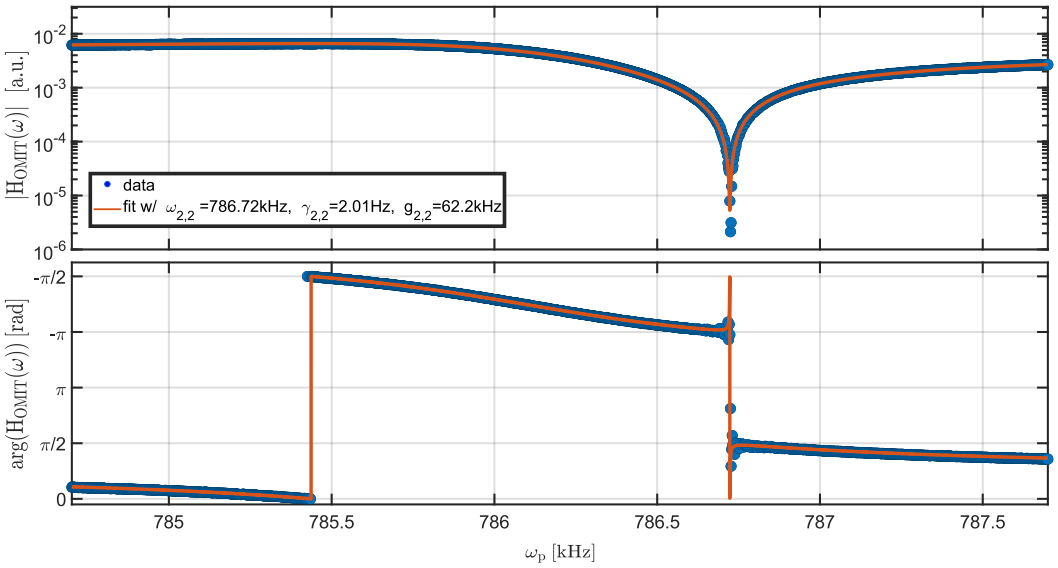

FIGURE D.2: OMIT measurement of $\omega_{2,2}$

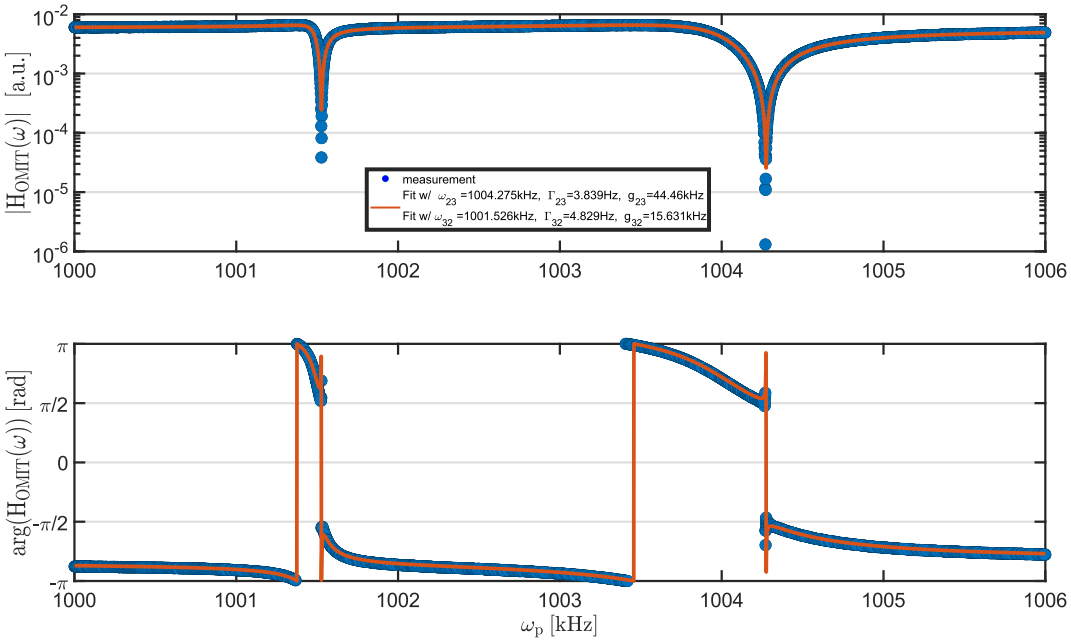

FIGURE D.3: OMIT measurement of $\omega_{2,3}$ and $\omega_{3,2}$

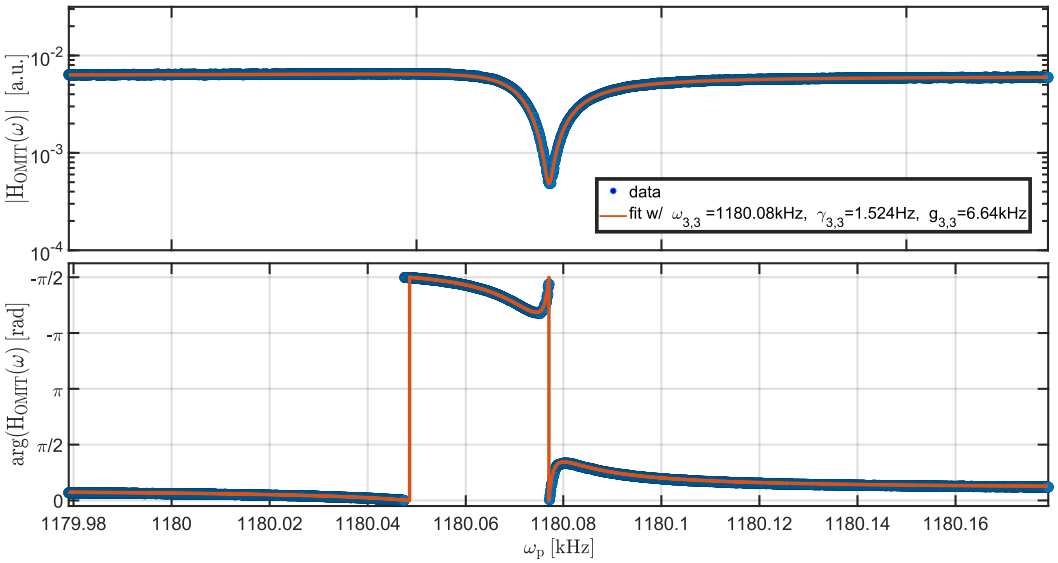

FIGURE D.4: OMIT measurement of $\omega_{3,3}$

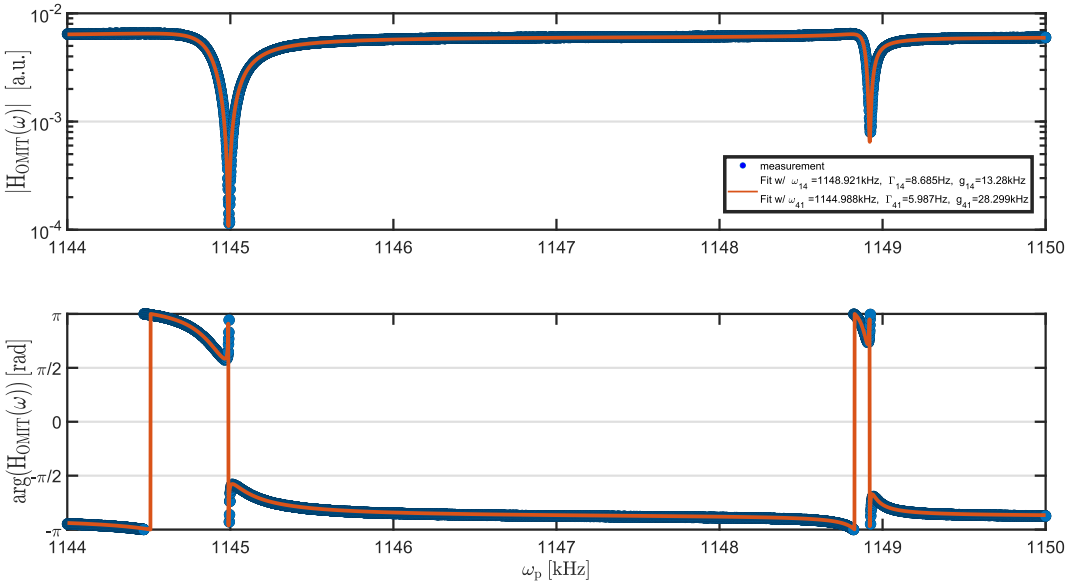

FIGURE D.5: OMIT measurement of $\omega_{1,4}$ and $\omega_{4,1}$

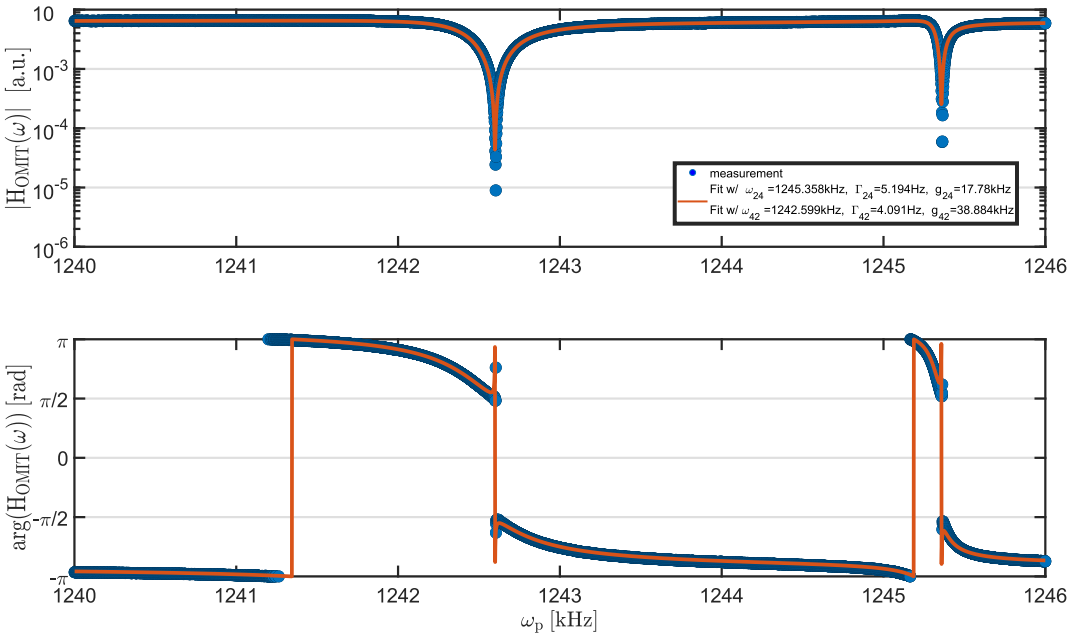

FIGURE D.6: OMIT measurement of $\omega_{2,4}$ and $\omega_{4,2}$

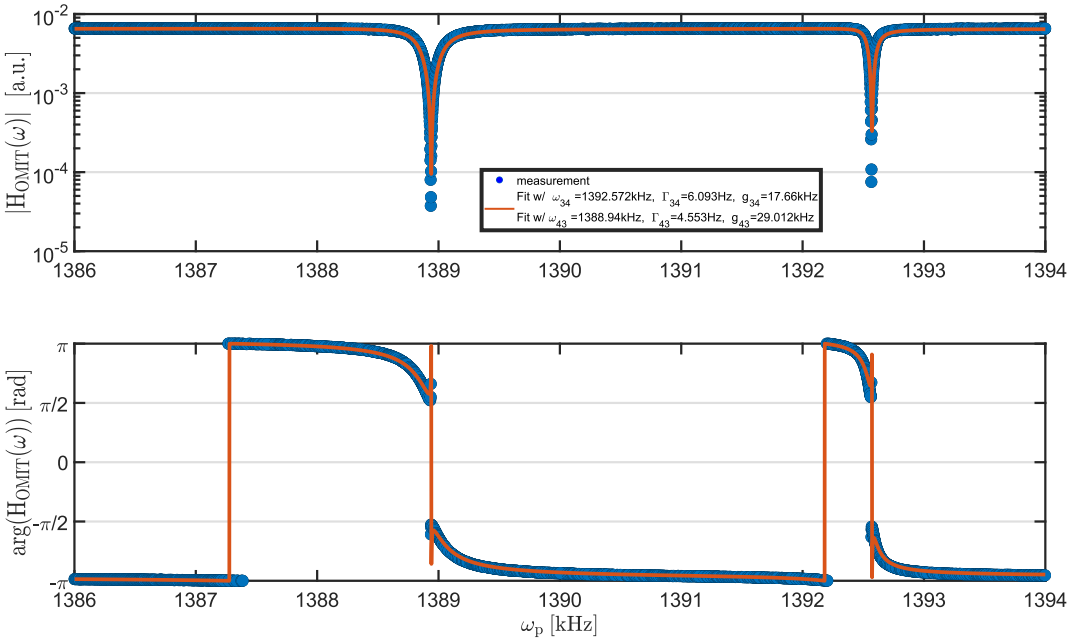

FIGURE D.7: OMIT measurement of $\omega_{3,4}$ and $\omega_{4,3}$

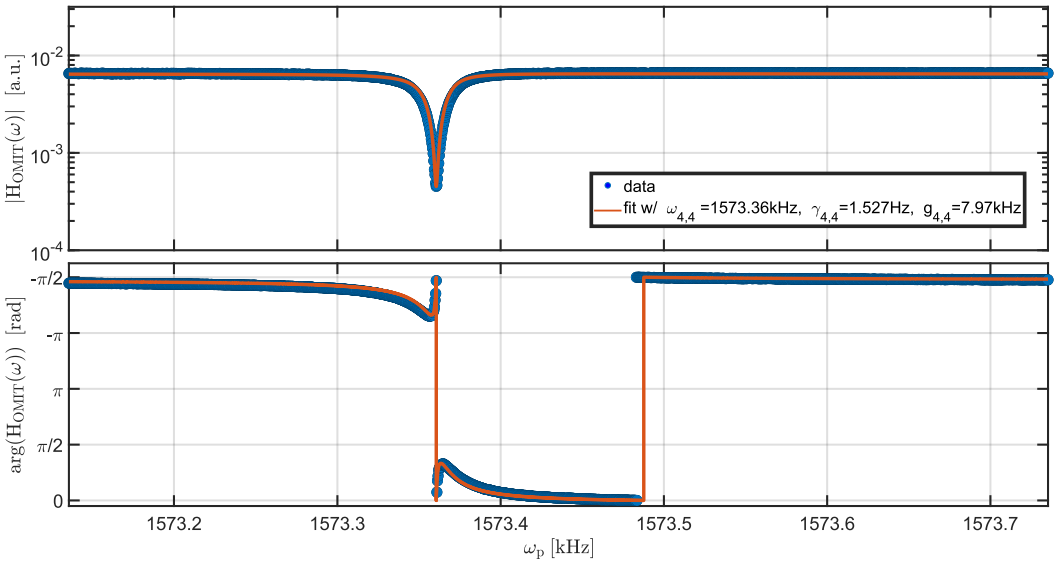

FIGURE D.8: OMIT measurement of $\omega_{4,4}$

Bibliography

[AKM14] M. Aspelmeyer, T. J. Kippenberg, and F. Marquardt. "Cavity optomechanics". In: *Rev. Mod. Phys.* 86 (4 2014), pp. 1391–1452. DOI: 10.1103/RevModPhys.86.1391.

[BR19] H. Bachor and T. C. Ralph. *A Guide to Experiments in Quantum Optics*. Wiley, 2019. DOI: 10.1002/9783527695805.

[Bia+06] S. Bianco et al. "Silicon resonant microcantilevers for absolute pressure measurement". In: *Journal of Vacuum Science & Technology B: Microelectronics and Nanometer Structures Processing, Measurement, and Phenomena* 24.4 (June 2006), pp. 1803–1809. ISSN: 1071-1023. DOI: 10.1116/1.2214698.

[Bla01] E. D. Black. "An introduction to Pound–Drever–Hall laser frequency stabilization". In: *American Journal of Physics* 69 (1 2001). ISSN: 0002-9505. DOI: 10.1119/1.1286663.

[Bon+16] C. Bond, D. Brown, A. Freise, and K. A. Strain. "Interferometer techniques for gravitational-wave detection". In: *Living Reviews in Relativity* 19 (2016). ISSN: 14338351. DOI: 10.1007/s41114-016-0002-8.

[BM15] W. P. Bowen and G. J. Milburn. *Quantum Optomechanics*. CRC Press, Nov. 2015. ISBN: 9780429159312. DOI: 10.1201/B19379.

[BM67] V Braginskii and A Manukin. "Ponderomotive effects of electromagnetic radiation". In: *Soviet Journal of Experimental and Theoretical Physics* 25 (1967), p. 653. URL: https://ui.adsabs.harvard.edu/abs/1967JETP...25..653B (visited on June 25, 2023).

[Bro99] S. Brozek. "Frequenzstabilisierung eines Nd:YAG-Hochleistungs-Laser-Systems für den Gravitationswellendetektor GEO 600". PhD thesis. Gottfried Wilhelm Leibniz Universität Hannover, 1999. DOI: 10.15488/5601.

[Bui+20] A. Buikema et al. "Sensitivity and performance of the Advanced LIGO detectors in the third observing run". In: *Phys. Rev. D* 102 (6 2020), p. 062003. DOI: 10.1103/PhysRevD.102.062003.

[Cat22] L. Catalini. "Nonlinear phenomena in dissipation-diluted nanomechanical resonators". PhD thesis. University of Copenhagen, 2022. URL: https://nbi.ku.dk/english/theses/phd-theses/letizia-catalini/ (visited on May 20, 2023).

[Che19] J. Chen. "Quantum Correlations Generated by a Soft-Clamped Membrane-in-the-Middle System". 2019. URL: https://nbi.ku.dk/english/theses/phd-theses/junxin-chen/ (visited on Feb. 20, 2023).

[Cle14] A. Clerk. "Quantum noise and quantum measurement". In: *Quantum Machines: Measurement and Control of Engineered Quantum Systems: Lecture Notes of the Les Houches Summer School: Volume 96, July 2011*. Oxford University Press, June 2014. ISBN: 9780199681181. DOI: 10.1093/acprof:oso/9780199681181.003.0002.

[DK12] S. L. Danilishin and F. Y. Khalili. "Quantum measurement theory in gravitational-wave detectors". In: *Living Reviews in Relativity* 15 (2012). ISSN: 14338351. DOI: 10.12942/lrr-2012-5.

[DKM19] S. L. Danilishin, F. Y. Khalili, and H. Miao. "Advanced quantum techniques for future gravitational-wave detectors". In: *Living Reviews in Relativity* 22.1 (2019), p. 2. ISSN: 1433-8351. DOI: 10.1007/s41114-019-0018-y.

[Dem08] W. Demtröder. *Experimentalphysik 1 (Mechanik und Wärme)*. Springer-Verlag Berlin Heidelberg, 2008.

[Dre+83] R. W. P. Drever et al. "Laser phase and frequency stabilization using an optical resonator". In: *Applied Physics B* 31.2 (1983), pp. 97–105. ISSN: 1432-0649. DOI: 10.1007/BF00702605.

[Dum+19] V. Dumont et al. "Flexure-tuned membrane-at-the-edge optomechanical system". In: *Opt. Express* 27.18 (2019), pp. 25731–25748. DOI: 10.1364/OE.27.025731.

[FAS66] J. J. Florentin, M. Abramowitz, and I. A. Stegun. "Handbook of Mathematical Functions." In: *The American Mathematical Monthly* 73 (10 1966). ISSN: 00029890. DOI: 10.2307/2314682.

[GZ10] C. Gardiner and P. Zoller. *Quantum Noise A Handbook of Markovian and Non-Markovian Quantum Stochastic Methods with Applications to Quantum Optics. A Handbook of Markovian and Non-Markovian Quantum Stochastic Methods with Applications to Quantum Optics*. Springer-Verlag Berlin Heidelberg, 2010. ISBN: 9783642060946.

[GK04] C. Gerry and P. Knight. *Introductory Quantum Optics*. Cambridge University Press, 2004. DOI: 10.1017/cbo9780511791239.

[Gor+10] M. L. Gorodetksy, A. Schliesser, G. Anetsberger, S. Deleglise, and T. J. Kippenberg. "Determination of the vacuum optomechanical coupling rate using frequency noise calibration". In: *Opt. Express* 18.22 (2010), pp. 23236–23246. DOI: 10.1364/OE.18.023236.

[HC80] T. Hansch and B. Couillaud. "Laser frequency stabilization by polarization spectroscopy of a reflecting reference cavity". In: *Optics Communications* 35.3 (1980), pp. 441–444. ISSN: 0030-4018. DOI: 10.1016/0030-4018(80)90069-3.

[Hen22] P. A. Henry. "Measuring the knot of non-Hermitian degeneracies and non-Abelian braids". PhD thesis. Yale University, 2022. URL: https://harrislab.yale.edu/files/thesis/Henry_Thesis.pdf (visited on Apr. 14, 2023).

[Heu+10] M. Heurs, I. R. Petersen, M. R. James, and E. H. Huntington. "Homodyne Locking of a Squeezer". In: *Conference on Lasers and Electro-Optics 2010*. Optica Publishing Group, 2010, QFA3. DOI: 10.1364/QELS.2010.QFA3.

[Hof15] S. G. Hofer. "Quantum Control of Optomechanical Systems". PhD thesis. Universität Wien, 2015. DOI: 10.25365/thesis.38975.

[Jay+12] A. M. Jayich et al. "Cryogenic optomechanics with a Si3N4 membrane and classical laser noise". In: *New Journal of Physics* 14.11 (2012), p. 115018. DOI: 10.1088/1367-2630/14/11/115018.

[Jay+08] A. M. Jayich et al. "Dispersive optomechanics: a membrane inside a cavity". In: *New Journal of Physics* 10.9 (2008), p. 095008. DOI: 10.1088/1367-2630/10/9/095008.

[Jun+22] J. Junker, D. Wilken, N. Johny, D. Steinmeyer, and M. Heurs. "Frequency-Dependent Squeezing from a Detuned Squeezer". In: *Phys. Rev. Lett.* 129 (3 2022), p. 033602. DOI: 10.1103/PhysRevLett.129.033602.

[KL66] H. Kogelnik and T. Li. "Laser Beams and Resonators". In: *Appl. Opt.* 5.10 (1966), pp. 1550–1567. DOI: 10.1364/AO.5.001550.

[Kol+95] K. S. Kolbig, I. S. Gradshteyn, I. M. Ryzhik, A. Jeffrey, and I. S. Technica. "Table of Integrals, Series, and Products." In: *Mathematics of Computation* 64 (209 1995). ISSN: 00255718. DOI: 10.2307/2153347.

[KWD11] P. Kwee, B. Willke, and K. Danzmann. "New concepts and results in laser power stabilization". In: *Applied Physics B* 102.3 (2011), pp. 515–522. ISSN: 1432-0649. DOI: 10.1007/s00340-011-4399-1.

[LSP12] T. Li, B. Sahoo, and P. K. Panda. "Fabrication of Simple and Ring-Type Piezo Actuators and Their Characterization". In: *Smart Materials Research* 2012 (2012), p. 821847. ISSN: 2090-3561. DOI: 10.1155/2012/821847.

[LR00] R. Lifshitz and M. L. Roukes. "Thermoelastic damping in micro- and nanomechanical systems". In: *Phys. Rev. B* 61 (8 2000), pp. 5600–5609. DOI: 10.1103/PhysRevB.61.5600.

[Lör15] N. Lörch. "Laser Theory for Quantum Optomechanics". PhD thesis. Gottfried Wilhelm Leibniz Universität Hannover, 2015. DOI: 10.15488/8519.

[Mas+19] D. Mason, J. Chen, M. Rossi, Y. Tsaturyan, and A. Schliesser. "Continuous force and displacement measurement below the standard quantum limit". In: *Nature Physics* 15.8 (2019), pp. 745–749. ISSN: 1745-2481. DOI: 10.1038/s41567-019-0533-5.

[McC+20] L. McCuller et al. "Frequency-Dependent Squeezing for Advanced LIGO". In: *Phys. Rev. Lett.* 124 (17 2020), p. 171102. DOI: 10.1103/PhysRevLett.124.171102.

[Meh12] M. Mehmet. "Squeezed light at 1064 nm and 1550 nm with a nonclassical noise suppression beyond 10 dB". PhD thesis. Gottfried Wilhelm Leibniz Universität Hannover, 2012. DOI: 10.15488/7913.

[Moe+17] C. B. Moeller et al. "Quantum back-action-evading measurement of motion in a negative mass reference frame". In: *Nature* 547.7662 (2017), pp. 191–195. ISSN: 1476-4687. DOI: 10.1038/nature22980.

[MN18] R. Moghadas Nia. "Multimode optomechanics in the strong cooperativity regime - Towards optomechanical entanglement with micromechanical membranes". PhD thesis. Gottfried Wilhelm Leibniz Universität Hannover, 2018. DOI: 10.15488/4083.

[Nie+17] W. H. P. Nielsen, Y. Tsaturyan, C. B. Møller, E. S. Polzik, and A. Schliesser. "Multimode optomechanical system in the quantum regime". In: *Proceedings of the National Academy of Sciences* 114.1 (2017), pp. 62–66. DOI: 10.1073/pnas.1608412114.

[Ors16] M. Orszag. *Quantum optics: Including noise reduction, trapped ions, quantum trajectories, and decoherence*. 2nd Edition. Springer-Verlag Berlin Heidelberg, 2016. DOI: 10.1007/978-3-319-29037-9.

[PM19] J. Pinto Moura. "Making light jump: Photonic crystals on trampoline membranes for optomechanics experiments". PhD thesis. Delft University of Technology, 2019. DOI: 10.4233/UUID:F090D58F-558C-47ED-8C9C-3152DADBC4AE.

[PH15] E. S. Polzik and K. Hammerer. "Trajectories without quantum uncertainties". In: *Annalen der Physik* 527.1-2 (2015), A15–A20. DOI: 10.1002/andp.201400099.

[PPR13] T. P. Purdy, R. W. Peterson, and C. A. Regal. "Observation of radiation pressure shot noise on a macroscopic object." eng. In: *Science (New York, N.Y.)* 339 (6121 2013), pp. 801–4. DOI: 10.1126/science.1231282.

[Qiu+20] L. Qiu, I. Shomroni, P. Seidler, and T. J. Kippenberg. "Laser Cooling of a Nanomechanical Oscillator to Its Zero-Point Energy". In: *Phys. Rev. Lett.* 124 (17 2020), p. 173601. DOI: 10.1103/PhysRevLett.124.173601.

[Sau17] P. R. Saulson. *Fundamentals of Interferometric Gravitational Wave Detectors*. 2nd Edition. WORLD SCIENTIFIC, 2017. DOI: 10.1142/10116.

[Sch09] A. Schließer. "Cavity Optomechanics and Optical Frequency Comb Generation with Silica Whispering-Gallery-Mode Microresonators". PhD thesis. Oct. 2009. DOI: 10.5282/edoc.10940.

[SVR16] S. Schmid, L. G. Villanueva, and M. L. Roukes. *Fundamentals of Nanomechanical Resonators*. Springer International Publishing, 2016. DOI: 10.1007/978-3-319-28691-4.

[Sch23] J. Schweer. "Quantum back-action evasion and filtering in optomechanical systems". PhD thesis. Gottfried Wilhelm Leibniz Universität Hannover, 2023. DOI: 10.15488/13289.

[Sch+22] J. Schweer, D. Steinmeyer, K. Hammerer, and M. Heurs. "All-optical coherent quantum-noise cancellation in cascaded optomechanical systems". In: *Physical Review A* 106 (3 2022). ISSN: 24699934. DOI: 10.1103/PhysRevA.106.033520.

[SGM99] D. A. Shaddock, M. B. Gray, and D. E. McClelland. "Frequency locking a laser to an optical cavity by use of spatial mode interference". In: *Opt. Lett.* 24.21 (1999), pp. 1499–1501. DOI: 10.1364/OL.24.001499.

[Ste19] D. Steinmeyer. "Subsystems for all-optical coherent quantum-noise cancellation". PhD thesis. Gottfried Wilhelm Leibniz Universität Hannover, 2019. DOI: 10.15488/9179.

[Tap+19] B. D. Tapley et al. "Contributions of GRACE to understanding climate change". In: *Nature Climate Change* 9.5 (2019), pp. 358–369. ISSN: 1758-6798. DOI: 10.1038/s41558-019-0456-2.

[TC10] M. Tsang and C. M. Caves. "Coherent Quantum-Noise Cancellation for Optomechanical Sensors". In: *Phys. Rev. Lett.* 105 (12 2010), p. 123601. DOI: 10.1103/PhysRevLett.105.123601.

[TC12] M. Tsang and C. M. Caves. "Evading Quantum Mechanics: Engineering a Classical Subsystem within a Quantum Environment". In: *Phys. Rev. X* 2 (3 2012), p. 031016. DOI: 10.1103/PhysRevX.2.031016.

[Tsa+17] Y. Tsaturyan, A. Barg, E. S. Polzik, and A. Schliesser. "Ultracoherent nanomechanical resonators via soft clamping and dissipation dilution". In: *Nature Nanotechnology* 12.8 (2017), pp. 776–783. ISSN: 1748-3395. DOI: 10.1038/nnano.2017.101.

[Tsa19] Y. Tsaturyan. "Ultracoherent soft-clamped mechanical resonators for quantum cavity optomechanics". PhD thesis. University of Copenhagen, 2019. URL: https://nbi.ku.dk/english/theses/phd-theses/yeghishe-tsaturyan/.

[Vah08] H. Vahlbruch. "Squeezed Light for Gravitational Wave Astronomy". PhD thesis. Gottfried Wilhelm Leibniz Universität Hannover, 2008. DOI: 10.15488/7152.

[Ver+06] S. S. Verbridge, J. M. Parpia, R. B. Reichenbach, L. M. Bellan, and H. G. Craighead. "High quality factor resonance at room temperature with nanostrings under high tensile stress". In: *Journal of Applied Physics* 99.12 (June 2006), p. 124304. ISSN: 0021-8979. DOI: 10.1063/1.2204829.

[VS14] L. G. Villanueva and S. Schmid. "Evidence of Surface Loss as Ubiquitous Limiting Damping Mechanism in SiN Micro- and Nanomechanical Resonators". In: *Phys. Rev. Lett.* 113 (22 2014), p. 227201. DOI: 10.1103/PhysRevLett.113.227201.

[WM08] D. F. Walls and G. J. Milburn. *Quantum optics*. Springer-Verlag Berlin Heidelberg, 2008. DOI: 10.1007/978-3-540-28574-8.

[Wei+10] S. Weis et al. "Optomechanically Induced Transparency". In: *Science* 330.6010 (2010), pp. 1520–1523. DOI: 10.1126/science.1195596.

[Wei72] R. Weiss. "Electromagnetically coupled broadband gravitational wave antenna". In: *Q.Prog. Rep. Research Lab. Electronics, Massachusetts Inst. Technol. 105* (1972). URL: https://dcc.ligo.org/LIGO-P720002/public.

[Wil12] D. J. Wilson. "Cavity Optomechanics with High-Stress Silicon Nitride Films". PhD thesis. 2012. DOI: 10.7907/VB3C-1G76.

[WR+11] I. Wilson-Rae et al. "High-Q Nanomechanics via Destructive Interference of Elastic Waves". In: *Phys. Rev. Lett.* 106 (4 2011), p. 047205. DOI: 10.1103/PhysRevLett.106.047205.

[Wim+14] M. H. Wimmer, D. Steinmeyer, K. Hammerer, and M. Heurs. "Coherent cancellation of backaction noise in optomechanical force measurements". In: *Physical Review A* 89.5, 053836 (May 2014), p. 053836. DOI: 10.1103/PhysRevA.89.053836.

[Yu+14] P.-L. Yu et al. "A phononic bandgap shield for high-Q membrane microresonators". In: *Applied Physics Letters* 104.2 (Jan. 2014), p. 023510. ISSN: 0003-6951. DOI: 10.1063/1.4862031.

Acknowledgements

After so many words have been written, they are now missing. So this is just an attempt to do justice to all who have supported me.

First of all, I would like to thank my supervisors.

Thank you, Michéle, for choosing me as a part of the group. Also, for the trust and opportunity you gave me to move freely in the field of optomechanics and, more importantly, for your support when the backaction part of it and other things became too big. Regardless of the topic, speaking to you was always possible.

Thank you, Klemens, for allowing me to ask questions about theory also at any time. Often I got lost in the theory, but thanks to the discussions, I got back on the right track.

Thank you, Stefan, for always finding the time in Hannover to support me in theory questions and agreeing to be one of my examiners.

Of course, this work would only have come up with old and current group members. Therefore, I want to thank Max, Timo, Dirch and Daniel, who made a start in the Quantum Control group and in Hanover, more enjoyable. If life gives you lemons, you know what to do ;) Furthermore, thanks to Dirch for ghost-reading my thesis ;D.

I would also like to thank Daniel for his help, during the last steps of writing and for making "pingeln" great again.

Thank you, Jonas and Dennis, not only for several discussions about membrane in the middle setups:D, also for, but not only for proofreading.

Thank you, Roman for supporting me and also for proofreading this thesis and not for supplying the office with MAOAM, which, by the way, I never saw ;)

Thanks, Jakob, for proofreading and helping me, even at unusual times.

I also want to thank my family, who have supported me unconditionally my whole life.

Finally, thank you, Anna-Lena. Without your support, not only within the last months, this work would not have been possible. Thank you very, very much (Kiek!).